A Power Converter with a Rotating Secondary Stage for an Airborne Radar System

Konstantinos D. Papastergiou

A thesis submitted for the degree of Doctor of Philosophy.
The University of Edinburgh.
November 2005

Abstract

Contact-less transfer of energy has always been a desired feature for systems that require reliable and durable power transfer across their moving parts. In rotary equipment in particular, slip-rings are the established solution with off-the-shelf and customised solutions readily available in the market. Despite the mature technology, slip-rings suffer wear and are prone to arcing, making frequent maintenance a necessity. In this project a rotating transformer is proposed as an alternative solution for contact-less transfer of energy across the revolving frame of an airborne electronic-scanning radar.

This thesis is based on the hypothesis that *the Phase-Shifted Full Bridge (PSFB) topology can effectively utilise the parasitic components of the rotating transformer to achieve efficient (over 90%) power conversion at the kW range.*

The first part of this work concentrates on the study of the magnetic interface and its electrical properties. Initially the magnetic structure of the transformer is studied in order to gain understanding of the effects of the physical layout of the component to its electrical behaviour. The problems of low magnetising and increased leakage inductance are quantified by measurements, calculations and finite element analysis. An accurate electrical model is built and used to calculate the transformer voltage and current gain.

The second part of the research programme aims at the compilation of a design strategy for a PSFB incorporating a rotating transformer. An algorithm is presented, that optimises the magnetic component structure in order to achieve minimum switching losses and spread the conduction losses between the transformer and power switches.

The last stage involves the evaluation of the design algorithm through prototyping and testing. Some topological variations are tested and compared with the original conventional PSFB converter. The thesis concludes with a discussion of the results and future challenges.

Declaration of originality

I hereby declare that the research recorded in this thesis and the thesis itself was composed and originated entirely by myself in the School of Engineering and Electronics at The University of Edinburgh.

Konstantinos D. Papastergiou

Κωνσταντίνος Δ. Παπαστεργίου

Acknowledgements

I would like to thank my supervisor Dr Ewen Macpherson for his guidance, encouragement and continued support during the last four years. His knowledge and expertise have been invaluable.

I must also express my gratitude to the funding bodies of this project, the British Aerospace Industry - BAE Systems and the School of Engineering and Electronics.

Mr Frank Fisher my industrial advisor has offered valuable information on the airborne radar systems. I would like to thank my colleagues at the University, Prof. Stephen Salter (for his advice on the mechanical design), Douglas Carmichael, Richard Loh, Edward Lord and Jonathan Shek for making the endless hours in in the lab enjoyable.

I would like to thank my parents Δημήτρης and Ολυμπία and my sister Μαρία and brother Αλέξανδρος for their continued love and care.

Last thank you Βίκυ μου for offering me a thousand good moments for every difficult one I had.

To my parents Dimitrios and Olympie.

Στους γονείς μου Δημήτρη και Ολυμπία.

"The book is on the table."

Αριστοτέλης, 384-322 BC

Contents

List of figures

List of tables

Acronyms and abbreviations

AC	Alternating Current
AP	Active to Passive
BAE	British Aerospace System
CCM	Continuous Current Mode
CD	Current Doubler
CTE	Contact-less Transfer of Energy
DC	Direct Current
DCM	Discontinuous Current Mode
EM	Electromagnetic
EMC	Electromagnetic Compatibility
EMI	Electromagnetic Interference
ESR	Equivalent Series Resistance
FWR	Full Wave Rectifier
MOSFET	Metal Oxide Field Effect Transistor
PA	Passive to Active
PCB	Printed Circuit Board
PFC	Power Factor Correction
PSFB	Phase-shifted Full Bridge
PWM	Pulse Width Modulation
RF	Radio Frequency
RMS	Root Mean Square
SMPS	Switched Mode Power Supply
SPICE	Simulation Program with Integrated Circuit Emphasis
TWT	Travelling Wave Tube
ZCS	Zero Current Switching
ZVS	Zero Voltage Switching
ZVT	Zero Voltage Transition

Nomenclature

In this work the symbols used for instantaneous values of variables such as voltage, current and power are the lowercase letters v(t), i(t), p(t). The upper case symbols refer to average and rms values and the peak values are indicated with the "" symbol on top of the uppercase letter.

B	Magnetic flux density
B_f	Final (peak value of the flux density in a B-H loop
H	Magnetic field intensity
H_1	Final value of magnetic field intensity in a B-H loop
ω_0	Angular velocity of the electron without external field
ω_1	Angular velocity of the electron under an external magnetic field
μ_a	Permeability of the air
μ_0	Permeability of the air
μ_r	Relative permeability of a material
μ_{ef}	Effective permeability of a material with a distributed air gap
P_h	Hysteresis losses
f_{sw}	Switching frequency
P_{eddy}	Eddy current generated losses
ρ	Electrical resistivity of a material
D_{pen}	Penetration depth due to skin effect
F	Magnetomotive force mmf
L_m	Magnetising inductance
L_{lk1}	Leakage inductance of the primary winding
L_{lk2}	Leakage inductance of the secondary winding
M	Transformer mutual inductance
$L_{p_{ss}}$	Inductance of the primary winding measured with the secondary winding short-circuited
$L_{p_{oc}}$	Inductance of the primary winding measured with the secondary winding open-circuited
$L_{s_{oc}}$	Inductance of the secondary winding measured with the primary winding open-circuited

V_{pri}	Primary winding voltage
N_{pri}	Primary winding number of turns
V_{sec}	Secondary winding voltage
N_{sec}	Secondary winding number of turns
Φ	Magnetic flux
R_m	Magnetic reluctance
P_m	Magnetic permeance
$\vec{J}$	Electric current density vector
$\vec{A}$	The vector field
l_g	Transformer Air gap length
l_c	Magnetic core effective length
A_g	Air gap cross sectional area
A_c	Magnetic core cross sectional area
l_sp	Effective length of the leakage inductance magnetic path
A_sp	Cross-sectional area of the leakage inductance magnetic path
R_{eff}	Effective resistance of the transformer winding
R_{dc}	DC resistance of the transformer winding
p	Number of layers of a transformer winding
d	Effective thickness of a layer of the transformer winding
δ_0	Skin (or penetration) depth
C_{A+}	The inherent capacitance of the PSFB MOSFET switch T_{A+}
D_{A+}	The body diode of the respective PSFB MOSFET switch T_{A+}
$v_c(t)$	Instantaneous voltage across the resonant capacitor
$i_L(t)$	Instantaneous current through the resonant inductor
I_{L0}	Initial current through the resonant inductor
V_{C0}	Initial voltage across the resonant capacitor
Z_0	Characteristic impedance of a resonant network
L_r	Resonant inductance
C_r	Resonant capacitance
Δ	d/δ_0
Ψ	$\frac{5\times p^2-1}{15}$
K	Loss or gain in dB between close-field probe and oscilloscope

Chapter 1
Introduction

Many applications require electrical energy to be transferred across an interface to moving equipment. If this can be achieved using contact-less techniques, there are clear advantages to be gained in terms of safety, reliability and endurance. Contact-less transfer of energy can be performed by establishing a magnetic link between the stationary and moving parts of a device. The revolution of high-frequency switching power conversion allowed the magnetic link to be implemented with reasonably sized components. Since then, a variety of inductive couplers have been proposed for, virtually, every power electronics application.

In rotary equipment in particular, slip-rings are the established solution, with off-the-shelf and customised solutions readily available in the market. Despite the mature technology, slip-rings suffer wear and are prone to arcing, making frequent maintenance a necessity. In this project a rotating transformer is proposed as an alternative solution for contact-less transfer of energy across the revolving frame of an airborne electronic-scanning radar.

This Chapter introduces the reader to the background of the research project. It summarises the main problems, challenges and objectives related to this technology, and describes the organisation of the work in three main parts; the analysis of the magnetic component, the power electronics optimisation and the experimental evaluation.

1.1 Research Background

The Travelling Wave Tube (TWT) is the most common power amplifier/transmitter for use in radar systems. It is a single amplifier that handles large amounts of pulsed power (up to the MW range peak). The TWT requires the appropriate power supply unit to provide an average of 15-20kW of power in very short time intervals. In practice, several supply voltages are required for the heater, modulator, grid bias, collector and beam (cathode) [2] of the tube. The cathode and collector voltages in particular are in

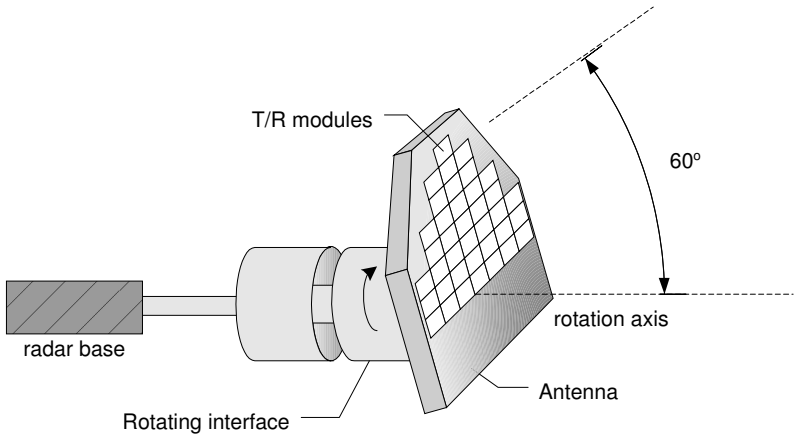

Figure 1.1: *The phased array radar comprising of 1024 transmit/receive solid state antennas. Rotation of the antenna around the horizontal axis to allow a greater scanning angle.*

the range 5 to 20kV resulting in stringent insulation requirements. Another difficulty derives from the requirement for very low noise or ripple of the power supplies. The reason is because any ripple on the TWT electrode voltages modulates the transmitted waveform in such a way as to appear as false targets to the radar system.

The TWTs of the type used in airborne radars are prone to arcing. This appears as a short-circuit from cathode to ground, grid to ground or collector to ground. The cathode to ground short is the most common. The design of the power supply must therefore be tolerant of short-circuit conditions. All of the above issues pose reliability issues to both the TWT and the power supply operation. The concentration of vast amounts of pulsed power in a single power supply-amplifier-transmitter had to be reconsidered.

The latest generation of radars moved away from mechanically scanned antennae and single transmitters and receivers. Instead an array of solid state microwave antennas is used. The phased-array is not new in radar applications. It appeared in 1943 (as did the TWT), however its manufacturing and operating complexity kept it in the dark for many years. The modern array consists of typically 1024 separate microwave transmit-receive modules (TRMs) that replace the single transmitter and receiver of TWT radar (see figure 1.1). The modular structure of the transmiter/receiver of the Electronically Scanned (ESCAN) radar has the advantage of immunity to single point failures. If one or two modules stop working, the radar still operates, though with reduced performance.

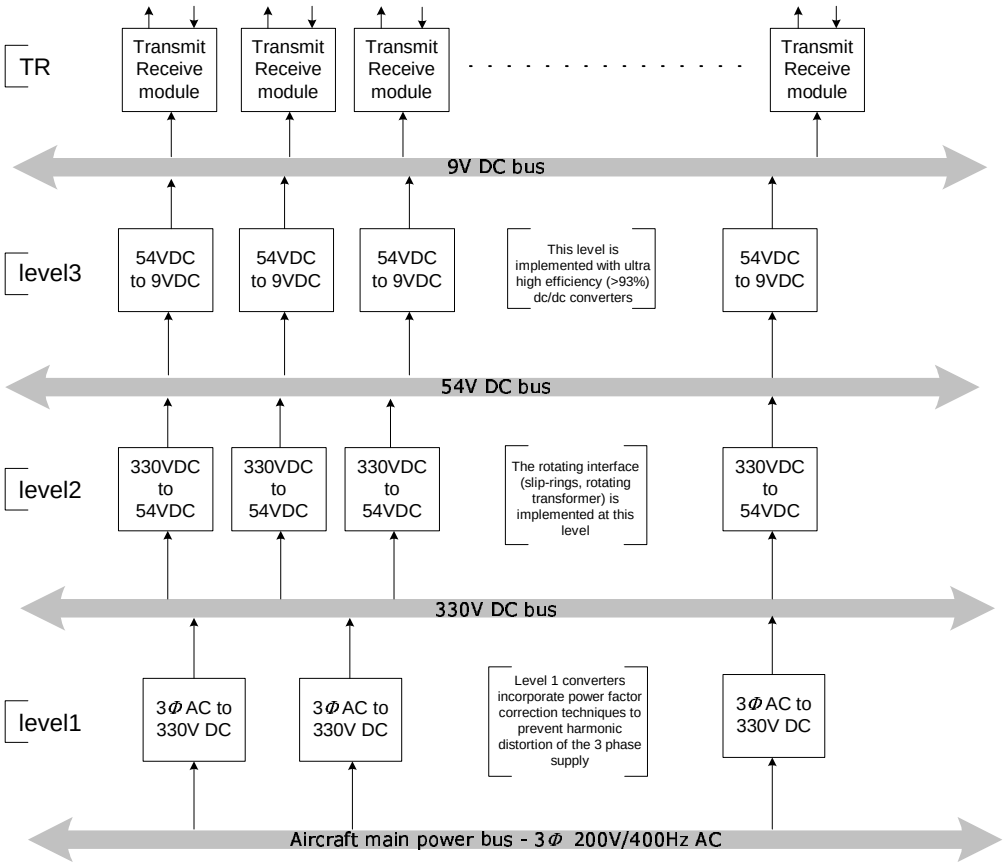

Figure 1.2: *A typical three level power supply system for an airborne electronic-scanning radar.*

Each of the TR modules requires a supply voltage in the range 5 to 15V dc. The total current requirement exceeds 1000A, hence the high voltage requirement of the TWT has now become a high current requirement.

The modularity of the ESCAN radar also applies to its power supply architecture. Frank Fisher of BAE Systems in one of his reports suggests [2] the architecture of figure 1.2. Rather than using a single high power converter, several modules are employed to feed a common power bus. In this arrangement the failure of one or more converters can be tolerated without any loss of system performance.

The same report suggested a 3-level power supply architecture. The first level contains the rectifiers that convert the main 3 phase (200V, 400Hz) supply to a 270V dc, combined with a power factor correction (PFC) unit that boosts the voltage from 270V dc to 330V dc. The PFC units are required in order to keep the aircraft mains free of harmonic

distortion. The level 1 converters deliver 2-3kW each, thus between 4 and 6 of them are needed to provide 10kW with a redundancy of 1 module.

The next level of the architecture comprises of a parallel combination of highly efficient (over 90%) dc/dc converters that convert the 330V to an intermediate 54V dc. This is the stage where the rotating interface is implemented. Slip rings are typically used to transfer energy to the rotating part of the radar. At 54V the current can be transferred through a reasonably sized slip-ring module due to the relatively low current and also low voltage that reduces the insulation requirements (and the possibility of arcing at high altitudes[1]).

The 3rd level of the power supply architecture comprises of several ultra efficient (typically higher than 93%) dc/dc converters that transform the 54V intermediate supply to the 9V dc that is required to feed the solid state TR elements.

1.1.1 Transfer of power across the moving part

The solid state phased-array provides much more flexibility in its beam steering and shaping, multiple target tracking, fast scanning and better anti-jamming functions. The disadvantages of the phased-arrays are the increased manufacturing cost, the need for more data links and more elaborate signal processing. Another significant limitation of the static phase-array radars is their relatively narrow scanning angle of 60% (maximum) [3, 4]. To enable the solid state radar to match the scan coverage of the conventional mechanically scanned radars, a slow 360^o rotation of the static array may be required. The above idea is illustrated in figure 1.1, where a rotary interface is used to rotate the antenna platform and double the scanning angle of the radar.

The rotating transformer could also be used to allow vertical rotation of the phased-array as shown in figure 1.3. In both cases the rotating transformer handles the same amount of power and therefore its size and geometry are practically the same.

The introduction of a rotating interface, such as the ones of figures 1.1 and 1.3, increase the risk of mechanical faults and compels frequent maintenance work. The established

[1] According to data taken from IPC-2221 [2] generic standard on printed circuit board design the distance between 2 tracks should be 2.5mm in the 301-500V range when operating at sea-level. For the same voltage range the tracks distance required at a height of 3050m is 12.5mm.

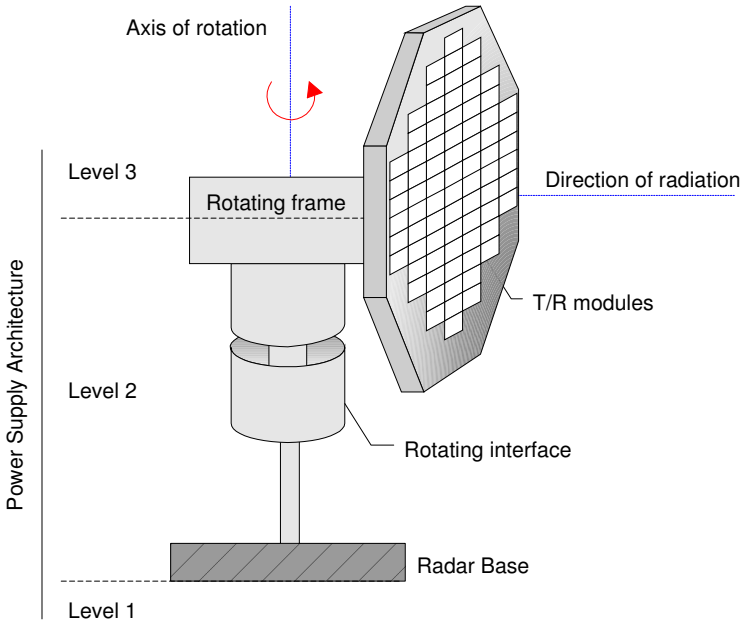

Figure 1.3: *360º rotation around the vertical axis of the phased array antenna*

technology for transferring energy to rotating equipment is slip-rings. Slip-rings rely on contact between a silver loaded graphite brush and a precious metal ring. Despite the maturity of the technology, slip-rings have a limited life span that depends on the speed of rotation[2]. Furthermore, slip rings are prone to arcing under certain conditions such as severe vibration and aircraft acceleration. In the event that interrupts do occur it is important to know how the slip-ring will behave. This depends on the instantaneous voltage and current and the circuit impedance. In an aircraft the situation deteriorates at high altitudes (low pressure) as the breakdown voltage of the air becomes smaller and arcing is more likely to happen. For the same reason there is a limitation in the distance between the slip-rings.

Another problem derives from the co-existence of 70 signal and power lines in the same slip-rings assembly. Electromagnetic Interference (EMI) problems have been reported because of the fundamental incompatibility of high current pulses and sensitive signal wires in close proximity. Crosstalk and noise problems can be treated by taking measures, such as keeping signals and power as far apart as possible and placing signals and their returns on adjacent connections.

[2]The brush life is typically 600hrs at 1000fpm (1 feet per minute=0.3metres per minute, referring to the speed of the brush with respect to the slip-ring) rising to 3000hrs at 250fpm.

Positive	Negative
◇ mature technology	◇ limited life span, frequent maintenance
◇ readily available and customisable designs	◇ prone to arcing
◇ reliable operation within nominal lifetime	◇ possible cross-talk and EMI
◇ large number of ac and dc contacts	◇ cost, volume and weight
◇ high power rating	◇ collaboration with slip-ring manufacturer

Table 1.1: *The positive and negative points of the slip-ring technology*

Table 1.1 summarises the advantages and disadvantages of the slip-rings.

1.1.2 Rotating transformer

The rotating transformer is proposed as an alternative to slip-rings. The rotating transformer is best suited for applications with special requirements such as mechanical endurance and increased reliability.

The rotating transformer establishes a magnetic link between the stationary and the rotating parts of the radar. It is free of electrical contacts, slip rings and brushes and thus the maintenance work and related costs are eliminated. Practically, the only life limiting factor of the rotating transformer is the ball bearings between the stationary and rotating parts. The life of these components can be increased significantly by carefully calculating the loading and various forces due to vibration etc. A technique that maximises the reliability and life cycle of the rotating transformer is proposed in Chapter 7.

The rotating transformer is advantageous when operating in harsh environments with severe equipment vibration, acceleration, explosive gasses and humidity. Another advantage is that it can be designed in-house as part of the radar power supply and can be manufactured in a workshop with the basic equipment.

The rotating transformer is therefore particularly suited for applications with minimum or no-access to the equipment (military, satellite, marine etc.) when a simple, reliable and economic solution is required.

The disadvantage of the rotating transformer is that it only provides one channel of power and the multiple signals that are required in a radar application need to be transferred through other routes (e.g. rotary optical joints, lasers etc). Additionally, multiple rotating transformers are needed in order to transfer the 15-20kW that are

Positive	Negative
◇ long-life expectancy	◇ integration with power electronics design
◇ maintenance free	◇ multiple transformers may be needed
◇ safe, no contacts, no arcing	◇ one AC power channel only
◇ economic, can be developed in-house	◇ possible EMI due to fringing field
◇ operates in harsh conditions	◇ power capacity limitation

Table 1.2: *The positive and negative points of the rotating transformer technology*

required in the current application. Finally, as will be seen in the following chapters, the low frequency electromagnetic noise appears to be increased around the transformer air-gap.

The positive and negative points of a rotating transformer are summarised in table 1.2.

1.2 Initial Hypothesis

The rotating transformer was suggested by BAE Systems (who sponsored this research) as an alternative means of transferring power to the rotating frame of an electronic scanning radar system. The inherent air-gap in a rotating transformer means that it resembles in its electrical properties a coupled inductor such as the one used in flyback converters[3]. The difference is that the rotating transformer is required to operate as a transformer and not as an energy storing element. The low magnetising inductance results in increased primary winding current, which in turn aggravates the primary side conduction losses. On the other hand, the physical separation between the primary and secondary windings results in increased leakage inductance, which impairs the voltage gain of the transformer.

The Phase-Shifted Full Bridge (PSFB) converter is known for its ability to utilise the transformer parasitics. A thorough search in the scientific literature revealed a need for further investigation of the potential combination of a PSFB with a rotating transformer. The hypothesis that is being tested in this work is that,

the Phase-Shifted Full Bridge (PSFB) topology can effectively utilise the parasitic components of the rotating transformer to achieve efficient (over 90%) power conversion at the kW range.

[3]The use of a flyback converter in this application is impractical due to the high power level required.

The aim is to test the feasibility of such an interface and, if possible, develop a design methodology to enable the integration of the rotary transformer into a PSFB converter.

1.3 Research Objectives and Project Milestones

This project has several distinct objectives:

1. To investigate the electric and magnetic behaviour of a rotating transformer.
2. To analyse the phase-shifted full bridge converter and its ability to effectively utilise the different parasitic components.
3. To identify possible ways of integrating the rotary interface into a PSFB.
4. To develop a design methodology which maximises the power transfer capability of the rotating transformer in a phase-shifted full bridge.
5. To adapt an existing PSFB prototype and evaluate its performance with a conventional and a rotating transformer.

To accomplish the above objectives a three-phase approach was employed;

- Phase 1: Analysis of the rotating transformer. During this phase the electrical behaviour of the rotating transformer was investigated and its electrical characteristics were quantified. The electrical properties of the transformer are associated with geometrical structure. Some guidelines were produced in order to minimise the leakage inductance and improve coupling. This phase resulted in the derivation of electrical models for the adjacent and coaxial winding transformers.
- Phase 2: Analysis of the phase shifted bridge converter. In particular, the effect of the high magnetising current was investigated. The interval-by-interval mathematical description of the converter was developed with special attention to the resonant operation of the bridge. A design methodology was derived to allow the integration of the rotating transformer in the PSFB with emphasis on the optimisation of the conduction and switching losses.

- Phase 3: Experimental evaluation. The PSFB prototype (including possible topological alternatives) was tested with the proposed rotating transformer arrangements. Conclusions are drawn regarding the accuracy of the proposed design methodology. The ability of the PSFB to tolerate the rotating transformer parasitics is assessed.

1.4 Contribution to Knowledge

In this research the electrical behaviour of a rotating transformer has been studied and its electrical properties have been associated with its geometrical characteristics. A set of simple rules has been proposed to minimise the leakage inductance and hence improve the transformer coupling.

The effect of the rotating transformer on the operation of the PSFB and especially the importance of the magnetising current in the soft-switching operation have been shown.

A design methodology has been proposed for integrating the rotating transformer into the phase-shifted full bridge converter. The resulting prototype was tested and demonstrated efficient operation.

This work suggests that the phase-shifted bridge converter not only tolerates the parasitic components of the rotating transformer but also utilises them to extend the soft-switching range of the primary switches. The result is highly efficient operation over the entire load range.

The penalty is an increased magnetic core size in order to reduce the magnetising current and accommodate a larger wire gauge. The elimination of the slip rings and of the auxiliary inductor may result in a smaller overall size.

1.5 Thesis Outline

Chapter 2 reviews the previous applications of contact-less transfer of energy in various fields of dc/dc power conversion. Emphasis is given on the magnetic interfaces that have been proposed and their electrical characteristics. The identification of their main deficiencies allows the optimisation of the magnetic structure to achieve better coupling.

The topological alternatives for contact-less transfer of energy are reviewed and the different applications are classified according to the type of their magnetic interface and power level.

Chapter 3 introduces the magnetics background theory that is needed for the analysis and optimisation of the magnetic component. The theory behind the transformer operation is summarised and used to perform the reluctance modelling of the adjacent and coaxial winding alternative arrangements for the rotating transformers. Three different transformer characterising methods are described in this chapter.

Chapter 4 presents a detailed analysis of the rotating transformer. Theoretical calculations, measurements, and finite element analysis are employed in order to obtain the electrical properties of the transformer. The three methods are compared regarding their accuracy and applicability in engineering design. The electrical properties of the transformer are directly associated with its physical structure and some valuable optimisation guidelines are given. Finally, an AC analysis is performed on the resulting electrical model in order to assess the voltage and current gain of the transformer.

Chapter 5 reviews the operation of a phase-shifted full bridge converter with a full wave and with a current doubler rectifier. The resonant operation is analysed and the effect of the magnetising current to the operation is discussed. Accordingly, the impact of the air-gap in soft-switching operation is also assessed.

Chapter 6 presents the main trade-offs when designing a PSFB with a rotating transformer. A routine is presented that attempts the optimisation of the PSFB design with a rotating transformer (for a fixed air-gap and operating frequency). The routine starts by optimising the soft-switching range of the converter. Then, based on the assumption that switching losses are eliminated, it derives the optimum wire thickness, number of strands and number of turns of the transformer windings. The conduction losses in the MOSFET switches and the transformer are estimated.

Chapter 7 presents the experimental verification of the proposed design methodology. Several instances of the PSFB converter with different transformers and rectifier circuits are compared. The switching losses, voltage gain, efficiency and the electromagnetic radiation are discussed and some conclusions are drawn.

An overview of the theoretical and experimental work is presented and the main conclusions are discussed in Chapter 8. The thesis concludes with a series of suggestions for further investigation.

Chapter 2
Contact-less Transfer of Energy

Contact-less transfer of energy (CTE) has been a challenge for many researchers over the years and many different alternatives have been proposed for the magnetic interface and the electronics around it. This Chapter introduces the reader to this technology, describes the main challenges and possible difficulties during designing.

The Chapter is organised into three sections. The first section focuses on the magnetic component itself and the related problems and design issues. The following section reviews the power electronics architectures that have been proposed for CTE systems. Finally, Section 2.4 groups the literature contributions of the last fifteen years into five main categories. The classification into biomedical, automotive, industrial, aerospace and commercial applications is based on the similarities (magnetic component characteristics, power level) they exhibit. Some conclusions are drawn and the future trends are assessed.

2.1 Introduction

The challenge of transferring energy to moving equipment without using electrical contacts has motivated many researchers in the past. A range of applications has been considered [5] and several approaches have been proposed based on the individual requirements.

Using contact-less transfer of energy is a necessity for some applications and a desired feature for others. In the biomedical sector the use of an inductive interface to power artificial organs or other implanted equipment is essential. Wires are medically unacceptable for the potential infection they may incur. Similarly, in the aerospace industry the contact-less interface may be the only way for transferring energy from the stationary to the moving parts of a satellite. This is because maintenance is usually not available and the required life expectancy of such equipment is constantly increasing. On the other hand, charging a PDA or a laptop wirelessly is only a desired feature and

not a necessity. To convince industry that this technology may be used in commercial applications, a highly efficient (at least as efficient as the conventional technologies) and possibly more economic interface should be designed.

Some other major CTE applications are in industrial robots (to transfer energy to the moving parts), mining industry (to power electric vehicles), electric cars and general battery charging, the replacement of slip rings in machines and other equipment.

A CTE interface may be used for different reasons. The construction cost, size and weight is almost certainly the highest priority in commercial applications (e.g. battery chargers). The elimination of slip rings and commutators in rotary devices and machines is another motive for using CTE. Apart from simplifying the design procedure, it reduces the cost and mass of the construction. It requires no other parties (i.e. slip ring manufacturers) to be involved in the design process. Furthermore, reliability is a key reason for most applications, especially in military and biomedical equipment. CTE is needed in applications where maintenance is rare or not available (e.g. outer space). Finally, the operation in explosive environments (e.g. mining industry) or underwater may also require magnetic instead of electric coupling.

Depending on the application, the CTE interfaces have different geometry, size and structure that define their electrical behaviour. A wide range of applications has been presented in the past and as a result a wide spectrum of problems had to be tackled. The geometry and layout of the inductive interface define its electrical characteristics (such as coupling coefficient, winding resistance etc). The magnetic path (ferrite, iron, air) and its geometry (Pot-core, E-core etc), the distance between the coupled inductors (or the air-gap between the cores), the inductors misalignment, the presence of separating walls between the coils, the operating environment (water, air) and the thermal resistances are only some of the factors that affect the electrical behaviour of the component.

Although the problems that have to be tackled are so diverse, they can be summarised in two words; poor coupling. The coupling coefficient is a measure of the ability of two coupled inductors to transfer electric power to each other. A poor coupling coefficient incurs a series of problems such us the reduced voltage gain of the magnetic device, high circulating currents and hence high conduction losses. In other words, it results in a portion of the total supplied energy being stored in the inductive component (leakage

and magnetising inductances) and another portion being dissipated in the winding and semiconductor resistances.

2.2 Inductive Couplers

There are two basic methods for transferring energy without electrical contact; the electromagnetic link and the inductive coupling method. The first uses electromagnetic waves that are emitted and received by antennas. The inductive coupling, that is the subject of this thesis, relies on the magnetic field and transformer action. Inductive coupling includes every component that uses a magnetic link to transfer energy from one side of the circuit to the other. Using the magnetic field developed by the primary inductor, energy is transferred to the secondary windings. The portion of the input power that is transferred to the secondary inductor(s) is a function of the coupling coefficient of the inductive interface. In practice the coupling coefficient is always smaller than 1.0 because not all of the primary generated magnetic flux links the secondary winding(s).

2.2.1 Transformer or coupled inductors?

The question arising is, how does the clearance between the windings affect the electrical behaviour of an inductive coupler? To answer this question the difference between a transformer and a coupled inductor should become clear. A transformer is a component that transfers electrical energy from its input (primary winding) to the output (secondary winding(s)). The coupling coefficient of an ideal transformer is 1.0. On the other hand, a coupled inductor stores energy in the form of a magnetic field and releases it when appropriate (from either side).

An inductive coupler is, in fact, a coupled inductor that is meant to operate as a transformer. In other words, the aim of an inductive coupler is to transfer power from one side to the other. However, in reality it also stores part of the energy in the air space between the windings. This energy storage is generally not desired and is considered as the main drawback in contact-less transfer of energy.

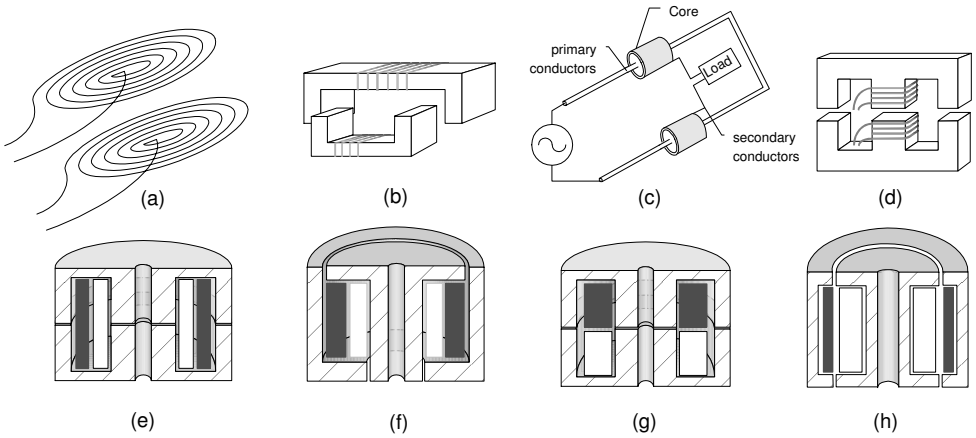

Figure 2.1: *Different transformer layouts; (a) core-less, (b) "plug-in" type, (c)linear transformer, (d) e-core, and rotating transformers; (e) coaxial windings, (f) LT transformer, (g) adjacent windings pot core h) concentric.*

2.2.2 Side effects of the coil distance

The geometry of the inductive coupler depends on the specific application requirements. For example, in biomedical engineering inductive couplers are generally discrete and light, operate under strict specifications (temperature, EMI etc) and can tolerate a significant relative displacement between the inductors. As a result, they are usually core-less and have a winding distance of 2-3cm. On the other hand, in automotive applications the inductive couplers handle kilowatts of power, hence a high permeability magnetic core with small air gap is required to increase the power density. The temperature of operation may be very high and forced cooling may be needed. Figure 2.1 illustrates some of the inductive couplers proposed in the past; the main types are (a) core-less [6–10], (b) "plug-in" type [11], (c)linear transformer [12–14], (d) e-core [15], and rotating transformers; (e) coaxial windings [16], (f) LT transformer [17], (g) adjacent windings pot core [17–19], h) concentric [17, 19–22].

Regardless of the application the inductive coupler's deficiency originates from the clearance between the windings and/or the magnetic core parts. As seen in figure 2.2(a) not all of the magnetic flux created by the primary winding links the secondary one. According to Faraday's law,

$$V_{sec} = N \cdot \frac{d\phi_{useful}}{dt} \tag{2.1}$$

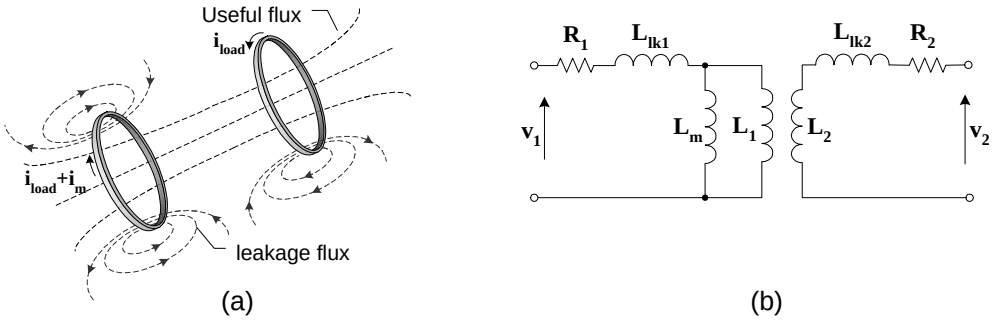

Figure 2.2: *Elementary inductive coupler; not all of the primary flux links the secondary winding.*

The voltage and hence the current in the secondary ring is less than that in the primary ring. Therefore to produce a current i_{load} in the secondary winding a $i_{load} + i_m$ is needed in the primary. The additional current i_m is called magnetising current and all it does is rearrange the magnetic dipoles of the core and air gap, storing magnetic energy. The magnetising current is approximately constant regardless of the load value as long as the geometry of the magnetic medium linking the two inductors (eg. air) remains the same. Electrically, the energy storage in the form of magnetic field is related with the presence of an inductance, and therefore the electrical model of a transformer includes a magnetising inductance L_m connected in parallel with the primary winding (figure 2.2(b)). If the magnetising inductance is low it draws a high current, thus increasing the conduction power losses.

Furthermore, the flux lines that link the primary but not the secondary winding are called *leakage flux* and store energy in the form of magnetic field by rearranging the magnetic particles of the air. The electrical equivalent of this energy storing space is the leakage inductance L_{lk} (figure 2.2(c)). Leakage inductance appears in series with the ideal transformer causing a voltage drop that reduces the output voltage.

In inductive couplers where magnetic cores are used the high-density stray flux (fringing field) around the air gap may affect the current flow in the windings. This is due to the generation of eddy currents that oppose the normal current flow thus increasing the AC resistance of the windings as shown in Chapter 7. This leads to excessive heating of the windings. The effect is particularly strong when the windings are close to the air-gap.

Finally, as the switching frequencies tend to increase the effect of high frequency phe-

nomena such as the proximity effect and skin effect in the windings cannot be ignored. These effects become more apparent when rectangular waveforms with a high harmonic content are used. The frequency dependent winding resistances (R_1 and R_2) are therefore taken into account in the equivalent model.

To summarise, the side effects of a large clearance between the primary and secondary inductors are:

- *low magnetising inductance*, causing high circulating currents in the primary winding.
- *high leakage inductance*, imposing a high impedance in series with the transformer windings which in combination with the high current, causes a significant voltage drop. The transformer output voltage is therefore significantly less than expected.
- *stray flux*, generating eddy currents and losses. This may cause EMI with nearby components.
- *high conduction losses*, caused by the increased primary current and the winding resistance (I^2R).

2.2.3 Optimisation of the magnetic component

Once the geometry of the magnetic interface has been selected (according to the application requirements), the air gap, core shape and windings layout are known. To optimise the magnetic component it is essential to understand the connection between its geometry and electrical properties [23, 24]. To associate the physical structure with the electrical behaviour a reluctance modelling and duality transformation [25] should be applied. These processes are described analytically in Chapters 3 and 4 and are depicted in figure 2.3.

Once there is a deep understanding of how the air-gap, core dimensions, number of winding turns and layers etc. affect the electrical behaviour, the component may be optimised to fit the converter topology that has been chosen. Or vice versa; a converter topology that best utilises the transformer parasitics may be chosen and adjusted. In both cases the optimisation process moves along two lines; the minimisation of the conduction power losses and the complete recovery of the stored inductive energy.

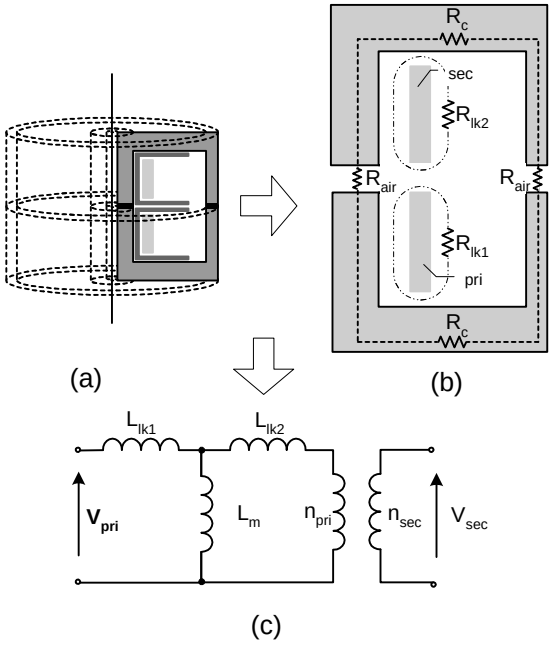

Figure 2.3: *Reluctance modelling for a pot core transformer with adjacent windings arrangement: (a) transformer geometry (b) the magnetic paths and (c) the resulting electrical equivalent network.*

C.M. Zeirhofer et al. [10] presented an interesting paper on the analysis of the spiral type air-coils (figure 2.1(a)) (used in biomedical applications). The authors derived simple design equations to optimise the size and coupling coefficient of the air-coils. They concluded that the spiral coils offer better coupling than the usual coils with all the turns wound on a circumference. Similar work was presented by Matsuki et al. in [7]. Severns et al. [26] concentrated their efforts on identifying the main loss mechanisms in a contact-less inductive interface. The authors looked at the geometric effects, eddy current losses and the electromagnetic or dimensional resonance that can take place under various circumstances. Their prototype was used in fast battery charging for automotive applications. C Fernandez et al. [27] presented a set of rules for designing core-less transformers. The authors studied the effects of the coil distance and inner and outer radius to the coupling. J. van Vlerken derived a high frequency model [28] for small rotary transformers used in heads and electronics for helical-scan recording. To do so they divided the transformer core to sub-geometries and calculated the permeance of each part. Similar work was performed by M.Jufer on a larger pot core [29] and a finite element analysis of a pot core geometry was performed by Y.Huang in [30].

Some basic principles the designer should have in mind include the following:

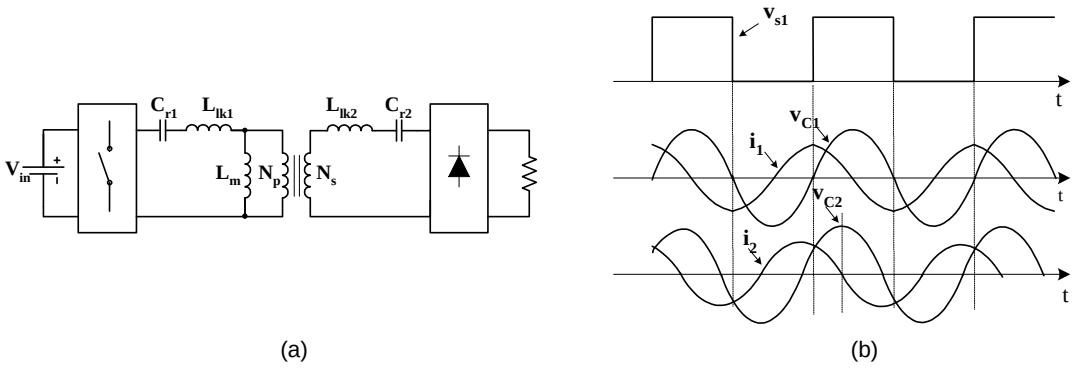

Figure 2.4: *A resonant topology; (a) the resonant capacitors compensate for the voltage drop caused by the leakage inductance when the circuit is operated at the resonant frequency and (b) the main voltage and current waveforms.*

- *Magnetic paths*: their length must be minimised and their cross-sectional area maximised (keeping size and weight constraints in mind).
- *Number of turns*: increasing the number of turns increases magnetising inductance and decreases magnetising current, but also increases the winding resistance. The best compromise must be found.
- *Operating frequency*: increasing frequency decreases energy storage; however, it increases the voltage drops across leakage inductances as well as the AC winding resistance.
- *Power handling capability*: each magnetic component is upper bounded regarding its power handling capability. The boundary depends on both the magnetic component (eg. thermal resistance) and the topology (eg. waveforms used).

2.3 Converter Topologies

To date most attention has been given to the optimisation of the inductive component, namely the reduction of the leakage and/or the maximisation of the magnetising inductance. Regarding the electronics topologies the solutions that have been proposed can be classified into four main categories; resonant, quasi-resonant, self-resonant and flyback converters. In all these architectures the idea is that the reactive energy stored in the magnetic component should be recovered and utilised effectively.

Figure 2.4(a) shows a resonant converter with a capacitor connected in series with the leakage inductances in the primary and secondary windings[1]. The converter operates around the resonant frequency, hence the impedance of the series resonant tank is almost 0 (figure 2.5(a)). In this way, the voltage drop across the leakage inductance is eliminated and the transformer voltage gain is kept high. The output is regulated using frequency control as the inductive coupler may have variable electrical characteristics (if the coil clearance or relative position changes). The frequency controller compensates for any change in the leakage inductance, interwinding capacitance etc [31]. Resonant converters usually result in higher peak currents and consequently higher losses and semiconductor stresses. On the other hand, they usually have an inherent short-circuit protection and they suffer less from high frequency winding losses. Their main advantage is that they exhibit zero voltage (ZVS) or current (ZCS) [18] switching, hence greatly reduced switching losses.

Resonant converters are mostly used where a long clearance distance ($> 5cm$) is required between the inductive couplers parts. Using sinewaves, the receiver can be tuned at the transmitting frequency and picks up power from the primary coil. In addition, the sinusoidal waveforms have low harmonic content result in reduced the EMI. Several variations of a resonant converter have been presented and some of them are reviewed in Section 2.4. The main resonant circuits along with their characteristic impedance graphs appear figure 2.5.

Valtchev et al. [32] have studied the most commonly used series resonant converter (SRC) with loosely coupled inductors. By showing a very small dependence of the leakage inductance on the air gap length, they conclude that the resonating frequency is almost fixed for relatively small (in comparison with the magnetic path length) air gaps.

The second topology that is commonly used in CTE applications, is the quasi-resonant converter that utilises the switch parasitics (mainly the junction capacitance) to achieve ZVS, avoiding at the same time the disadvantage of high peak currents of the resonant converters. In quasi-resonant converters resonance takes place during a fraction of the switching period (figure 2.6(b)). The resonant frequency is several times greater than

[1]Note here that the secondary and primary leakage inductances cannot be lumped into one element as the currents through them are different, unlike in a conventional transformer.

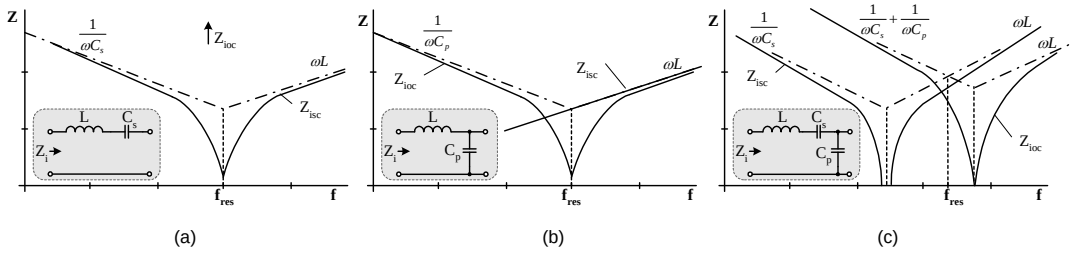

Figure 2.5: *Impedance of the (a) series resonant, (b) parallel resonant and (c) series-parallel resonant circuits that are used to compensate for the high leakage inductance effects.*

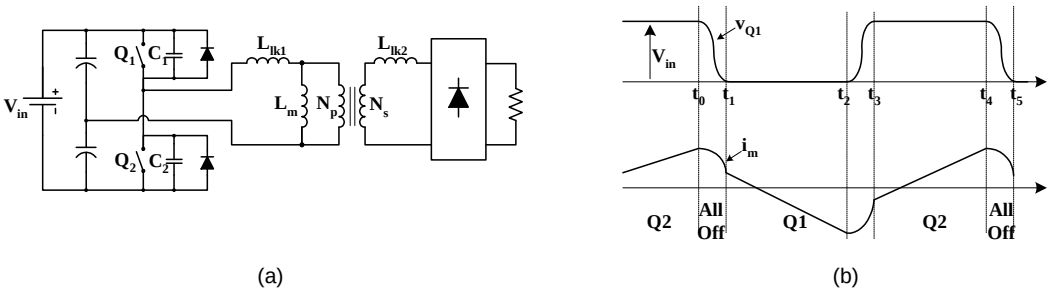

Figure 2.6: *A quasi-resonant topology; the leakage inductance oscillates with the switch inherent capacitance.*

the switching frequency and the voltage regulation is usually based on pulse width modulation. A general view of a quasi-resonant converter and its main waveforms appear in figure 2.6.

The quasi-resonant converters are used with inductive couplers that exhibit medium to small leakage inductance (i.e. those interfaces with a small distance between the windings). Experience has shown that the utilisation of the leakage inductance for resonant switch transitions to reduce the switching losses can fully (or partially) compensate for the increased conduction losses caused by the high primary circulating current.

A converter topology that could naturally be considered for such applications is the flyback of figure 2.7(a). Using a coupled inductor, the flyback stores energy into the magnetic component and releases it through the secondary winding. The flyback is generally considered only for low power applications [33] due to the voltage stresses at the main switches as well as due to the partial utilisation of the magnetic core (due to the unidirectional flux excursion). These stresses are the result of switching on and off a current through a large inductance ($L \cdot \frac{di}{dt}$). There are attempts to use the flyback

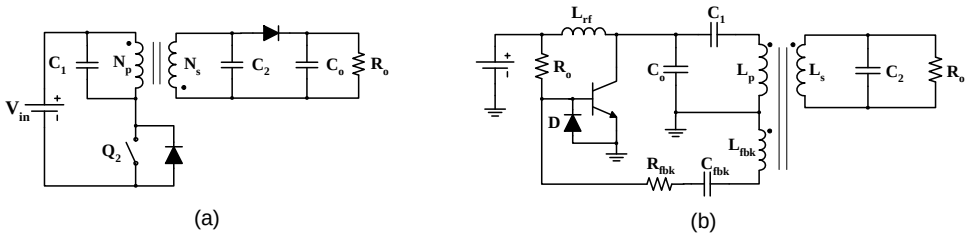

Figure 2.7: *Topologies proposed for contact-less transfer of power; (a) double tuned very low power flyback converter and (b) a class E tuned power oscillator with an inductive link.*

for contact-less applications of up to 2kW [34] by using an active voltage clamp. The leakage energy is thereby transferred to the output side through the auxiliary flyback that acts as a voltage clamp.

The use of sinusoidal waveforms to control the impedance of the inductive coupler has been attempted by many researchers. A class E self-resonant amplifier was proposed in [35] for transdermal transfer of energy to implanted devices. The amplifier used an auxiliary winding to feedback to the transistor and maintain the oscillations and to track the resonant frequency while the inductive coupler's characteristics varied. A class C amplifier is also mentioned in [36–38] for low power battery chargers. The circuit is self-resonant primary-tuned with a feedback loop to maintain the resonance at the resonant tank frequency. To regulate the output voltage an additional driving circuit is used to inject a current and alter the biasing of the MOSFET gate. Resonance may be the only solution at high power and low voltage applications when the magnetic component introduces very high series impedances (i.e. high leakage inductance), despite the higher component stresses it incurs.

2.4 Contact-less Transfer of Energy Applications

CTE has been used in many different applications, each of them having particular specifications, requirements and restrictions. It is possible to group the applications into five main categories:

- Biomedical
- Automotive

- Aerospace
- Industrial
- Commercial

2.4.1 Biomedical

Biomedical engineering favours contact-less transfer of energy, mainly because of the electrical isolation feature it offers. Applications [39–43] such as pacemakers, artificial organs and VNS (vagnus nerve stimulation) therapy devices, require reliable operation for their entire life. Medical implications (i.e. infection etc) due to contacts, wires and other equipment are simply unacceptable. Remote charging and wireless operation considerably improves the patient's quality of life and the aesthetics of the implanted equipment.

In biomedical applications such as artificial organs, an air-gap of 10-20mm is required and the designer should account for a possible misalignment of the magnetic core parts. The implants and external devices must be kept at around the human body temperature and the volume and weight are equally important in a realistic design.

Some of the most significant literature contributions were made by A. Ghahary and Bo H. Cho [44] at the beginning of the previous decade. They presented a design methodology for a dc/dc converter with a loosely coupled transformer. The circuit is intended for circulatory assist devices that incorporate a wireless supply for the implanted device. The converter featured resonant transitions of the power semiconductors and series resonance at the secondary side of the transformer. The design was able to deliver 12-48W of power through an air-gap of 10-20mm. The authors employed a state plane analysis to calculate the resonant voltage and current at the secondary of the transformer, and from that to select the frequency of operation given the resonating inductance and capacitance. As the electrical characteristics of a transformer vary due to the core relative displacement, frequency control is employed in this work. The authors did not proceed to the design of a wireless feedback loop though some thoughts were mentioned in their work. A P66/56 magnetic core was used for the experiments, however a considerably smaller core would be needed in a practical design. The design methodology can be applied to low frequencies (below 50kHz) where the winding resistances can be assumed

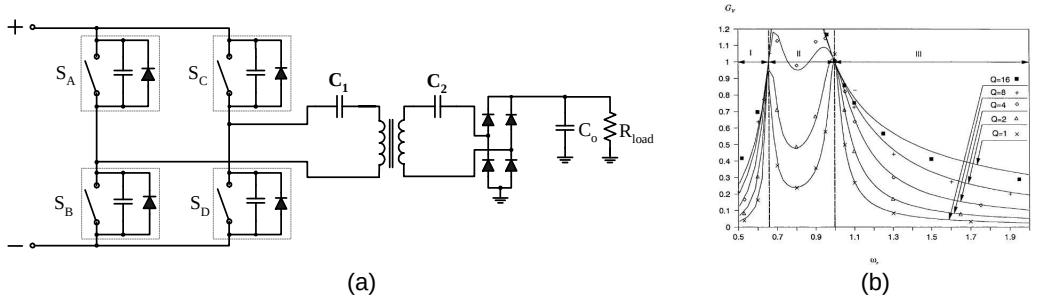

Figure 2.8: *(a)Primary and secondary side capacitors improve the converter voltage gain and secure soft-switching of the MOSFETs, (b) the compensated transformer voltage gain graphs.*

to be negligible for the state plane analysis.

A fundamental paper for this type of application was written by G.B. Joung and Prof Bo H. Cho [45],[46] in the mid 90's. This paper targeted the two basic problems of the contact-less transfer of energy; the transformer low voltage gain and the low efficiency. To facilitate the ac analysis and the derivation of the circuit transfer functions, the authors assumed that the two windings have the same structure and are symmetrically placed, in other words they have the same self-inductance. They produced a voltage gain function with respect to the transformer coupling coefficient. To maintain the voltage gain they employed leakage inductance compensation in both the primary and secondary sides (figure 2.8), and derived equations for the calculation of the required resonant components.

C.M. Zierhofer and E.S. Hochmair [35, 47] worked on a different concept, that of a relatively simple and inexpensive self oscillating class E amplifier with a single switch. This work assumed two air-core coils with a distance of 0-8mm. The frequency of the oscillation depends on the inductance of the interface and hence automatically adjusts as the coupling changes (because of any displacements of the inductors). The authors claim that the frequency automatically tracks the maximum power transfer point thus maximising the efficiency of the power supply up to 72%. C.C. Tsai et al. proposed an additional boost stage in front of the main converter to stabilise the input voltage. The two stage converter included a series resonant half bridge converter with a 68% efficiency. The primary side frequency control is based on a phase shift measurement between the voltage and currents at the primary side. The advantage of this method is a good voltage regulation of ± 0.4V and its drawback is a relatively low efficiency mainly due to the

Author	Air-gap	Frequency	Power	Efficiency	Topology
Ghahary et al.[44]	10-20mm	50kHz	12-48W	66-78%	Full Bridge,sec leakage compensation
Joung et al.[45, 46]	10-20mm	120kHz	12-48W	68-78%	ZVS Full Bridge,leakage compensation
Zierhofer et al.[35]	0-8mm	7-10MHz	-	45-72%	Class E,resonant tanks
Tsai et al.[8]	6-18mm	430kHz	30-50W	$\leq$68%	Half Bridge, series resonant

Table 2.1: *Contact-less transfer of energy in biomedical applications*

conduction losses in the coils. These losses and the resulting high coil temperature put this system's applicability under question. Matsuki et al. [6] implemented a synchronous rectifier at the secondary side to reduce the conduction losses.

2.4.2 Automotive

During the past decade many automobile companies have invested vast amounts of money towards the all-electric car for their environment-conscious clients. Electric car technology has made huge advances regarding the power electronics and motor design and towards the miniaturisation of the components. According to [48] most of the projects related with the all-electric cars were abandoned due to two major issues: a) the low capacity provided by the current battery technology and b) the diversity in the charging methods that were used by different companies (despite the SAE J-1773 recommendation published by the Society of Automotive Engineers).

Despite the shortfall in the electric vehicle technology there was a significant boost to research into inductive charging. The automotive industry aimed for a high power inductive interface that would replace the less safe electrical outlets. Typical power levels of several kilowatts were needed to be transferred over a 3cm air gap.

Hayes et al.[31] proposed a full bridge converter incorporating two resonant tanks, one series and one parallel. The authors concentrated on the optimisation of the power electronics component by utilising the transformer parasitics and some additional external components. The proposed circuit operated with zero voltage switching hence reducing the power losses. The circuit employed frequency control to regulate the output voltage. The authors concluded that the proposed topology performs well for level 1 and level 2 charging (120V, 15A and 230V, 40A respectively according to SAE J-1773), but it is not appropriate for level 3 (25-160kW) charging.

Kutkut et al.[49] proposed a 120kW converter for fast charging of electric vehicle batteries. The full bridge series-parallel resonant topology featured IGBTs that were switching under zero current conditions. The authors characterised and assessed the semiconductors by studying the IGBT loss mechanisms. They calculated the losses under zero voltage switching and compared them with those under zero current switching. Although more passive components were needed to achieve zero current switching, it resulted in considerably lower losses. Design equations were given for the selection of proper resonant components.

The same research group under Klontz have emphasised magnetic interface optimisation for fast charging of an electric vehicle [50]. The authors calculated the AC resistance of the windings and the optimum number of winding layers and wire thickness to minimise the conduction losses. The resulting 120kW full bridge series-resonant converter operating at 20kHz demonstrated a high efficiency although active cooling was essential.

Sakamoto et al. [51, 52] proposed a half bridge converter with frequency control. The converter achieved zero voltage switching of the two MOSFETs by using the transformer inductance to resonate with the drain-source capacitance of the MOSFET. The authors proved that although leakage inductance is needed in such circuits to accomplish the soft-switching, it results in high voltage drops and thus it must be minimised. Different arrangements for the power transformer winding layouts, including a coaxial winding arrangement, were proposed to reduce the leakage inductance. The authors claimed a 97% efficiency at 3kW of output power. The conduction losses were not discussed in this paper although their impact at the frequency of 100kHz is significant. In [53] the authors proposed an alternative energy coupler with a large cross-sectional area to allow for longer clearance and relative misalignment between the core halves. The weight of the magnetic interface alone was 17.2kg and allowed the transfer of 8.3kW of power with a 97% efficiency (for a small 3mm air gap). The efficiency of the converter was only measured for very small air gaps. The misalignment and increased distance of the cores is expected to degrade the efficiency significantly.

2.4.3 Aerospace and military

Aerospace and military applications differ from other applications in that reliability and endurance are the principal objectives, with cost a lower priority. Military technologies

Author	Air-gap	Frequency	Power	Efficiency	Topology
Kutkut N.H. et al.[49]	0.14in	75kHz	96kW	94.7%	Full bridge, ZCS series-parallel resonant
Klontz K.W. et al.[50]	-	20.43kHz	96kW	99.6%	Full bridge, series resonant
Sakamoto H. et al.[51, 52]	5mm	100kHz	3kW	$<$97%	Class-C with ZVS
Sakamoto H. et al.[53]	5mm	100kHz	8.3kW	$<$97%	Full bridge with ZVS
Hayes J.G. et al.[31]	-	150-200kHz	1kW	$<$95%	Full bridge,series-paraller resonance

Table 2.2: *Contact-less transfer of energy in automotive applications*

must pass extensive testing before reaching the market and are usually in the vanguard of technology. The power level and the inductive interface layout largely depend on the application. This type of applications is often classified, so the volume of published research is limited. Although this review focuses on the recent advancements in the field, it is considered that some older fundamental papers should be briefly cited to help researchers investigating this field.

McLyman et al [17] worked on the replacement of the slip-rings in a satellite application. The author mainly looked at the geometry of the magnetic interface and proposed some interesting geometrical alternatives to improve coupling. Marx et al. [20] proposed replacement of slip-rings with a rotary transformer and designed a push-pull converter to evaluate it. The author compared the performance of the conventional circuit with that of the proposed one and also estimated the differences in cost, weight and life expectancy. The resulting converter ran at 18kHz and delivered 500W with a 90.8% efficiency. Landsman [19] made one of the first attempts to design a rotary transformer for transferring energy to the body of a satellite from its rotating solar panels. The author concentrated on the magnetic component design and its geometrical optimisation. A resonant converter with transistors was developed and 1.2kW of power delivery with 92% (transformer) efficiency was claimed.

2.4.4 Industry

The industrial sector invests in reliable technologies that have minimum maintenance requirements and long life expectancy. Precision and reliability may be the priority in certain applications (production, assembly lines etc) and reliable operation in harsh environment may be in others (mining etc).

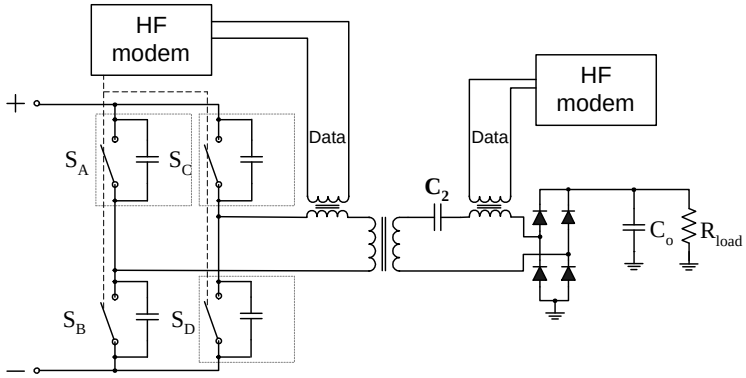

Figure 2.9: *The wireless transmission of power and information WTPI scheme proposed by Hirai.*

Mecke et al. presented a general purpose inductive energy transmission system [9] for supplying 1kW of power to electric loads at a maximum distance of 300mm. The authors used large primary and secondary windings (diameter of 400mm) glued on ferrite plates to improve coupling. The leakage inductance of these oversized windings was compensated by using a series resonant capacitor in the primary and a parallel resonant capacitor at the secondary. The authors first used the phase-shifted full bridge with IGBT switches to demonstrate that it is possible to transfer 1kW of power over a 300mm air gap with a relatively high (around 80%) efficiency.

J. Hirai and his colleagues made a significant contribution to the literature by proposing two inductive interfaces (figure 2.1(d),(g)) for wireless transfer of power and information (figure 2.9). In paper [21] a low power battery charger for a robot was proposed. The system incorporated a data link between the charger and the battery supervisory module in order to optimise the charging pattern and battery life. In [13, 22] the authors looked upon a complete interface for distributing power and exchange data magnetically to industrial actuators and machines. Two different magnetic components were proposed; a pot-shaped interface that could allow rotary movement between the core parts with a very small air-gap ($200\mu m$) and a linear interface made of an E-core with no air-gap. Both interfaces exhibited high leakage inductance and to compensate for that the authors used a current resonant bridge converter with extra capacitors across the switches to resonate with the leakage inductance and thus provide zero voltage switching. According to the authors the maximum efficiency is 92% for a small air-gap of $200\mu m$. The same interfaces were also used to transfer data during the non-conducting intervals

of the power stage. The theoretical model estimated a possible data transfer rate of 8.5Mbps. In practice, the maximum bit rate was only 100kbps as the transmission was limited to the switch off-time intervals to avoid interference with the power signals. A channel cross-talk study was presented in [54].

The contact-less power delivery to linearly moving loads was investigated by Klontz et al in [12]. They looked at a high power (1MW) haulage equipment application based on a low frequency (2kHz) resonant inverter with a 1km long 1-turn primary winding and a moving toroid core with the secondary wound around it. A parallel connected capacitor compensated for the interface's leakage inductance. The concept was applied to a small scale prototype and the authors claimed a good performance.

Green and Boys [55] have also proposed a 10kHz inductive power transfer (IPT) system operating at a frequency of 10kHz. This attempt was based on a secondary resonant tank made of the pick up coil and a parallel capacitor. The aim was to reduce the sharp edges of the current waveforms and hence the high frequency losses. They managed to couple 6kW of power across a 70mm air-gap with an efficiency up to 75% at maximum loading. To regulate the output voltage which greatly varied over the load range, they employed a series-connected secondary side boost converter. The same group worked on inductive coupler stability issues [56] and derived a dc equivalent circuit to analyse the dynamics of a high frequency AC resonant pick-up converter [57].

Esser et al.[18] worked on a rotary transformer interface for contact-less transfer of energy across the moving parts of a robot. The power converters are connected in a chain to supply the successive segments of robot arms. The proven power capability of the system was 10kW of continuous or 20kW of instant power with an efficiency around 95% at full load for an interface with a $100\mu m$ between the core parts. The authors employed an IGBT bridge with a series resonant tank in the primary and secondary windings and derived equations for calculating the required capacitors value. In [58] the same authors investigated the simultaneous transmission of data through the magnetic component by incorporating two capacitive channels. The two channels were implemented in a 1.2kW power converter prototype for the transmission of 2.5Mbits with an low bit error rate.

Author	Air-gap	Frequency	Power	Efficiency	Topology
Mecke et al [9]	300mm	20-150kHz	1kW	$<$83%	Full bridge,series pri and parallel sec resonance
Hirai et al., [13, 21, 22, 54]	200μm	50kHz	-	$<$92%	Resonant full bridge,100kbps data link
Klontz et al.[12]	-	2kHz	1MW	-	Series-parallel resonant
Green et al.[55]	70mm	10kHz	6kW	$<$75%	Secondary parallel resonance,frequency control
Esser et al.[18],[58]	100μm	25kHz	10kW	$<$97%	IGBT bridge, series resonance(ZCS), 2.5Mbps data

Table 2.3: *Contact-less transfer of energy in industrial applications*

2.4.5 Commercial

Contact-less transfer of energy has been employed in low power commercial devices in order to enhance safety. Products such as contact-less electric toothbrushes and other portable equipment gradually gain ground over their wired competitors. Safety regulations as well as convenience are the main motivations for the manufacturers to embed CTE in their products.

Jang and Jovanovic [59] have developed a resonant converter that utilises the inevitable leakage inductance to perform zero-voltage or zero current transition at both primary and secondary switches. Here, the mode of operation (ZVS or ZCS) depends on whether the circuit operates above or below the resonant frequency. They have also implemented separate control circuits in each side of the converter; to compensate for the input voltage variations the authors of this paper designed a controller that adjusts the oscillation frequency to adjust the gain of the resonant circuit. In the secondary side a control circuit adjusts the duty ratio of the rectifier switch by observing the output voltage as well as, indirectly, the secondary current. This interesting work resulted in the design and testing of a 4.5W battery charger with an efficiency in the range between 60 and 70%. The authors reported increased winding conduction losses.

Kim et al described a different approach for designing the contact-less inductive interface [15]. The authors associated the coupling coefficient of the transformer with the component's geometry based solely on the core structure, dimensions and relative position. By varying the ratio between the core width and the gap length they concluded that by increasing this ratio the coupling coefficient increases too. The authors also studied the power electronics stage and attempted to optimise its operation by defining the normalised power stress factor (P_{SWN}) for the switching devices. Because of the

problematic voltage and current gain of the power transformer, high voltage or current stresses occurred in the primary side to achieve the desired current and voltage at the output. Therefore, the optimisation objective in this paper is the product of voltage and current which is the power P_{SWN}. The half bridge resonant converter featured a simple control circuit with an infrared LED to couple the control signal to the primary side. The evaluation of the proposed system showed an efficiency of not more than 75% with 3mm gap between the core parts.

Pedder et al have investigated a contact-less energy transmission system in [11]. The authors proposed a U-core with one of the core sections penetrating into the other to reduce the fringing field effect. They provided some design guidelines mainly concerning the selection of the core in order to keep the flux density in reasonable levels. Furthermore, the authors proposed an interesting control strategy that extracts the phase information of the reflected load current ignoring the triangular magnetising current. This is achieved by using a double differentiator to first convert the triangular magnetising current to a square pulse and accordingly to a series of alternating narrow pulses thus leaving the reflected sinusoidal load current unaffected. Using the limiting amplifier the sinusoidal waveform is converted to a square wave and the phase information is extracted. Two prototypes, a 1W and a 5kW were built and the efficiency of the magnetic interface was found to be around 95%. At 2.5kW the transformer power loss was around 230W making its cooling difficult. This paper clearly shows that the magnetic interface imposes some upper boundaries to the maximum power of such an application.

Sakamoto and his research group at Kumamoto Institute of Technology investigated several solutions for the inductive charging battery cells. In [36–38, 60] they proposed the use of a self-oscillating C-class amplifier with a positive feedback loop that initiates and maintains the self-resonance. The switch is operated with zero voltage transitions and the voltage on the transistor appears to be a chopped sine-wave with a controlled duty cycle. The topology is fairly simple and cost-effective using only one switch. The authors claimed that the efficiency of the above circuit is over 90%. Although not mentioned in the paper, the sinusoidal waveforms usually result in high voltage stresses to the semiconductor components as the absolute amplitudes are usually higher than these of a square waveform. Researchers from the same group (Abe et al.) developed a half bridge converter with parallel resonant capacitors across both the primary and

Author	Air-gap	Frequency	Power	Efficiency	Topology
Jang et al. [59]	60mils	65-140kHz	4.5W	60%-70%	Series resonant,frequency and PWM control
Kim et al.[15]	3mm	65kHz	3.3W	<75%	Half-bridge,series resonant
Sakamoto et al. [36–38, 60]	-	100kHz	5W	<90%	C-class,self resonant,ZVS
Abe al. [53, 61–63]	4mm	58-107kHz	5W	<60%	Half Bridge,pri and sec parallel resonance
Pedder et al. [11]	6mm	120kHz	5kW	<83%	Half/full bridge,sec series resonance,ZVS

Table 2.4: *Commercial applications*

Converter Type	Inductive coupler type	References
Resonant converter	small to medium distances(mm to cm)	[15, 32, 44–46, 49]
Quasi-resonant converter	small distances (milimiters)	[16]
Class E self-resonant amplifier	medium distance, small power	[35]
Flyback	small distances	[33, 34]

Table 2.5: *Proposed topologies for contact-less transfer of energy*

secondary windings [53, 61]. They claimed that the secondary capacitor improved the load matching and consequently the power transfer capability. The primary resonant circuit adjusts the resonant transition period according to the load current. Finally, in [62] the authors formed an additional resonant tank composed by the filter inductor and a parallel capacitor that keep a continuous current flow during low-load or no-load conditions, hence keeping the voltage gain at reasonable levels. Design guidelines for the component selection are given in the paper and the resulting converter demonstrated a relatively low efficiency (60%) across an air gap of 4mm.

Table 2.5 summarises the proposed architectures according to the converter topology. The research projects in this table are a representative fraction of the work that has been carried out in the last 15 years.

2.5 Chapter Summary

A broad range of inductive couplers for various applications has been proposed in the literature. The required power and the distance between the stationary and moving parts define the type of the inductive coupler that should be used. Planar windings and core-less transformers are used in biomedical applications, where the weight and size are critical factors and low power transfer is required. Heavier and bigger transformers with

a magnetic core have been used in inductive charging of batteries. Linear and rotating transformers have been used in industrial applications.

Regarding the power electronics topology, resonant and quasi-resonant circuits are popular as they can utilise the transformer leakage inductance to perform ZVS and ZCS of the semiconductors. Leakage inductance compensation is common in applications with long distance between the windings, where the voltage gain of the transformer is impaired. In cases with relative displacement between the core halves, the electrical characteristics of the transformer change, therefore frequency tracking control is employed to preserve optimum voltage gain of the transformer.

The flyback converter is also a possibility when the inductive coupler has relatively low leakage inductance. Energy is stored in the magnetic component during the on-time and released at the secondary side during the off-time of the switch. The disadvantage of this topology is high voltage and current surges occurring during the switch transitions. Some self-resonant amplifiers have also been proposed for contact-less transfer of energy, however the sinusoidal waveforms cause higher voltage and current stresses on the switches.

The rotating transformer has certain characteristics that differentiate it from other inductive couplers; a fixed clearance between the primary and secondary coils and practically fixed electrical properties. A basic requirement of the radar application is a fixed operating frequency, in order to synchronise the power supply with the radar pulse repetition frequency. This limitation makes difficult the use frequency control. The phase-shifted full bridge converter often presents significant advantages in terms of size, cost and efficiency in applications near the kilowatt range. It is expected that the PSFB combined with a carefully designed inductive coupler could result in a compact and efficient converter. The conditions under which this statement holds true are investigated in this work.

The aim is to design an efficient (>90%), lightweight and compact power converter. The existing designs one of the the above features was compromised in order to improve an other. As a result, highly efficient/high power converters such as the ones by Sakamoto and Klontz and Hirai employed an oversized magnetic core, a low switching frequency (to reduce switching and conduction losses) or a very small air-gap to achieve good coupling.

Similarly, B. Cho and his colleagues proposed a non-realistic solution employing an oversized magnetic core in an artificial heart application. This thesis aims at a realistic design with a good balance between size, cost and performance.

Chapter 3
Transformer Theory

Bearing in mind that the inductive coupler is, actually, a transformer with its primary and secondary windings taken apart, it is useful to associate its geometrical characteristics with its electrical behaviour. This would allow the transformer design to be optimised for a specific topology. A short introduction to basic magnetics and transformer operation is essential to gain a good understanding of how the geometrical layout affects its performance. The aim of this chapter is to help understanding terms such as magnetisation, magnetising inductance, leakage inductance and AC losses that are critical in power electronic designs.

When reading this Chapter, the reader should keep in mind that a gapped transformer, such as the contact-less energy interface, combines the magnetic properties of both an ideal transformer and those of an inductor.

To explain the magnetic behaviour of a transformer, and especially the characteristics of a rotating transformer, this Chapter begins with an introduction to the magnetic phenomena and then focuses on the magnetic materials and the magnetic components. The notions of magnetising and leakage inductance are defined and their connection with the transformer geometry is investigated.

The chapter ends with the description of three transformer characterising methods (measurement, calculations, finite elements analysis) that have been used to analyse the rotating transformer.

3.1 Magnetism

Magnetism is a property of the matter. Different substances of the matter have different magnetic properties. As a result some materials interact with a magnetic field and some others are effectively inert.

The fundamental substance of matter is the atom (figure 3.1). The atom consists of

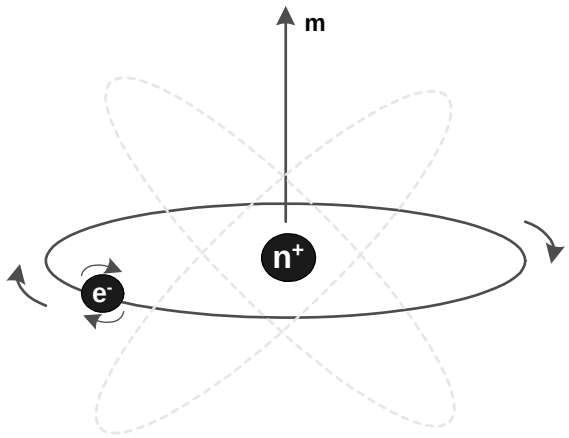

Figure 3.1: *The atom; basic magnetic moment sources*

a positive nucleus, and a number of electrons revolving around the nucleus in different valencies. Just as a current currying loop creates a magnetic moment, the revolving electrons create very weak magnetic moments.

In addition to the circular movement, the electrons are also spinning around their own axis. This phenomenon also contributes to the total magnetic moment of the element, although the way this is done can only be described by quantum theory that is beyond the scope of this text [64].

The third source of magnetic moment is that of the nuclear spin. This has a negligible contribution and therefore is usually omitted.

In each case the magnitude of the moment is the product of the electron charge and the area of the described loop. Millions of atoms all together constitute a domain which has a south and a north pole and can be re-aligned when a magnetic field is applied.

3.1.1 Magnetic properties of matter

From all elements the transition metals (such as the trivalent Fe) exhibit the most uncompensated spins and therefore present strong magnetic properties. All materials can be classified according to their magnetic behaviour into three major categories; diamagnetic, paramagnetic and magnetic materials. The diamagnetic and paramagnetic materials are usually referred to as non-magnetic, although the only real non-magnetic

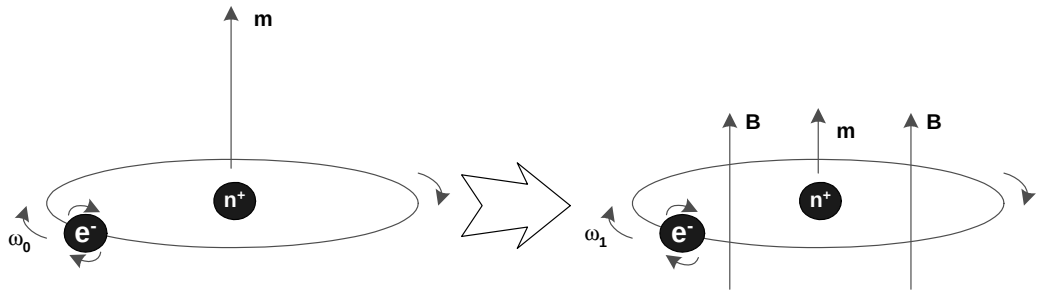

Figure 3.2: *The magnetic moment of the atom is decreased upon the presence of a homo-directional external field, i.e.* $\omega_0 > \omega_1$.

medium is a vacuum.

In diamagnetic materials the net magnetic field that is created by the revolving electrons and by their spinning movement is zero as the different fields cancel each other. If an external magnetic field is applied, for example, in the same direction with the moment created by an orbiting electron, then a torque would be developed on the electron in the outward direction. However, the radius of rotation cannot be changed if the energy balance within the atom is to be preserved (according to quantum theory for an electron to move from one valence to another a specific amount of energy must be absorbed or released). Therefore, in order to balance the forces within the atom the orbiting velocity of this electron should decrease. This unavoidably results in a reduction of the net magnetic moment and of the total field density (figure 3.2. When an external magnetic field H is applied to a diamagnetic material the total field density produced by the combined external and internal fields decreases [65].

In contrast, in a paramagnetic material the net moment of the atom is not zero. Therefore the atom looks like a magnetic dipole. When there is no external magnetic field the average magnetic field in a volume of such a material is zero. However, if an external field is applied on a paramagnetic material, the magnetic dipoles tend to align and therefore the field density in the volume increases slightly.

The third and most interesting category is that of the so called magnetic materials. They are called magnetic materials because they become magnetised (look like a magnetic dipole) in the presence of an external magnetic field. This category includes the ferromagnetic and ferrimagnetic materials as well as the antiferromagnetic and superparamagnetic materials. The first two are of interest as they are used for magnetic

components design.

The ferromagnetic and ferrimagnetic materials consist of atoms that exhibit a strong magnetic moment and therefore they look like magnetic dipoles. Due to the magnetic forces that are developed among the atomic dipoles they form groups of uniformly aligned atoms, the domains. The domains are randomly aligned over the material's volume so that in macroscopic view the material presents a zero net magnetic moment. However, when an external field is applied the domains align and form a convenient path for the magnetic field to appear. The difference between ferromagnetic and ferrimagnetic materials is that the atomic moments within the material are not equal. In ferrimagnetic materials the domains respond well to the presence of an external magnetic field but not as well as in a ferromagnetic material. Also an important property of the ferrimagnetic materials is their higher resistivity which makes them suitable for higher frequencies of operation.

The ferrites are the most commonly used ferrimagnetic materials. They are ceramic materials made of iron (Fe^{+++}) oxides with ions of other transition metals like Nickel (Ni^{++}), Manganese (Mn^{++}) and Zinc (Zn^{++}). The ferrites as well as all ferrimagnetic and ferromagnetic materials lose their magnetic properties above a temperature called the Curie temperature (1043K for iron)[64].

3.1.2 Magnetic permeability

A measure of the ability of a material to realign its domains in the presence of a magnetic field is the magnetic *permeability*. There are different definitions for permeability:

- Absolute permeability, which is given as the ratio of flux density B to the applied field H
- Relative permeability, which is a dimensionless number given by the ratio of absolute permeability to the permeability of free space ($\mu_0 = 4 \times \pi \times 10^{-7} H/m$)
- Effective permeability, is used when an air gap is introduced in the magnetic circuit. It is dependent on the initial permeability of the soft magnetic material and the dimensions of the air gap.

The diamagnetic materials have a relative permeability that is below 1.0, so that if an external field is applied to such a material the resulting field density in it would be less than the field density in air under the same field.

The paramagnetic materials respond to a magnetic field slightly better that the air space. Therefore their magnetic permeability is slightly more than 1.0.

The ferromagnetic and ferrimagnetic materials, on the other hand, experience a much higher relative permeability as their structure allows the magnetic field to re-align their domains to the direction of the magnetic field.

3.1.3 Magnetisation and hysteresis

As mentioned before, upon the presence of an external field the domains in a ferromagnetic material start aligning. This process is called *magnetisation*. As a result the field density B in the material increases as the field intensity H rises. It has been noted that the ratio between the field density and field intensity is called permeability of the material. However, the permeability is not constant. As more and more of the domain dipoles are aligned, the material's ability to respond to an increased field is reduced. At some point, when all the domains have been aligned to the external field, any increase of the field intensity has no effect in the field density. This situation is known as magnetic saturation of the material. It is a very important property as it defines the amount of energy that the material can store.

The relationship between the B and H magnitudes is illustrated on the magnetisation curve. The magnetisation curve of a material with infinite number of dipoles would be a straight line (figure 3.4). The amount of dipoles per volume of the material would define the slope of the curve. However, due to the magnetic saturation, the curve becomes flat when the field is increased above a certain point. Figure 3.3 illustrates the magnetisation process of a magnetic material showing also the domain positioning for different field intensities (H_1, H_2, H_3).

Assume now that the field is removed after the material was saturated. Although the field becomes zero some of the domains will stay aligned keeping the flux density at a level that is called the *residual* density.

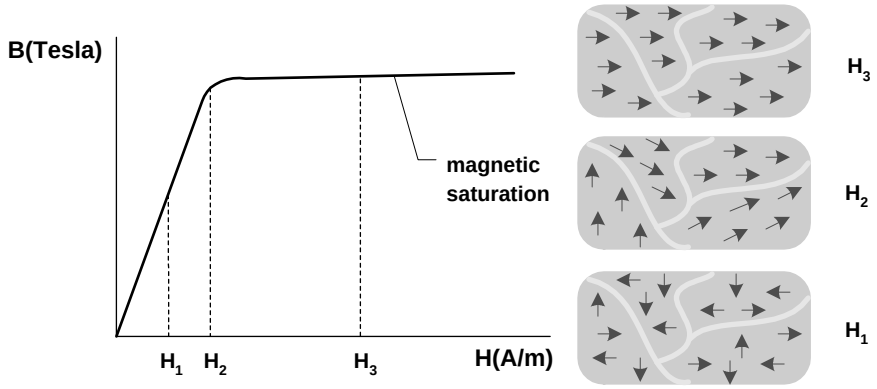

Figure 3.3: *The magnetisation curve and the domains alignment for an increasing field intensity*

The fact that the magnetic state of the material depends on its history is called *hysteresis* [64]. To re-align the domains in a ferrite an opposite field must be applied.

On the magnetisation curve the hysteresis is illustrated as in figure 3.4. This is called a $B-Hloop$

Before applying an external field the domains have arbitrary positions in the structure and therefore the net flux density in the material is 0 (point O). When initially magnetised under the influence of an external field the process is described by the line OA. At the point A the material is saturated and the flux density from this point onwards increases very slowly (as in air). When the field is removed the flux slightly drops to the residual flux level (point B). In order for the flux to be reset an opposite external field is needed. The de-magnetisation follows the path BC. If the field intensity keeps increasing the domains will be aligned in the opposite sense until the material will saturate (point D). Following a similar route the rest of the loop is traversed.

There is some energy spent when magnetising a material. This energy is given by:

$$W = \int_0^B H \cdot dB \qquad (joule/m^3) \tag{3.1}$$

which is equivalent to the enclosed area between the magnetisation curve (FA route) and the B axis (figure 3.5).

When B and H are linearly related (the magnetisation curve is a straight line) the above

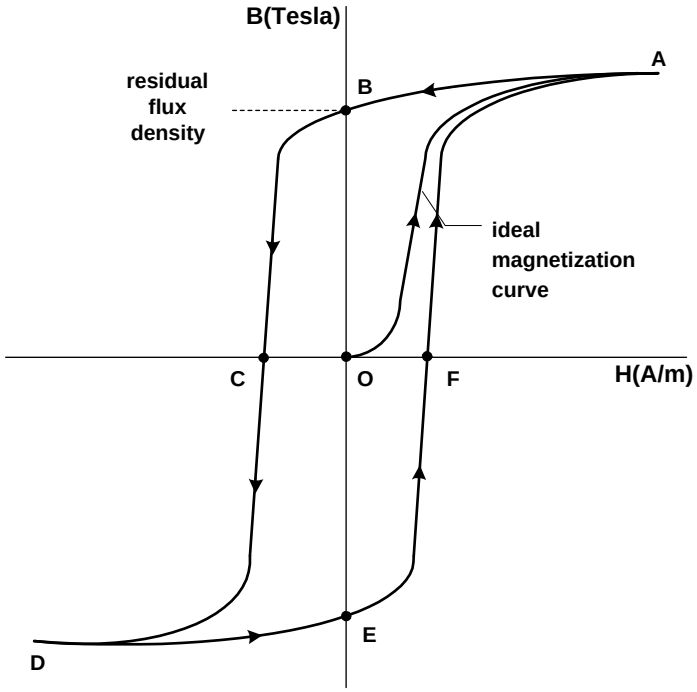

Figure 3.4: *The magnetisation curve illustrating the hysteresis phenomenon*

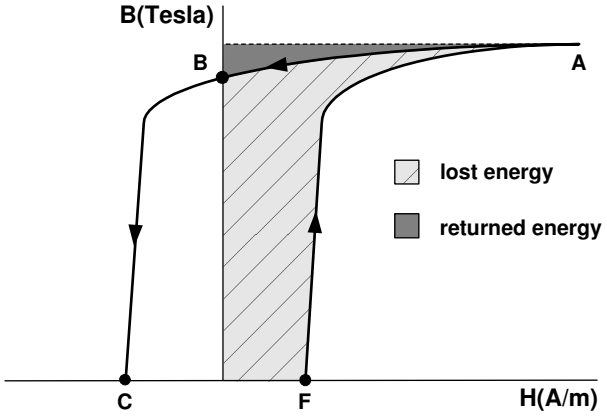

Figure 3.5: *Energy loss due to hysteresis*

integral simplifies to:

$$W = \frac{1}{2} \cdot B_f \cdot H_f \qquad (joule/m^3) \tag{3.2}$$

where B_f and H_f are the final values of the two field quantities. Equation 3.2 is the basis for inductance calculation with the method of finite elements analysis (as discussed in Chapter 4).

Some of the energy is released when the field is removed. However, due to the hysteresis effect an opposite field needs to be applied and more energy needs to be spent in order to demagnetise the material (see figure 3.4 above). The energy spent for repositioning the domains finally develops heat.

When used as a core material for a transformer the ferrite experiences a different magnetisation process depending on the power electronics topology. For example, in a forward converter the transformer would operate above the H axis often making the flux-resetting an important issue (thus requiring reset windings etc). However, when the transformer is driven by a bipolar waveform as in a push-pull converter, a loop like that of figure 3.4 describes the relationship between B and H. The flux excursion ΔB is a function of the switching frequency. Operating at a higher frequency usually results in reduced flux excursion.

3.2 Losses in Magnetic Components

The main mechanisms that cause losses in a magnetic component are:

- Hysteresis losses
- Eddy currents
- Conduction losses

As these are key parameters for the efficiency of a high frequency power converter an overview of the different phenomena is essential at this point. Some of these phenomena play an important role during the design of a rotating transformer. This is because the

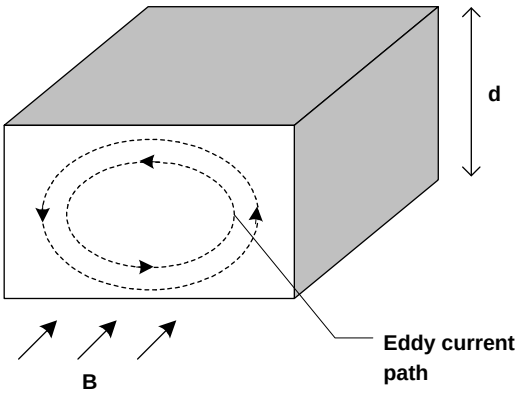

Figure 3.6: *Eddy currents created in a magnetic material under a varying magnetic density*

magnetic field in such a transformer does not strictly follow the magnetic core path but stores energy in different places within the volume of the transformer.

3.2.1 Hysteresis losses

As mentioned above, hysteresis losses appear in the magnetic core material due to the energy spent to reposition the magnetic dipoles within the material. The hysteresis losses per unit volume are approximated by the following relationship:

$$P_h = k \cdot f_{sw}^a \cdot \left(\frac{\Delta B}{2}\right)^d \qquad (W/m^3) \tag{3.3}$$

where k, a, and d are material related constants. As seen from equation 3.3, hysteresis losses depend on the switching frequency f_{sw} and also on the flux excursion ΔB. This equation is the result of a curve fitting process and the data is extracted from the graphs provided by the magnetic core manufacturers [66].

3.2.2 Eddy losses in the core

When a low resistivity material is placed in a variable magnetic field, electric currents are induced in the material (figure 3.6). These currents, known as *eddy currents*, cause a power dissipation in the material. The power primarily depends on the resistivity of the material and the magnetic field density.

The eddy current losses in a volume like that of figure 3.6 are approximated by the following relationship:

$$P_{eddy} = \frac{B_f^2 \cdot f_{sw}^2 \cdot d^2}{\rho} \qquad (W/m^3) \tag{3.4}$$

The ferrimagnetic materials (eg. ferrites) have a considerably lower resistivity making them more suitable for high frequency applications than ferromagnetic materials.

3.2.3 Conduction losses

The conduction losses in magnetic components can be classified in two major categories; the DC and the AC losses. The result of a current I flowing in a wire of resistance R (measured under a DC voltage) is power (I^2R) being dissipated and therefore heat being developed on the wire, where I is the rms value of the current. These are known as the *DC losses* of a transformer or inductor.

However, due to the varying magnetic field around the windings, the current distribution in the conductors is not uniform. The self-inductance of the conductor, as well as the magnetic field created by adjacent turns of the same winding, redistribute the current flow within the wire and reduce the effective cross-sectional area of the conductor and increase the *AC resistance*. These effects, namely the *skin* and the *proximity* effect, become stronger for higher frequencies of operation. The currents that cause these losses are all different occurrences of eddy currents [66].

The skin effect The skin effect is illustrated in figure 3.7. The current flowing in the conductor generates a magnetic field around it. This field in turn creates circulating currents in the wire as shown in figure 3.7. These currents are opposite to the main current flow in the centre of the conductor and add to the main current closer to the surface of the wire. The result is that more net current is flowing closer to the surface of the conductor. This is called the *skin* effect. The distance from the conductor surface to where the current density is $1/e$ times the surface current density is called *penetration depth* (or *skin depth*). Defining the penetration depth of the current for a specific frequency is very important for correctly choosing the wire thickness. It is given by [67],

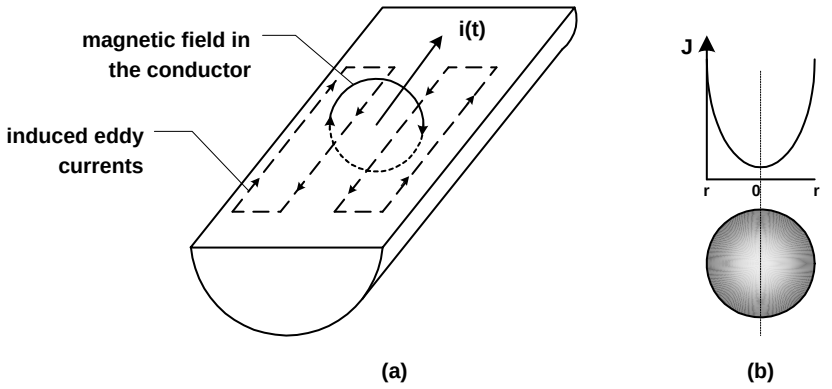

Figure 3.7: *The skin effect; (a) eddy currents induced in the conductor and (b) resulting current density.*

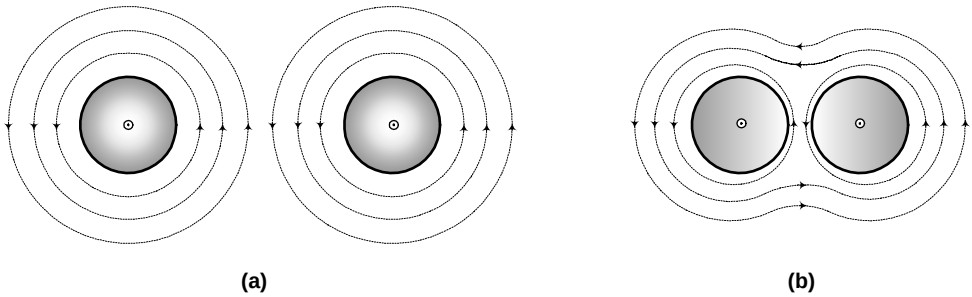

Figure 3.8: *The proximity effect within two current carrying conductors (a) negligible or no proximity effect (b) changed current distribution due to proximity of conductors [1].*

$$D_{pen} = \sqrt{\frac{\rho}{\pi \cdot \mu_0 \cdot \mu_r \cdot f_{sw}}} \tag{3.5}$$

Proximity losses When two parallel current carrying conductors are brought into proximity their magnetic fields interact as shown in figure 3.8. The overlapping fields between the wires cancel each other and this results in a reduction of the current density across the two opposing surfaces. This is called the *proximity effect*. Essentially, the magnetic fields produced by each one of the conductors is producing eddy currents within the other conductor. These currents are perpendicular to the field and therefore on the same axis with the original conductor current. However, they flow in the opposite direction (trying to eliminate their cause) thus effectively reducing the current density at the side of the wire where the field is stronger. The result of the proximity effect is a reduction of the effective cross-section of the conductor and consequently an increase

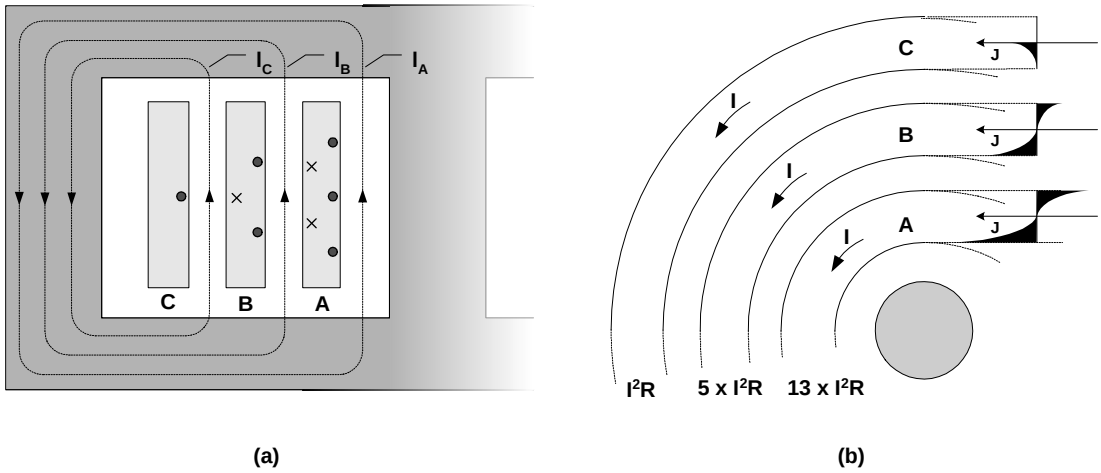

Figure 3.9: *The proximity effect in the winding of an inductor; (a) the magnetic flux in the winding space induces different eddy currents in each layer and (b) top view of three layers and the current distribution in them.*

of what is called AC resistance. This, in turn, results in higher I^2R losses on the wire. These are referred as *proximity losses*.

The proximity effect occurs in a winding that consists of more than one successive layer. The cross-sectional view of an inductor with a three layer winding is illustrated in figure 3.9(a). The basic principle that applies here is that the net current flowing in each winding is I. This current creates a magnetic field whose intensity is described at each point by the vector $\vec{H}$. Each layer creates an mmf relative to the current flowing in it. Figure 3.9(a) shows a magnetic line of length l_A created by layer A. According to Ampere's law this layer of the winding creates an mmf F given by

$$F_A = \oint H \cdot dl_A = NI \tag{3.6}$$

The same is valid for layers B and C,

$$F_B = \oint H \cdot dl_B \qquad F_C = \oint H \cdot dl_C \tag{3.7}$$

where N is the number of turns, each carrying a current I, encircled by the respective path of integration. The flux path created by layer A also encircles layers B and C and the flux created by layer B also encircles layer C. The mmf builds up as more layers

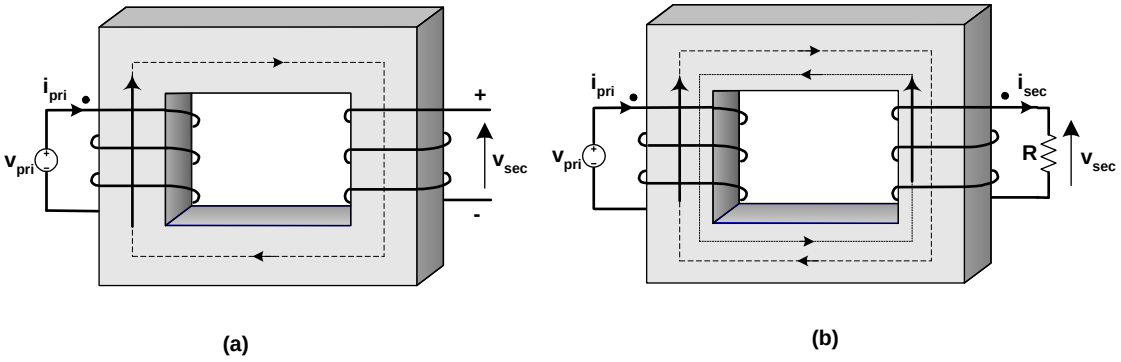

Figure 3.10: *Transformer Action.*

are added, hence, the one applied in A is three times that applied in C. The magnetic moments F_A, F_B, F_C are given by,

$$F_C = I \qquad F_B = 2 \cdot I \qquad F_A = 3 \cdot I \tag{3.8}$$

Again, the result of a varying magnetic field is eddy currents induced in each layer of the winding. Since the field magnitude is different at each layer the eddy currents will vary accordingly. These additional currents flowing into the conductors increase the current density although the net current is always kept fixed. Finally, the increased current density results in higher ohmic losses. The current distribution in each of the winding layers is illustrated in figure 3.9(b). The ohmic losses increase significantly for each extra layer added to the winding.

Faraday's law (equation 3.10) defines that the voltage (and thus the current) induced on a conductor is proportional to the rate of change of the magnetic flux. This implies that the faster the flux density changes the higher the eddy currents will be. In other words higher frequency of operation results in greater proximity losses.

The proximity effect together with the skin effect are the two high frequency effects that change the *AC resistance* of the conductors.

3.3 Transformer Action

A voltage is applied to the primary winding (left hand side) of figure 3.10(a) and a current, called *magnetising current*, flows in it. This current creates a magnetic field

and the domains of the magnetic core start aligning in the direction of the field vector. Due to the increasing magnetic flux Φ_{pri} in the core, a voltage V_{sec} will be induced across the secondary winding (right hand side) of figure 3.10(a).

If a load is connected to the secondary winding and a current I_{sec} starts flowing in it too (figure 3.10(b)). This current will create another magnetic flux Φ_{sec} (according to Ampere's law) that will oppose the initial flux (and thus subtract from it). The total flux in the magnetic core is:

$$\Phi = \Phi_{pri} - \Phi_{sec} \tag{3.9}$$

Consequently, the primary and secondary voltages are according to Faraday's law:

$$V_{pri} = N_{pri}\frac{d\Phi}{dt} \quad and \quad V_{sec} = N_{sec}\frac{d\Phi}{dt} \tag{3.10}$$

One would expect that the total flux through the core would be reduced because of the secondary created counter-flux (Φ_{sec}). If this was the case, the primary voltage would have been reduced as well to abide with Faraday's law. This is not possible as the primary winding is driven by a voltage source. Instead, the current in the primary is increased to compensate for the opposing flux generated by the secondary winding. The amount by which the primary current is increased when the secondary winding is loaded is called the reflected *load current*.

In an ideal transformer the flux Φ that links both sides is the same, hence, the volts per turn is the same in both windings. The relationship between primary and secondary voltage is:

$$\frac{d\Phi}{dt} = \frac{V_{pri}}{N_{pri}} = \frac{V_{sec}}{N_{sec}} \Rightarrow \frac{V_{pri}}{V_{sec}} = \frac{N_{pri}}{N_{sec}} \tag{3.11}$$

Therefore, a transformer is used to couple the electrical energy from a circuit to another with no electrical contact between them and also to transform the voltage and current from one level to another.

It is now time to introduce the transformer equivalent circuit shown in figure 3.11. As

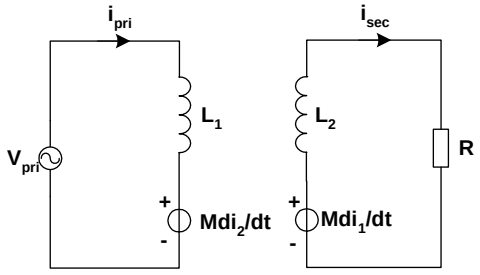

Figure 3.11: *Equivalent model for a transformer*

mentioned above, when a voltage is applied to a non-loaded transformer a magnetising current will flow. According to Ampere's law a magnetic flux will be produced that stores magnetic energy into the transformer structure (hence the inductors L_1 and L_2 in the model). In addition to that, if a load is connected to the secondary then energy taken from the source will be transferred from the primary winding to the secondary. Also, any change in the secondary current is reflected to the primary and vice versa. A common inductance, which is called mutual inductance M, is used to represent this effect. Any current change in one winding is reflected to the other as an opposing voltage by means of the mutual inductance.

By applying Kirchoff's law to the network of figure 3.11 the two basic equations that govern the transformer operation are obtained.

$$V_{pri} = L_1 \cdot \frac{di_1}{dt} + M \cdot \frac{di_2}{dt} \tag{3.12}$$

$$V_{sec} = L_2 \cdot \frac{di_2}{dt} + M \cdot \frac{di_1}{dt} \tag{3.13}$$

3.3.1 Mutual flux

Concepts such as mutual flux and mutual inductance are very important in a transformer as they are a measure of the component's ability to transfer energy from one winding to the other. Mutual flux, as mentioned, is the magnetic flux linking both windings. In an ideal transformer mutual flux is equal to the total flux created by the primary and secondary windings (the combination of their fluxes). This, practically, means that in an ideal transformer like the one shown in figure 3.10(b) the windings are tightly wound

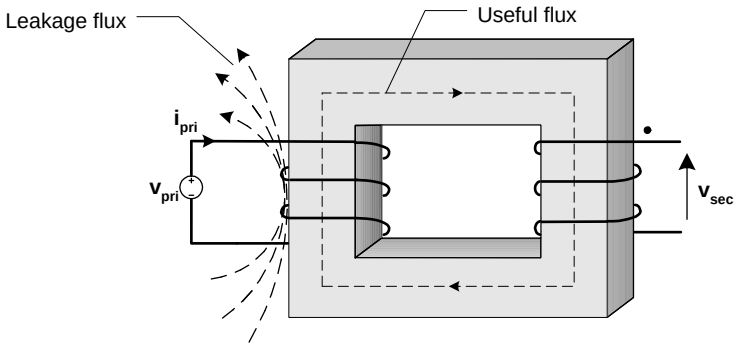

Figure 3.12: *The leakage flux.*

around the magnetic core so all the magnetic flux is following the ferrite path.

However, this is not the case in a real transformer. The magnetic flux is not always flowing through the core material. This creates the so-called leakage flux which is explained in the following section.

3.3.2 Leakage flux

The magnetic flux (equivalent to electric current in an electric circuit) created by a magnetomotive force (equivalent to electric voltage) will tend to follow the path with the smallest reluctance (equivalent to electric resistance). This means that the magnetic flux will easily flow through a ferrite whose permeability is very high but will resist flowing through the air that has a very small magnetic permeability. However, the permeability of the magnetic core is not infinite which means that a small amount of flux will follow the air path (just like a small electric current would flow through a huge resistance which is in parallel to a small one). This is illustrated in figure 3.12. Some of the flux escapes from the magnetic core and returns to the source through the air. This *leakage flux* stores energy in the air space (by re-aligning its magnetic dipoles). This is electrically described as an additional inductance called *leakage inductance*.

In electrical terms the leakage inductance is much smaller than the mutual inductance and therefore the energy stored in it is much less than the energy transferred to the other winding.

A cross-sectional view of a transformer is illustrated in figure 3.13. The secondary winding is wound on top of the primary and therefore the estimation of leakage phenomena

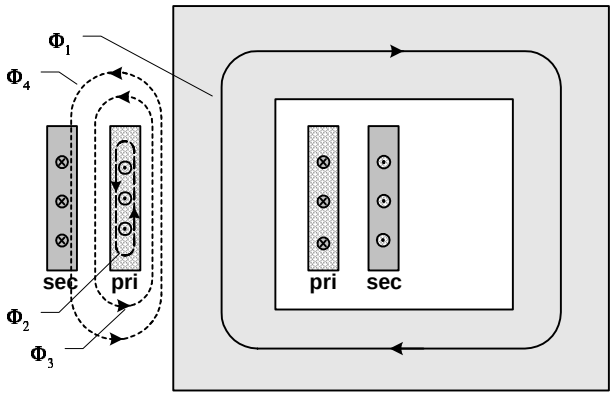

Figure 3.13: *The different paths that the magnetic flux follows in a typical transformer.*

becomes more complex. Identifying the paths that the flux can leak through is the initial step in order to eliminate them. The following leakage flux paths are shown using dashed lines [68].

1. the mutual flux Φ_1 that is generated by the primary and also links the secondary winding
2. the leakage flux Φ_2 developed within the generating winding itself
3. the leakage flux Φ_3 in the air-space between the two windings and
4. the combined mutual/leakage flux Φ_4 that partially encircles the secondary winding

3.3.3 Rotating transformer

In general, the role of a transformer is to transfer energy from one circuit to another without an electrical contact. Storing energy into the magnetic core or the air-space around it, is not desired. On the contrary, energy storage is the objective of a coupled inductor.

A rotating transformer has an air gap of non-magnetic medium (air-gap) between the core halves. It partially behaves as a coupled inductor storing energy into the gap and in the leakage inductances of the windings.

It is clear that there is not an absolute distinction between a transformer and a coupled inductor. They are physically similar. It is the particular application that requires the

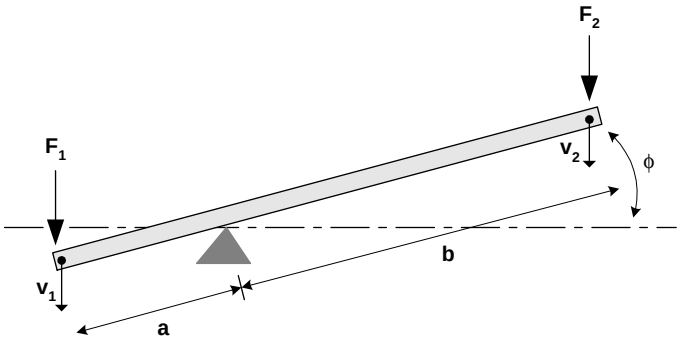

Figure 3.14: *The physical model of an ideal transformer*

component to operate as a transformer or as a coupled inductor. If only the transforming operation is desired, emphasis must be given on maximisation of the mutual flux and eliminating any possible paths of flux leakage. If storage of energy is the objective, emphasis must be given to the design of the air-gap and the energy storage elements.

The key point is that in a rotating transformer energy storage and transformation are two parallel processes. Careful engineering is needed to design the magnetic component and the power electronics around it for optimum performance.

3.4 Transformer Modelling

Magnetics Modelling, in general, is the process of representing a magnetic component by means of an equivalent electrical, mechanical or other system or a set of mathematical expressions. Modelling a transformer as an equivalent mechanical system, for example, would allow a visualisation of the different effects that are taking place in a transformer. Modelling the transformer as an electrical network would let an engineer include it in a simulation and analyse its operation within a wider system. Finally, a set of mathematical equations can be derived to quantify each aspect of a magnetic component.

3.4.1 A physical model

The inductive interface that is being analysed is neither an ideal transformer nor a pure inductor. It transfers energy to the secondary, but at the same time, it stores energy in the magnetic and non-magnetic materials of the interface. A mechanical equivalent [69] of the magnetic interface is presented in figure 3.14.

The velocity of the primary side $v_1$can be related to the velocity of the secondary side v_2 by taking into consideration the geometrical characteristics of the lever. Each edge of the lever travels a distance,

$$y_1 = a\sin(\phi) \quad y_2 = -b\sin(\phi) \tag{3.14}$$

The relationship between the tip velocities is found by differentiating the last equations and dividing,

$$v_1 = -(a/b)v_2 \tag{3.15}$$

The energy storage in a transformer can be modelled by an elastic lever that can bend and store some energy when a force is applied to it. As a result, the length ratio a/b (equivalent of the turns ratio) is not enough to describe the relationship between the "primary" and "secondary" speeds. The elasticity properties of the lever come into the design (in analogy to the leakage and mutual inductances of the transformer).

3.4.2 Obtaining electrical characteristics from geometry

A simple equivalent model for the transformer has been presented (figure 3.11). This model has a disadvantage; its elements are not directly inherited from the geometrical characteristics of the transformer. It is rather an empirical model built by considering the transformer as a black box and measuring the input and output impedances. The basic problem that arises when modelling a magnetic component is to derive the electrical equivalent network from its physical structure. This would allow the designer to reverse engineer the component and adjust its physical structure according to the results of the electrical simulation. This procedure is generally tedious as it involves studying the magnetic fields in the component, identifying the focal points of energy storage etc.

Reluctance modelling is one of the methods used for analysing a magnetic component. It is based on finding the equivalent magnetic circuit by identifying the different magnetic flux paths in it. Then using the duality between magnetic and electric quantities, the reluctance model can be converted to an electric equivalent [70]. Assume the transformer of figure 3.15(a). There are two magnetic flux sources or *magnetomotive force* (MMF)

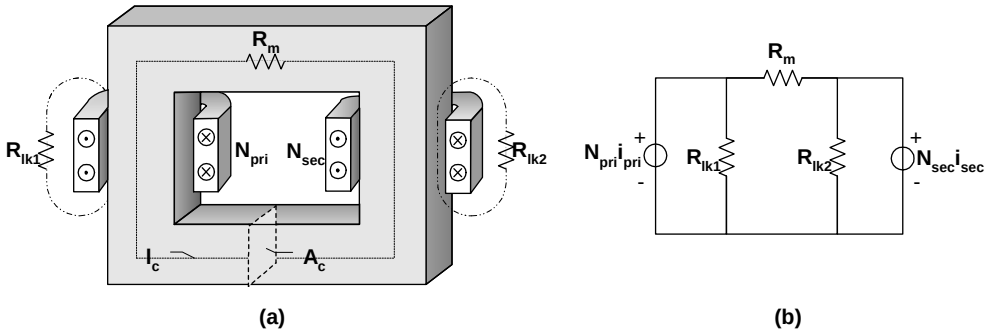

Figure 3.15: *Reluctance modelling (a)the magnetic flux paths in a transformer, (b) the equivalent reluctance model.*

sources; the two windings N_{pri} and N_{sec} that are conducting currents i_{pri} and i_{sec} respectively. The flux paths in the magnetic core and the air space are shown with dashed lines. The equivalent magnetic circuit or *reluctance model* appears in figure 3.15(b).

Each of the magnetic flux paths has a reluctance (which is represented by a resistor) that is a function of the material permeability, the cross-sectional area and the length of the path (Equation 3.16).

$$R_m = \frac{l_c}{\mu_0 \cdot \mu_r \cdot A_c} \tag{3.16}$$

This is in analogy to the resistance of a conductor that is a function of the resistivity of the material and its cross-sectional area and length. The inverse of reluctance is called *permeance* P of the flux path and can be physically interpreted as the inductance measured across one turn wound around the path of reluctance R. The magnetising inductance L_m of the primary winding of N turns which is wound around a path of permeance P_m is calculated in Appendix A.1 and is given by,

$$L_m = \frac{N_{pri}^2}{R_m} = N_{pri}^2 \cdot P_m \tag{3.17}$$

where N_{pri} is the number of turns and R_m the reluctance of the core path. The mutual inductance, on the other hand depends on both windings. A quantitative definition of the mutual inductance of the transformer of figure 3.15(a) can be given,

$$M = \frac{N_{pri} N_{sec}}{R_m} \tag{3.18}$$

Similarly, the primary and secondary winding leakages can be approximated by,

$$L_{lk1} = \frac{N_{pri}^2}{R_{lk1}} \tag{3.19}$$

$$L_{lk2} = \frac{N_{sec}^2}{R_{lk2}} \tag{3.20}$$

where R_{lk1} and R_{lk2} are the reluctances of the medium (air in this case) where the leakage flux appears.

To convert the reluctance model of figure 3.15(b) to an electrical equivalent we make use of the duality between magnetic and electric networks. According to [25], the network of figure 3.16(a) is derived by changing the MMF sources ($N_{pri} i_{pri}$, $N_{sec} i_{sec}$) to voltage sources and series branches to parallel branches. Figure 3.16(b) illustrates the permeances transformation to inductances by multiplying them with the respective number of turns squared (eg. $(N_{pri})^2$) and adding the ideal transformer. The final stage of transformation (figure 3.16(c)) involves moving the secondary leakage inductance to the secondary side by scaling it by the square of the turns ratio.

The equivalent model of figure 3.16(c) has a direct physical meaning. L_{lk1} and L_{lk2} are the leakage inductances of the primary and secondary side and their value can be calculated directly by working out the reluctances. Similarly, the magnetising inductance L_m can be calculated from the characteristics of the magnetic core. The ideal transformer is used to provide the stepping up or down function. This model can be directly incorporated in a simulation. Any possible deficiencies can be located and the physical structure can be modified accordingly.

3.4.3 Obtaining electrical characteristics from measurements

After a transformer has been designed and manufactured, its electrical characteristics can be verified by performing some simple tests using an LCR bridge or a magnetics analyser. This method cannot be used until the actual prototype is built. However,

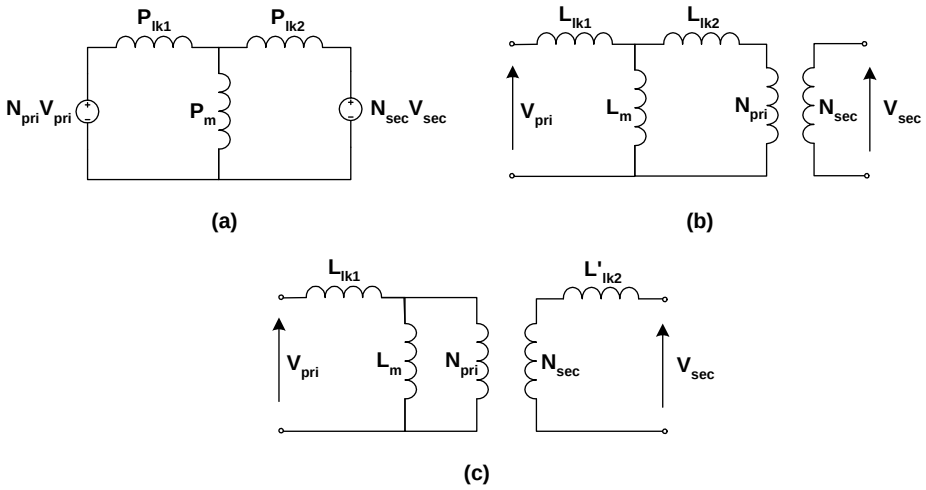

Figure 3.16: *Converting the magnetic model to its electric dual: (a) the permeances model (b) permeances converter to inductances and (c) the resulting τ-equivalent electric model.*

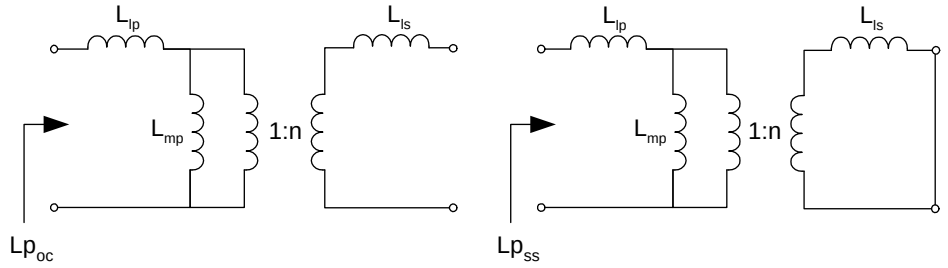

Figure 3.17: *The two test approach (a)measuring input impedance with an open-circuited secondary winding and (b) measuring input impedance with a short-circuited secondary winding.*

many designers use it in a trial and error approach, especially at the final stages of development. It is important to choose the appropriate measuring techniques in order to obtain trustworthy results. Therefore, several different techniques have been developed according to the transformer's type and use [71]. A typical method for measuring the electrical characteristics of a transformer is by performing the basic open-circuit and short-circuit tests (figure 3.17). These are:

- Measure $L_{p_{ss}}$ (primary winding inductance when the secondary is short-circuited)
- Measure $L_{p_{oc}}$ (primary winding inductance when the secondary is open-circuited)

The two test approach gives accurate results, if the following conditions hold; a) the transformer magnetising inductance L_{mp} is much higher than the leakage inductances

L_{lp}, L_{ls} and b) the primary and secondary leakage inductances can be assumed to be equal. Under those assumptions the electrical characteristics of such a transformer are approximated by the following relationships derived in Appendix A.3,

$$L_{mp} = L_{p_{oc}} - L_{lp} \tag{3.21}$$

$$L_{lp} = \frac{L_{p_{ss}}}{2} \tag{3.22}$$

$$L_{ls} = \frac{n^2 L_{p_{ss}}}{2} \tag{3.23}$$

Clearly, in a coupled inductor or gapped transformer neither of the above assumptions hold. The magnetising inductance is very low (and in some cases comparable to the leakage inductances) and therefore the secondary leakage cannot be combined with the primary leakage inductance. Also the primary and secondary leakage inductances are not always equal. An extra test is performed in order to allow an accurate calculation of the electrical parameters. This is measuring the output inductance by having the primary winding open-circuited. Hence, the three tests performed are:

- Measure $L_{p_{ss}}$ (primary winding inductance when the secondary is short-circuited)
- Measure $L_{p_{oc}}$ (primary winding inductance when the secondary is open-circuited)
- Measure $L_{s_{oc}}$ (secondary winding inductance when the primary is open-circuited)

Using the data obtained from the three test method the electrical characteristics of the transformer can be calculated using the following formulae. The derivation can be found in Appendix B.

$$M = \sqrt{(L_{p_{oc}} - L_{p_{ss}})L_{s_{oc}}} \tag{3.24}$$

$$L_{mp} = \frac{1}{n}M \tag{3.25}$$

$$L_{ms} = nM \tag{3.26}$$

$$L_{lp} = L_{poc} - L_{mp} \tag{3.27}$$

$$L_{ls} = L_{soc} - L_{ms} \tag{3.28}$$

where M is the mutual inductance, L_{mp} the primary inductance of the secondary and L_{ms} the one reflected to the secondary side and L_{lp}, L_{ls} the primary and secondary leakage inductances.

The above three-test approach gives satisfactory results for transformers with low coupling coefficients. An accuracy problem arises when the transformer windings have a high resistance relative to the the magnetising inductance impedance, in which case the series-coupling test described in [71] can be used.

3.4.4 Obtaining electrical characteristics from finite element analysis

3.4.4.1 The 2D finite element analysis

Finite Element Analysis (FEA) is a mathematical tool for analysing complex and usually non-homogeneous structures by dividing them to smaller pieces for which the behaviour can be approached mathematically. The first step of the FEA method is approximating the domain with a union of simple geometric objects (eg. triangles). These elementary geometries form a *mesh* in the language of FEA and each vertex is called a *node*. So far a large non-homogeneous non-standard geometry has been divided to small enough geometries, so that any problem can be considered as linear on it with a small error. The solutions in neighbouring triangles connect to each other continuously across the nodes. The next step is approximating the solution on each sub-geometry by a polynomial. Polynomials are easy to solve and usually give a close approximation on small domains. The solutions of the polynomials of two neighbouring sub-geometries must converge at the common points (or nodes) of the geometries. If this is not the case, the degree of the polynomials has to be increased in order to get an acceptable convergence between the two solutions.

The FEA method can be used to solve the magnetic field within a structure like an inductor and the surrounding space. This can give an insight as to how the inductor operates, where the energy is stored and even calculate eddy currents and losses. All the user has to do is to set up the FEA model. The drawback of FEA is its advanced features are only available to those having a strong electromagnetic background. Apart from the complexity, the computational power may be restrictive in complex problems. The time and resources needed for the analysis of a 3-D structure are sometimes restrictive and therefore some assumptions can be used to simplify a problem. A simple way of doing that is by finding an axial or rotational symmetry in the model to be analysed.

3.4.4.2 Setting-up a model

Setting up the model for a finite elements analysis generally includes three steps.

1. Design 2-D or 3-D model,
2. Define material properties,
3. Define boundary conditions and excitation sources

Design 2-D or 3-D model The new generation of FEA software has simplified this procedure by providing a graphical user interface (GUI) for designing the model. Thus a set of graphical tools can be used to design the structure or even import it from other schematic programs such as $AutoCad^{TM}$. For an object without any axial symmetry the whole structure has to be designed, whereas for an object with some kind of axial symmetry the cross-section of the object is drawn and the axis of symmetry is declared. The geometries that have some kind of symmetry can be classified in two categories; the cartesian or XY plane geometries and the Axisymmetric or RZ plane geometries. Figure 3.18 illustrates two example geometries with different kind of symmetry.

Define material properties After the structure has been designed, the material properties must be defined so that the 2-D or 3-D solver knows how each element of the design behaves in the presence of an electric or magnetic field. The magnetic permeability and electric conductivity are two of these properties. In a transformer

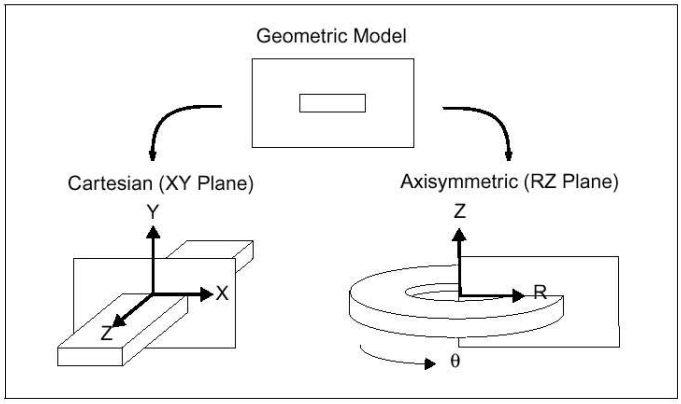

Figure 3.18: *Illustration of the Cartesian and Axisymmetric geometries*

model, for example, the user must declare that the object representing the core is made of ferrite and define its magnetic permeability. Similarly the round objects representing the wires must be assigned a material (eg. copper) and the space around the objects must be defined as air or vacuum.

Define Boundary conditions and excitation sources This is usually the final step of setting up a FEA model. The boundary conditions are basically defining the solver's behaviour at the surface of the different objects. In terms of mathematical analysis the boundary conditions describe the behaviour of a function at the boundaries of a domain (eg. [a,b]). In the models analysed here the surfaces of all objects are Newmann or natural boundaries [72]. That is, the magnetic field is defined to be perpendicular to the edges of the problem space and continuous across all object interfaces.

Finally, the exciting (mmf) sources need to be defined by specifying the current or current density through the conductor(s).

3.4.4.3 Calculating the electrical characteristics

Once the 2-D or 3-D solver has converged to a solution there are many possible manipulations to analyse this solution. The post processor is a powerful tool that can illustrate the field distribution and density, the field intensity, the current density and all other scalar or vector quantities in the structure. Most important, the post-processor can evaluate complex expressions and calculate inductances, capacitances and other useful

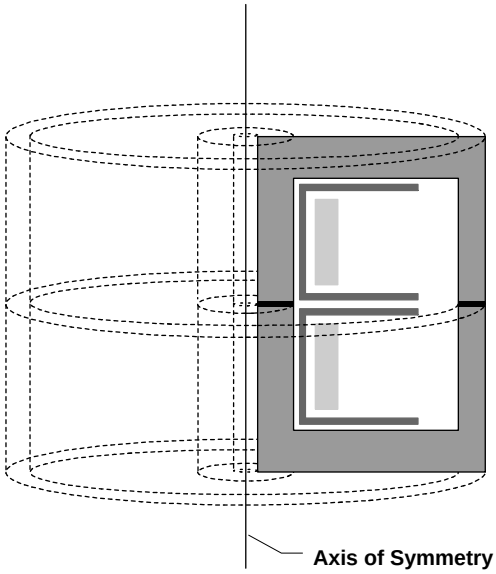

Figure 3.19: *The cross-sectional area of a pot core transformer as modelled in the 2D plane*

properties of the analysed geometry.

Although finite element analysis provides an accurate representation of the field distribution, the engineer's intuition is needed for translating the geometrical to electrical characteristics. This is simply because the space where energy can be stored has to be located before the respective inductances (mutual and leakage) can be calculated.

Assume the transformer of figure 3.19 where the cross-sectional area of a pot core transformer is illustrated. Notice that if this cross-section is rotated around axis Z the pot transformer will be drawn. Thus the 3-D problem can be reduced to 2-D assuming that the magnetic field lines are identical in all cross-sections of the transformer. It is easy to calculate the self-inductance of each winding. This is done by applying a current to one winding at a time and leaving the other one open-circuited (as in the open-circuit test of Section 3.4.3). The self inductance of the winding can be calculated by finding the energy stored in the form of magnetic field within the volume of the transformer and then solving the following equation for self inductance L,

$$E = \frac{1}{2} \cdot L \cdot I^2 \tag{3.29}$$

where I is the current through the winding and E the magnetic field energy. This

energy can be calculated in two different ways (both give identical results). The first is by evaluating the integral of the current density $\vec{J}$ times the *vector field* $\vec{A}$ over the volume of the transformer. The product $\vec{J} \times \vec{A}$ is non-zero only in the wire volume V_w,

$$E = \frac{1}{2} \cdot \int_{V_w} \vec{A} \cdot \vec{J} dV \tag{3.30}$$

By combining equations 3.29 and 3.30 and solving for inductance L,

$$L = \frac{\int_{V_w} \vec{A} \cdot \vec{J} dV}{I^2} \tag{3.31}$$

Due to the symmetry of the problem it can be reduced into two dimensions. The result is then multiplied by the perimeter of the core to account for the total volume V of the pot core. Equation 3.31 becomes,

$$L = 2 \cdot \pi \cdot R \cdot \frac{\int_{V} \vec{A} \cdot \vec{J} dV}{I^2} \tag{3.32}$$

where R is the radius of the core. Calculating the value of this integral with the post processor calculator is a straightforward procedure.

The second way this can be done is by calculating the magnetic energy itself. To compute the magnetic energy the following integral needs to be evaluated,

$$E = \frac{\mu_r}{2} \cdot \int_{V} \cdot \vec{H}^2 dV \tag{3.33}$$

where μ_r the relative permeability of the material and $\vec{H}$ the field intensity in the vector. This requires evaluating the integrals separately for the different mediums in the transformer as the permeability changes.

Adding the energies and substituting in Equation 3.29 and solving for L gives:

$$L = \frac{1}{I^2} \cdot \left(\mu_0 \cdot \int_{V} \vec{H}^2 \cdot dV + \mu_{r_{ferrite}} \cdot \int_{V} \vec{H}^2 \cdot dV \right) \tag{3.34}$$

where I is again the total inductor current, μ_0 the air space permeability and $\mu_{r_{core}}$ the magnetic core permeability.

The engineers intuition is again useful in order to attempt a direct calculation of leakage or mutual inductance. This is because the leakage or mutual energy has to be located so that the integral will be calculated over the appropriate area.

3.5 Chapter Summary

An introduction to magnetism and its properties is presented in this chapter. The aim is to convey a better understanding of the physical operation of a transformer with and without an air gap. The notions of leakage and magnetising inductances were introduced and explained physically and electrically. The operation of a transformer was explained and a full electrical equivalent circuit was derived.

Three methods were presented for deriving the electrical characteristics of a transformer; (a) using its physical structure (geometry and materials) (b) by electrical measurements (c) by finite element analysis. Each of the above methods has its merits and drawbacks. Calculating the electrical equivalent purely from the geometry of the transformer is advantageous, as it can predict the electrical properties prior to manufacturing of the component. However, in complex transformer designs this method requires advanced knowledge of electromagnetic theory in order to manipulate vector quantities over complex geometries and it becomes impractical for engineering design. On the other hand, deriving the electrical characteristics by performing electrical tests gives accurate readings but it can only be applied after the transformer has been designed and manufactured. The FEA method relies on the computer performing the advanced electromagnetic analysis. The operation of a transformer is accurately simulated (usually error$<$ 1%) and the only difficulty arising here is translating the magnetic field information to electrical circuit parameters, namely leakage and magnetising inductance.

Overall the reluctance modelling method can be the basic route to a qualitative analysis (eg. selection of core shape, winding layout etc.) and a rough estimation of the different electrical properties. A finite elements analysis can be easily performed to give the designer an insight to the magnetic flux paths, focal points of energy storage, air gap effects and high frequency losses. An optimisation can be performed based on the

FEA results and a prototype can be manufactured and measured using the three-test approach. An accurate electrical model for simulation purposes can be then derived.

Chapter 4
The Rotating Transformer

As seen in Chapter 2 there are different types of contact-less energy transfer (CET) devices for different applications. Each of those has its own mechanical and electrical characteristics as the size, winding layout and clearance length varies. Consequently, the need for a customised power electronics design is profound.

The rotating transformer is one form of CET device. An insight to its operation and design is attempted in this chapter. Its electrical characteristics are quantified using the theory presented in Chapter 3. Two different transformer geometries are considered and their advantages and disadvantages are discussed.

Finally, the AC analysis of the equivalent electrical model is presented in order to gain a better understanding on how the electrical characteristics affect the transformer voltage gain and efficiency. Some design guidelines are given to allow more efficient and reliable operation.

4.1 Electrical Characteristics

The rotating transformer has a low coupling coefficient because of the air gap between the two core halves. In electrical terms this means that the magnetising inductance of the transformer is low, thus resulting in a high magnetising current needed to realign the magnetic dipoles of the air. The magnetising current is generally not desirable as it does not contribute to the reflected secondary current: it only stores magnetic energy in the magnetic core material, hence making the magnetic component behave as a coupled inductor rather than a transformer. At the same time the leakage inductance of the primary and secondary windings is higher due to their physical separation.

The rotating transformer differs from other inductive couplers in that it has electrical characteristics. Due to the fixed air gap length and the fixed horizontal and vertical relative position between the primary and secondary core halves the magnetising and

leakage inductances are also fixed. The rotary movement does not affect the electrical characteristics, if the cross sectional area of the core, and especially the gap space, remains constant for any degree of rotation.

The radar application that is considered here does not require a separating wall between the transformer halves. Therefore, the gap length is only subject to the machinery that is available for manufacturing.

Based on the above principles the design procedure of a DC to DC converter with a rotating transformer must be conducted via two parallel routes; the mechanical optimisation and the optimisation of the power electronics. The mechanical design must be based on the following principles:

Core size. This is directly related to the amount of power that the transformer is expected to handle and the air gap between the core halves.

Coupling capability. This can be optimised by reducing the air gap length, increasing the cross sectional area of the magnetic core or placing the primary and secondary windings closer.

Energy storage capability. The energy storage is directly related to the coupling. There are two basic energy storing elements; the magnetising inductance (inversely proportional to the air gap length) and the leakage inductance (related to the windings layout and relative positioning).

The second process, that of optimising the power electronics part of the DC to DC converter, is topology-dependent and is examined in Chapter 6.

4.1.1 Magnetising inductance

As mentioned in a previous section any contact-less energy transfer device such as the rotating transformer stores energy in the magnetising inductance due to the air gap that is introduced between the core halves. The value of the magnetising inductance becomes smaller for longer clearance distances between the core halves. In a carefully designed conventional non-gapped transformer for switching power applications the magnetising inductance varies typically from 1mH to 10mH (mainly depending on the number of the

winding turns). Once the air gap is introduced between the core halves the magnetising inductance decreases by more than 10 times for 1mm gap or more.

As proved in Appendix A.1,

$$L_m = N_{pri}^2 \cdot \frac{1}{R_g + R_c} \tag{4.1}$$

or

$$L_m = N_{pri}^2 \cdot (\frac{l_g}{\mu_0 \cdot A_g} + \frac{l_c}{\mu_{a_c} \cdot A_c})^{-1} \tag{4.2}$$

Equation 4.2 implies that the magnetising inductance increases by the square of the winding turns N_{pri}. In the parentheses the absolute magnetic permeability of the core material is much higher than the air permeability ($\mu_{a_c} >> \mu_0$), so the core reluctance is much smaller than the air gap reluctance. This practically means that the air gap defines the order of magnitude of the magnetising inductance[1].Therefore, Equation 4.2 simplifies to,

$$L_m = N_{pri}^2 \frac{A_g \mu_0}{l_g} \tag{4.3}$$

which is the standard equation for the inductance of a solenoid. Hence, the magnetising inductance can be increased by decreasing the air gap length between the core halves. For a smaller clearance a precise machining procedure is required and the cost of the design increases rapidly for very small lengths. Additionally, the rotating part must be well positioned and have a perfect axial symmetry in order not to touch the stationary part when rotating.

4.1.2 Leakage inductance

Another property of the rotating transformer is the high leakage inductance of its windings. This is mainly due to the fact that the windings have to be placed at a reasonable distance from each other to allow rotation. The leakage inductance depends on the

[1] This is valid for a relatively long air gap

length of the flux path and also the magnetic permeability of the medium (as discussed in Chapter 3).

More analytically, according to Appendix A.1, the leakage inductance of the primary winding is given by,

$$L_{lk1} = N_{pri}^2 \cdot \frac{\mu_0 \cdot A_{sp}}{l_{sp}} \tag{4.4}$$

where l_{sp} is the length of the magnetic leakage flux lines and A_{sp} the cross-sectional area of the flux path[2].

In Chapter 3 it was mentioned that leakage inductance is a property of a winding relative to another winding. It is important to explain at this point how the leakage inductance is affected by the relative position between the two (or more) windings.

There are two basic cases of relative positioning of the windings. In figure 4.1(a) the primary and secondary windings of the transformer are placed far from each other so that the leakage flux paths are not overlapping. In such an arrangement changing the geometry of one of the windings has a negligible effect on the other winding's leakage inductance. In that case the leakage inductance of the winding is a function of the number of turns, its distance from the core and its radius. Figure 4.1b illustrates the case where the primary and secondary leakage flux paths are overlapping at the space between the two windings and therefore any change in the position of one winding affects the other winding's leakage inductance.

Based on the above observation two winding arrangements are proposed in section 4.2 and their electrical properties are evaluated.

4.1.3 Inter-winding and inter-turn capacitances

The *inter-turn* capacitance is the result of two turns being in proximity. Due to the proximity of the successive or neighbouring turns, energy can be stored between them in

[2]This formula cannot always be applied as the geometry of the air space may not be a regular shape (with some kind of symmetry). If this is the case, the geometry has to be divided to smaller volumes which can be approximated by a cubic, cylindrical or any other fully defined geometrical shape. The integration of the magnetic field intensity over these elementary volumes (Equation A.1) will then give the total energy. This energy can be then used in Equation A.4 to get the leakage inductance value.

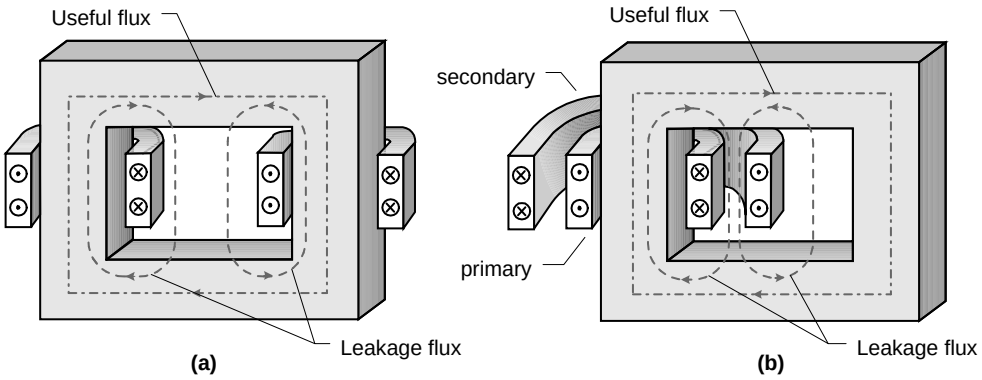

Figure 4.1: *Winding layout and leakage inductance (a)primary and secondary leakage paths are independent(b) primary and secondary leakage paths overlapping.*

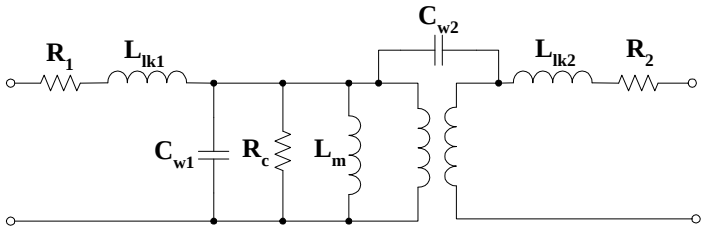

Figure 4.2: *The full transformer model including the parasitic end-to-end and inter-winding capacitance.*

the form of electric field. The resulting capacitance that appears across a winding is often called *end-to-end* capacitance. The end-to-end capacitance is generally small (order of magnitude of few pico-farad) and can be reduced by using *bank winding* techniques.

The end-to-end capacitance that appears in shunt with the winding is responsible for causing resonance with the series and parallel inductances of the transformer model. By locating those resonant points its value may be approximated.

The *interwinding* capacitance is the result of two or more windings of a transformer being in proximity. This capacitance is even smaller and its effect can only be seen at very high frequencies.

Both inter-turn and interwinding capacitances are of small importance in a rotating transformer due to the low magnetising inductance that in combination with the low capacitance values, moves the resonant point to a very high frequency. As the operating frequencies tend to increase, the parasitic capacitances effect needs to be considered in future work.

4.1.4 Winding resistance

The elements that have been studied so far (magnetising and leakage inductances and interwinding capacitances) are all energy storage elements, which means that they are not directly affecting the transformer's efficiency. The winding resistance and magnetic core losses, on the other, hand have a direct impact on the efficiency.

The windings resistance is the result of two components. The first is the traditional (dc) resistance of the wires. The second is the result of the high frequency effects described in Section 3.2.3. The resulting resistance is termed *effective* resistance.

The effective resistance increases due to the proximity and skin effects and can be controlled by reducing the number of primary and secondary turns and by carefully selecting the wire thickness.

As seen in Chapter 3, the proximity effect is caused due to the proximity of the successive layers of a winding. The more layers present in the winding, the more intense the effect is. In a conventional transformer interleaving of primary and secondary layers can be applied as a remedy. However, in a rotating transformer interleaving is not possible, thus the only way to control the proximity losses is to eliminate the number of layers by either choosing a wide core window area (that fits more turns in each layer) or by decreasing the number of the winding turns.

A considerable amount of work has been done in the past towards the accurate calculation of the effective resistance of a winding. Originally, Dowell [73] [74] derived a set of equations. This method assumed a sinusoidal waveform across the winding and the results for non-sinusoidal power supply waveforms were not accurate. Bruce Carsten [1] extended this work in order to apply it to a complex waveform. To do this he performed a Fourier analysis to de-synthesise the original waveform. Dowell's method could be then applied to each of the resulting sinusoidal components and the total losses were calculated by summing the losses of each frequency. This method is accurate but complex to apply. As a result Hurley presented a series of papers [75], [76], [77], [78], [79] that reduce the calculation of the effective resistance to one equation. The only prerequisites are the knowledge of the rms values of the current waveform and that of the derivative of the current waveform. Hurley's equation is,

$$R_{eff} = R_{dc} + \frac{\Psi}{3} \cdot \Delta^4 \cdot R_{dc} \cdot \left[\frac{I'_{rms}}{\omega I_{rms}}\right]^2 \tag{4.5}$$

where R_{eff} is the effective resistance of the winding and R_{dc} its DC resistance,

$$\Psi = \frac{5 \cdot p^2 - 1}{15} \tag{4.6}$$

where p is the number of winding layers,

$$\Delta = \frac{d}{\delta_0} \tag{4.7}$$

where d the thickness of the layer and,

$$\delta_0 = \sqrt{\frac{2}{\omega_0 \cdot \mu_0 \cdot \sigma}} \tag{4.8}$$

I_{rms} is the rms value of the winding current waveform and I'_{rms} is the rms value of the derivative of the winding current. The value of this work is that it simplifies the calculation of R_{eff} considerably as no Fourier analysis is needed. By using a modern oscilloscope and an AC current probe the rms value of the current and of its derivative can be calculated in real-time. Due to the assumptions the author made this method is very accurate for two winding layers or more and its accuracy in less than two-layer windings depends on the waveforms applied. The equation gave accurate results for the waveforms appearing in the PSB transformer and hence it has been used down to 1 layer of winding.

For windings of that comprise of a single layer the proximity effect is negligible (it only exists between successive turns), thus it can be ignored. In this case the only high frequency effect is the skin effect and the R_{eff} is much easier to calculate using the standard equation for the calculation of the DC resistance and by taking into consideration the fact that not all of the wire cross-sectional area is conducting.

4.2 The proposed layouts

Extensive research has been conducted in the past on contact-less energy transfer devices. Many different transformer arrangements have been proposed for different applications (see Chapter 2). The different specifications and requirements of each project made difficult the unification of the design procedure. The difference between various applications lies in the magnetic interface geometry and also in the required power and voltage levels.

In this project the rotating transformer application requires that the energy is coupled via an inductive interface from the stationary to the rotating section of an airborne radar. The air gap between the primary and secondary core halves of the transformer can be as small as the machining facilities permit. The air gap between the primary and secondary coil formers is also dependent on the machining tolerances that can be achieved, as well as on the insulation requirements. The design should be realistic and robust. Furthermore, to allow quick prototyping and evaluation, preference was given to commercial magnetic cores.

The evaluation of the rotating transformer in a phase shifted full bridge topology requires that the transformer must provide a certain amount of energy storage to assist with the soft switching operation of the primary semiconductors. This energy storage capability could be provided by either the leakage or the magnetising inductance or by both simultaneously. Using the energy in the leakage inductance is the traditional way of assisting the resonant transitions in a phase shifted bridge. However, making the leakage (or additional external) inductance sufficiently large so that it stores enough energy to enable soft-switching, would cause duty cycle loss problems as the current cannot build up fast enough. Hence, the higher this inductance is the more time is needed before the primary current can be reflected to the secondary winding. It must be clear now that there is an upper limit to the leakage inductance of the main transformer. On the other hand, when the output load of the converter is very light the current through the leakage inductance is also very low. There is a possibility that the energy stored in the inductor will not be enough to accomplish the resonant transition of the power semiconductors. This implies that there is a lower limit to the leakage inductance, which defines the boundary condition between the *soft* and *hard* switching of the semiconductors.

If the magnetising inductance is used (which for many cases of inductive couplers is comparable with the leakage inductance value), the disadvantage of duty cycle loss vanishes. Furthermore, the current through the magnetising inductance is load independent, hence storing a constant amount of power in the leakage inductance even at minimum load. However, another disadvantage appears now; the increased primary rms current, due to the considerable current that is needed to magnetise the core material. This can result in excessive conduction losses in the transformer windings and the semiconductor devices.

Two different transformer structures are investigated here: (a) the adjacent windings and (b) the coaxial windings transformers. They are both built on a commercially available magnetic core. The core shape that was chosen for the rotating transformer application is the pot core. Its axial symmetry provides an (almost) fixed cross sectional area for any angle of rotation. This, in combination with the fixed air gap length, results in the most important property of a rotating transformer; fixed electrical characteristics.

Apart from the magnetic core choice, the coil former's geometry was found to be very critical for the prediction of leakage phenomena. A higher degree of freedom was given by experimenting with the bobbin's design as they can be easily manufactured in any workshop with basic processing equipment (such as the School's workshop facilities).

4.2.1 Rotating transformer with adjacent windings

The adjacent winding arrangement appears in figure 4.3.

The primary and secondary windings are fitted in separate bobbins in the respective core half. The bobbins are placed around the centre limb of the core in an adjacent arrangement (hence the name). [3]

Inherently, this arrangement exhibits high primary and secondary leakage inductance due to the physical separation of the primary and secondary windings. Consequently, the coupling between the two windings is not strong resulting in small amounts of energy being transferred and a significant amount being stored in the core itself.

[3] This arrangement was originally proposed by BAE Systems who found it suffered from high leakage inductance and high conduction losses.

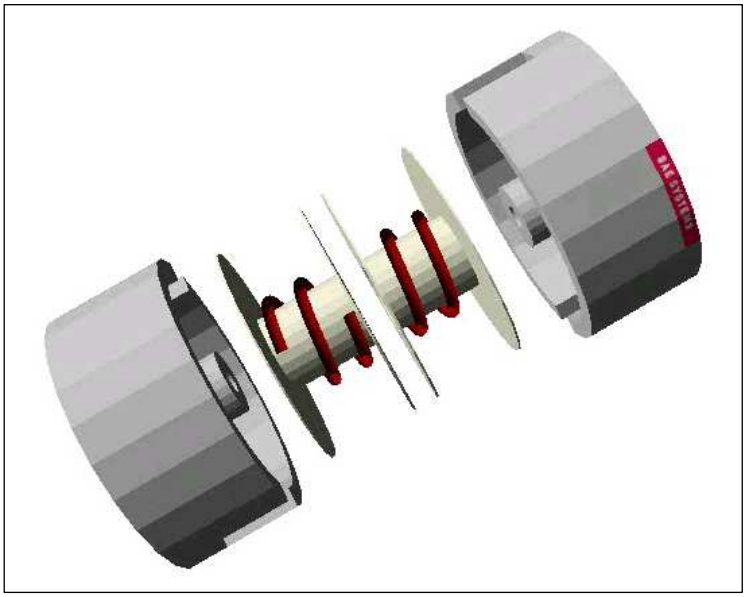

Figure 4.3: *Three-dimensional representation of the adjacent transformer layout.*

It is essential to quantify the problem of low coupling before attempting to design the power converter. According to the reluctance modelling technique (discussed in Chapter 3) a reluctance model can be derived from a simple perpendicular cut of the transformer as in figures 4.4(a) to 4.4(c).

Figure 4.4(b) shows the magnetic flux paths. The useful flux is the one traversing the magnetic core R_c and air gaps R_{air}. This flux links both windings and transfers the power from one to another. The alternative paths R_{lk1} and R_{lk2} represent the leakage flux generated by one of the windings and not linking the other. Note that the reluctance of the air-gap is in series with that of the core (figure 4.4c). Also, according to equations A.7 (Appendix A) the reluctance of the air-gap is dominant for large air-gaps thus suppressing the magnetic flux that is flowing through the core. To conclude, as the clearance between the core halves increases, more magnetic flux is redirected from the magnetic core to alternative paths (among them the leakage).

As was mentioned in Chapter 3, there is a *duality* between magnetic and electric circuits. This means that the magnetic circuit of the transformer can be transformed to an electric equivalent, which can be used in electric simulations etc. This transformation is useful because the magnetic quantities such as magnetic flux and magnetic permeability of materials can be associated with electric quantities such as current, voltage

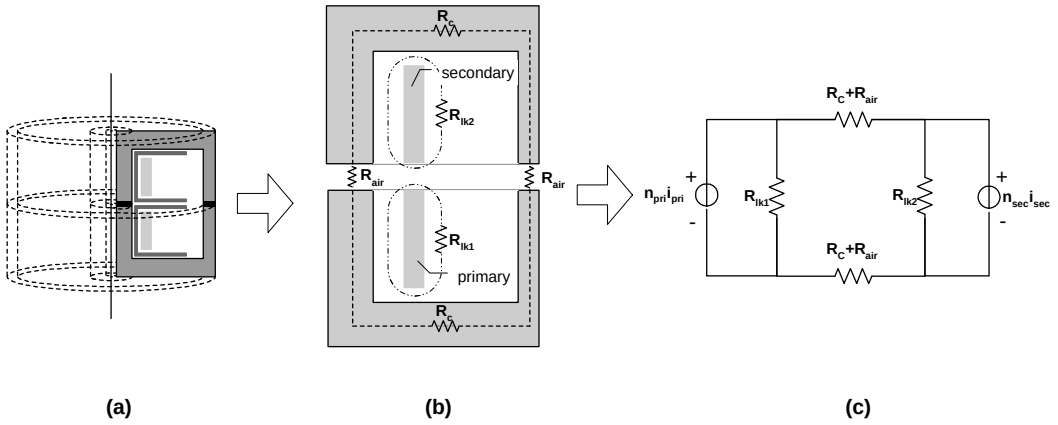

Figure 4.4: *Reluctance modelling of the adjacent windings arrangement (a) a perpendicular cut of the transformer (b) the magnetic flux paths and (c) the equivalent reluctance model*

and inductances. In Figure 4.5 the magnetic circuit is converted to an electric one by applying the duality transformation. For example, the relationship that associates the reluctance of the core R_c with the resulting magnetising inductance is:

$$L_m = N_{pri}^2 \cdot \frac{1}{R_c} \tag{4.9}$$

In figure 4.5(b) a simple network transformation is applied and the reluctances are transformed to permeances $P = 1/R$, which is the first step for the formation of the second part of equation 4.9[4]. Next, the inverse reluctances are multiplied by the number of turns squared and the sources are accordingly modified to compensate for the multiplication (figure 4.5(c)). Last, figure 4.5(d) shows the resulting electrical equivalent as the reluctances (and magnetic sources) can be replaced by their electrical counterparts [25].

It turns out that this is the π equivalent model suggested by most textbooks. It consists of the primary and secondary leakage inductances that represent the energy storage space around the windings and the magnetising inductance that represents the energy storage in the magnetic core and the air-gap. Note that the two leakage paths have the same geometry and dimensions (provided that the number of primary and secondary turns is the same), so the leakage inductances are equal in such an arrangement. The leakage inductance depends on the distance of the winding from the core and on the

[4]This is the equivalent of converting a resistance R to conductance G by changing the series elements to parallel branches and vice-versa.

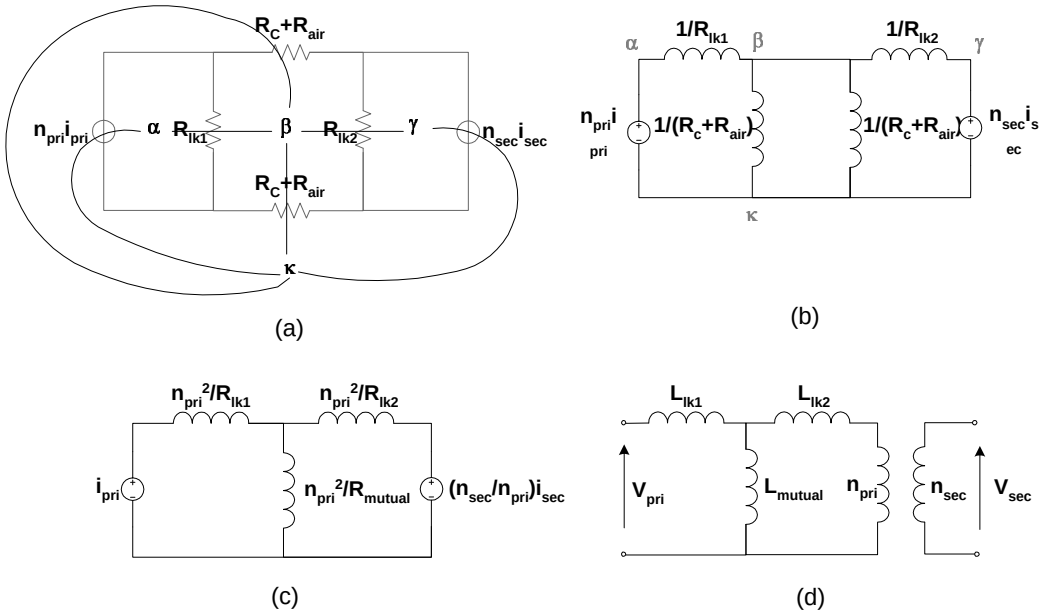

Figure 4.5: *Duality transformation of the adjacent windings arrangement (a) the duality transformation (b) the permeances model (c) adjusting according to the number of turns and (d) the electrical equivalent model.*

number of turns. The two leakage fields are independent: this is important because it results in the two components being displayed separately in the electrical equivalent network. Unlike leakage, the magnetising inductance is clearly dependent on the magnetic core and particularly the air-gap length.

4.2.2 Rotating transformer with concentric windings

The concentric windings layout shown in Figure 4.6 takes advantage of the lack of a separating wall between the stationary and the rotating part of the transformer. The primary or/and secondary windings penetrate the opposite core section of the transformer in order to reduce the air space where energy is unnecessarily stored. This arrangement requires precise machining and assembly as the clearance between the two windings must be as small as possible.

The reluctance modelling is also performed on this arrangement to obtain the equivalent electrical network. Due to the rotational symmetry of the transformer, a perpendicular cut (Figure 4.7(a)) is used. The distinction between magnetising ('useful') and leakage ('useless') flux is not easy in this arrangement. Assuming a small air-gap between the

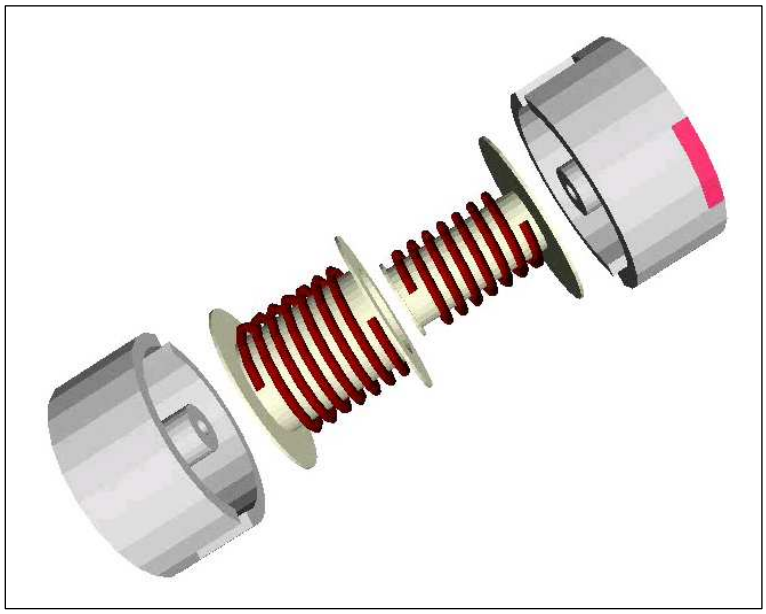

Figure 4.6: *Three dimensional representation of the concentric transformer layout.*

core halves, most of the magnetic flux created by the primary winding will follow the ferrite material (reluctances $R_1 - R_8$ and R_{air}). The alternative flux paths through the air are represented by the elements R_{i1}, R_{lk} and R_{i2}. Note that according to equations A.7 (Appendix A) the reluctance of the air-space is greater than that of the magnetic core. Moreover, in a transformer with a large air-gap, due to the high reluctance R_{air} that appears in series with the core reluctance, the total path's reluctance becomes comparable to the air-path reluctances R_{i1}, R_{lk} and R_{i2}. Electrically, this is represented by a low magnetising inductance.

The reluctance modelling yields the magnetic equivalent of figure 4.7(c). An interesting point that derives from this magnetic circuit is that the reluctance R_1+R_{air}+R_8 of the centre limb of the core appears in parallel with the reluctance R_{i1} giving a total reluctance that for small air gaps is defined by R_1+R_{air}+R_8. The same happens with the reluctances R_4+R_{air2}+R_5 and R_{i2}.

After applying the duality transformation and manipulating the resulting network (figure 4.8(a)-(c)), the electrical equivalent of figure 4.8(d) is derived. The electrical properties of the coaxial transformer, as seen in the model of figure 4.5(d), can be associated with the geometrical structure presented in figure 4.7(b). The leakage inductance, for example, is the result of the volume between the two windings. Note that this induc-

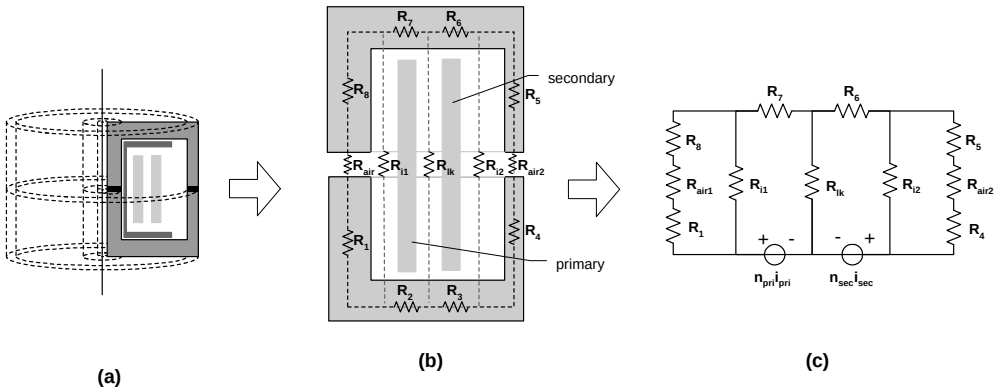

Figure 4.7: *Reluctance modelling of the concentric windings arrangement (a) a perpendicular cut of the transformer (b) the magnetic flux paths and (c) the equivalent reluctance model.*

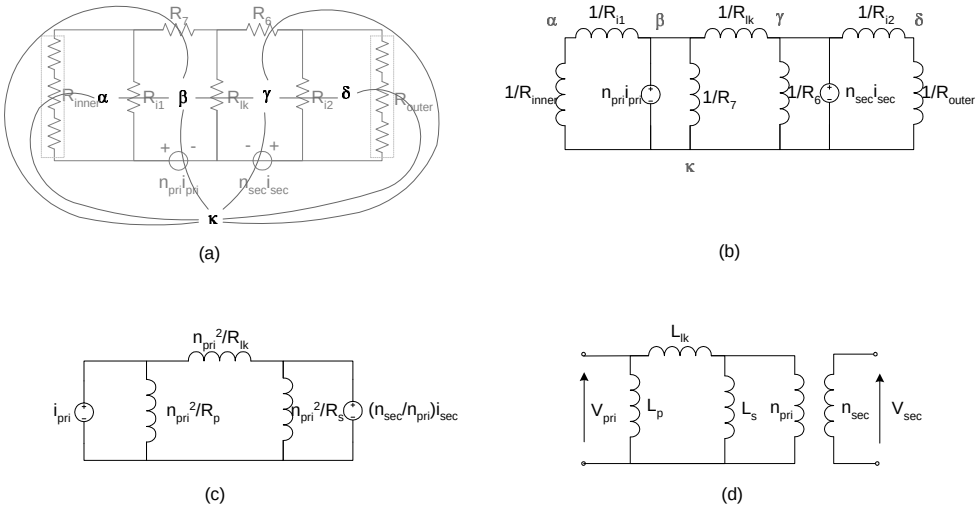

Figure 4.8: *Reluctance modelling and duality transformation for the concentric windings arrangement*

tance is dependent on the distance between the two windings, their radius and also on the vertical dimension of the core window. Due to the high magnetic reluctance this space does not store much energy and this appears in the electrical equivalent as a low inductance L_{lk} (the leakage inductance). The leakage inductance does not change, if the windings are inter-changed[5], unless their distance changes.

Regarding the magnetising inductance components, L_p and L_s, their value depends on two components; (a) the reluctance of the respective core limb and air-gap (for the central limb and the outer limb respectively) and (b) the reluctance of the path between the core and the respective limb. In figure 4.7(b) the inner winding is the primary winding thus the respective magnetising inductance L_p is derived by the parallel combination of the reluctances $R_1 + R_{air} + R_8$ and R_{i1}. The dominant reluctance $(R_1 + R_{air} + R_8)$ is the smallest. However, depending on the air-gap length (i.e. R_{air}) the distance of the winding from the core (i.e. R_{i1}) can prove to be significant.

Similarly, the secondary magnetising inductance R_s is defined by the parallel combination of the reluctances $R_4 + R_{air2} + R_5$ and R_{i2}. The dominant reluctance here is the smallest, hence $R_4 + R_{air2} + R_5$. Again, depending on the air-gap length (i.e. R_{air2}) the distance of the winding from the core (i.e. R_{i2}) can prove to be significant.

4.3 Comparing the Proposed Arrangements

4.3.1 The electrical models

By looking at the two electrical models (figure 4.5(d) and figure 4.7(d)) carefully, it can be seen that they are electrically equivalent (they have the same AC response) as they can be transformed to either form using a π to τ transformation or the opposite. However, note that a τ-equivalent has less meaning for a coaxial type of transformer. In a π-equivalent network each inductance can be directly associated with a geometrical property of the coaxial winding transformer (eg. the volume of the air space between the windings defines L_{lk}). Similarly, for the adjacent winding arrangement the τ model has a direct connection with the transformer geometry.

[5] Assuming the two windings are identical.

4.3.2 Characterising the two arrangements

A prototype was built for each of the presented transformer structures. The reason for prototyping at this stage was to evaluate the three characterising methods reported in Chapter 3 and also to quantify the problem of poor coupling between the windings. The evaluation involved two pot core transformers of the same power rating with two different winding arrangements. The transformers were designed for use with the PSFB converter that is proposed. Both transformers were required to handle 1kW of power. The input voltage was in the range 255-380V and the secondary voltage was around 120V (using a current doubler rectifier 54V was delivered at the converter output). The operating frequency was 100kHz.

The first geometry under investigation is a 56mm Philips pot core (P56/66, 3C3 material) with adjacent winding arrangement (figure 4.3). The primary winding has 26 turns and is made of 5 strands of 0.8mm wire. The turns are stacked in 4 full layers of 7 turns each, apart from the upper layer that only has 5 turns. The secondary is comprised of 12 turns made of 3 strands of 0.8mm wire stacked in 1 full layer (9 turns) and one with 3 turns. The bobbins were manufactured in-house using a nylon material. The designed bobbin mechanical layout appears in Figures A.8 of Appendix A.

The adjacent windings arrangement was evaluated against the coaxial windings arrangement. An impression of the coaxial transformer is presented in figure 4.6. The coil former mechanical layout appears in figures A.9 and A.10 of the Appendix A. The secondary winding is wound around the inner bobbin as this secures a slightly smaller leakage inductance (which is only needed in the primary). It has 12 turns made of 24 strands of 0.4mm wire. The bobbin has almost twice the width of the adjacent winding bobbins hence it can fit almost all turns in one layer. The primary winding consists of 26 turns made of 10 strands of 0.4mm wire. This is wound on the outer bobbin of the transformer to help the cooling (as it has many turns and also holds the magnetising current which on average accounts for 30% of the total primary current).

4.3.2.1 Measured results

The measurement method described in section 3.4.3 was applied to obtain the electrical characteristics of the transformer. This method is generally very accurate though some

additional parameters must be taken into account:

Frequency dependence. When measuring the inductances and capacitances the frequency of the applied sinewave must be carefully considered. The inductive and capacitive components comprising the model cannot be isolated from each other and are interacting. Hence the inductance "seen" at one side of the transformer varies with frequency.

Voltage dependence. It appears that the inductance readings taken are dependent on the voltage level of the applied signal. This is due to the non-linear behaviour of the transformer core whose permeability is fixed (straight B-H curve) when low volt-seconds are applied, but generally decreases when the material is operated at high magnetic flux levels.

Tolerances of the materials' properties. This mainly refers to the magnetic core permeability which can vary considerably (according to Ferroxcube up to 25%). It has been observed in the lab that the same type of material originating from different suppliers exhibited different magnetic properties.

The strategy chosen for the following measurements was to produce the inductance curves for a frequency range from 20Hz to 3MHz and extract the respective inductance at the frequency of interest (in this case it is 100kHz). The quality factor was also obtained as an indicator of the accuracy of the measured values (a low quality factor indicates a lossy network where the resistive components are a significant part of the total impedance).

The measured inductances for the adjacent and coaxial winding arrangements appear in Tables 4.1 and 4.2.

Air gap (mm)	0	0.25	0.5	1	1.5	2
L_m (mH)	11.9	1.2	0.637	0.368	0.265	0.208
L_{lk_1} (μH)	44.34	53.41	54.42	58.17	59.6	61.83
L_{lk_2} (μH)	12.75	11.37	11.58	11.86	11.56	12.24
R_{eff_1} (Ω)	-	-	6.5	5.8	5.55	5.53
R_{eff_2} (Ω)	-	-	0.85	0.7	0.64	0.64
C_1 (pF)	24.2	-	22.8	22	24	26.8

Table 4.1: *Measured results for the adjacent-winding transformer prototype*

In these tables the R_{eff} is, essentially, the effective resistance of the winding when a sinusoidal waveform is applied. This is because the bridge that has been used for testing

Air gap (mm)	0	0.25	0.5	1	1.5	2
L_m (mH)	15.37	1.245	0.677	0.399	0.286	0.230
L_{lk_1} (μH)	7.56	6.52	6.64	7.02	7.27	7.41
L_{lk_2} (μH)	1.42	1.67	1.648	1.497	1.418	1.38
R_{eff_1} (Ω)	-	-	2.6	1.80	1.65	1.62
R_{eff_2} (Ω)	-	-	0.51	0.37	0.33	0.32
C_p (pF)	18.4	-	19.5	18.4	17	17.6

Table 4.2: *Measured results for the coaxial-winding transformer prototype*

only applies sinusoidal waveforms. As a result, this resistance will vary slightly from the actual resistance when a switching waveform is applied.

As the effective resistance is usually a small portion of the winding's impedance, it can be difficult to measure. Measuring the R_{eff} becomes even more difficult to measure at frequencies close to the winding self resonance. This is the case for the transformers measured in this section when there is no air-gap between the core parts. In this case (0mm air-gap) the magnetising inductance of the winding is so high around (12mH) that the self-resonating frequency of the winding formed by the magnetising inductance and the inter-turn capacitance is very low (around 200kHz).

4.3.2.2 Calculated results

Calculating the magnetising and leakage inductance of the transformer is the result of the reluctance modelling presented in Chapter 3 and Appendix A. The length of the magnetic path as well as its cross-sectional area can be found in the technical characteristics of the magnetic core. Using Equations A.10 and A.11 the following results were derived for the adjacent (Table 4.3) and for the coaxial (Table 4.4) winding arrangements.

Air gap (mm)	0	0.25	0.5	1	1.5	2
L_m (mH)	10.64	1.093	0.576	0.296	0.199	0.015
L_{lk_1} (μH)	33.9	33.9	33.9	33.9	33.9	33.9
L_{lk_2} (μH)	7.22	7.22	7.22	7.22	7.22	7.22
R_{eff_1} (Ω)	-	-	-	-	-	-
R_{eff_2} (Ω)	-	-	-	-	-	-

Table 4.3: *Calculated results for the adjacent-winding transformer prototype*

Air gap (mm)	0	0.25	0.5	1	1.5	2
L_m (mH)	12.87	1.108	0.577	0.292	0.194	0.145
L_{lk_1} (μH)	5.023	5.033	5.043	5.065	5.086	5.109
L_{lk_2} (μH)	1.07	1.07	1.07	1.08	1.08	1.09
R_{eff_1} (Ω)	-	-	-	-	-	-
R_{eff_2} (Ω)	-	-	-	-	-	-

Table 4.4: *Calculated results for the coaxial-winding transformer prototype*

4.3.2.3 Finite element results

The finite element analysis is used to predict the properties of a magnetic component. The procedure is comprised of four stages;

- drawing the 2-D structure,
- defining material properties and boundary conditions,
- solving the problem, and finally,
- post-processing the results.

The software used was the Maxwell 2D by Ansoft Corp. Due to the axial symmetry of the investigated layouts (Figures 4.3 and 4.6) a 2-D analysis over the symmetric area was enough as the magnetic field distribution is symmetrical.

The visualisation of the magnetic field and the calculation of the magnetising and leakage inductances takes place during the post-processing stage. This visualisation of the magnetic field (flux lines etc) also helps with the reluctance modelling of the transformer as it shows the exact paths of the magnetic flux in the component. Figure 4.9 depicts the magnetic flux in the transformer structure for a 10A current flowing through the primary with the secondary winding open (no current). The open-circuit test is mainly performed in order to calculate the magnetising inductance seen from the primary side. The flux lines that link both windings are useful and can potentially transfer energy from the primary to the secondary side of the transformer. This flux also stores energy in the high reluctance areas such as the air gap. This energy is the magnetising energy. By integrating the magnetic energy in the areas where it is being stored the magnetising inductance (equation 4.10 derived in Chapter 3) can be calculated.

The integration can be done using the post-processing tools of the finite element analysis software.

$$L = \frac{\pi \cdot \int_r \int_z \overrightarrow{A} \cdot \overrightarrow{J}\, drdz}{I^2} \tag{4.10}$$

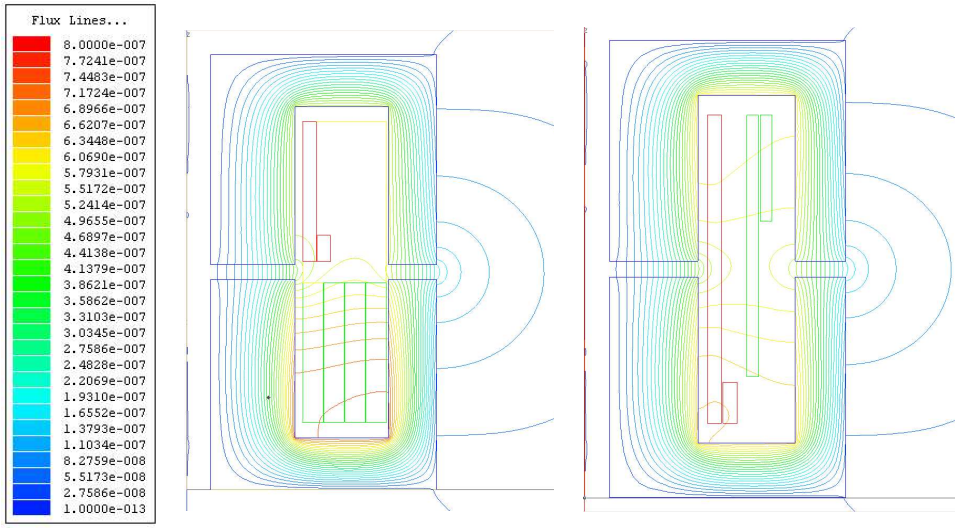

Figure 4.9: *The magnetic flux generated by the primary winding when the secondary is open-circuit. This test is used to estimate the primary magnetising inductance of the transformer.(a) Adjacent winding and (b) coaxial winding arrangement.*

Figure 4.10 depicts the short-circuit test that is used to calculate the leakage inductance of the transformer. During the short-circuit test the primary and secondary ampere-currents are equal. As a result the magnetic flux generated by each winding cancels the equal flux generated by the other winding. However, a small portion of the total generated flux remains in the core and air space. This is the primary and secondary leakage flux. Having eliminated the mutual flux, it is easy to locate the leakage flux and integrate the energy to calculate the leakage inductance.

Figure 4.11 illustrates the magnetic energy storage in the magnetic component. The primary winding carries a 10A current whereas the secondary is open circuit. The areas coloured red store more magnetic energy than those in blue. It is clear that the air gap stores much more energy than the magnetic core. This is expected due to its higher reluctance, similar to a series electrical network where the higher value resistors run hotter than the lower value ones. Comparing magnetising energy in the adjacent winding arrangement (figure 4.11(a)) with that in the coaxial winding arrangement

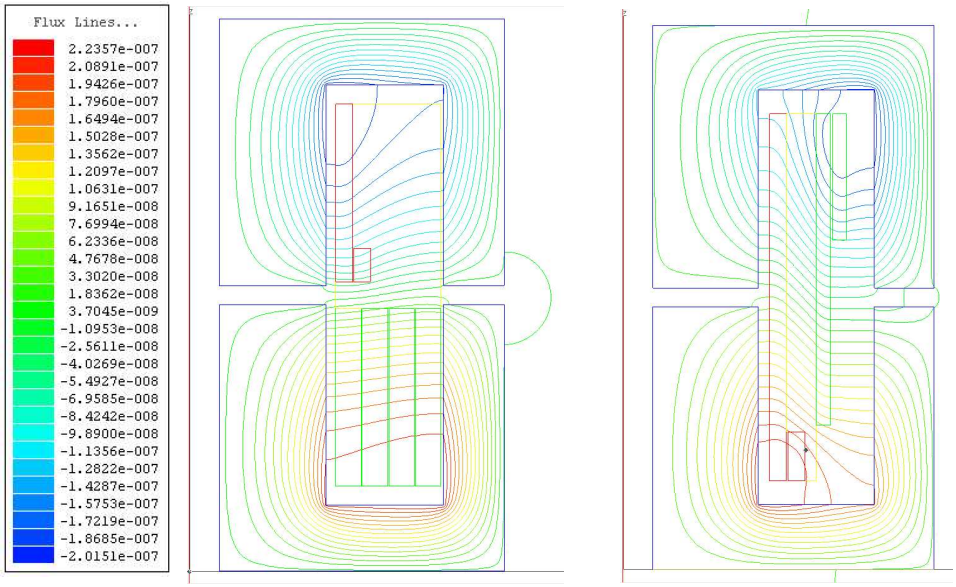

Figure 4.10: *The magnetic flux generated by the primary and secondary windings when 10 Ampere-turns are applied in each. This test is used to estimate the leakage inductances of the two windings. (a) Adjacent windings and (b) coaxial windings arrangement.*

(figure 4.11(b)) they appear to be of the same magnitude (note that the scale is the same). Furthermore, it can be seen that the magnetising energy is not restricted in the air gap but spreads around it (due to the fringing flux lines). It is clear that if a winding is positioned close to the air gap the magnetic field may affect the current flow in the winding. This aspect has been found to be important and is discussed in Chapter 7 along with possible solutions.

Figure 4.12 illustrates the energy allocation during the short-circuit test (both windings carry 10A). The magnetising energy is minimised as the mutual flux cancels out and the only energy that remains in the transformer is leakage energy, stored mainly in the air space around the windings. Figures 4.12 and 4.10 allow an accurate visualisation of the leakage effect. Note that although there is a high flux density in the magnetic core around the windings the corresponding energy storage is low and most of the leakage energy is stored in the air. In the coaxial winding transformer (Fig. 4.12(b)) the leakage energy is mainly stored between the two windings. Making this area smaller is the obvious way of decreasing the leakage inductance. In contrast, in the adjacent winding

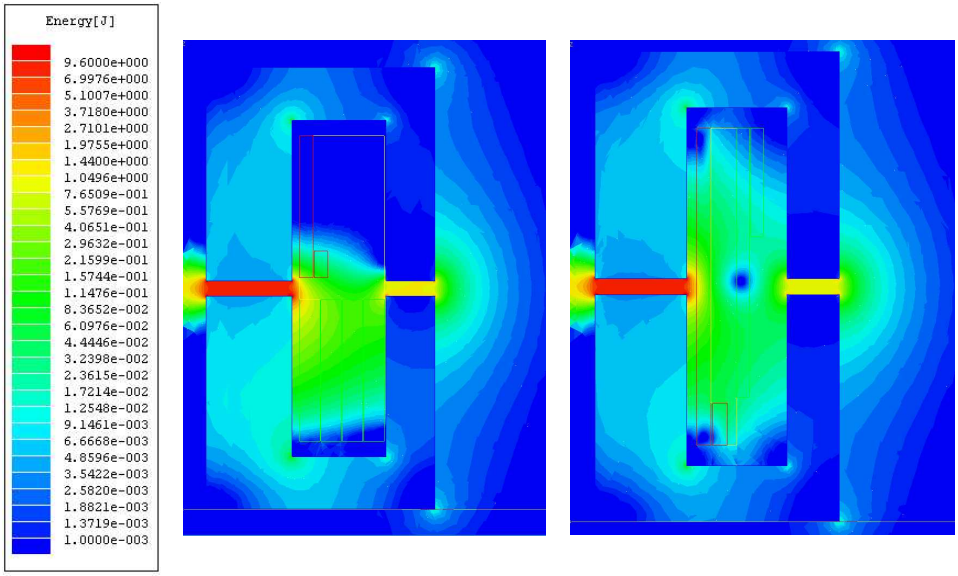

Figure 4.11: *Illustrates the magnetic energy stored in the transformer structure when 10A flow in the primary winding and the secondary winding is open-circuited (a) adjacent winding arrangement and (b) coaxial winding arrangement.*

arrangement the leakage flux of each winding is distinct[6]. To calculate the various inductances from using the FAE post-processor equation 4.11 is evaluated.

$$L = \frac{\pi \int_r \int_z \vec{H}\vec{B} dr dz}{I^2} \tag{4.11}$$

The finite element results for the adjacent winding transformer appear in Table 4.5

Air gap (mm)	0	0.25	0.5	1	1.5	2
L_m (mH)	12.03	1.354	0.759	0.428	0.309	0.247
L_{lk_1} (μH)	13.12	41.3	45.5	46.7	45.7	45
L_{lk_2} (μH)	2.85	8.02	8.33	8.23	7.99	7.72

Table 4.5: *Finite element results results for the adjacent-winding transformer prototype*

The simulated (FEA) electrical characteristics of the coaxial transformer appear in Table 4.6.

The above results make it clear that the second layout exhibits much lower magnetic leakage due to the relative positioning of the windings.

[6]It is now justified why the electrical model of this transformer has a uniquee leakage inductance whereas the adjacent arrangement has one for each winding.

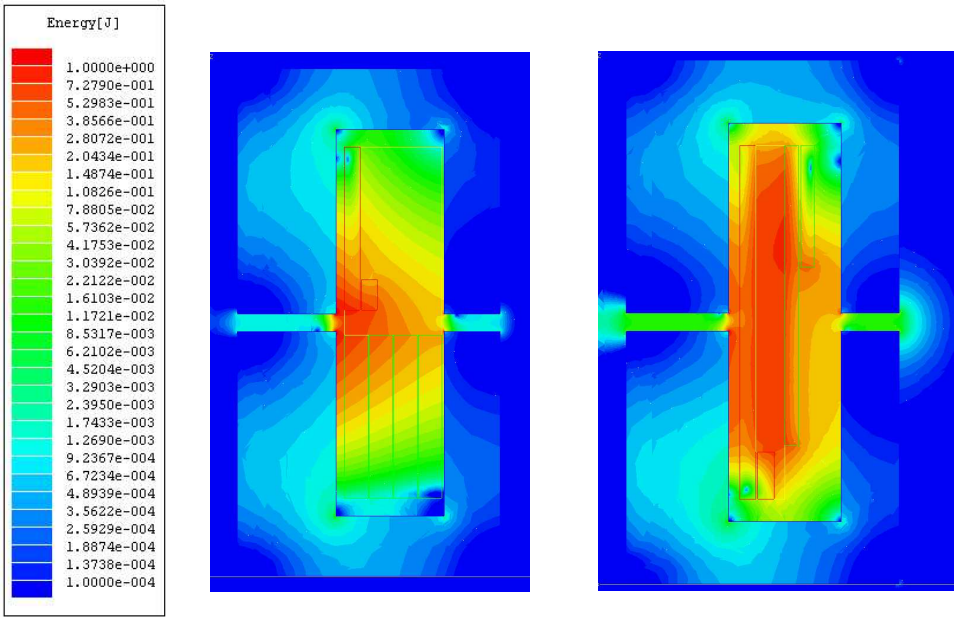

Figure 4.12: *Illustrates the magnetic energy stored in the transformer structure when 10A flow (in opposite directions) in the primary winding and secondary windings (a) adjacent winding arrangement and (b) coaxial winding arrangement.*

Air gap (mm)	0	0.25	0.5	1	1.5	2
L_m (mH)	14.55	1.4	0.784	0.449	0.327	0.264
L_{lk_1} (μH)	9.207	5.93	6.97	7.11	7.23	7.62
L_{lk_2} (μH)	0.654	0.998	0.939	0.94	1.08	1.05

Table 4.6: *Finite element results for the coaxial-winding transformer prototype*

4.3.3 Discussion of the results

Associating the physical structure of the rotating transformer with its electrical characteristics is a complex task. It usually involves many assumptions to overcome the modelling difficulties arising mainly from the asymmetries of the core and windings and the non-uniform magnetic materials. As a result, both calculations and the finite elements analysis give results whose accuracy is inversely related to the number of assumptions made during the modelling procedure.

Figure 4.13 and 4.14 present the results of the three characterising methods (measurements, calculation and FEA). As expected, the graphs show a significant decrease of the magnetising inductance as the air-gap increases. The leakage inductance on the other hand remains unchanged regardless of the air-gap length. Although of the same

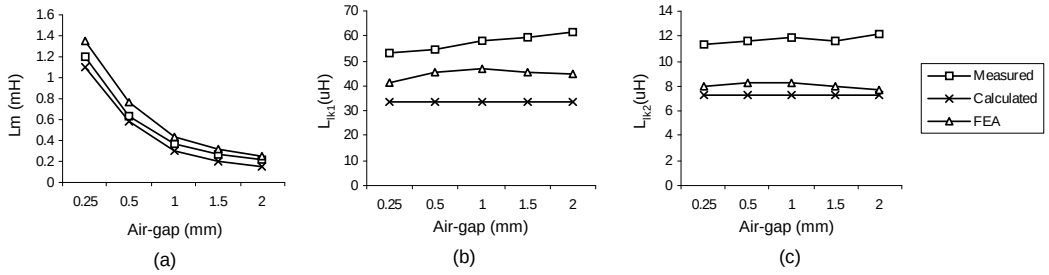

Figure 4.13: *The (a) primary magnetising inductance L_m, (b) primary leakage inductance L_{lk1} and (c) secondary leakage inductance L_{lk2} of the adjacent windings transformer as found by three different characterising methods.*

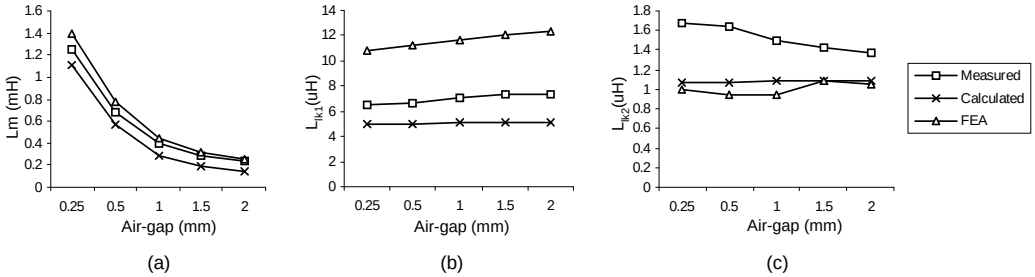

Figure 4.14: *The (a) primary magnetising inductance L_m, (b) primary leakage inductance L_{lk1} and (c) secondary leakage inductance L_{lk2} of the coaxial windings transformer as found by three different characterising methods.*

order of magnitude, the calculated and FEA results of leakage inductance differ from the measured ones. This is mainly because of the difficulty in defining the area where the leakage flux resides. In the case of the magnetising flux, most of the flux is known to be in the magnetic core hence the integration in (4.11) is performed over the volume of the core. On the other hand, the leakage flux is spread in the air space and the boundaries between useful (magnetising) flux and leakage (useless) flux are vague. Additionally, the leakage energy is a small fraction of the total transformer energy, so any "noise" (other magnetic flux) accounted as leakage flux can easily falsify the results.

The key conclusions are discussed here:

- In a rotating transformer (with a relatively small air-gap) the value of the magnetising inductance mainly depends on the length and the cross-sectional area of the air-gap and not on the position of the windings
- The leakage inductance is relatively independent of the air-gap length and only

depends on the relative position of the windings.

- The leakage inductance can be reduced mainly by placing the windings physically together. It may also help placing the windings as close to the core as possible

Comparing the adjacent and coaxial winding arrangements, it can be seen that the coaxial has a much lower leakage inductance. The leakage inductance is important because along with the effective winding resistance it determines the voltage gain of the transformer. The leakage inductance appears in series with the transformer causing a voltage drop across it (which is proportional to the applied di/dt). This voltage drop reduces the transformer secondary voltage. As a result, an excessive leakage inductance such as the one imposed by the adjacent winding could make the use of a rotating transformer impossible.

As seen, the theoretical analysis is rather a qualitative analysis that gives a good insight to the connection between the dimensions of the core and windings and the resulting electrical characteristics. The measurement method is generally accurate but has the disadvantage that it can only be applied in actual prototypes. The finite element analysis can run over any imaginary transformer shape and size and gives a relatively accurate prediction of the transformer electrical characteristics. Consequently, FEA is appropriate for initial calculations and simulations.

4.4 AC Analysis

A complete electrical model of the rotating transformer has been derived and, by now, the particular problems of such an interface must be clear; the increased leakage inductances and the winding resistances cause voltage drops and consequently impair the output voltage. At the same time only a portion of the primary current is being reflected to the secondary side as the rest is being drawn by the low magnetising inductance.

In the following paragraphs the transformer model will be analysed in the time and frequency domains. The time domain or *transient analysis* demonstrates the effect that the transformer has on the shape and the amplitude of a switching waveform. The rms values of the input and output waveforms can be calculated and the transformer losses can be estimated.

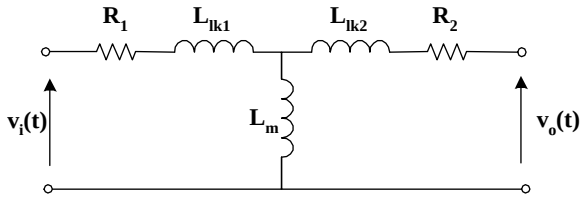

Figure 4.15: *The τ-equivalent of the transformer.*

The frequency domain analysis is based on the evaluation of the transformer's transfer function. The transfer function describes the response of the electrical network over a frequency range. Taking into account the harmonic content of the switching waveforms it becomes clear why a frequency sweep is needed. Both voltage and current gain functions will be derived. The gain functions are important because they show the effectiveness of the transformer in stepping a voltage up or down (voltage gain), reflecting the primary current to the secondary side (current gain) and transferring power from one side to the other.

4.4.1 Frequency response of a rotating transformer

An ideal transformer model has no frequency dependance; its voltage gain is fixed and equal to the turns ratio. This is because the ideal windings have no resistance and capacitance and also they are perfectly coupled. A rotating transformer exhibits increased windings resistance due to AC phenomena and stores magnetic energy due to the low magnetising inductance and weak coupling between the windings. These effects are reflected in the non-ideal transformer equivalent of figure 4.15

4.4.1.1 Voltage gain

The voltage gain of the transformer is the magnitude of the transfer function of the network in figure 4.15. The voltage gain depends on the loading of the transformer as this defines the currents in it and the voltage drops across the parasitic elements. The voltage gain varies due to the frequency-dependent elements (windings resistance) of the transformer as well as due to the resonance between the inductive and capacitive elements.

Figure 4.16 and 4.17 present the magnitude and phase of the transfer function of the

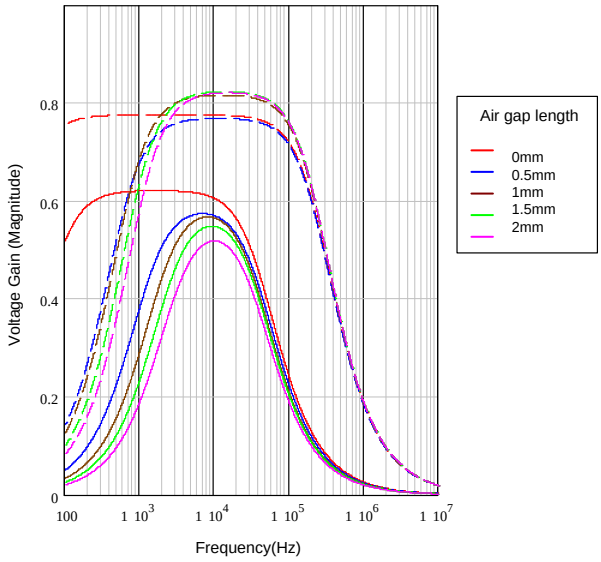

Figure 4.16: *The simulated voltage gain magnitude of the (P66/56, 26:12, 27SWG) transformer including the AC resistance effect. It assumes an 800W output load (at 54V). The solid lines correspond to the adjacent and the dashed ones to the coaxial winding arrangement.*

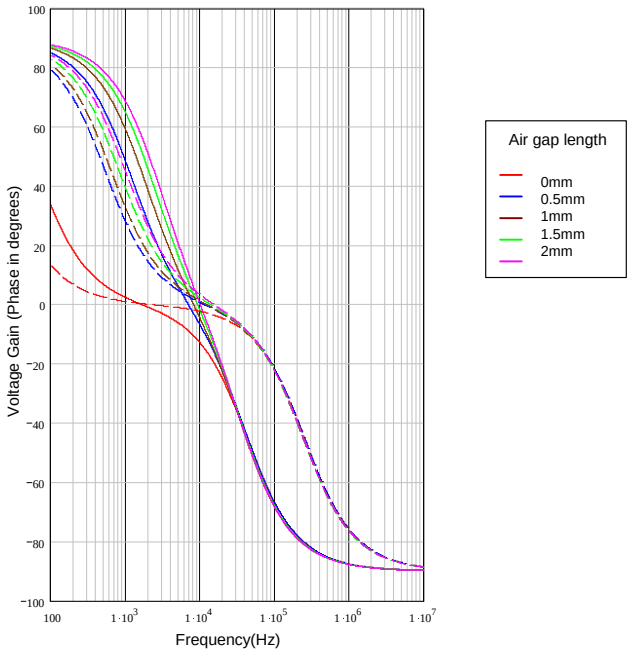

Figure 4.17: *The simulated voltage gain phase of the (P66/56, 26:12, 27SWG) transformer including the AC resistance effect. It assumes an 800W output load (at 54V). The solid lines correspond to the adjacent and the dashed ones to the coaxial winding arrangement.*

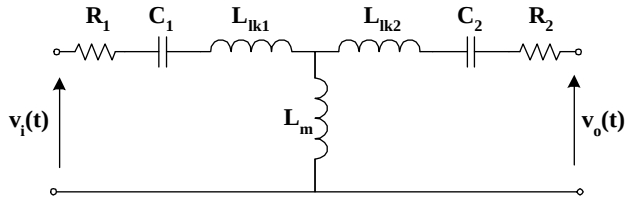

Figure 4.18: *The τ-equivalent of the transformer with series tuned compensating capacitors.*

adjacent (solid line) and the coaxial (dashed line) winding arrangement transformer respectively. The different colours correspond to different air-gap lengths. The results correspond to the transformer model of figure 4.15 omitting the windings capacitance, which is found to have a negligible effect at the frequencies of interest. The voltage gain graphs in figure 4.16 show that the transformer acts as a band-pass filter. It can be seen that the gain of the coaxial transformer is significantly greater (>0.8) due to the lower leakage inductances. Furthermore, the high gain area of both transformers is restricted to a narrow band. At low frequencies (<2kHz) the gain is reduced due to the magnetising inductance drawing a high current and causing large voltage drop across the primary leakage inductance. This is evident by the flat low frequency gain of the ungapped transformer (both coaxial and adjacent) represented by the red line. At high frequencies (>100kHz) the gain is mainly reduced due to the high di/dt through both primary and secondary leakage inductance components. The high-gain band of the adjacent winding transformer is narrower than the coaxial alternative. The reason is once more the higher leakage inductance of the windings. Overall it is clear that the voltage gain impairment derives from the windings leakage inductance.

The voltage gain characteristics of the transformer have been studied in the past by several researchers. The authors of [44] and [15] have derived the voltage gain equation for a transcutaneous transformer with two compensating capacitors in series. These compensation capacitors form a series resonant tank with leakage inductances and are tuned to the operating frequency (figure 4.18). This study derives the voltage gain as a function of the coupling coefficient of the transformer. To do so the author substitutes the output rectifier, filter and load with an equivalent resistance (this is possible due to the sinusoidal waveforms and the fact that the rectifier voltage is in phase with the input voltage). G.B.Joung et al. have also come up with a voltage gain equation in [46]. They make the assumption that the primary and secondary windings have identical

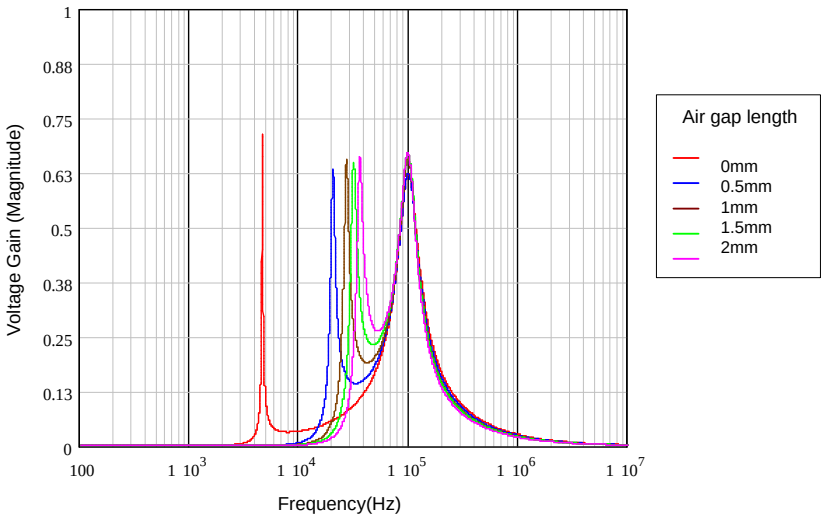

Figure 4.19: *The simulated voltage gain magnitude of the (P66/56, 26:12, 27SWG) adjacent winding transformer with leakage inductance compensation. It assumes an 800W output load (at 54V).*

geometry. However, this is not realistic for non 1:1 transformers. The simulated voltage gain magnitude for the leakage compensation scheme is depicted in figure 4.19 and 4.20 and the phase in figure 4.21(a) and (b).

Figure 4.19 depicts the voltage response of the adjacent windings transformer with leakage compensation. The low resonant peak is due to the magnetising inductance resonating with the capacitors (this is why the resonant frequency shifts as the air gap changes). The fixed frequency peak on the right is due to the resonance between the leakage inductances and the external compensating capacitors. This is the desired operating frequency of the transformer as the voltage gain is kept high due to the cancellation of the leakage impendence. The coaxial windings transformer (figure 4.19 demonstrates a similar behaviour, though the gain is generally kept higher and the potential operating frequency range is wider.

Figure 4.22 illustrates the effect of the load on the transformer voltage gain. The curves correspond to different loading conditions (from 50 to 800W at 54V). The figure shows that the curve becomes flat (similar to a non-compensated case) as the load becomes lighter. This is due to the reduction of the current and consequently the reduction of the voltage drops. In contrast, the low frequency resonant peak increases with output resistance as the damping of this oscillation reduces.

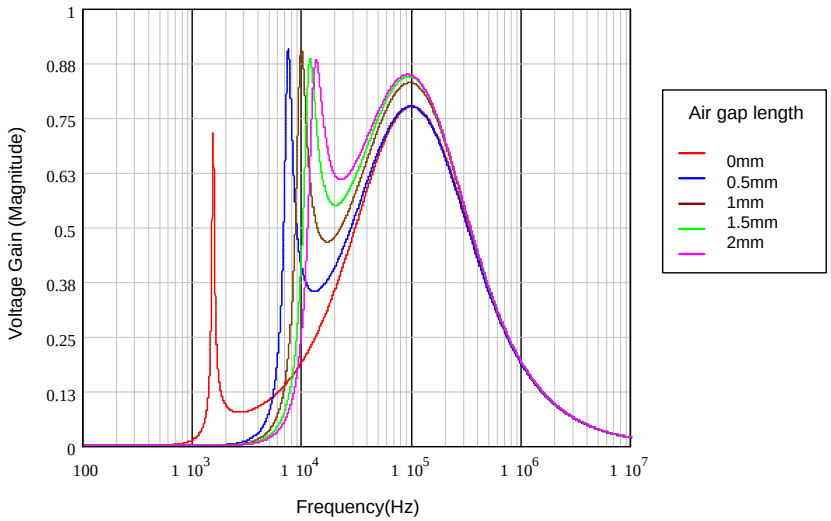

Figure 4.20: *The simulated voltage gain magnitude of the (P66/56, 26:12, 27SWG) coaxial winding transformer with leakage inductance compensation. It assumes an 800W output load (at 54V).*

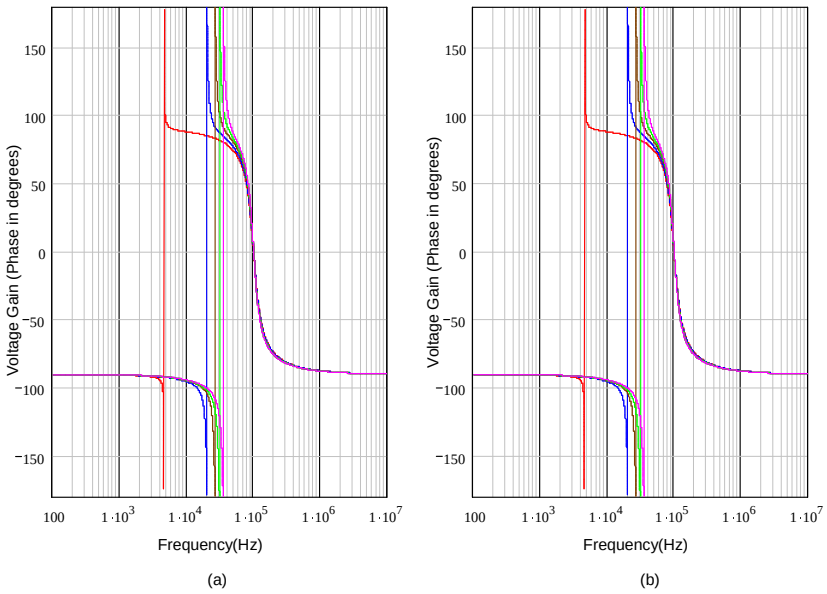

Figure 4.21: *The simulated voltage gain phase of the (P66/56, 26:12, 27SWG) (a) adjacent and (b) coaxial winding transformer with leakage inductance compensation. It assumes an 800W output load (at 54V).*

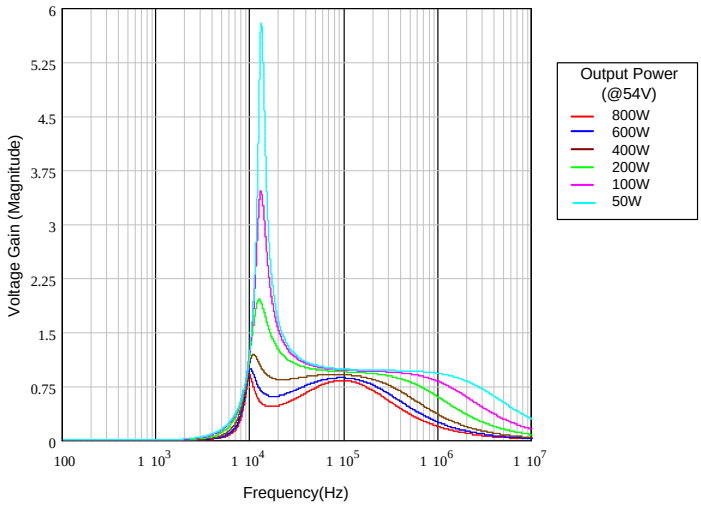

Figure 4.22: *The simulated voltage gain magnitude of the (P66/56, 26:12, 27SWG) coaxial winding transformer with leakage inductance compensation under different loading conditions(at 54V).*

4.4.1.2 Current Gain

The current gain is also important because it represents the ability of the transformer to transfer power from the primary to the secondary winding. A low current gain signifies poor transformer performance due to the high magnetising current flowing in the primary winding. The information extracted from the current and voltage gain functions is valuable in assessing a rotating transformer design for a particular application.

Figures 4.23 and 4.24 plot the current gain (magnitude and phase respectively) of the rotating transformer when it is loaded with a 3.65Ω resistor (800W at 54V). At low frequencies the impedance of the parallel magnetising inductance branch is very low. As a result the magnetising current is a large portion of the total primary current and the current gain is poor. At 100kHz and higher the current gain is stabilised at its maximum value. The adjacent winding transformer demonstrates lower current gain due to the higher secondary leakage inductance that increases the secondary winding impedance and reduces the secondary current.

Regarding the current gain of the transformer with leakage inductance compensation, the results appear in figures 4.25 and 4.26 for the coaxial and adjacent windings arrangement respectively. The current gain stabilises above 100kHz and is about 0.99 for the coaxial and 0.9 for the adjacent winding arrangement. The resonant peak appears where the

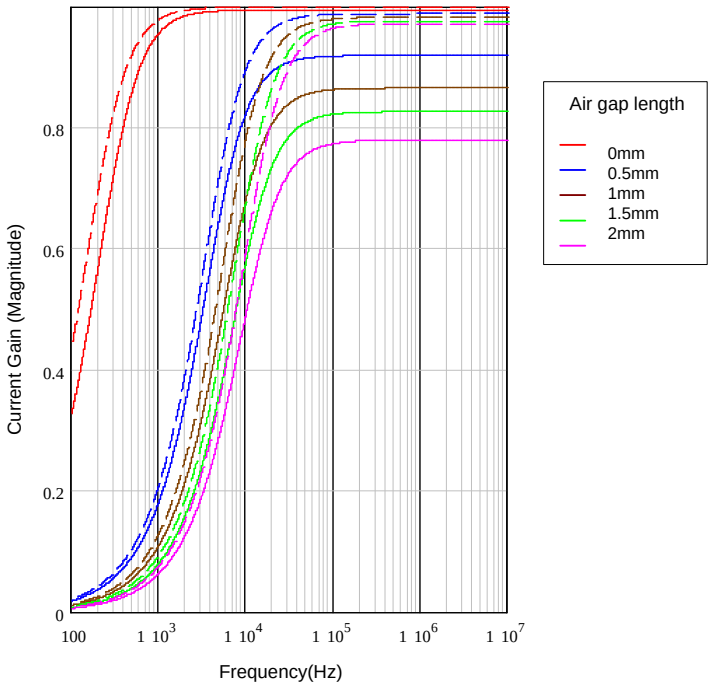

Figure 4.23: *The simulated current gain magnitude of the (P66/56, 26:12, 27SWG) coaxial (dashed lines) and adjacent (solid lines) winding transformers. The model takes into account the windings AC resistance.*

valley between the two voltage resonances are.

Using the above current and voltage graphs the designer can locate a suitable operating area for the transformer where both voltage and current gain criteria could be satisfied. It is clear that the voltage and current gains depend on the load value. It is the absolute load value that matters (ie ohmic value) and that the voltage magnitude is not involved in the transfer function.

The above transfer functions have been built on the assumption that the transformer model is valid over the entire frequency range. However, it is known that at high frequencies (>100kHz) the operation of a transformer is more complex. The winding resistance may be considerable as an inductive interface, usually, requires more turns to increase the magnetising inductance and reduce the circulating current. Furthermore, the AC resistance is frequency-dependent and using a fixed value to produce the transformer response may not be accurate. The effect of the AC resistance on the voltage gain would be a gain reduction at higher frequencies due to the voltage drop across it.

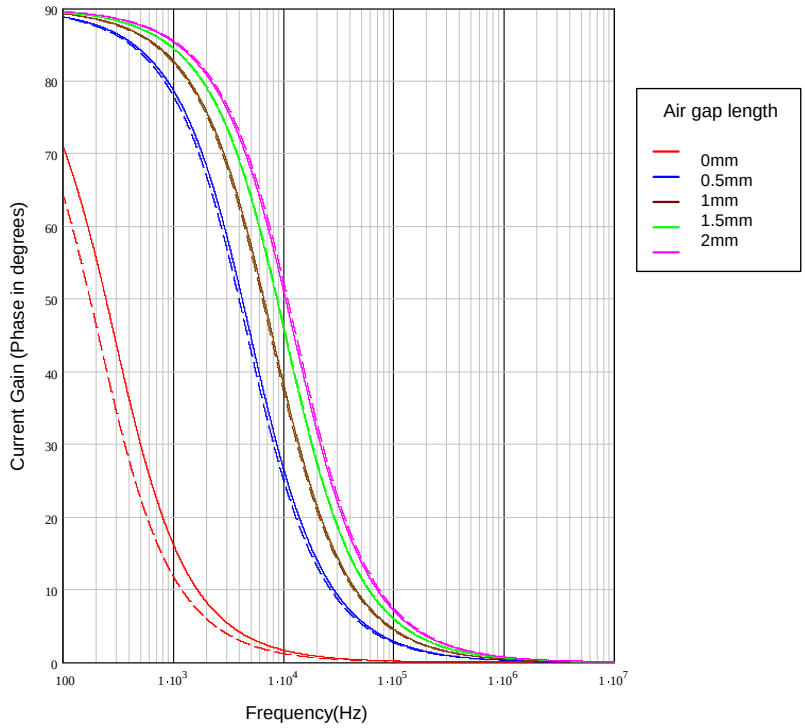

Figure 4.24: *The simulated current gain phase of the (P66/56, 26:12, 27SWG) coaxial (dashed lines) and adjacent (solid lines) winding transformers. The model takes into account the windings AC resistance.*

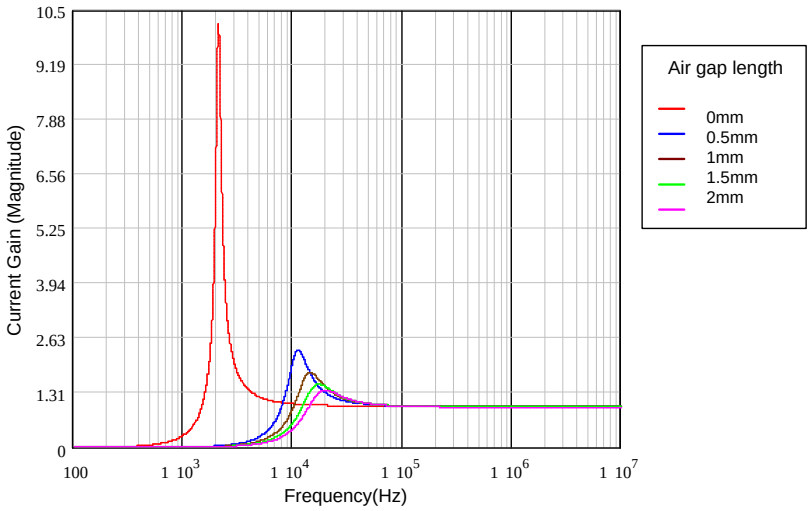

Figure 4.25: *The simulated current gain magnitude of the (P66/56, 26:12, 27SWG) coaxial winding transformer with leakage inductance compensation.*

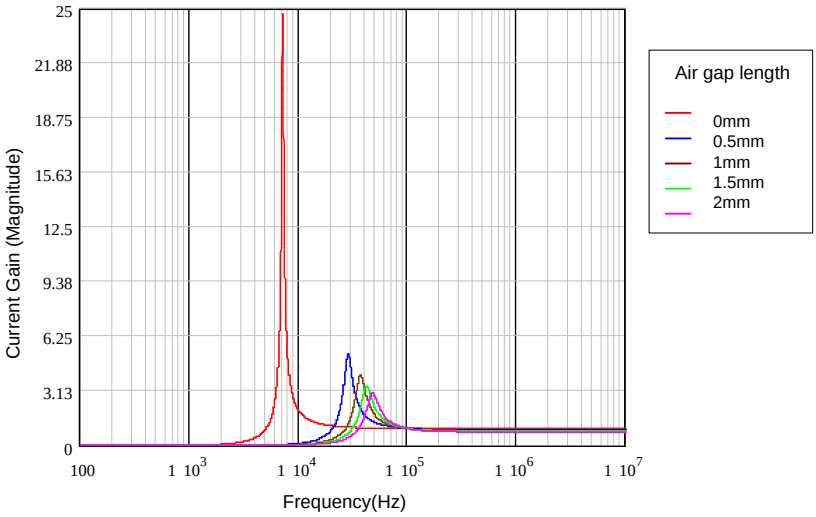

Figure 4.26: *The simulated current gain magnitude of the (P66/56, 26:12, 27SWG) adjacent winding transformer with leakage inductance compensation.*

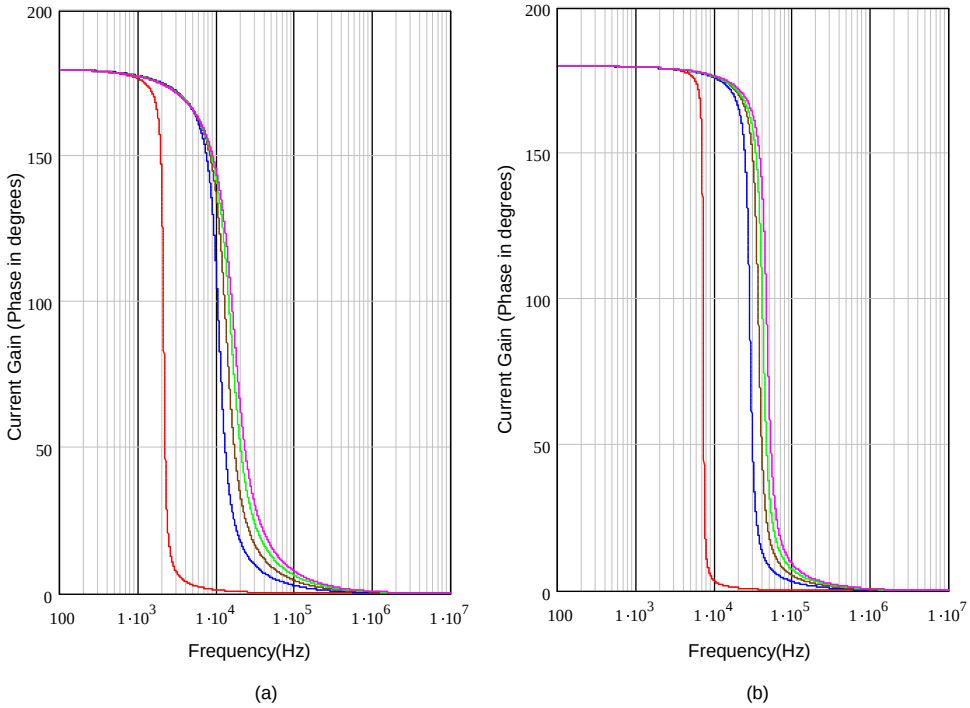

Figure 4.27: *The simulated current gain phase of the (P66/56, 26:12, 27SWG) (a) coaxial and (b) adjacent winding transformers with leakage inductance compensation.*

Another concern about using the transfer function to assess the transformer's performance is the above gain graphs correspond to sinusoidal excitation and not the typical square waveforms that appear in power supplies. The harmonic content of the square waveforms is rich and the high frequency components considerably increase the AC losses of the windings. The time domain analysis is more enlightening because by using equation 4.5 the exact R_{ac} can be calculated and used to predict with a good accuracy the output of the transformer.

By working out the reactive energy that is stored in the magnetising inductance the flux density in the core can be calculated and the core losses can be obtained from the respective nomogram (power losses versus flux density and frequency) found in the core manufacturer's data sheet. Thus, core losses can be included in the overall calculation of the efficiency of the transformer.

4.4.1.3 Transformer efficiency

An equally important parameter with the voltage gain is the transformer efficiency. The efficiency of conventional transformers is nearly 1.0 as most of the input power is transferred to the output. The power consuming elements in a transformer are the winding resistances and the core losses. In a rotating transformer the flux density is kept low and the core losses are negligible. The air gap fringing flux, however, tends to generate eddy currents in any conductive materials that happen to be around the air gap. The use of non-conductive materials for the mechanical construction is a solution though the ferrite core and windings cannot be avoided. The most significant loss factor is the windings resistance that becomes significant at higher switching frequencies.

Figure 4.28 shows the efficiency of the coaxial windings transformer (blue line) and that of the compensated coaxial winding (red line). The low frequency efficiency of the compensated network is poor as the resonance between the compensating capacitor and magnetising inductance results in high current flowing in the primary winding. At the point where the peak of the current gain occurs in the compensated network (see figure 4.25), the efficiency is maximum at about 99% as the output current is higher than the input at the expense of the respective voltages. When the frequency increases above the resonant points the efficiencies of the compensated and non-compensated networks become equal.

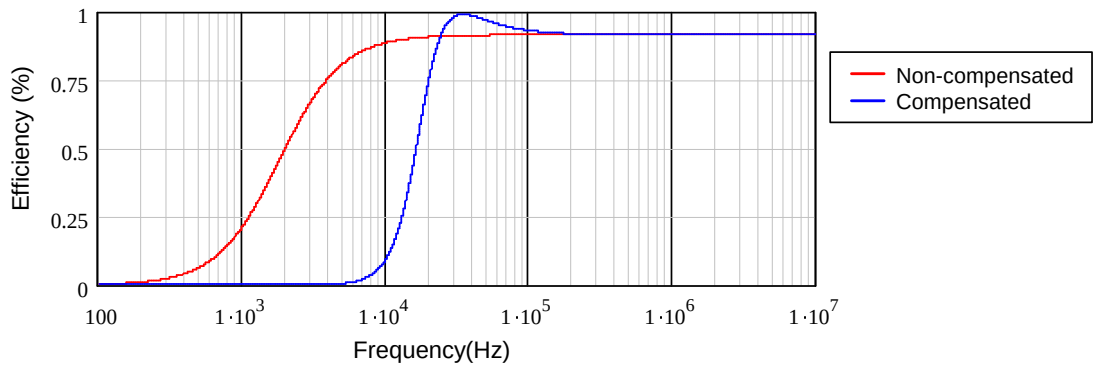

Figure 4.28: *Simulated efficiency of the non-compensated coaxial winding transformer (red line) and of the compensated coaxial windings transformer (blue line) at 800W of output power.*

4.4.2 Time domain analysis

The frequency domain analysis is a useful tool that describes the behaviour of the magnetic component across a frequency range assuming sinusoidal excitation. However, it is not adequate when it comes to switching waveforms with a broad spectral content. The network equations can be solved in the time domain for any type of periodic excitation and the output waveform can be predicted.

This type of analysis consists of two stages. The first stage includes the derivation of a set of differential equations that describe the electrical network. Secondly, a waveform is applied as input to these equations and the output waveform can be derived.

The adjacent winding transformer (introduced in Section 4.3.2.3) with 1mm of air-gap and a 3.65Ω load is considered in this example. The magnetising, leakage inductances and winding resistances are taken from Table 4.1 and 4.2. The inter-winding and intra-winding capacitances are negligible at this operating frequency (100kHz). A typical bridge converter waveform is supplied to the model

The network in Figure 4.15(a) is described by the following differential equations,

$$\frac{di_1(t)}{dt} = \frac{L_m v_{in}(t) - L_m i_1(t) R_1 - R_2 i_2(t) L_m - i_2(t) R_o L_m + v_{in}(t) L_2 - i_1(t) R_1 L_2}{L_1 L_m + L_1 L_2 + L_m L_2} \tag{4.12}$$

$$\frac{di_2(t)}{dt} = \frac{L_m v_{in}(t) - L_m i_1(t) R_1 - L_1 R_2 i_2(t) - R_2 i_2(t) L_m - L_1 i_2(t) R_o - i_2(t) R_o L_m}{L_1 L_m + L_1 L_2 + L_m L_2} \tag{4.13}$$

$$\frac{di_1(t)}{dt} = \frac{v_{in}(t) L_2 - i_1 t R_1 L_2 + L_1 R_2 i_2(t) + L_1 i_2(t) R_o}{L_1 L_m + L_1 L_2 + L_m L_2} \tag{4.14}$$

By solving the system of linear differential equations 4.12,4.13,4.14 the voltages and currents can be calculated. A typical bipolar waveform $v_i(t)$ of a full bridge converter is applied to the transformer primary winding and the transformer output $v_o(t)$ is calculated.

Figures 4.29 and 4.30 illustrate the input/output voltages and currents of the adjacent and coaxial windings transformer respectively. Note that the secondary side waveforms are scaled by the turns ratio to allow direct comparison with the primary waveforms. The output waveform $v_o(t)$ is in both cases distorted and its amplitude is reduced. The transformer is acting as a low pass filter reducing the high frequency content of the primary waveform. This is mainly the result of the series leakage inductance (the leakage inductance is a low pass filter by itself). The higher the leakage inductance is the greater the distortion of the waveform is. The effect of the air-gap to the waveshape is also significant: the longer the air-gap is the more current will flow through the primary turns and, consequently, the greater the voltage drop across leakage inductance is. In the graphs of figure 4.30 the distortion of the waveform is less than that in figure 4.29. The coaxial winding is advantageous mainly for two reasons; a) the windings are physically closer and the leakage inductance is smaller and b) the bobbin width is bigger spreading the turns across the core window and having fewer layers in each winding (less proximity losses).

Figures 4.31(a), (b), (c) illustrate the simulated results for various loading conditions of the adjacent windings transformer with leakage inductance compensation (with series tuned capacitors). The waveforms of figure 4.32(a), (b), (c) correspond to various loading conditions of the coaxial windings arrangement with leakage inductance compensation.

The voltage and current waveforms of adjacent windings are significantly improved especially at high loading (figure 4.31(a)). The coaxial windings voltages and current

do not appear to change considerably especially for low loading of the transformer. In both winding arrangements the high frequency components of voltages and currents are eliminated and waveforms are almost sinusoidal. This is due to the tuned L-C circuit having zero impedance at the resonant frequency which in this case equals the switching frequency. The frequency-dependent impedance of the L-C network is used in these circuits to regulate the output (by adjusting the switching frequency).

A comparison between the compensated and non-compensated circuit results reveals that compensation may be essential with high leakage inductance transformers. When the leakage inductance can be controlled then the designer may avoid leakage compensation and retain the advantage of higher power density that the square waveforms offer.

4.5 Chapter Summary

Both the leakage inductance and the R_{eff} of the transformer are clearly the most decisive parameters that define the operation of the power transformer and have a negative impact. The former increases the reactive power stored in the transformer and the latter increases the power dissipation on the windings.

To reduce the power storage and dissipation, a careful mechanical design of the power transformer is required. Depending on the specified operating conditions of the power converter (efficiency, maximum temperature rise, and size) there is a barrier to the maximum power that an inductive interface (such as the rotating transformer) can transfer. Both the rms losses and the voltage gain are two parameters that need to be satisfied.

Three methods have been employed to assess the rotating transformer's electrical behaviour. Direct measurements on a prototype give accurate values for the leakage and magnetising inductances as well as for the windings resistances and capacitances. The theoretical estimation of the above electrical characteristics requires several simplifications and assumptions to be made during the calculations. As a result the theoretical predictions are not highly accurate and can only be used in the initial design steps to guess the order of magnitude of the electrical properties.

A 2-D Finite element analysis has also been employed for the first time to predict the rotating transformer characteristics prior to manufacturing. It is a useful analysis that offers a better insight to the rotating transformer magnetic field and it proved to be a reliable technique for soft-prototyping. The results were close to the measured values and the analysis is relatively easy to conduct. FEA is recommended for the early stages of development when the optimum shape and size of the magnetic core and windings are investigated.

Simulations of the proposed winding layouts demonstrated the voltage gain problems of the adjacent windings at high transformer loading. The coaxial windings improve the transformer voltage gain with a penalty in the manufacturing complexity. Leakage inductance compensation has been proposed in many applications where an adjacent winding arrangement is needed.

Despite improving the voltage gain, the tuned L-C network acts as a low pass filter resulting in almost sinusoidal output voltages and currents. To retain the advantage of better component utilisation that the square waveforms offer, a quasi-resonant converter is considered.

In the following Chapter the phase shifted full bridge converter is introduced. Its operation is described and a joint power electronics-transformer design methodology follows.

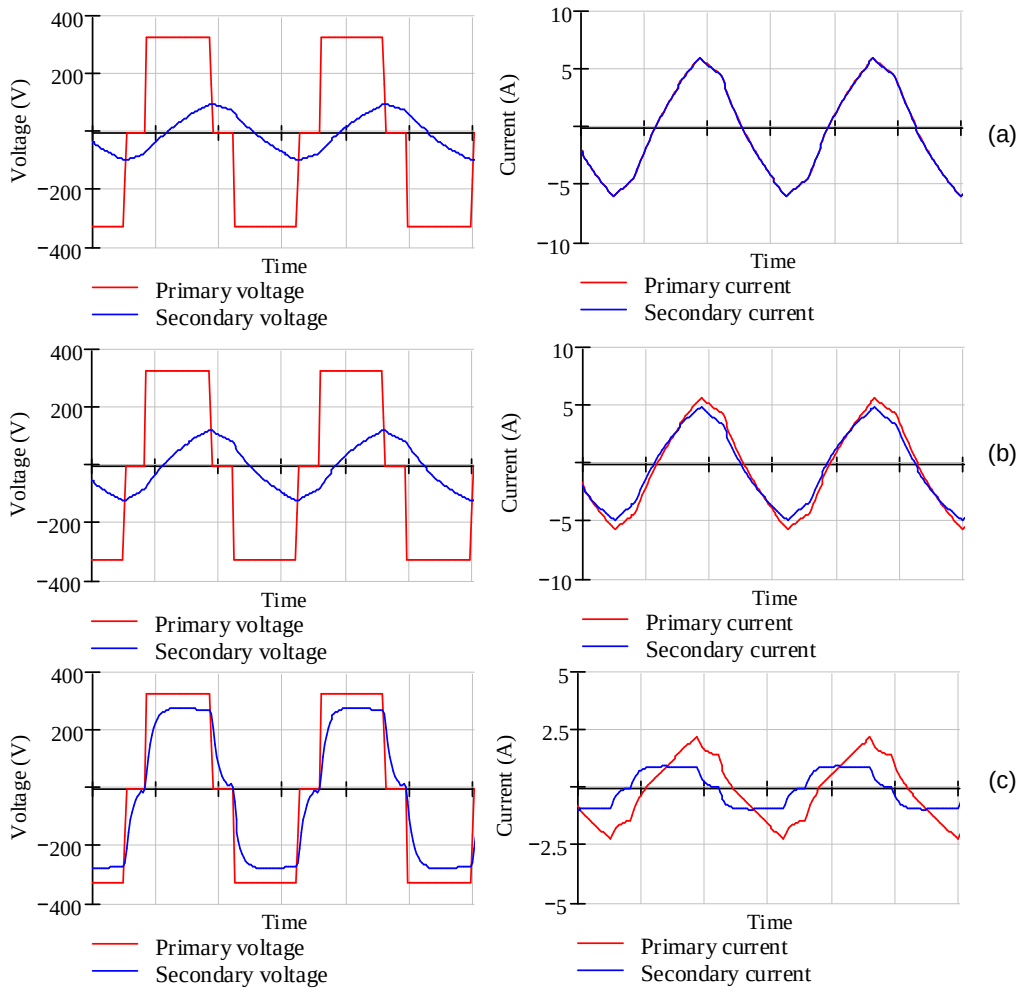

Figure 4.29: *The simulated input and output voltages and currents of the (P66/56, 26:12, 27SWG) adjacent winding transformer with an 1mm air gap.(a) 1000W (b) 500W (c) 10W of output power. The secondary waveforms are scaled by the turns ratio to allow direct comparison with the primary waveforms.*

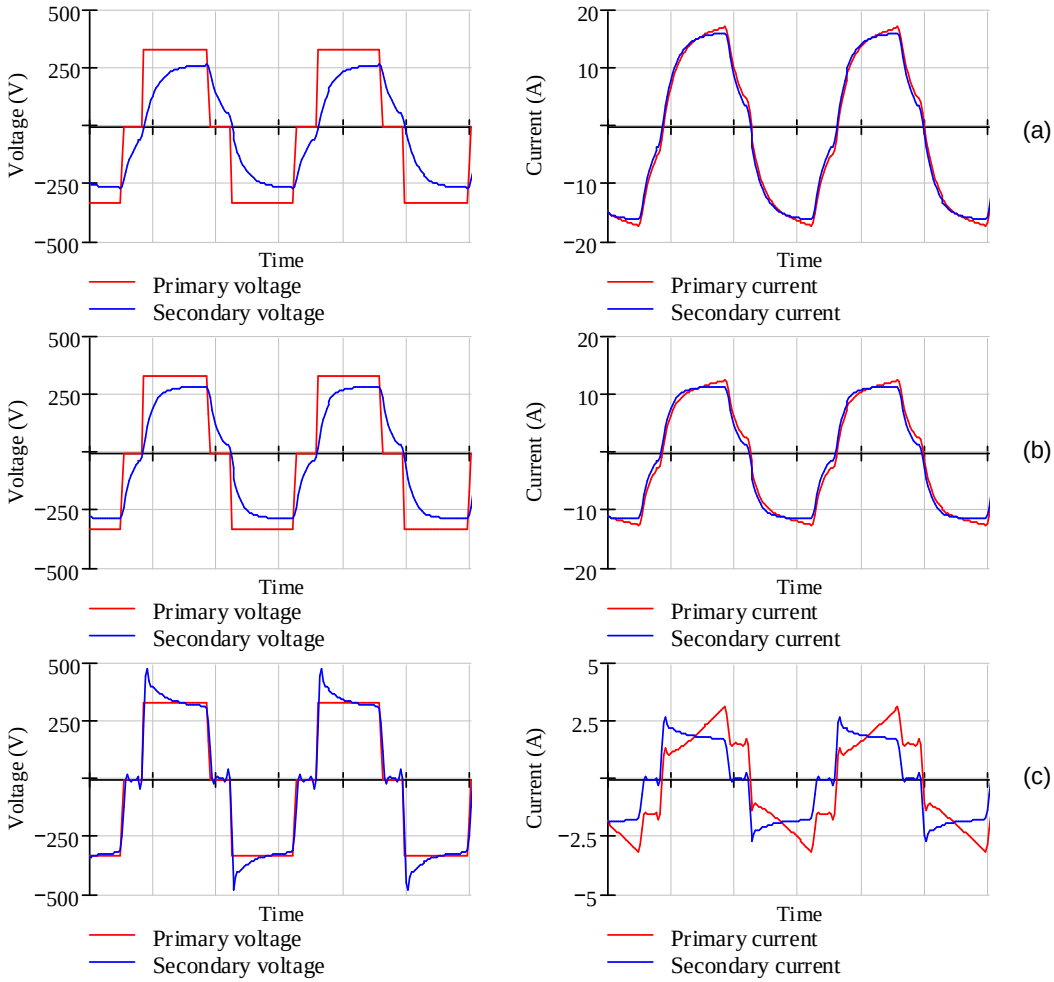

Figure 4.30: *The simulated input and output voltages and currents of the (P66/56, 26:12, 27SWG) coaxial winding transformer with an 1mm air gap.(a) 1000W (b) 500W (c) 10W of output power. (a) 1000W (b) 500W (c) 10W of output power.*

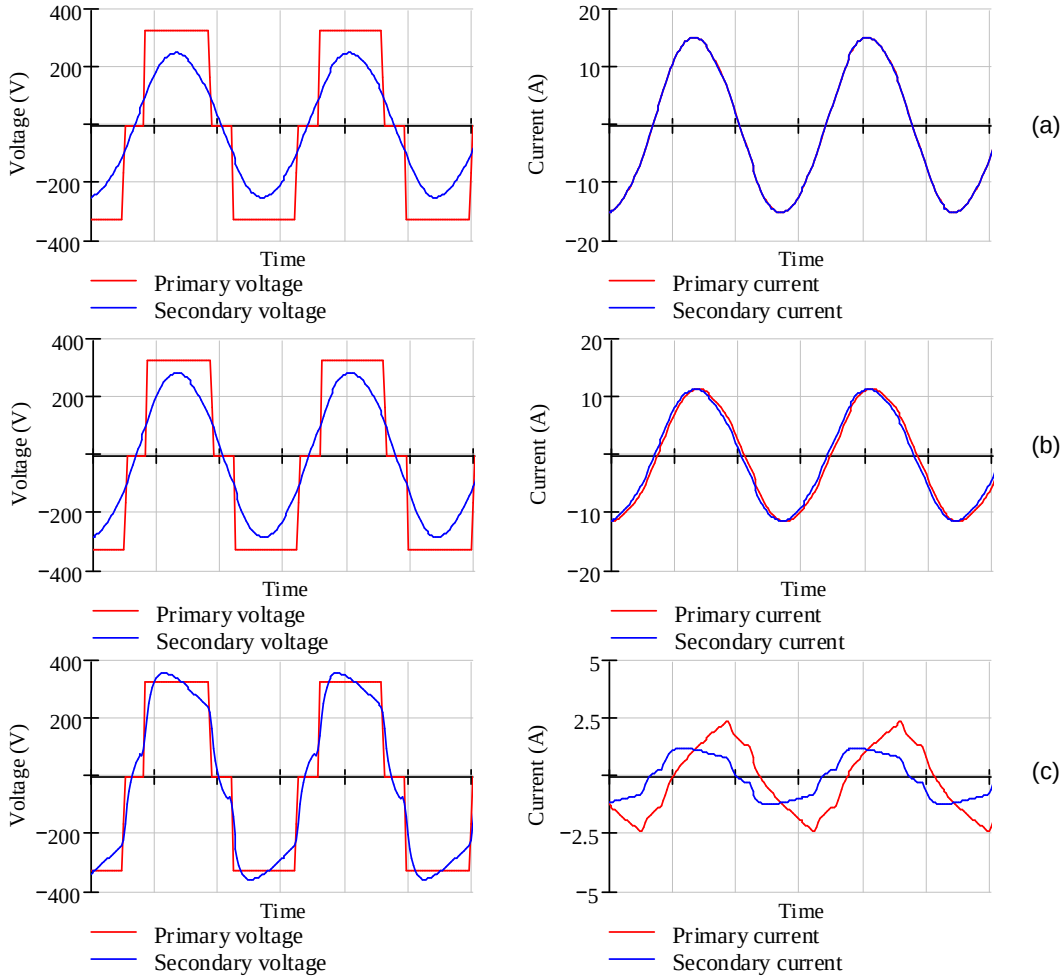

Figure 4.31: *The simulated input and output voltages and currents of the (P66/56, 26:12, 27SWG) adjacent winding transformer with an 1mm air gap and leakage inductance compensation. (a) 1000W (b) 500W (c) 10W of output power.*

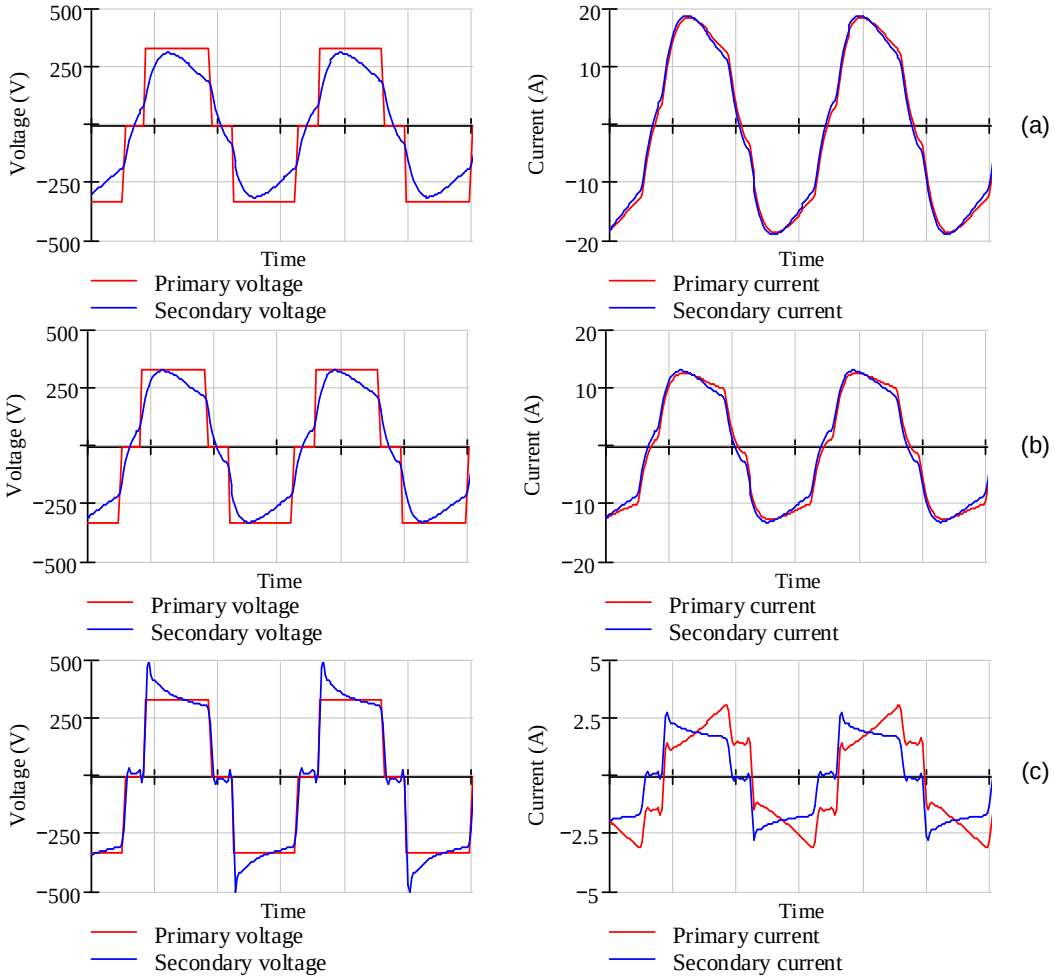

Figure 4.32: *The simulated input and output voltages and currents of the (P66/56, 26:12, 27SWG) coaxial winding transformer with an 1mm air gap and leakage inductance compensation. (a) 1000W (b) 500W (c) 10W of output power.*

Chapter 5

The Phase-shifted Full Bridge

The motivation behind this relatively new control strategy, the phase-shift modulation, is the constant need for higher operating frequency. The phase-shifted full bridge converter combines the advantages of switch resonant transitions to reduce the switching power losses and square wave power conversion to maintain optimal utilisation of the magnetic components and semiconductors.

The concept of phase-shifted modulation was first introduced in 1984 in an internal paper written by Z.D. Fang et al. at the Virginia Power Electronics Center (VPEC). The full technical details of this new control strategy were not officially published until 1987, when Steigerwald and Park, and later in 1988 Steigerwald and Ngo, were granted the US patents #4,672,528 [80] and #4,864,479 [81] respectively. Soon after the same group of researchers including Fisher and Kuo published a paper [82] at the 1988 High-frequency Power Conversion Conference (HFPC) presenting a design example of a 500kHz pseudo-resonant (as it was originally named) converter. The operation of this converter was based on phase-shifted gate pulses that were achieving zero voltage transitions of the active switches. The Phase Shifted Full Bridge (PSFB) topology was soon investigated by other researchers [83–86] and was explicitly analysed and improved.

The aim of this chapter is to introduce the phase-shifted full bridge converter as a solution for contact-less transfer of energy applications. The merits and weaknesses of this technology are investigated and the foundation for the development of a design methodology is set. Initially, two instances of the conventional topology (the PSFB with a full wave rectifier and the PSFB with a current doubler) are analysed and their operational differences are stated. Accordingly, the effect of the rotating transformer to the PSFB operation is studied.

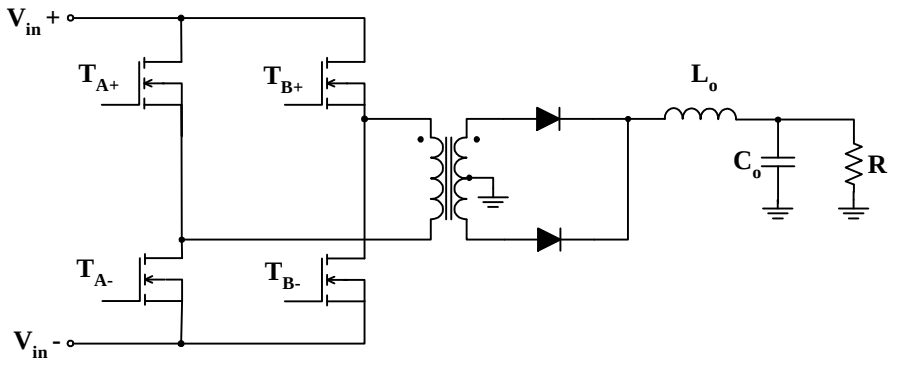

Figure 5.1: *A typical full-bridge converter*

5.1 Introduction

5.1.1 The full bridge converter

The phase-shifted full bridge converter is based on a standard full bridge topology. A typical full bridge converter appears in figure 5.1 This topology is used in medium to high power applications where the use of four switches is justified. One of the main advantages is the bidirectional current flow in the transformer windings. This results in an alternating magnetic flux and hence optimum use of the magnetic core. Other advantages are the automatic flux resetting due to the bipolar waveforms and the reduced voltage and current stresses of the switches that reduce the cost and increase the reliability of the design.

The operation of the full bridge is based on a switching cycle that comprises of two power transfer intervals and two intervals of inactivity. During the power transfer intervals two diagonal switches are on (either of the pairs: T_{A+}-T_{B-} or T_{A-}-T_{B+}). During the inactive interval all switches are off and no voltage is applied across the primary. The result of this switching pattern is an alternating voltage across the transformer primary winding. At the secondary side, the stepped up or down voltage is then rectified, the voltage and current ripple are removed by the L-C filter and a DC voltage appears across the load.

The main switches can be Metal Oxide Semiconductor Field Effect Transistors (MOSFETs) or Insulated Gate Bipolar Transistors (IGBTs) depending on the converter input voltage, current and operating frequency. Both semiconductor types are not perfect switches; they possess parasitic inductances and capacitances in the p-n junctions, case

and leads. These inductances and capacitances limit the rate of voltage and current variations (dv/dt and di/dt) imposing a frequency limitation at the switching operation. Furthermore, these parasitic components cause voltage and current ringing and the use of snubbers is essential. The snubbers can be made of passive components or a combination of passive and active (semiconductor) components. They usually dissipate the power that they remove from the parasitic components and therefore they lower the overall converter efficiency.

5.1.2 Modulation

A DC/DC converter can step the source voltage up or down depending on the topology (buck, boost, buck-boost) that is being used. The isolating transformer performs scaling of the alternating voltage that is produced by the switches. The final voltage adjustment or *regulation* is performed by the control circuit; it observes the output voltage (or current) and adjusts the on-time of the power switches accordingly. The control strategies can be classified in two broad categories; fixed frequency control and the variable frequency control.

Fixed frequency control. With a fixed-frequency control, the switching frequency (cycle period) remains constant and the driver adjusts the on-time of the switch, in other words the driving waveform duty cycle. This strategy is known as Pulse Width Modulation (PWM) and offers the advantage of easy paralleling and synchronising of several converter modules to achieve higher output power. The overall design of the converter for a fixed frequency operation is easier and the losses can be accurately predicted.

Variable frequency control. This method assumes a fixed on-time and a variable off-time (or vice versa) for the switches (thus variable switching period time/frequency). This method may be easily implemented in a stand-alone converter, however it makes it difficult to synchronise more parallel modules. It is also not possible to use it in applications where some sort of synchronisation with the load is required, such as in radars where the power supply is often synchronised with the pulse repetition frequency. Furthermore, this modulation is not suitable for multi-stage power supplies (where syn-

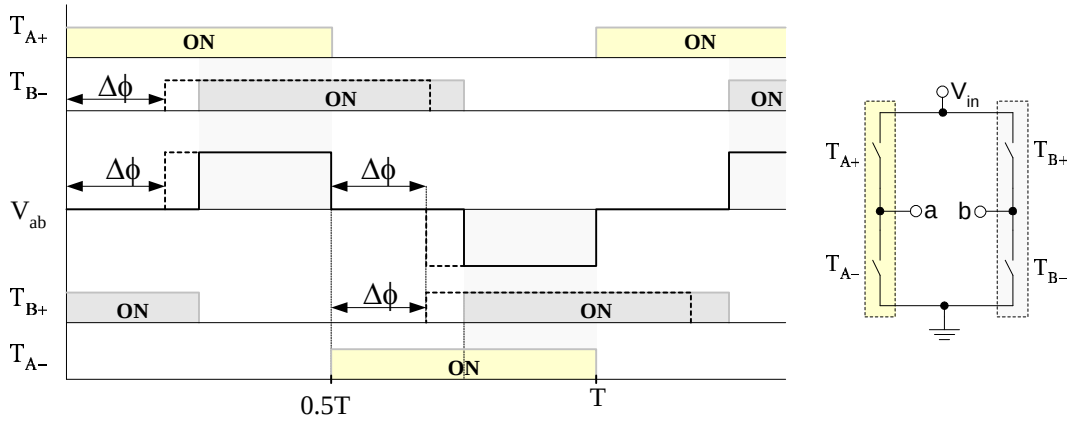

Figure 5.2: *The phase shift modulation; all switches operate with fixed on-time. The right leg (T_{B+} and T_{B-}) driving waveforms are shifted by $\Delta\phi$ to achieve regulation.*

chronisation of PFC, cascaded power stages etc is required to reduce harmonics and comply with regulations).

Phase-shifted control. This belongs to the fixed frequency modulation strategies.

The phase-shifted modulation is applied in a full bridge topology to allow quasi-resonant operation. The power transfer is taking place every time two diagonal switches are ON. The on-time of all switches is fixed and the driving pulses of the right leg switches are shifted with respect to those of the left leg (figure 5.2). The amount of phase-shift (between T_{A+} and T_{B-}, T_{A-} and T_{B+}) defines the duty cycle of V_{ab} and consequently the output regulation.

The phase-shifted operation results in the introduction of a resonant time-interval in the switching cycle. During this interval the MOSFET junction capacitance C_{oss} resonates with the series inductance (e.g. leakage inductance). At the moment that the voltage across the drain-source junction becomes zero, the switch can be turned ON with minimum power loss. This lossless transition takes place every time a switch turns ON and thereby the total switching losses are significantly reduced.

Operating in this quasi-resonant mode the phase shifted full bridge produces less electromagnetic radiation and demonstrates a better performance. Typical efficiency values for a PSFB are 92-95%. The PSFB converter is used in medium and high power applications (although the PSFB with a current doubler has also been used in low power

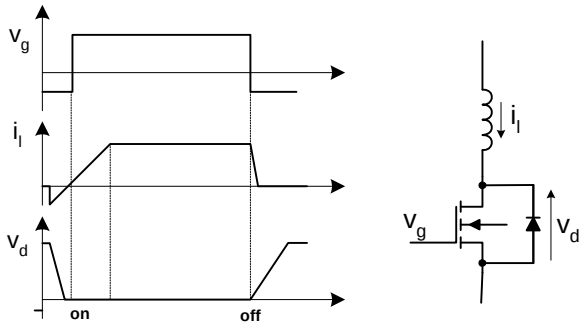

Figure 5.3: *ZVS: the voltage across the switch becomes zero prior to switching.*

applications due to its ability to perform well where low output voltages are needed [87]) that justify the use of four MOSFETs in the primary side.

5.1.3 Zero voltage switching

Figure 5.3 illustrates the turn-off and turn-on action of the switch [88]. Shortly before the driver turns the MOSFET on a reverse (source-to-drain direction), current flows through the inherent body diode. Once the diode is ON, the voltage across it (and across the switch) is latched at zero volts. Therefore, the switch is ready for a lossless transition. The current that flows through the switch to prepare the lossless transition causes conduction losses, which at low frequencies may be comparable with the switching losses. As the switching frequency increases the benefit from the switching losses reduction becomes clear.

Unfortunately, the switch turn-off is still lossy. However, the power dissipation can be minimised using high current drivers to reduce the switching time.

5.1.4 Zero current switching

Figure 5.4 illustrates the zero current switching. This is achieved thanks to the series inductor that holds the current low while the voltage is quickly zeroed reducing the turn on losses. Similarly, the switch is turned off once the current has dropped to zero.

Note here that prior to turning the MOSFET on, the drain-source capacitance is charged. During the turn on it is rapidly discharged and this *charge dumping* dissipates energy which is proportional to the die size of the semiconductor and also to the square of the

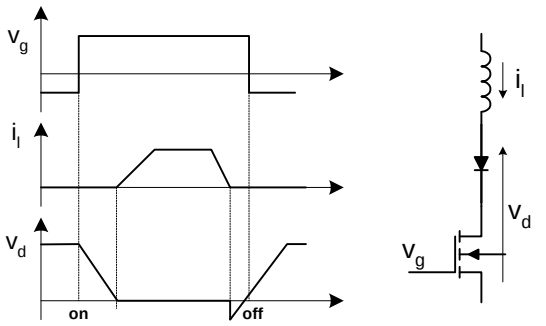

Figure 5.4: *ZCS: the current through the switch becomes zero prior to switching.*

voltage at which the capacitance was charged.

As ZCS mostly reduces the turn off losses, it is usually used in high power converters utilising IGBTs, which generally suffer from a turn-off tail current [89]. Often ZCS may be used together with ZVS to combine the switching loss reduction benefits.

5.2 Phase-shifted Full Bridge with a Full Wave Rectifier

A common instance of the PSFB converter appears in figure 5.5. It uses a centre-tapped secondary winding with two diodes or a single winding with a bridge rectifier along with a low pass filter (usually L-C) to remove the AC fluctuation of the output voltage. The main waveforms appear in figure 5.5.

Several papers have been written on the operation of a PSFB. Those by Sabate [90] and Vlatkovic [91] are offering an in-depth interval-by-interval analysis of the switching cycle and also derive the small-signal model of the topology.

5.2.1 Operation of the PSFB with a full-wave rectifier

The following analysis assumes all components are ideal. The different operational states are summarised in table 5.1

The switching cycle of the phase-shifted full bridge converter is sub-divided into ten time intervals. During the different intervals each of the active components (MOSFETs and diodes) appears as either a short-circuit or as an open-circuit. Hence, each state can be analysed as a higher order linear network.

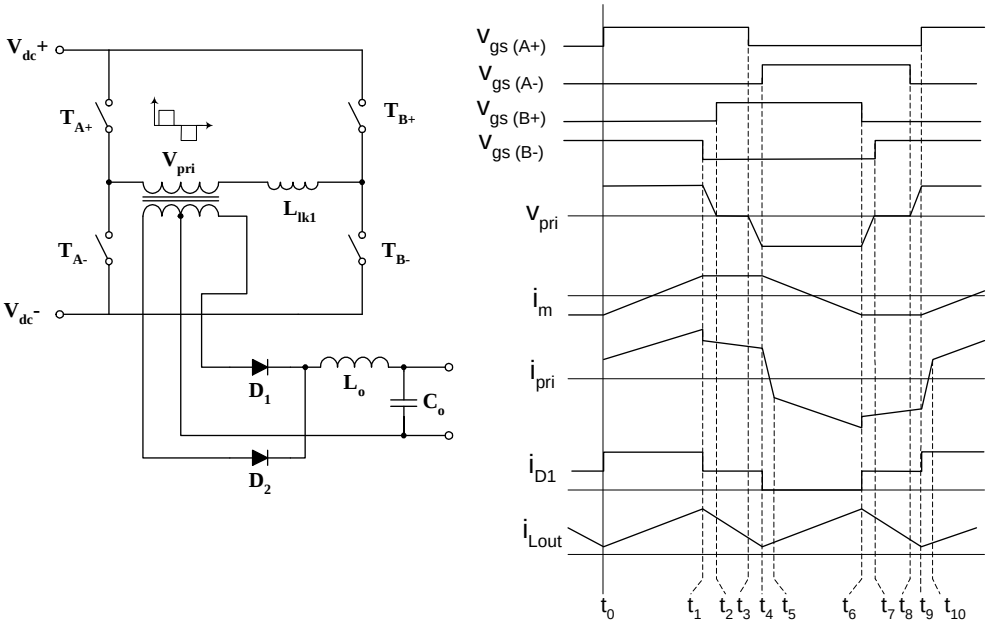

Figure 5.5: *Idealised waveforms of a phase-shifted full bridge with a full wave rectifier.*

Interval	T_{A+}	T_{A-}	T_{B+}	T_{B-}	Interval name
1	ON			ON	Active
2	ON				AP Resonant
3	ON		ON		Passive
4			ON		PA Resonant
5		ON	ON		Current reversing
6		ON	ON		Active
7		ON			AP Resonant
8		ON		ON	Passive
9				ON	PA Resonant
10	ON			ON	Current reversing

Table 5.1: *The phase-shifted full bridge operational states.*

The power transfer from the primary to the secondary side of the converter starts whenever a switch of the right leg turns on. On the contrary, when a left leg switch turns on, a passive interval starts. Based on this observation we call the right leg the *passive-to-active (PA) leg* and the left one the *active-to-passive (AP) leg*. The following analysis assumes that the only series (resonant) inductance is the transformer leakage inductance L_{lk1} although an additional external inductor is often used to improve the resonant behaviour. The equivalent models that are produced are inclusive of the magnetising and secondary leakage inductance. In a conventional converter, where the magnetising current is negligible, the magnetising inductance can be ignored and the secondary leakage can be lumped with the primary leakage inductance (as the same current flows through them). In the following analysis any parasitic capacitances, other than the MOSFET intrinsic capacitances, will be ignored for the sake of simplicity (they are, however, included in the converter design process presented in Chapter 6).

The description starts with the converter being at the power transfer interval; power is transferred from the primary to the secondary side thus charging up the output inductor. At t_0 just before the first interval starts the switches T_{A+} and T_{B-} are ON and a current $i(t_0) = I_p$ is flowing through the transformer's primary winding. The secondary current is now equal to the output inductor's current and this is the point where the first time interval begins.

5.2.1.1 The power transfer interval ($t_0 < t < t_1$): Interval 1

This time interval is called the *power transfer interval* because energy is being transferred from the dc source to the converter output. During this time the primary current is flowing through the switch T_{A+} into the transformer primary and via T_{B-} back to the dc source. Most of the primary current is reflected at the secondary side and a small portion of it flows through the magnetising inductance. The secondary current is flowing through the upper section of the centre-tapped winding, the diode D_1 and the output filter and load. The current in the inductor L_o builds up to its maximum value.

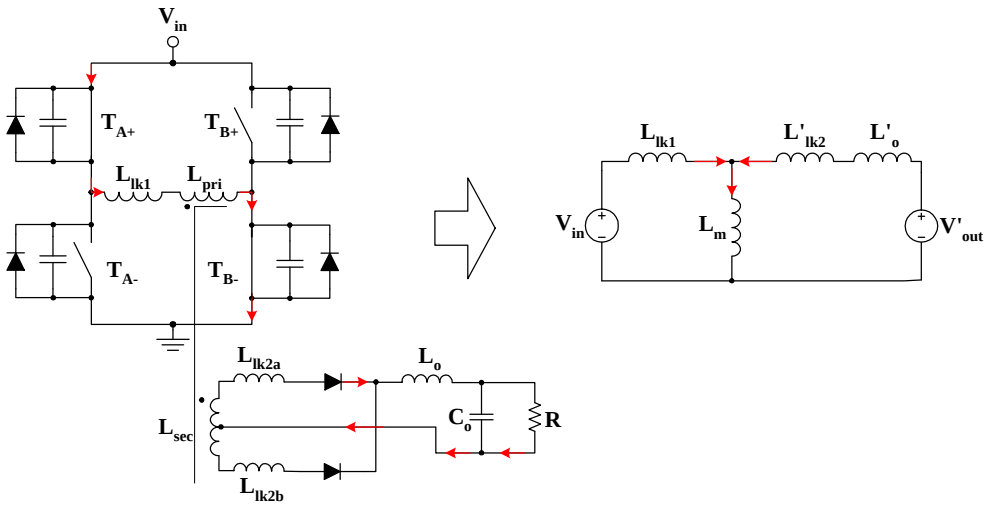

Figure 5.6: *Interval 1: PSFB and the equivalent network during the power transfer state.*

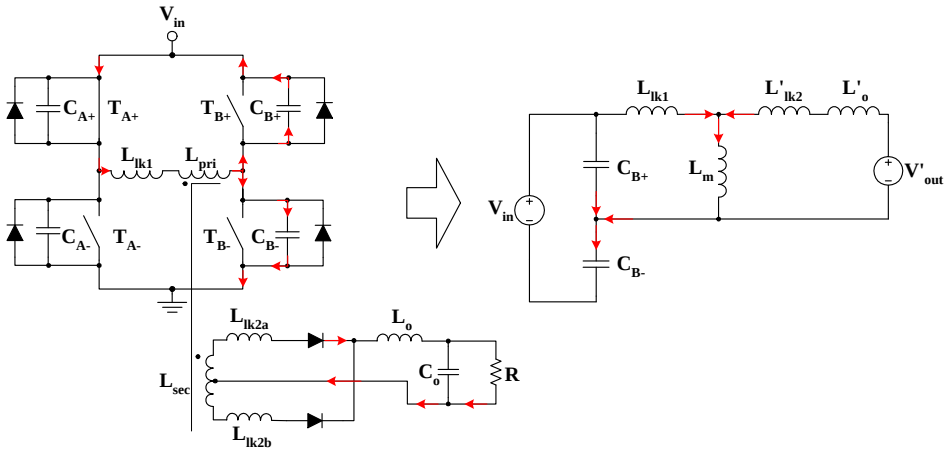

Figure 5.7: *Interval 2: PSFB and the equivalent network during the active to passive resonant transition.*

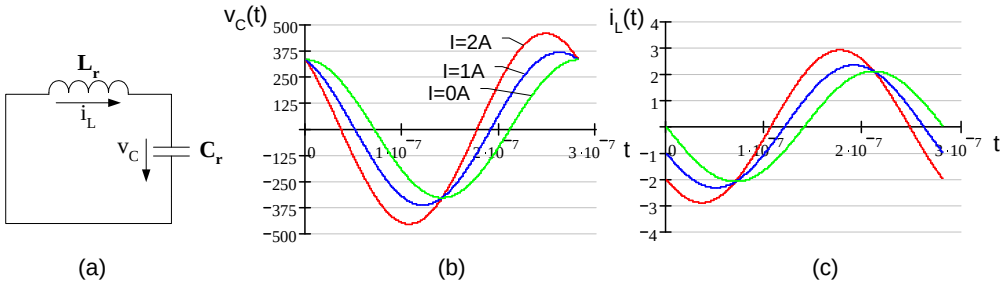

Figure 5.8: *Active-to-passive resonant transition a) a simple equivalent circuit b) the voltage waveform across the switch for different initial current values and c) the resonant current.*

5.2.1.2 The Active-to-Passive resonant transition ($t_1 < t <_t 2$): Interval 2

This interval (figure 5.7) starts when the control circuit turns T_{B-} off. The current that is now maintained by the various inductances is forced to flow through the MOSFET parasitic capacitances C_{B+} and C_{B-}. C_{B+} was initially charged at V_{in} as T_{B+} was off and C_{B-} was discharged, as T_{B-} was conducting.

L_{lk1}, C_{B+} and C_{B-} form an L-C network. The resonant voltage and current of switch T_{B+} can be calculated based on the simple equivalent network of figure 5.8(a). The voltage across the switch is given by,

$$v_C(t) = V_{in} \cdot \cos(\omega_0 t - \omega_0 t_1) + Z_0 \cdot I_{L_0} \cdot \sin(\omega_0 t - \omega_0 t_1) \tag{5.1}$$

where I_{L_0} is the initial resonant inductor current, ω_0 is the resonant cyclic frequency,

$$\omega_0 = \frac{1}{\sqrt{L_r \cdot C_r}} \tag{5.2}$$

and Z_0 is the characteristic impedance,

$$Z_0 = \frac{L_r}{C_r} \tag{5.3}$$

C_r is the sum of the MOSFET capacitances (C_{oss}) and L_r is the resonant inductance (a combination of the primary and secondary leakage inductances and output inductor as seen in the equivalent circuit of figure 5.7).

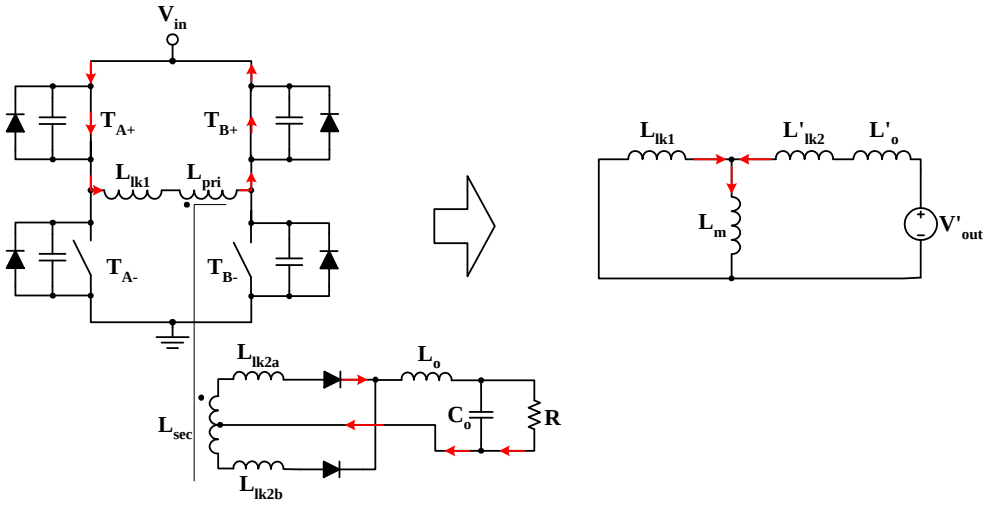

Figure 5.9: *Interval 3: PSFB and the equivalent network during the passive state.*

The resonant current is given by,

$$i_L(t) = I_{L_0} \cdot \cos(\omega_0 t - \omega_0 t_1) - \frac{V_{C_0}}{Z_0} \cdot \sin(\omega_0 t - \omega_0 t_1) \tag{5.4}$$

The voltage across C_{B+} will become 0 in any case (even if the initial inductor current is 0) provided that enough time is allowed for the resonant operation to be completed. The amount of initial current defines the time needed for the capacitor voltage to become 0.

Once C_{B+} is completely discharged, the current is redirected through the inherent diode D_{B+} that is now forward biased. As a result the voltage across the capacitor remains zero until the next time interval when switch T_{B+} is turned on under zero voltage conditions.

At the secondary side the current keeps flowing through the upper section of the winding and diode D_1. The secondary current supports the resonant transition by acting as an additional current source reflected to the primary side.

5.2.1.3 The Passive Interval ($t_2 < t < t_3$): Interval 3

Just after the resonant transition interval, T_{B+} turns on at time t_2, while the voltage across it is 0V. The energy stored in the parasitic (leakage inductance) maintains the primary current through T_{A+} (split between the MOSFET channel and parasitic diode) and T_{B+}.

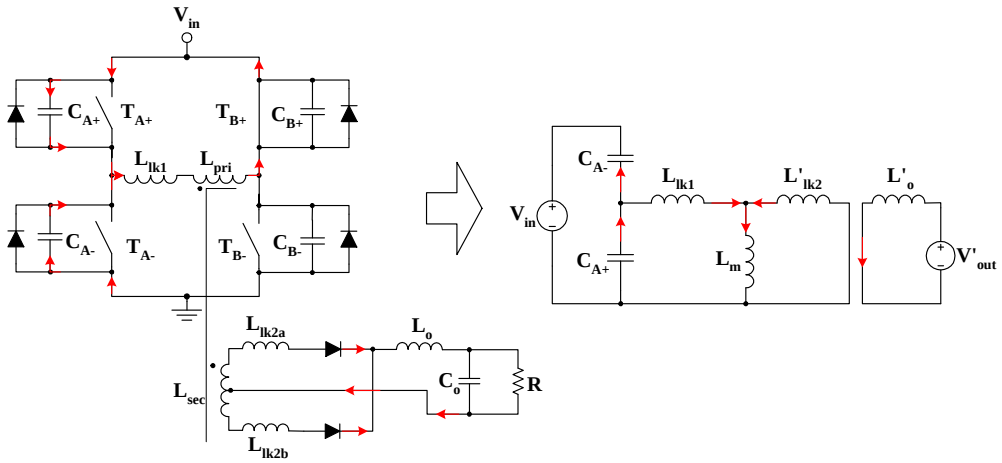

Figure 5.10: *Interval 4: PSFB and the equivalent network during the resonant transition.*

During this interval the primary winding of the transformer is effectively shorted. The primary current is reflected at the secondary winding and flows through diode D_1 and the load. All currents decrease as the dc source is disconnected during this interval (hence the name *passive*).

5.2.1.4 The Passive-to-Active Zero Voltage Transition Interval ($t_3 < t < t_4$): Interval 4

The left-leg resonant interval starts with the control circuit turning T_{A+} off at time t_3. The transformer parasitic inductor maintains the current flow through the MOSFET inherent capacitances C_{A+} and C_{A-}. C_{A+} was previously discharged as T_{A+} was conducting and C_{A-} was charged, as it was across the dc source. During this time the above capacitors resonate with the leakage inductance of the transformer L_{lk1}. This interval ideally ends when the voltage across C_{A-} is 0V and thus a zero voltage switching can follow. In practice, the current that stimulates the resonance may not be enough to complete the resonant operation.

The resonant voltage and current of the switch T_{A-} can be calculated based on the simple equivalent network of figure 5.8(a). The voltage across the switch is given by,

$$v_C(t) = V_{in} - (V_{in} - V_{C_0}) \cdot \cos(\omega_0 t - \omega_0 t_3) + Z_0 \cdot I_{L_0} \cdot \sin(\omega_0 t - \omega_0 t_3) \qquad (5.5)$$

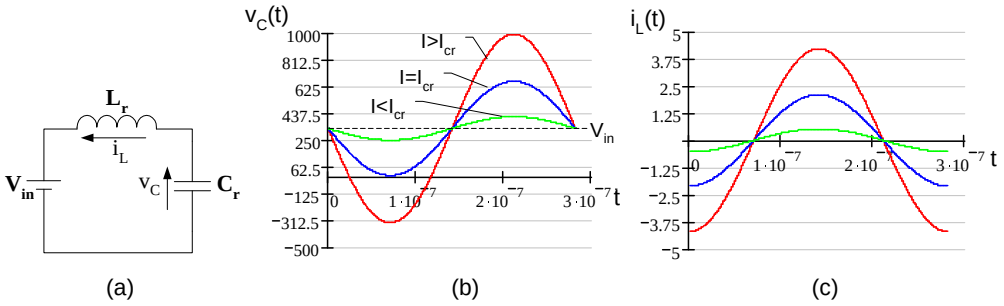

Figure 5.11: *Passive-to-active resonant transition a) a simple equivalent circuit b) the voltage waveform across the switch for different initial current values and c) the resonant current.*

During this interval the resonant inductance L_r is approximately the sum of the primary and secondary leakage (as the magnetising inductance is considered much larger than the secondary leakage inductance) as seen in the equivalent of figure 5.10).

The resonant current is given by,

$$i_L(t) = I_{L_0} \cdot \cos(\omega_0 t - \omega_0 t_3) - \frac{V_{in} - V_{C_0}}{Z_0} \cdot \sin(\omega_0 t - \omega_0 t_3) \tag{5.6}$$

As it can be seen is figure 5.11(b), the voltage across the capacitor is offset by V_{in}. This means that it may never reach zero, if not enough initial current is available. The voltage across the capacitor for different initial current values appears in figure 5.11(b). The amount of initial current defines the time needed for the the capacitor voltage to become 0.

At the secondary, the current supplied by L_{out} freewheels through the two secondary sections and the diodes D_1, D_2 (see figure 5.5). As a result the secondary winding appears to be short-circuited and this is reflected in the equivalent network of figure 5.10.

Research on extending the ZVS operation down to low loading conditions has been conducted by several researchers [92–95].

5.2.1.5 The Current Reversing Interval ($t_4 < t < t_5$): Interval 5

Half of the switching cycle will be completed within the fifth interval. At time t_4 the switch T_{A-} turns on and the primary winding is set across the source with the opposite polarity. The current that was flowing through the primary now decreases following

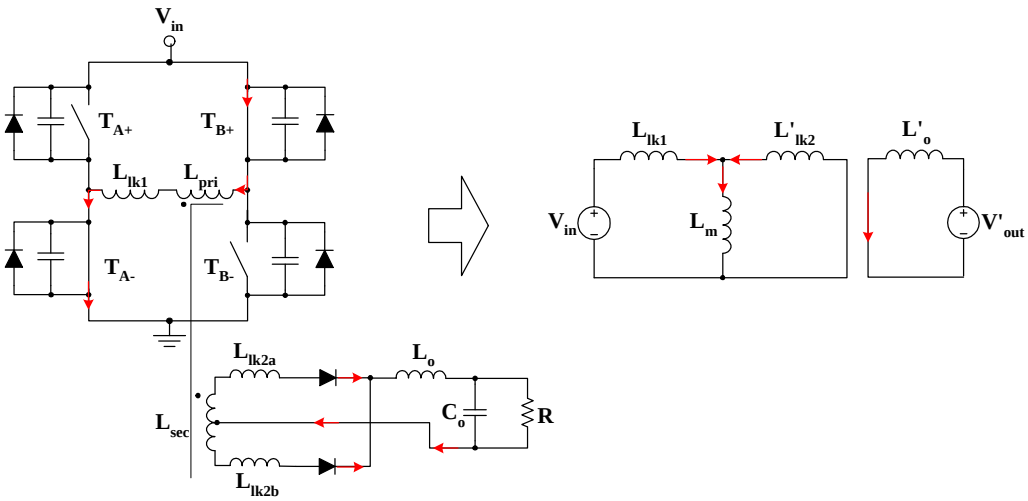

Figure 5.12: *Interval 5: the PSFB and its equivalent network during the current reversing state.*

a steep slope, because the secondary appears as a short-circuit to the primary side as seen in figure 5.12. The current reaches zero and then reverses and increases with the same rate (di/dt). The duration of this interval depends on the transformer parameters (leakage and magnetising inductances) and also on the output filter inductor value and the load. The interval ends at the moment when the reflected primary current exceeds the output inductor current. The slope of the increasing primary current depends on the primary and secondary leakage inductances,

$$i_{pri}(t) = \frac{V_{in}}{L_{lk1} + L_{lk2}} \cdot t \tag{5.7}$$

At the secondary side the current is still freewheeling though the two rectifying diodes D_1, D_2. As the increasing primary current is reflected to the secondary, the current in diode D_2 increases and the one through D_1 decreases. At the end of this interval the whole current flow has been redirected to D_2 and a new power transfer interval starts.

5.2.1.6 Second half of the switching cycle ($t_5 < t < t_{10}$): Intervals 6-10

An identical sequence of 5 time intervals follows for the rest of the switching period with reverse currents. The equivalent converter networks appear in figures B.1, B.2, B.3, B.4, B.5 of Appendix B for the respective time intervals.

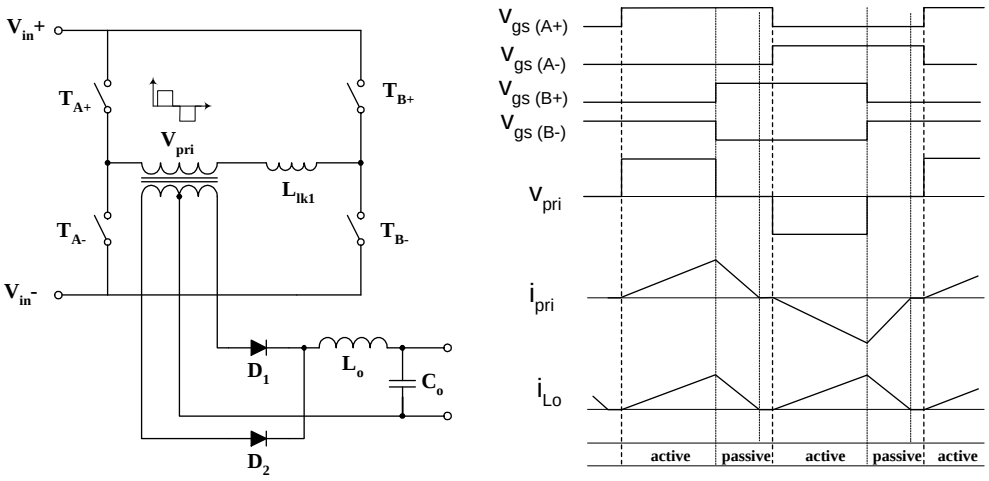

Figure 5.13: *Discontinuous mode of operation of the PSFB-FWR topology. Note the importance of the magnetising current magnitude for the passive-to-active transition.*

5.2.2 Discontinuous mode of operation

The discontinuous mode of operation in a full wave rectifier happens when the energy stored in the primary and filter inductors during the active interval is not enough to feed the load during the passive interval (figure 5.13). Hence, both primary and the output inductor currents become zero for a period of time.

This mode of operation is problematic as the passive-to-active resonant transition fails due to the lack of primary current. The current fall during the passive interval is,

$$\Delta i_{pri} = \frac{V_o \cdot D \cdot T_{sw}}{L_{lk1} + L_o} \tag{5.8}$$

5.2.3 Design

The drawback of the phase-shift modulation is the complexity of the driving circuit. This problem was solved with the release of several driving chips that simplified the design and manufacturing of the phase-shifted full bridge converter. The only driving-related parameters that the designer needs to specify are the switching frequency and the transition time. The resonant transition duration varies depending on the energy that is stored in the reactive components, and the designer should ensure the completion of the transition under any loading condition.

Assuming L_r and C_r are the resonant inductance and capacitance respectively, the resonant frequency is given by,

$$\omega_0 = \frac{1}{\sqrt{L_r \cdot C_r}} \tag{5.9}$$

The *first condition* for a successful resonant operation is to allow enough time for it. In the worst case a quarter of the switching cycle is needed as seen in figure 5.8,

$$t_{tr_{max}} = \frac{1}{4} \cdot \frac{2\pi}{\omega_0} = \frac{\pi}{2 \cdot \omega_0} \tag{5.10}$$

The resonant capacitance C_r is a combination of the MOSFET capacitances C_{oss} and the transformer capacitance C_{xfmr}. The total capacitance is,

$$C_r = 2 \cdot \frac{4}{3} \cdot C_{oss} + C_{xfmr} \tag{5.11}$$

where C_{oss} is multiplied by 4/3 [87] to account for the capacitance change with respect to the voltage. The capacitive energy at the beginning of the transition interval is,

$$E_{C_{A\rightarrow P}} = \frac{1}{2} \cdot C_r \cdot V_{in}^2 \tag{5.12}$$

The second condition for a successful resonant transition is related to the availability of inductive energy. The inductive energy $E_{L_{A\rightarrow P}}$ that is stored in the transformer leakage (or additional external) inductance when a current I_{pri} flows through it is given by,

$$E_{L_{A\rightarrow P}} = \frac{1}{2} \cdot L_{lk1} \cdot I_{pri}^2 \tag{5.13}$$

The following condition must hold,

$$E_{L_{A\rightarrow P}} \geq E_{C_{A\rightarrow P}} \tag{5.14}$$

Combining 5.9, 5.10 and 5.11 the required resonant inductance L_r is,

$$L_r = \frac{4 \cdot t_{tr_{max}}^2}{\pi^2 \cdot (8/3 \cdot C_{oss} + C_{xfmr})} \tag{5.15}$$

Note that this is the total primary side inductance and includes any parasitic inductances due to wires, connections, pcb tracks etc. Although increasing L_r extends the soft-switching capability of the converter, it also affects the maximum primary current slew rate di/dt which is given by,

$$\frac{di}{dt} = \frac{V_{in}}{L_r} \tag{5.16}$$

Equation 5.16 shows that as L_r increases, it takes more time for the primary current to reach its maximum value. As a result a higher duty cycle may be needed in order to allow enough time for the current to build up. Therefore, using a high series inductance to achieve soft-switching limits the maximum power transfer capability of the converter.

Another way of increasing the inductive energy is by connecting an inductor across the transformer primary, though this results in increased primary conduction losses. Depending on the priorities and the limitations the designer may decide on the best compromise.

The transformer secondary to primary turns ratio is,

$$n = \frac{2 \cdot V_o}{V_{in_{min}} \cdot D_{max}} \tag{5.17}$$

where V_o is the converter output voltage, $V_{in_{min}}$ the minimum input voltage and D_{max} the maximum duty cycle.

Regarding the specifications of the power switches and diodes, the decision is based primarily on the rms currents and voltages that can be estimated based on the converter waveforms.

The rms value of the primary current is approximated by

$$I_{pri} = \frac{P_o}{\alpha \cdot V_{in_{min}} \cdot D_{max}} \tag{5.18}$$

where α is the converter efficiency [96].

Paralleling more power switches may be an option at very high power applications. It is important to remember that an overrated MOSFET may result in lower conduction losses (due to lower $R_{ds_{on}}$), although the junction capacitance C_{oss} increases with the die size. It may be a reasonable choice to select different MOSFETs for the PA and AP legs. Since the available reactive power for the transition of the AP switches is generally more than that for the PA ones, the AP MOSFETs may be bigger to reduce the conduction losses without a significant penalty in the soft-switching operation.

The voltage rating of the MOSFETs should be within the limits of the input voltage range.

Regarding the secondary rectifiers, Schottky diodes are typically used in low output voltage applications for fast-switching with smaller reverse recovery effect. The secondary current and voltage waveforms set the peak and rms voltage and current requirements. Unlike the MOSFETs the Schottky diodes impose a fixed voltage drop across them regardless of the magnitude of the current. Therefore, paralleling more diodes would not reduce the conduction power losses and would only split them among the parallel semiconductors.

5.3 Phase-shifted full bridge with Current Doubler

The main problem of the PSFB with a full wave rectifier is the loss of soft-switching (especially at the passive-to-active leg) when operating with light loading. The PSFB with a current doubler (CD) at the secondary is used to mitigate or, in some cases, eliminate this problem.

The current doubler topology is derived from the full wave rectifier after a series of transformations [87] (illustrated in figure 5.14). The single filter inductor of the FWR topology (figure 5.14(a)) is replaced by two inductors in the CD, each of them carrying half of the load current. The operation of this topology is described in the following paragraphs in order to reveal the effects of the higher than usual magnetising current.

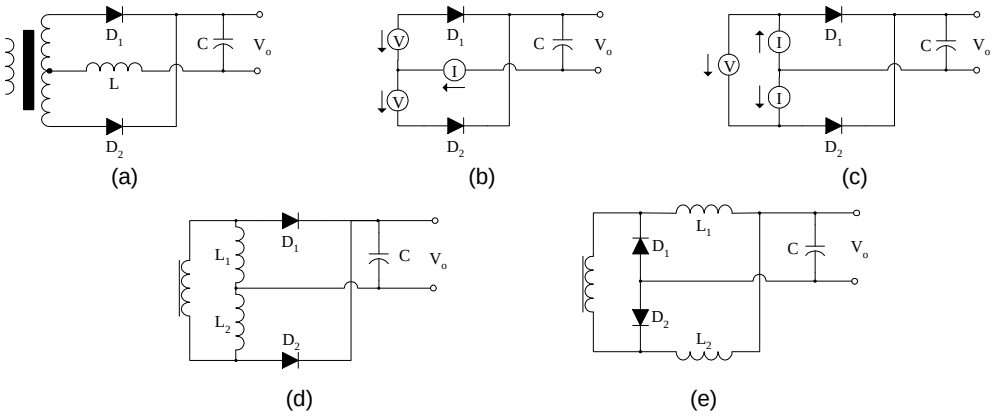

Figure 5.14: *The derivation of the current doubler topology from the full wave rectifier; (a) the full wave rectifier (b) the voltage and current sources in a FWR (c) voltage and current sources interchanged (d) the primitive current doubler circuit (e) the current doubler topology.*

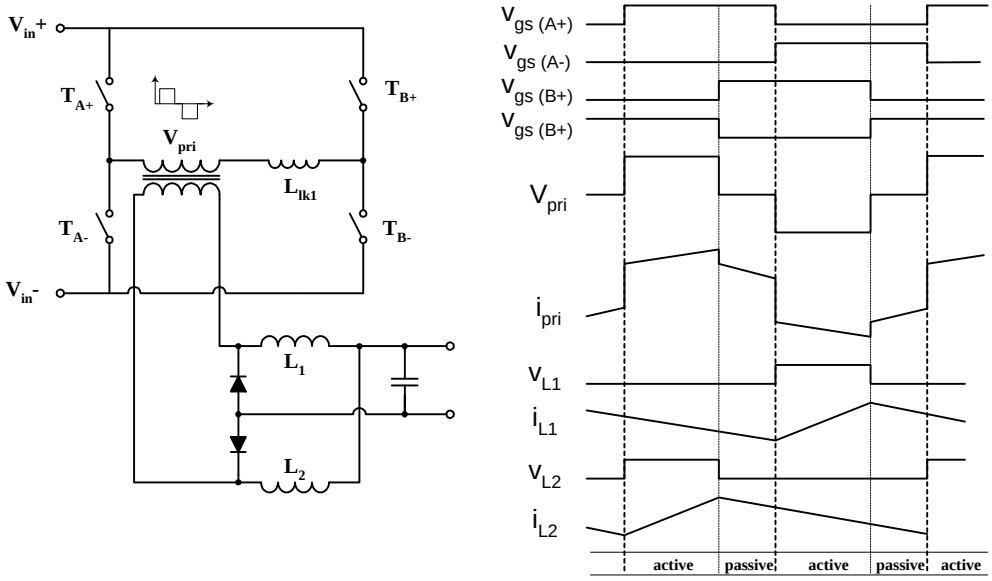

Figure 5.15: *The phase-shifted bridge with a current doubler and the main waveforms.*

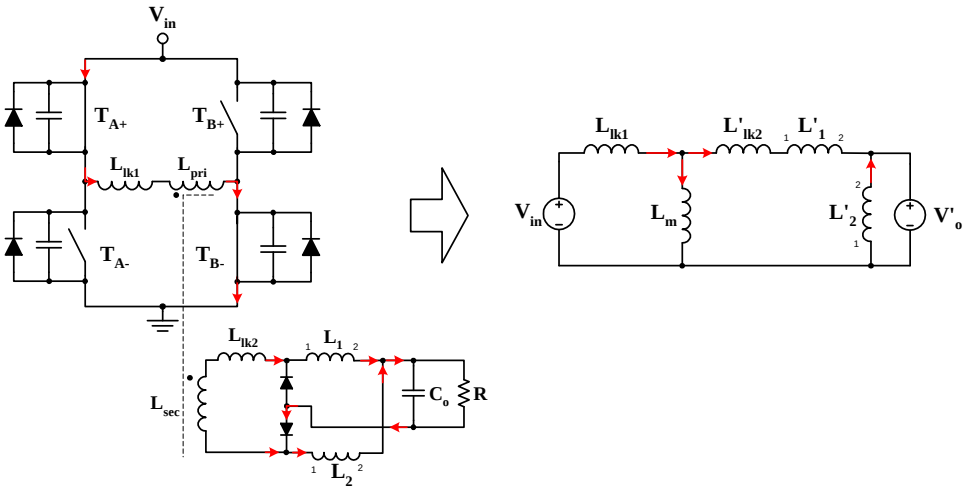

Figure 5.16: *Interval 1: the PSFB-CD and its equivalent network during the power transfer.*

5.3.1 Operation

The voltage and current waveforms of a PSFB with a current doubler appear in figure 5.15 and its operation is described analytically in the following paragraphs.

The main difference from the full wave rectifier is that the output inductor current never becomes discontinuous. This, in combination with the fact that the secondary current can flow in either direction (unlike in an FWR), has a positive effect especially in the passive to active transition process. The following analysis assumes a continuous current flow through the current doubler output inductors. The other modes of operation are briefly described in 5.3.1.4.

5.3.1.1 The active interval ($t_0 < t < t_1$): Interval 1

During the active or power transfer interval, energy is transferred from the primary to the secondary side of the circuit. As seen in figure 5.16 the diagonal switches T_{A+} and T_{B-} are ON. On the secondary side, inductor L_1 is storing magnetic energy as its current builds up. At the same time L_2, which stored energy in the previous active interval, is now supplying the load with an average current of $I_o/2$. The magnitude of the CD secondary winding current is half of the current in an FWR. However, due to having double the number of turns used in a CD arrangement the primary reflected current is the same.

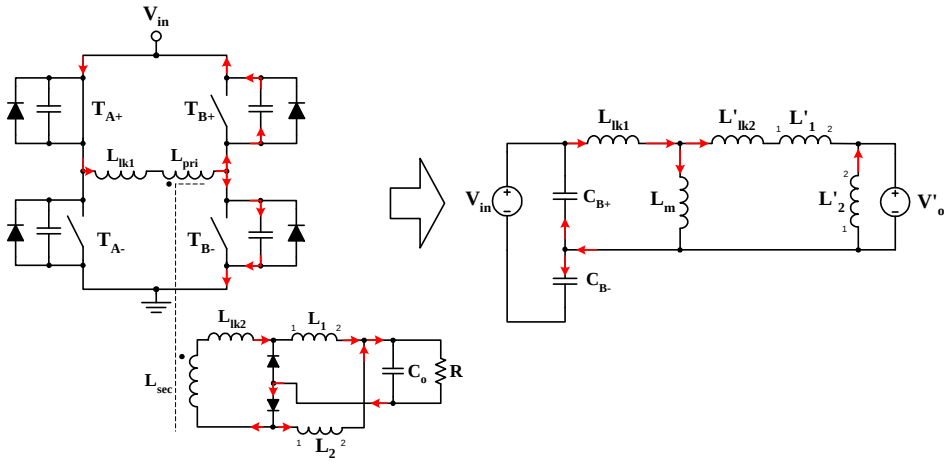

Figure 5.17: *Interval 2: the PSFB-CD and its equivalent network during the active to passive transition.*

5.3.1.2 The active to passive transition ($t_1 < t < t_2$): Interval 2

The AP interval starts once the active-to-passive leg switch T_{B-} is turned off. The primary current is now redirected to the MOSFET intrinsic capacitances C_{B+} and C_{B-}. The resonance between the MOSFET C_{oss} and the leakage inductance starts at this instant. The primary current comprises of two current components; a negligible magnetising component that will be ignored and the reflected load current whose value at the beginning of the resonant transition is,

$$\hat{I}_{L_1} = \frac{1}{2} \cdot \left(I_0 + \frac{V_o \cdot (1-D) \cdot T_{sw}}{L_1} \right) \tag{5.19}$$

The reflected load current takes its maximum value at the beginning of this interval. As a result the resonant transition will almost certainly be completed if enough time is allowed for this.

Assuming the condition in equation 5.20 holds true, the voltage across the resonant capacitor will become zero.

$$E_{L_{A\rightarrow P}} > E_{C_{A\rightarrow P}} \tag{5.20}$$

where,

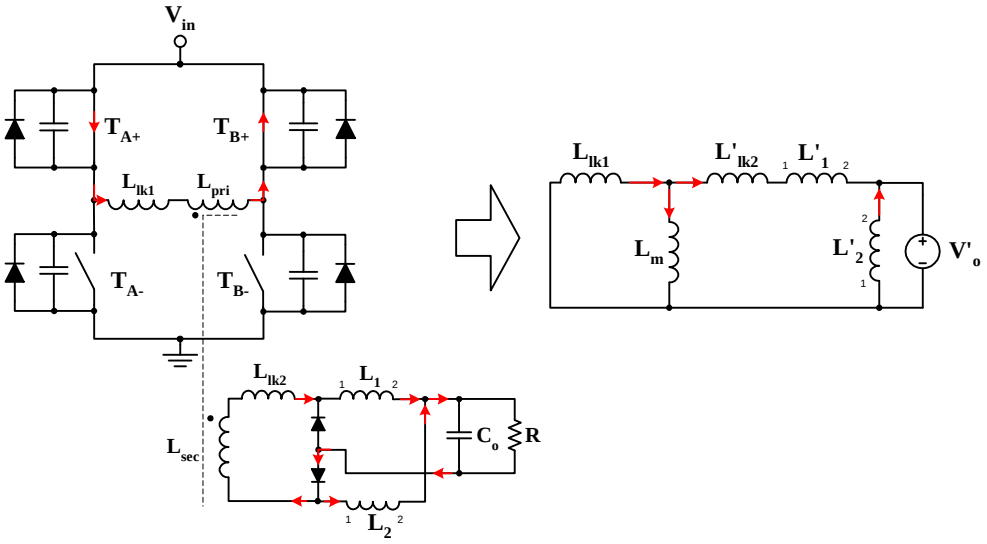

Figure 5.18: *Interval 3: the PSFB-CD and its equivalent network during the passive time.*

$$E_{L_{A\rightarrow P}} = \frac{1}{2} \cdot \frac{L_1}{n^2} \cdot (n \cdot \hat{I}_{L_1})^2 + \frac{1}{2} \cdot L_{lk} \cdot (n \cdot \hat{I}_{L_1})^2 \tag{5.21}$$

As the energy that is available for the resonant operation during this interval is usually well above the required value, the inductors that fuel the transition can be simulated as current sources. Based on this approximation, the delay time is calculated using,

$$t_{delay_{A\rightarrow P}} = \frac{2 \cdot C_r \cdot V_{in}}{N \cdot \hat{I}_{L_1}} \tag{5.22}$$

5.3.1.3 The passive interval ($t_2 < t < t_3$): Interval 3

When T_{B+} is turned ON a passive interval starts. The primary current flows through the circuit formed by T_{A+}, the primary winding and T_{B+}. As seen in the equivalent network, the current is supplied by the leakage (or external) and the output inductor. At the secondary side both inductors L_1 and L_2 are supplying the load, hence the current is decreasing.

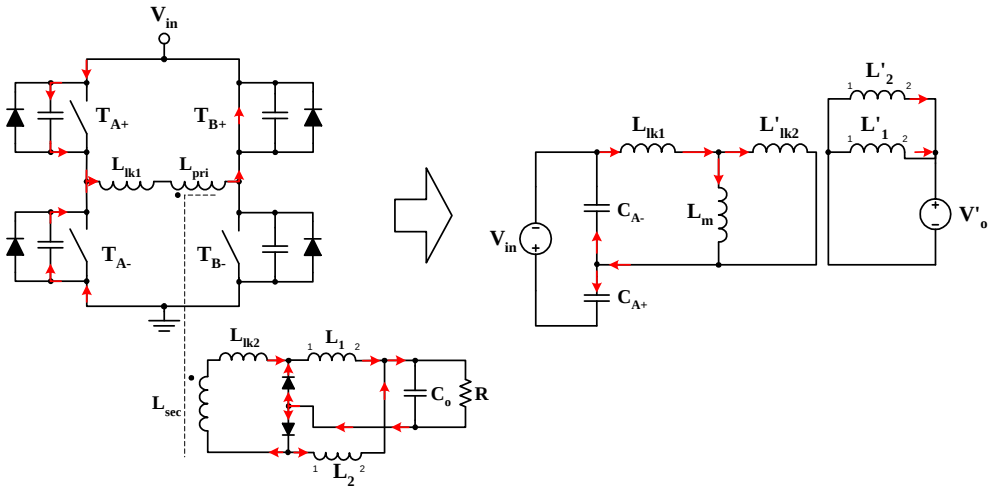

Figure 5.19: *Interval 4: the PSFB-CD and its equivalent network during the passive to active transition.*

5.3.1.4 The passive to active transition ($t_3 < t < t_4$): Interval 4

The PA interval is more complex as it depends on the output current as well as the leakage inductance of the transformer. Unlike in a full wave rectifier, the inductor current in the current doubler cannot become discontinuous. Depending on the loading condition, the inductor value and operating duty cycle, the inductor current may change direction.

Figure 5.20 illustrates the inductor current waveforms under different loading conditions.

In figure 5.20(a) the converter load is enough to keep the inductor current positive. The peak value of the current I_a is given by,

$$I_a = \frac{1}{2}\left(I_0 + \frac{V_{sec} - V_0}{L_1} \cdot D \cdot T_{sw}\right) \tag{5.23}$$

and its minimum value I_b by,

$$I_b = \frac{1}{2}\left[I_0 - \frac{V_0}{L_1} \cdot (1 - D) \cdot T_{sw}\right] \tag{5.24}$$

The current I_c through L_1 at the moment the second active interval starts is given by,

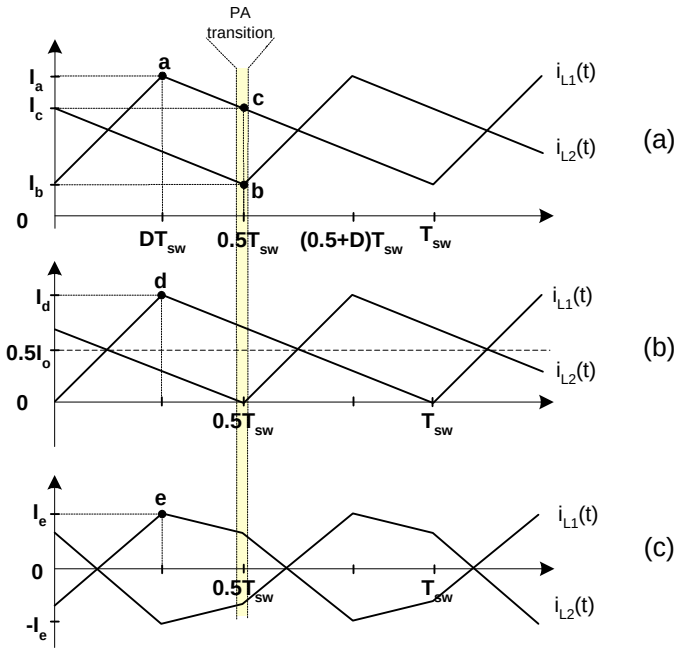

Figure 5.20: *The secondary inductors (L_1,L_2) current waveforms when the output load is (a) greater than R_{cr} (b) equal to R_{cr} and (c) smaller than R_{cr}*

$$I_c = \frac{1}{2}\left(I_0 + \frac{V_0}{L_1} \cdot D\right) \tag{5.25}$$

Figure 5.20(b) illustrates the currents at the boundary conditions before the current in the inductors goes negative. At these boundary conditions I_d is,

$$I_d = \frac{V_o}{L_2} \cdot (1 - D) \cdot T_{sw} \tag{5.26}$$

and also

$$I_d = I_o = \frac{V_o}{R} \tag{5.27}$$

and thereby the critical load R_{cr} (boundary condition) is derived,

$$R_{cr} = \frac{L_2}{(1 - D) \cdot T_{sw}} \tag{5.28}$$

Finally, the last case is when the inductor current reverses for a portion of the switching

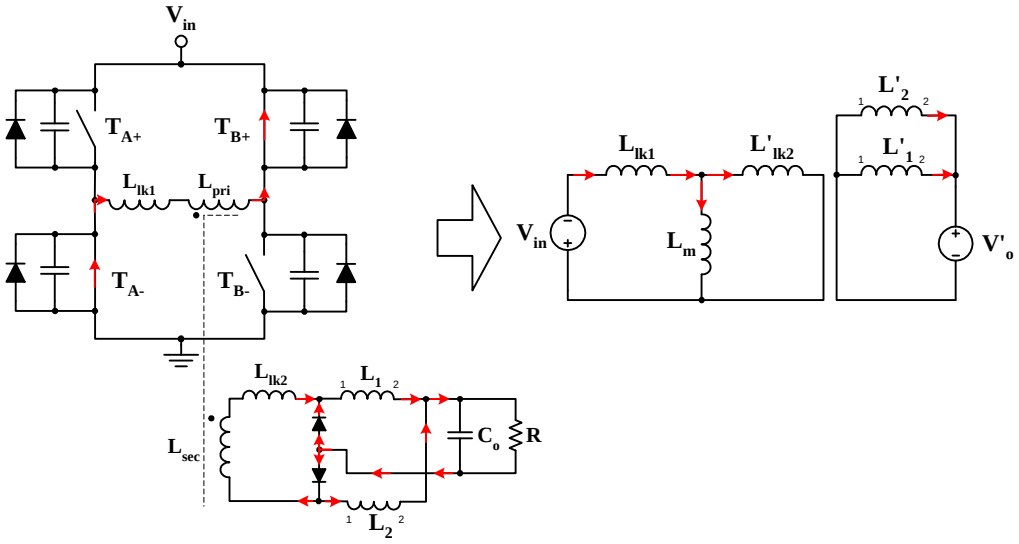

Figure 5.21: *Interval 5: the PSFB-CD and its equivalent network during the current reversing.*

cycle. The extreme case appears in figure 5.20(c), where the load current is practically zero (the inductors average (dc) current is zero) and the secondary "alternating" current circulates through the two inductors.

The passive to active transition takes place just before a PA switch turns on. In all cases appearing in figure 5.20 the output current contributes to the transition process.

5.3.1.5 The current reversing interval ($t_4 < t < t_5$): Interval 5

Finally, current reversal is forced when the switch T_{A-} is turned on and the transformer is placed across the dc input voltage source. The primary current first decreases to zero and then reverses and reaches a critical value, above which energy starts being transferred to the secondary (and a new active interval starts). At the secondary side the current is freewheeling through diodes D_1 and D_2. The inductors L_1 and L_2 are acting as current sources supplying the load with the required current. When the voltage across L_{sec} and the current through it increases enough to turn diode D_2 off (at time t_5), the new active interval starts.

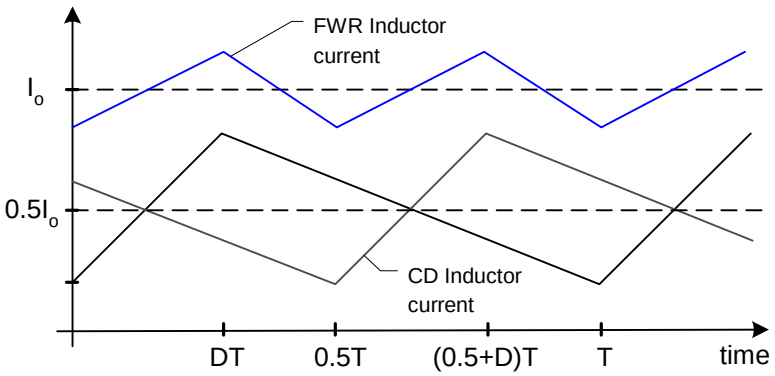

Figure 5.22: *Comparison of the FWR single inductor current and the CD inductors current.*

5.3.1.6 Second half of the switching cycle ($t_5 < t < t_{10}$): Interval 6-10

An identical sequence of 5 time intervals follows during the rest of the switching period with reverse currents.

5.3.2 Design

The PSFB with a current doubler requires two identical output inductors operating at half the switching frequency and the rated current (figure 5.22). To achieve the same output ripple that would be generated by a full wave rectifier circuit, the inductance of each output choke has to be doubled. Considering that the size of the inductors is proportional to the energy they can store, the total size of the two output inductors is the same as the single filter inductor of the full-wave rectifier circuit.

The transformer used in a current doubler has a single secondary winding with the same total number of turns as the centre-tapped winding in the full-wave rectifier. The author of [87] claims a losses reduction of up to 50% that is due to the reduced current flowing through the current doubler winding.

The current double active components may be Schottky diodes or MOSFETs that form a synchronous rectifier to further reduce the on-time conduction losses and the reverse recovery effect.

The selection of the output capacitor is based on the output ripple requirement, according to its equivalent series resistance (ESR) value.

5.4 Phase-shifted Full Bridge and Contact-less Transfer of Energy

The phase-shifted full bridge topology has an inherent ability to utilise the transformer parasitic components to perform zero voltage transitions of the main switches. This property makes it the ideal hosting-topology for a rotating transformer. In this way the reactive energy that is being stored in the magnetising and leakage inductances of the rotating transformer is being released twice in every switching cycle to assist with the reduction in switching losses.

Zero voltage switching is a valuable feature of the phase-shifted bridge. In a CTE application soft-switching becomes even more important due to the additional current (magnetising) component that circulates in the primary side. In a conventional converter ZVT is not vital at light loads as the current is low and the switching losses are insignificant. However, in a CTE application ZVT is particularly important due to the high switching losses incurred from the increased magnetising current even at no-load conditions.

The PSFB with CTE can be implemented with either a full-wave or a current doubler rectifier. The phase-shifted full bridge topology with a current doubler is often used in order to extend the soft-switching capability of the converter. The fact that the load current is reflected at the primary side during the resonant intervals makes this topology more popular than the full wave rectifier solution. In a phase-shifted full bridge with a rotating transformer the magnetising current that circulates in the primary winding also supports the resonant operation. Therefore the requirement for a current doubler needs to be reassessed.

5.4.1 Operation

The main differences between the phase-shifted full bridge with a rotating transformer and a conventional one originate from the reduced coupling coefficient of the rotating transformer. The existence of a high magnetising current affects the converter operation as can be seen in the following paragraphs.

Active intervals During the active or power transfer intervals the primary current is significantly increased due to the magnetising component. This in combination with the leakage inductance of the rotating transformer is expected to impose an increased voltage drop,

$$V_{lk1} = L_{lk1} \cdot \frac{n\hat{I}_{L1} + \hat{I}_m}{D \cdot T_{sw}} \tag{5.29}$$

where the magnetising current $\hat{I}_m$ is given by

$$\hat{I}_m = \frac{1}{2} \cdot \frac{V_{in} \cdot D \cdot T_{sw}}{L_m} \tag{5.30}$$

This voltage drop will reduce the transformer voltage gain. In a rotating transformer the leakage inductance can be minimised on purpose (as much as the windings separation permits) as the increased magnetising current secures enough energy storage for the switch transition. For a leakage inductance of about $7\mu H$ (typical in this application) and a magnetising current of 2.5A, a switching frequency of 100kHz and a duty ratio of 0.45 the voltage developed across the leakage inductance due to the magnetising current during the active interval is 2.2V which is only 0.7% of the primary applied voltage. A small increase in the duty cycle can compensate for the volt-seconds loss across the leakage inductance.

This is clearly a serious problem in low voltage/high current converters where the leakage inductance effect is considerably stronger.

Active to passive transition The active to passive interval is similar to the one of a conventional PSFB with the difference of the additional magnetising current. At the beginning of this resonant interval, the reflected load current $n \cdot I_{L_1}$ of a current doubler is given by equation 5.19 and the magnetising current by equation 5.30.

The inductive energy that is available in a current doubler is,

$$E_{L_{A\rightarrow P}} = \frac{1}{2} \cdot L_m \cdot \hat{I}_m^2 + \frac{1}{2} \cdot \frac{L_1}{n^2} \cdot (n \cdot \hat{I}_{L_1})^2 + \frac{1}{2} \cdot L_{lk} \cdot (\hat{I}_m + n \cdot \hat{I}_{L_1})^2 \tag{5.31}$$

The current that is available in a full wave rectifier is,

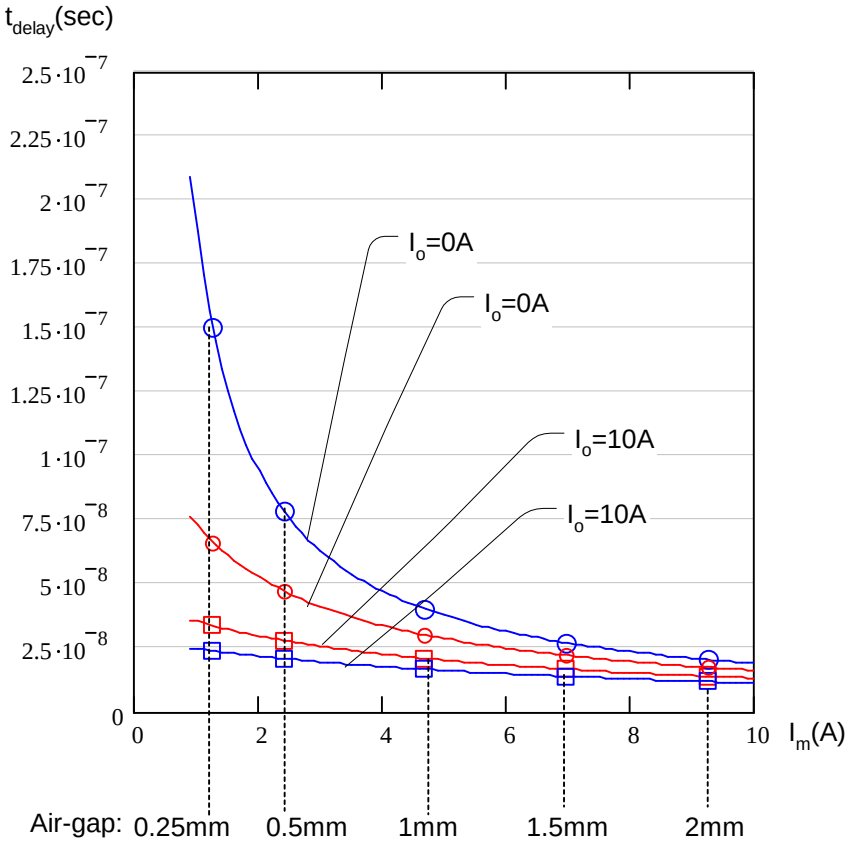

Figure 5.23: *The delay time that is required in a PSFB-CD (red line) and in a PSFB-FWR (blue line) for a complete transition of an AP switch with regard to the magnetising and load current. When the converter operates at no-load conditions the time needed for the transition with various air gap lengths is marked with circles. For a 10A output current the required times are marked with squares.*

$$\hat{I}_{L1} = I_0 + \frac{(V_{sec} - V_0) \cdot D \cdot T_{sw}}{2 \cdot L_1} \tag{5.32}$$

and the inductive energy is also given by equation 5.31. This energy is higher when a rotating transformer is used due to the magnetising current. Therefore the following equation (which assumes a linear current-time relationship) gives the required time for a complete voltage transition,

$$t_{delay_{A \to P}} = \frac{2 \cdot C_r \cdot V_{in}}{\hat{I}_m + n \cdot \hat{I}_{L_1}} \tag{5.33}$$

The difference is that (due to the magnetising current) the time to reach zero volts across

the resonant capacitance is considerably shorter. By evaluating the above equation (5.33) for different values of the magnetising current (figure 5.23) the advantage of shorter transitions becomes clear. The effect of the air-gap length to the transition time is also significant. It can be seen in figure 5.23 that the PSFB-CD is advantageous at no-load conditions due to the current flowing through the output inductors. However, at higher loading the transitions of the full wave rectifier circuit are shorter as the peak output current is higher and so is the energy stored in it.

Equations 5.1 and 5.4 are valid for the rotating transformer case with the initial current I_{L0} being the sum of the magnetising and reflected load current.

$$I_{L_0} = \hat{I}_m + n \cdot \hat{I}_{L_1} \tag{5.34}$$

Passive interval The passive interval of the PSFB with a rotating transformer maintains the current flow in the primary and secondary windings, with some energy being transferred from the primary to the secondary side (provided the secondary voltage is not yet shorted by the freewheeling diodes).

Passive to active transition The passive to active transition is also significantly assisted by the magnetising current of the transformer. Under circumstances, which will be analysed in Chapter 6, the magnetising current alone can fuel the L-C resonance.

This interval is governed by the equations presented in Sections 5.3.1.4 and 5.2.1.4. The only difference is that in a PSFB with a rotating transformer the magnetising current can be (depending on the air gap length and core size) the dominant current component that handles the resonant transition. It is important to mention here that the magnetising current is neither dependent on the converter load nor on the input voltage[1]. This allows the designer to reduce the so called *delay time* of the small resonant intervals, provide longer active intervals and hence increase the power rating of the converter.

A complete methodology for the transformer and PSFB joint design is presented in Chapter 6.

[1]This is valid if constant volt-seconds are applied across the primary winding. In other words if the duty ratio is adjusted according to the input voltage so that the product $D \cdot V_{in}$ is constant

5.5 Chapter Summary

The advantage of the phase modulation is that it allows the release of the reactive energy that is stored in the transformer leakage and magnetising inductance. This energy fuels a resonant operation between the participating MOSFET capacitances and the leakage inductance. Thus, the MOSFET inherent capacitance can be discharged before turning the switch ON. This zero voltage transition of the MOSFET results in a significant improvement of the converter's power efficiency.

Furthermore, securing the resonant transitions across the entire load range has a benefit in the stresses of the semiconductors as it generally incurs longer transition times for the voltages and currents (dv/dt and di/dt) as well as lower thermal variations. The resonant operation is known to reduce the harmonic content of the radiated electromagnetic waves and therefore reduces the emitted electromagnetic interference (EMI).

A rotating transformer can be considered as an integrated magnetic solution as it replaces the conventional transformer, the external energy storing inductor and the usual auxiliary circuit that has been traditionally used to extend the soft switching ability of the converter.

This chapter presented a novel analysis of the PSFB-FWR and PSFB-CD operation with emphasis on the magnetising current of the rotating transformer and its effect on the soft-switching operation of the semiconductors.

More analytically, in a PSFB with a rotating transformer a significant part of the primary current flows through the magnetising inductance. Similarly, when the current source is at the secondary side (e.g. the output inductors during the transition intervals), part of the secondary current will flow through the magnetising inductance and part of it will be reflected in the primary winding. It is, therefore, important to highlight that despite illustrating the magnetising inductance as property of the primary winding, it is actually shared between the windings. Hence each winding that couples energy to the other winding(s) is at the same time storing some energy in the magnetising inductance. This may be an indication that the current doubler, which returns energy to the primary winding, may actually aggravate the conduction losses.

This chapter looks at the classic PSFB converter and also at the PSFB with a rotating

transformer. Substituting a conventional transformer with a rotating one will modify the operation of the circuit mainly with regards to the transition intervals. More energy will be available during the resonant intervals and this is expected to improve the circuit performance and allow further increase in the switching frequency.

However, this highly available reactive energy results in a significant increase of the primary circulating current and this inevitably leads to higher winding losses and also higher MOSFET conduction losses. Among the objectives of the following chapter is to quantify these losses and investigate whether the reduction in switching losses can compensate the increment of the conduction losses.

Chapter 6
Design and Optimisation

The operation of a phase-shifted full bridge converter was analysed in Chapter 5. The main differences between a conventional PSFB topology and one with a rotating transformer were also stressed. The design of the converter can be optimised by concentrating on those parameters that affect its performance both in terms of efficiency and achieving the design specifications.

The high magnetising current has a series of implications in the overall operation of the power converter. The poor voltage gain, increased conduction losses and electromagnetic issues are only some of the parameters that have to be taken into account during designing.

In a conventional design the operating frequency is essentially limited by the switching losses of the power MOSFETs. In a CTE application the operating frequency is also limited by the transformer parasitics; leakage inductance and windings resistance that cause voltage drops and conduction losses. To account for these new constraints due to the rotating transformer a design methodology is proposed in this chapter; the optimisation of the design is performed using a mathematics software package.

6.1 Design Trade-offs

In the previous chapters it became clear that there are two ultimate implications arising from the physical separation of the primary and secondary parts of the transformer;

- *The high conduction losses*
- *The impaired voltage gain*

These two parameters are investigated in the following paragraphs. A method is presented for minimising the overall power losses and securing a voltage gain that complies

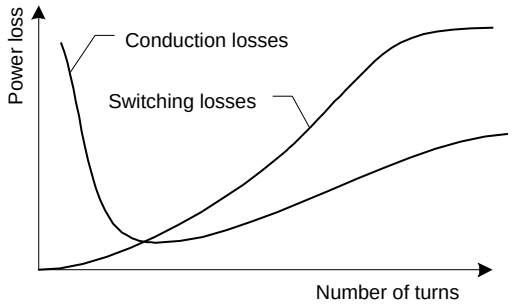

Figure 6.1: *A qualitative representation of the switching and winding conduction losses.*

with the design specifications. This method also re-distributes the heat dissipation between the primary semiconductors and the transformer to eliminate hot spots in the converter.

6.1.1 Conduction losses

The high transformer conduction losses are the result of two independent parameters;

Low magnetising inductance The low magnetising inductance is the result of the air-gap between the primary and secondary cores. The coupling between the two windings is poor and as a result a high (magnetising) current is needed to reposition the magnetic domains of the magnetic path. This current is independent of the transformer load and simply circulates in the primary winding.

High winding resistance The effective winding resistance is the result of more primary turns being used to reduce the magnetising current. Generally, more turns result in multi-layer windings and therefore the proximity effect and the AC resistance are greatly affected.

The MOSFET and transformer conduction losses are given by equation 6.1.

$$P_c = I_p^2(R_{p_{eff}} + R_{DS_{on}}) + I_{srms}^2 R_{s_{eff}} \tag{6.1}$$

where I_p is the primary winding rms current, $R_{p_{eff}}$ is the primary winding effective resistance, $R_{s_{eff}}$ is the secondary winding effective resistance and I_s is the secondary

winding rms current.

The primary current I_p consists of two components;

The reflected load current, depends on the transformer load only. This current is equal to the secondary load current I_s scaled by the turns ratio.

The magnetising current, I_m depends, as mentioned, on the magnetising inductance of the transformer and does not depend on the transformer load.

Secondly, the conduction losses of Eqn.6.1 are due to two resistive components;

The windings resistance that is due to the DC resistance and the high frequency effects taking place in a high frequency multi-layer transformer winding.

The MOSFET $R_{DS_{on}}$, which represents the resistance of the drain-source channel of the MOSFET switch when it is ON.

As a result, the conduction power losses developed on the rotating transformer and the MOSFET are a function of a number of parameters; frequency of operation, magnetic core size and material, air-gap, number of winding turns and winding layout.

As seen in Figure 6.1, the switching losses are very small for a small number of turns. This is because the magnetising inductance is low and consequently, the magnetising current is high securing the complete discharge of the MOSFET capacitance prior to the turn-on. The winding conduction losses are high for a small number of turns due to the high magnetising current flowing in the primary. Also, the conduction losses increase with the number of turns as the winding resistance increases. However, there is an area in Figure 6.1 where the conduction losses are minimum. By combining the switching and conduction losses a global minimum can be found for the total losses.

6.1.2 Voltage gain

The voltage gain of a rotating transformer is impaired due to the high leakage inductances and the effective resistance of the transformer windings. In a conventional transformer the leakage to magnetising inductance ratio is typically 1:500. The same

relationship in a rotating transformer is around 1:30. Thus at a high frequency of operation the voltage drop across the leakage inductance may be a significant portion of the total supplied voltage. This voltage drop increases as the magnetising and load currents increase.

6.2 Design Methodology

The proposed methodology consists of a series of criteria for producing a feasible design of a phase-shifted full bridge converter incorporating a rotating transformer. This novel design method leads to the selection of appropriate components, magnetic core, number of turns and conductor type, given the basic converter design specifications (input and output voltages, power level, frequency of operation, cooling method).

By evaluating the algorithm the designer can predict the power losses on the power switches and the rotating interface as well as, indirectly [1], the losses on the output rectifiers. All design equations and the optimisation algorithm run using a mathematical/engineering software (in this case MathCad).

The proposed design methodology appears in Figure 6.2. An overview of the six stage procedure is given below. It starts with the assumption that the primary side MOSFETs perform resonant transitions for the entire range of output load (in other words the switching losses are minimised). The major stages of the algorithm are:

1. *Set design specifications.* The input and output voltages (V_{in} and V_o), a tentative frequency of operation[2] and the power level of the converter and the type of cooling should be specified.

2. *Select converter topology and components.* During this stage the designer selects the rectifier type (full wave, current doubler). The calculation of the current and voltage levels is essential to select the components, transformer turns ratio etc

3. *Decide on the soft-switching range.* The resonant tank components are calculated at this stage. The target is a soft-switching operation under the entire range

[1] After running the algorithm, the rms currents flowing in the secondary side are also known and therefore the ON-time losses of the semiconductor materials can be calculated.

[2] In a radar application this frequency may be fixed or may be taking various discrete values in order to synchronise the power supply switching with the radar pulse repetition frequency.

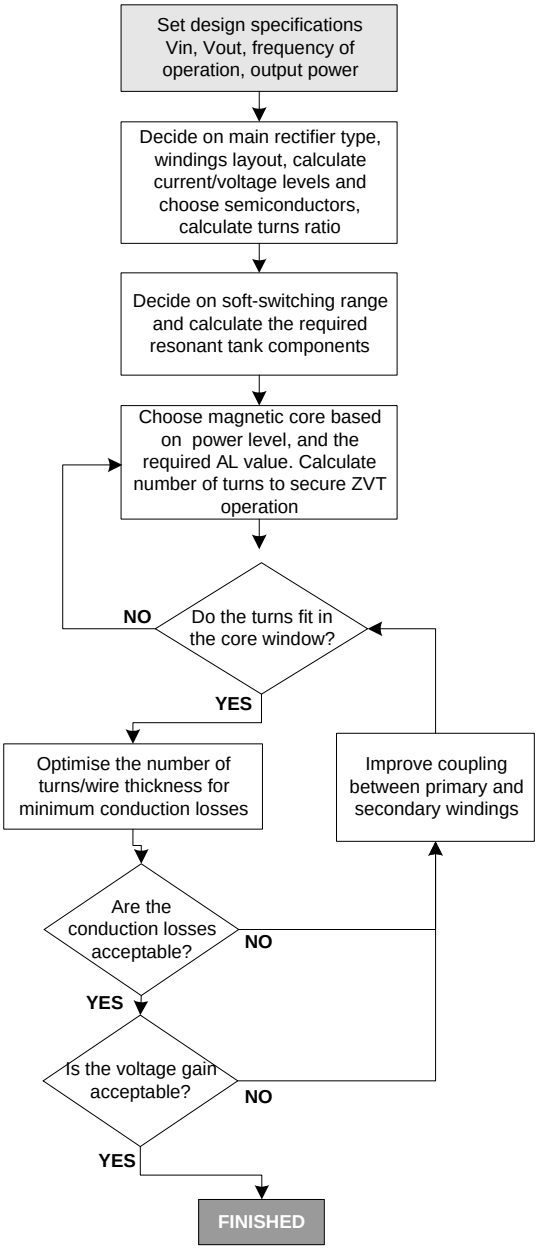

Figure 6.2: *A novel design and optimisation methodology for a power converter employing a rotating transformer.*

of loads. The energy needed to charge/discharge the MOSFET inherent capacitances must be calculated. The magnetising current flowing through the leakage inductance will provide the required energy to drive the resonant transition. The magnitude of the critical magnetising current $I_{m_{cr}}$ is calculated and this allows the calculation of the maximum number of turns and core size.

4. *Select core shape and size.* Due to its rotational symmetry, the appropriate shape for a rotating transformer application is the pot core. Regarding the size of the magnetic core, a tentative selection is made based on the flux density versus power losses graph of the selected material. The required cross sectional area is selected to keep the losses down and the required number of turns (to produce $I_{m_{cr}}$) is calculated. In a rotating transformer application the limitation is rarely the high flux density (or hysteresis losses). It is rather limited by the coupling requirements (the length of the air-gap and the number of winding turns). Once the core has been specified, the required number of primary turns N_p can be calculated for a known critical current.

5. *Winding optimisation.* The winding optimisation algorithm takes as an input the winding geometry and the rms values of the current waveforms. It calculates the optimum values for the number of turns and wire thickness in order to minimise the goal function, which is the overall conduction losses in the MOSFETs and the transformer windings. Other parameters, such as the switching frequency, winding layout and gap length may also be modified to obtain optimum results.

6. *Check the voltage gain.* After the transformer design process has been completed an AC analysis is performed to test the resulting voltage gain. If the duty cycle cannot compensate for a possible impairment of the voltage gain, the leakage inductance of the transformer or the windings effective resistance (or both) needs to be minimised. This will most likely require the use of fewer winding turns and possibly the increase of the magnetic core cross-sectional area.

A detailed analysis of each stage is presented in the following sections and a design example is given.

6.2.1 Converter specifications

To design the phase-shifted full bridge converter the main specifications must be set: the input and output voltages, the power level and the desired frequency of operation. The optimisation of the design could be performed for a range of frequencies, although this could restrict the power output of the resulting converter. The cooling method is also important because it defines the level of power that can be dissipated across the different components. The efficiency of the converter may also be part of the specifications. In an aerospace application efficiency is a key objective. Therefore any improvement in efficiency that involves reasonable costs is well-received.

The converter studied here is part of a radar power supply and its main specifications are presented in the table 6.1.

	Min.	**Nom.**	**Max.**
Input voltage (V_{in})	255V	330V	380V
Output Power (P_{out})	0W		1000W
Output voltage (V_o)		54V± 2%	
Switching frequency (F_{sw})		100kHz	
Efficiency		$\geq$ 90%	
Cooling		Natural Convection	

Table 6.1: *Converter Specifications*

Furthermore, the maximum duty cycle (that corresponds to the lowest input voltage) is defined: $D_{max} = 0.48$. The voltage drop across the rectifier diodes and wires is assumed to be a fixed 2.0V.

The desired turns ratio is given for a minimum input voltage and a maximum duty cycle,

$$n = \frac{N_p}{N_s} = \frac{V_{in}D}{V_o} \tag{6.2}$$

which gives: $n = (250 \times 0.48 - 2)/54 = 2.18$

The duty ratio D_{norm} for the normal input voltage is around 0.35.

6.2.2 Selection of active components

The topology analysed in this work is a phase-shifted full bridge converter. There are several modifications of the basic phase-shifted bridge and each of them improves different aspects of the converter. Two fundamental circuits are studied in this work; the full wave rectifier and the current doubler.

The full wave rectifier is a common rectifier that uses a centre-tapped secondary winding and two diodes operating in a complementary way (see Section 5.2.1). On the other hand, the current doubler is intended for higher power levels because it extends the soft-switching range of the primary-side semiconductors and also reduces the secondary winding conduction losses.

The selection of the primary switches is based on the current/voltage requirements of the design. In a rotating transformer application a low MOSFET $R_{DS_{on}}$ is required to reduce the conduction losses generated by the high primary circulating current. The designer comes across an additional trade off that of deciding on the $R_{DS_{on}}$ and C_{oss} values of the MOSFET; $R_{DS_{on}}$ decreases and C_{oss} increases as the semiconductor die size increases. Therefore the engineer should compromise with a big enough MOSFET to keep conduction losses low but at the same size secure the complete discharge of C_{oss} to secure zero voltage transitions.

The primary current [96] is approximately,

$$I_{pri} = \frac{P_o}{\alpha \cdot V_{in} \cdot D_{norm}} \tag{6.3}$$

where α is the converter efficiency. The IRFP450LC (500V, 14A, $R_{ds_{on}} = 0.4\Omega$) MOSFET was selected.

Regarding the rectifying diodes, they must feature short reverse-recovery times and small capacitive effects to reduce the resonance with the possibly higher leakage inductance of the secondary windings. The forward current of each diode is equal to half of the average load current ($P_o/2V_o = 1000/2 \cdot 54 = 9.25A$) and the maximum reverse voltage is equal to the voltage across the secondary. At the prototyping stage somewhat bigger diodes (BYW99P-200 fast recovery diode) were selected to account for unexpected current variations.

6.2.3 Selection of magnetic core

In a normal power supply with a conventional isolating transformer the magnetic core size and ultimately the transformer size is dictated by losses. The core losses limit can be set in absolute terms (watts) or in terms of temperature rise [67]. A temperature rise of 20-40 degrees is usually acceptable. Consequently, the appropriate core size is the minimum size that can handle the required amount of power by satisfying the losses requirement.

When designing a magnetic interface such as the rotating transformer for the phase-shifted full bridge converter the design priority is essentially different; the core type and size are selected based on the magnetic coupling they can provide rather than the power rating. Naturally, to achieve acceptable coupling between the windings, the magnetic core is bigger than it would be in an un-gapped design. As a result core losses prove to be an insignificant percentage of the total losses (this is shown Chapter 7).

For a rotating transformer application a pot-shaped core must be used. This type of core has a rotational symmetry that keeps the electrical behaviour of the transformer fixed for any angle of rotation.

Regarding the core size, the selection process starts with the assumption that the magnetic core is fully utilised by the power converter. That means that the flux excursion should be as high as possible while at the same time keeping the core losses at a reasonable level. Faraday's law states:

$$V = N \cdot \frac{d\phi}{dt} \tag{6.4}$$

where V is the winding voltage, N the number of turns and ϕ the magnetic flux. Combined with,

$$\phi = B \cdot A_e \tag{6.5}$$

and,

$$\Delta t = D \cdot T \tag{6.6}$$

where Δt is the ON time of the power switches. Combining the above equations,

$$V = A_e \cdot \frac{N_p \cdot \Delta B}{dt} \qquad or \qquad A_e = \frac{V \cdot D \cdot T}{N_p \cdot \Delta B} \tag{6.7}$$

ΔB being the flux density change during ΔT and A_e the magnetic path's cross-section.

In Equation 6.7, V and $D \cdot T$ are part of the converter specifications. For a specific magnetic material there is a maximum permissible ΔB obtained from the power loss curves of the material for a specific frequency of operation. By pulling the voltage V, duty cycle D, period T and flux density excursion ΔB values into equation 6.7 a relationship between A_e and N_p may be obtained. A reasonable cross sectional area is required as this is directly related to the size and weight of the magnetic core. At the same time the number of primary turns must be carefully calculated in order to control the conduction losses.

As A_e increases the number of required turns decrease; however, as shown below the number of turns is tuned to account for both switching and conduction losses.

The tentative selection of pot core size is done by evaluating equation 6.7 for different core sizes of the Ferroxcube pot core collection.

For the specified amount of power it is reasonable to start with a medium-sized P42/29, which has a $265mm^2$ cross-section. For a 3C91 material (best suited for a 100kHz operating frequency) a ΔB of 0.2T will result in about 0.9watt of power loss and 26 turns will be needed. For a ΔB of 0.3T, 17 turns would be needed and the power loss would be 3watt. Finally, 13 turns would yield ΔB=0.4T and the core would dissipate around 7watt. The next step is to check whether 13 turns fit in the core window. The rms primary current and the required wire gauge is calculated. The magnetising inductance is calculated for a 1mm air gap:

$$L_m = \frac{N_p^2}{\left(\frac{l_g}{\mu_0 \mu_{r_{air}} A_g}\right)} \tag{6.8}$$

and,

$$L_m = \frac{13^2 \times 4 \times \pi \times 10^{-7} \times 265 \times 10^{-6}}{1 \times 10^{-3}} = 56.3\mu H$$

The magnetising current will be

$$\hat{I_m} = \frac{V \cdot D \cdot T}{2 \cdot L_m} \tag{6.9}$$

and,

$$\hat{I_m} = \frac{330 \times 0.42 \times 10^{-5}}{2 \times 56.3 \times 10^{-6}} = 12.31A$$

Assuming a current density of $1.55 \cdot 10^6 A/m^2$ the required wire diameter is 1.6mm. At 100kHz the penetration depth is 0.2mm. Therefore, the effective conductive area of the wire would be much smaller and thinner wires should be used to make sure the entire conducting area is used. It is clear that 13 turns of a multi-strand (possibly 0.4mm) wire do not fit in the 20.3x18mm core window area (taking into account the 1mm clearance between the rotating and stationary windings and also the bobbin volume). With similar calculations the P66/56 ferroxcube is selected as the starting core for this design. The optimal number of turns and wire thickness for this core is calculated in the following steps.

6.2.4 Securing the soft-switching operation

In this stage of the procedure the resonant circuit parameters are calculated in order to secure the soft-switching operation.

The phase-shifted bridge is known for its ability to maintain the soft-switching of the primary side semiconductors. This reduces the power losses and allows the designer to choose a higher operating frequency. The resonant elements are, as seen in previous chapters, the MOSFET inherent channel capacitance, the capacitance appearing across the transformer primary winding and the series (leakage or external) inductance.

In a PSFB with a rotating transformer the magnetising current plays a key role in assisting the resonant operation. Because of the additional current component, the soft-switching can be maintained for a wider range of loading.

As seen in Chapter 5 the total capacitance C_r of the resonant tank is:

$$C_r = \frac{8}{3} \cdot C_{oss} + C_{xfmr} \tag{6.10}$$

where C_{oss} is the MOSFET channel capacitance at the specific voltage of operation, and C_{xfmr} is the primary winding capacitance.

$$C_r = 2 \cdot \frac{4}{3} \times 100 \times 10^{-12} + 18.4 \times 10^{-12} = 285pF$$

The $C_{oss} = 100pF$ is an estimate from the C_{oss} vs V_{DS} graph of the IRFP450LC MOSFET. The energy needed to charge/discharge this combined capacitance is given by:

$$E = \frac{1}{2} \cdot C_r \cdot {V_{in_{max}}}^2 \tag{6.11}$$

and its actual value in the current design is:

$$E = \frac{1}{2} \times 285 \times 10^{-12} \times 380^2 = 20.58\mu J$$

and hence the required current through the resonating inductance is:

$$\hat{I}_{m_{cr}} = \sqrt{\frac{2 \cdot E}{L_{lk_1}}} \tag{6.12}$$

$$\hat{I}_{m_{cr}} = 2.422A$$

The worst case scenario for the soft-switching operation would be for the minimum load current (i.e. zero). The assumption here is that the duty cycle compensates for any input voltage variation so, that the volt-seconds applied to the primary winding is always the same (i.e. the magnetising current is constant). The magnetising inductance $L_{m_{cr}}$ needed to secure $\hat{I}_{m_{cr}}$ is,

$$L_{m_{cr}} = V_{in} \cdot \frac{T_{sw} \cdot D_{norm}}{2 \cdot I_{m_{cr}}} \tag{6.13}$$

$$L_{m_{cr}} = 330 \times \frac{10^{-5} \times 0.42}{2 \cdot 2.422} = 286\mu H$$

Using $L_{m_{cr}}$ the maximum number of primary turns $N_{pri_{max}}$ can be calculated. If more turns are used then soft-switching operation may cease, depending on the loading conditions.

$$N_{pri_{max}} = \sqrt{L_{m_{cr}} \cdot (\frac{l_{core}}{A_c \cdot \mu_0 \cdot \mu_{r_c}} + \frac{l_g}{A_g \cdot \mu_0 \cdot \mu_{r_g}})} \tag{6.14}$$

For the selected core type and an air gap of 1mm, $N_{pri_{max}}$ is,

$$N_{pri_{max}} = 25$$

Reducing the number of turns,

- extends the soft-switching range of the converter
- reduces the effective R_{eff} resistance of the windings
- reduces the windings' leakage inductance

but,

- increases the primary (and secondary) circulating current.

The optimum N_{pri} and accordingly the N_{sec} should be found in order to eliminate the losses and also minimise the stored energy in the leakage inductance. Energy storage in the leakage inductance implies a voltage drop across it and hence the voltage gain of the transformer is reduced.

6.2.5 Calculation of winding and semiconductor conduction losses

The conduction losses of the power switches and those of the primary and secondary windings can be minimised using the following optimisation process. Initially, the losses on the switches and the primary and secondary windings are calculated. Accordingly, some design parameters are adjusted to reduce the total amount of losses and also distribute them evenly across the components to eliminate hot spots.

Generally the conduction losses are given by equation 6.15

$$P = I^2 \cdot R \tag{6.15}$$

where I is the rms current and R is the electrical resistance. In a high frequency design, the effective resistance of the windings depends on the current waveform. Hence, the secondary (and consequently the primary losses) depend on the converter topology that is being used.

In a rotating transformer the primary current consists of two components; the reflected load current and the magnetising current. These can be estimated by using an interval-by-interval approach, such as the one in Chapter 5. The magnetising current $\hat{I}_m$ is independent of the load current and the type of the rectifier. As seen in equation 6.13, it only depends on the input voltage, the frequency of operation and the magnetising inductance value. Its peak value is given by:

$$\hat{I}_m = \frac{V_{in} \cdot D \cdot T_{sw}}{2 \cdot L_m} \tag{6.16}$$

The primary voltage and the magnetising current waveform of the bridge converter appear in figure 6.3.

The magnetising inductance depends on the number of winding turns; the inductance value vs number of turns in a P66/56 pot core is shown in figure 6.4.

As the number of turns changes two parameters vary; the winding geometry (wire thickness, number of strands, number of layers) and the magnetising current waveform. These parameters affect the windings' effective resistance. By varying the wire thickness and number of winding turns optimum operating conditions can be obtained.

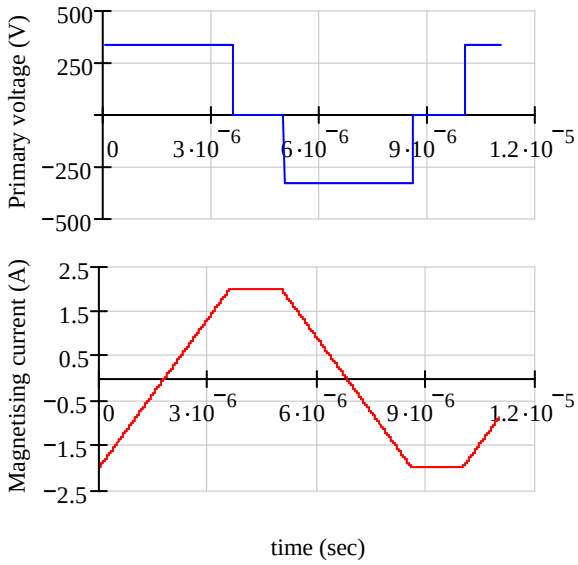

Figure 6.3: *The primary voltage and magnetising current. The current is independent of the converter loading.*

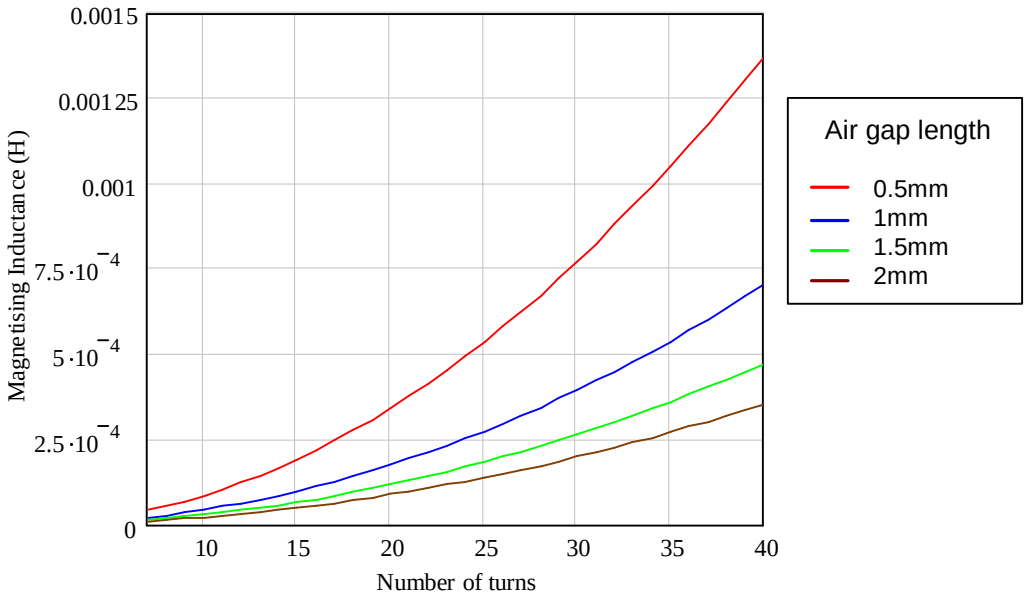

Figure 6.4: *The magnetising inductance with respect to the number of primary turns for different air gap lengths.*

6.2.5.1 Wire thickness, strands and winding structure

The first step is to approximate the winding layout. The following parameters are passed to the algorithm; the core window/coil former width and diameter B_w and D_{bob}, number of turns N, maximum current I_{pri}, current density J_{max} and the frequency of operation f_{sw}. First the penetration depth δ_0 is calculated,

$$\delta_0 = \sqrt{\frac{2}{\omega_0 \cdot \mu_0 \cdot \sigma}} \tag{6.17}$$

where ω_0 is the fundamental cyclic frequency of the current waveform, μ_0 is the magnetic permeability of air ($4 \times \pi \times 10^{-7} \frac{H}{m}$) and σ is the electrical conductivity of the conductor material (for copper this is $5.882 \times 10^7 \frac{S}{m}$). For a 100kHz fundamental frequency the penetration depth is around 0.2mm, therefore the useful area of any wire of diameter greater than 0.4mm is only 0.2mm from the surface of the conductor towards the centre. The effective copper area of a conductor of diameter D_c is,

$$A_{wire} = \pi \cdot \left[\left(\frac{D_c}{2} \right)^2 - \left(\frac{D_c}{2} - \delta_0 \right)^2 \right] \tag{6.18}$$

Knowing the effective conductor area, the number of strands needed to carry the total current can be calculated. The maximum current density (J_{max}) should be around $1.55 \times 10^6 A/m^2$ to keep the wires running at about $25C$ (in fact this can be increased, as the acceptable temperature range is to up 60^oC and because forced cooling is used in this design).

$$Strands(N, D_c) = \frac{I_{pri}(N)}{\beta \cdot J_{max} \cdot A_{wire}(D_c)} \tag{6.19}$$

where β is a factor to adjust J_{max} depending on the allowed temperature range and type of cooling.

The next stage is to investigate the structure of the winding: namely, the number of turns that fit in each layer, and the number of layers with respect to the number of the winding turns N, the strands, and the wire thickness D_c. The number of turns that fit into each winding layer in a bobbin of width B_w and diameter D_{bob} is given by,

$$N_{one_{layer}}(N, D_c) = \frac{B_w}{r \cdot D_c \cdot \sqrt{Strands(N, D_c)}} \tag{6.20}$$

where r is the inter-turns spacing factor, a factor that depends on the wire insulation thickness and space between the conductors. The number of full layers can be calculated by truncating the decimal numbers of $Layers_{full}$,

$$Layers_{full}(N, D_c) = \frac{N}{N_{one_{layer}}(N, D_c)} \tag{6.21}$$

and the last layer will possess $N_{last_{layer}}(N, D_c)$ turns, where,

$$N_{last_{layer}}(N, D_c) = N - Layers_{full}(N, D_c) \cdot N_{one_{layer}}(N, D_c) \tag{6.22}$$

The thickness of each layer is approximated by,

$$D_{layer} = \sqrt{Strands(N, D_c)} \cdot D_c \tag{6.23}$$

6.2.5.2 DC resistance

The mean length of each turn MLT with respect to the number of turns N and the wire thickness D_c can be calculated using,

$$MLT(N, D_c) = \begin{cases} \frac{\pi}{N} \cdot (D_{bob} + 0.5 \cdot D_{layer}) & if N \leq N_{one_{layer}}(N, D_c) \\ \frac{1}{N}\Big[\sum_{j=1}^{Layers_{full}(N,D_c)} \big(\pi \cdot (D_{bob} + \\ +(j - 0.5) \cdot D_{layer}(N, D_c)\big) \cdot N_{one_{layer}}(N, D_c)) + \\ N_{last_{layer}}(N, D_c) \cdot \pi \cdot [D_{bob} + \\ (Layers_{full}(N, D_c) + 0.5) \cdot D_{layer}(N, D_c)]\Big] & if N \geq N_{one_{layer}} \end{cases}$$

The length of the wire used for this winding can be calculated by,

$$l_{win}(N, D_c) = MLT(N, D_c) \cdot N \tag{6.24}$$

The DC resistance is given by,

$$R_{dc}(N, D_c) = \rho \cdot \frac{N \cdot MLT(N, D_c)}{Strands(N, D_c) \cdot \pi \cdot \left(\frac{D_c}{2}\right)^2} \tag{6.25}$$

6.2.5.3 AC resistance

The number of the winding layers is given by,

$$p(N, D_c) = Layers_{full}(N, D_c) + \frac{N_{last_{layer}}(N, D_c)}{N_{one_{layer}}(N, D_c)} \tag{6.26}$$

and

$$\Psi(N, D_c) = \frac{5 \cdot p(N, D_c)^2 - 1}{15} \tag{6.27}$$

The thickness of one layer of the winding is,

$$d(N, D_c) = \frac{Foil_{area}(N, D_c)}{B_w} \tag{6.28}$$

and

$$\Delta(N, D_c) = \frac{d(N, D_c)}{\delta_0} \tag{6.29}$$

The next step towards the calculation of R_{eff} is the computation of the rms value of the winding current I and the rms value of its derivative I'.

Regarding the reflected load current, this is of the same form as the secondary current and depends on the rectifier circuit. In this work, two topological variations are considered; the full wave rectifier (FWR) and the current doubler (CD). Their effect in the overall losses is examined.

In terms of the transformer structure both the FWR and the CD have the same number of primary turns and, essentially, the same number of secondary turns. The fact that

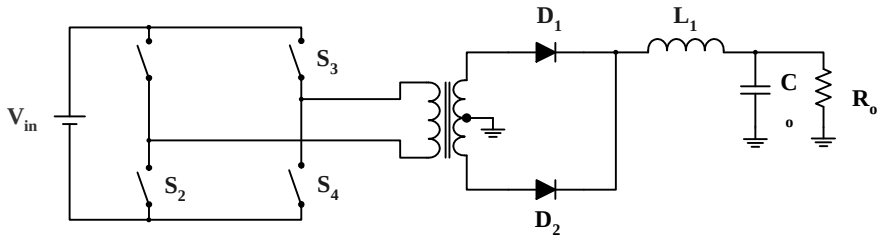

Figure 6.5: *The phase-shifted full bridge with a full wave rectifier.*

the current waveforms are different (and have different rms values for the same output load) means that their impact on the conduction losses is different. A comparison of the losses of the full wave rectifier and current doubler is presented in Chapter 7.

Full Wave Rectifier The operation of the phase-shifted full bridge with a full wave rectifier (PSFB-FWR) of figure 6.5 is explained in Chapter 5. It uses a centre-tapped secondary winding. Each of the secondary winding sections conducts at a different time interval. The rms value of the current is the same in both winding sections due to the symmetry.

During the power transfer interval, the current builds up through the filter inductor which acts as a current source during the passive (or freewheeling) intervals. The current waveform for 700watts of output power appears in figure 6.6(a). The secondary current that is reflected to the primary winding appears in figure 6.6(b). This is the combination of the currents in the upper and lower section of the centre-tapped winding. Furthermore, the total primary current appears in figure 6.7.

The rms value of the primary and secondary currents can be calculated using engineering software such as Mathcad©. The results appear in figure 6.8.

Current doubler The current doubler (CD) is generally considered as a better solution for high power and low voltage applications, as it reduces the magnitude of the current in the transformer windings while ensuring soft-switching at low load. Featuring two large inductors used as current sources, the current flowing to the load is twice the current in the secondary winding (figure 6.9).

The secondary winding current of this topology and its reflected primary current for a

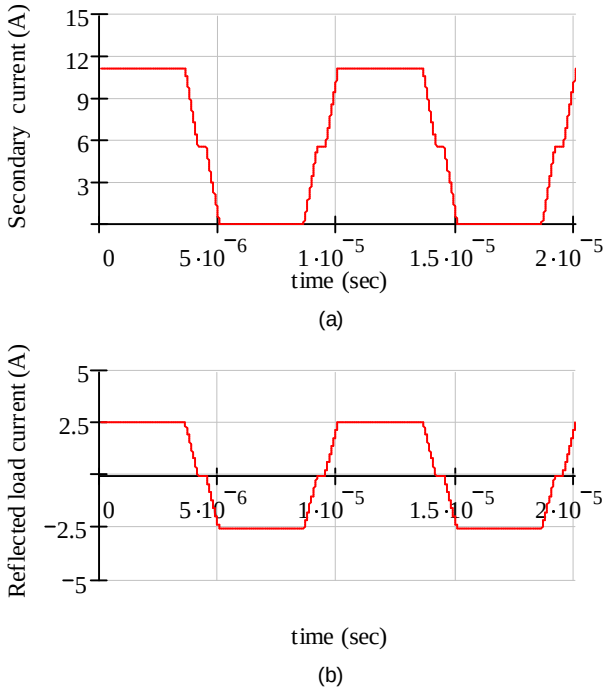

Figure 6.6: *The (a) secondary (inductor) current and (b) primary winding reflected load current in the phase shifted bridge with full wave rectifier.*

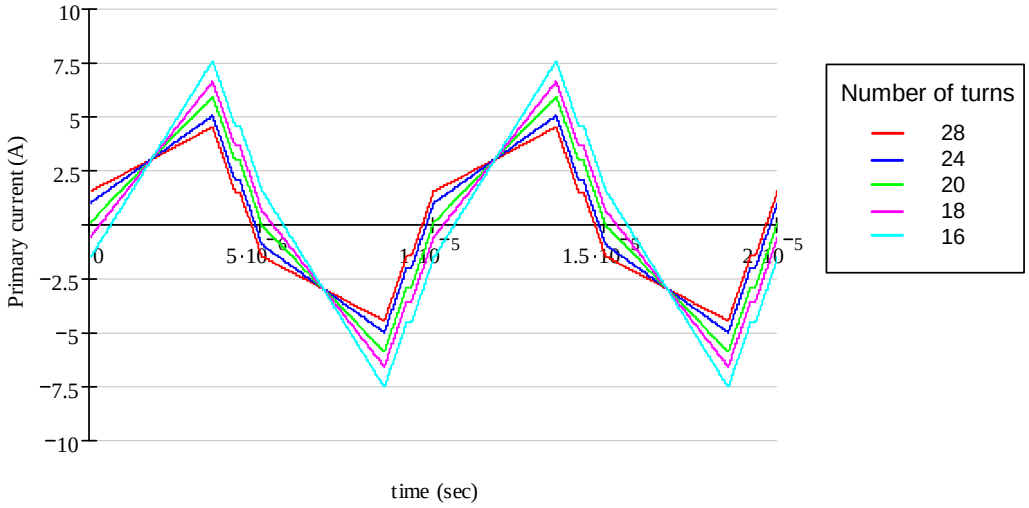

Figure 6.7: *The effect of the magnetising current variations to the primary (magnetising and load) current waveform in a PSFB-FWR. Different colours correspond to different numbers of primary turns as indicated in the legend.*

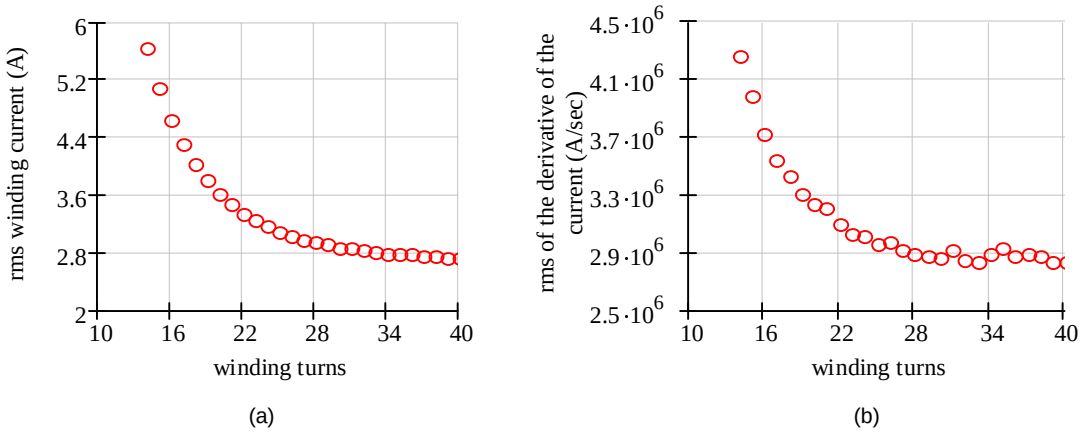

Figure 6.8: *The rms value of the primary current and of the derivative of the primary current with respect to the number of winding turns in a PSFB-FWR.*

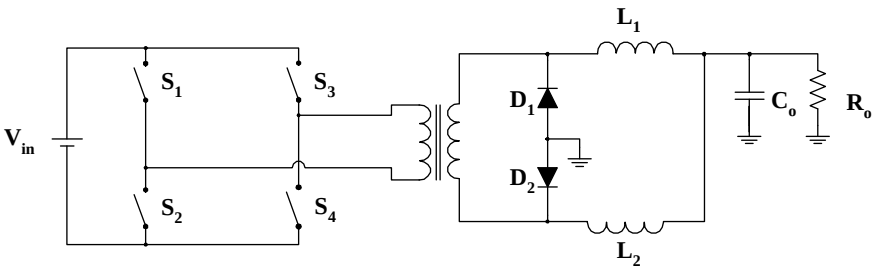

Figure 6.9: *The phase-shifted full bridge with a current doubler.*

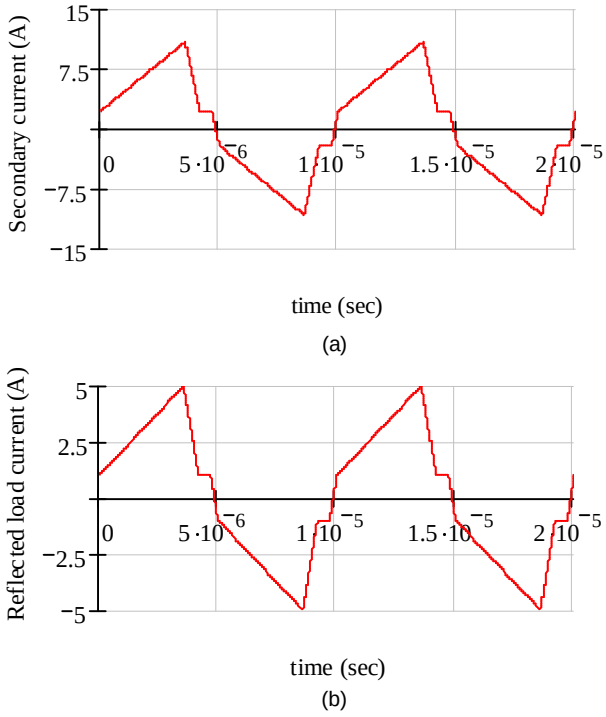

Figure 6.10: *The (a) secondary winding current and (b) primary reflected load current waveforms in a PSFB-CD.*

700watts output power appear in figure 6.10(a) and (b) respectively. Furthermore, the total primary current appears in figure 6.11.

The rms values of the primary current and the derivative of the primary winding current can be calculated using MATHCAD. The results for the example current doubler appear in figures 6.12 (a) and (b).

Once the rms values of the current and of the derivative of the current are obtained, the effective resistance of the windings can be calculated by applying equation 6.30 (established by Hurley et al. in [75]) that is described in Chapter 3.

$$R_{eff}(N, D_c) = R_{dc}(N, D_c) + \frac{\Psi(N, D_c)}{3}\Delta(N, D_c)^4 R_{dc}(N, D_c)\left[\frac{I'_{rms}}{\omega I_{rms}}\right]^2 \qquad (6.30)$$

where R_{eff} is the effective resistance of the respective winding.

Figure 6.13 illustrates the effective resistance of the primary winding as a function of the number of turns and wire thickness. Figure 6.13(a) refers to the converter with an

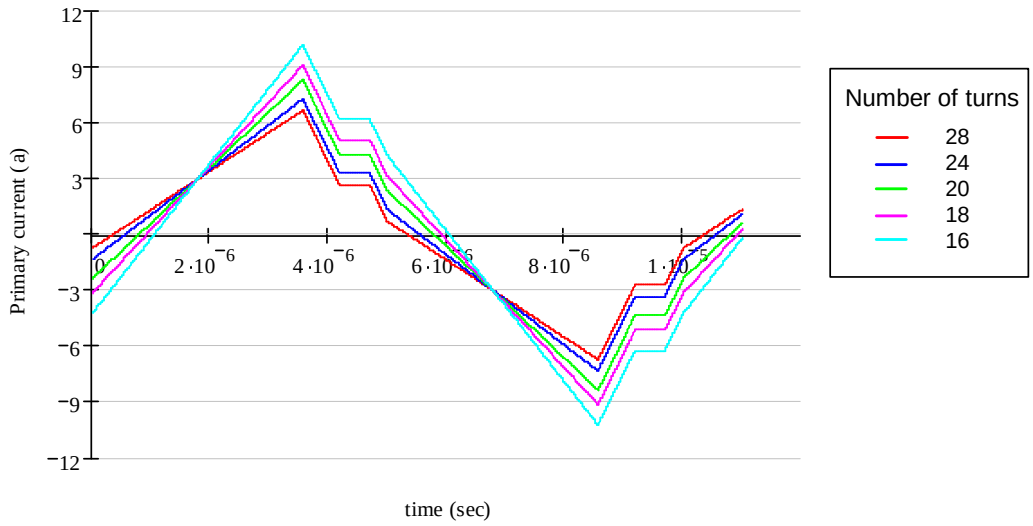

Figure 6.11: *The effect of the magnetising current variations to the primary (magnetising and load) current waveform of a PSFB with a current doubler. Different colours correspond to different numbers of primary turns as indicated in the legend.*

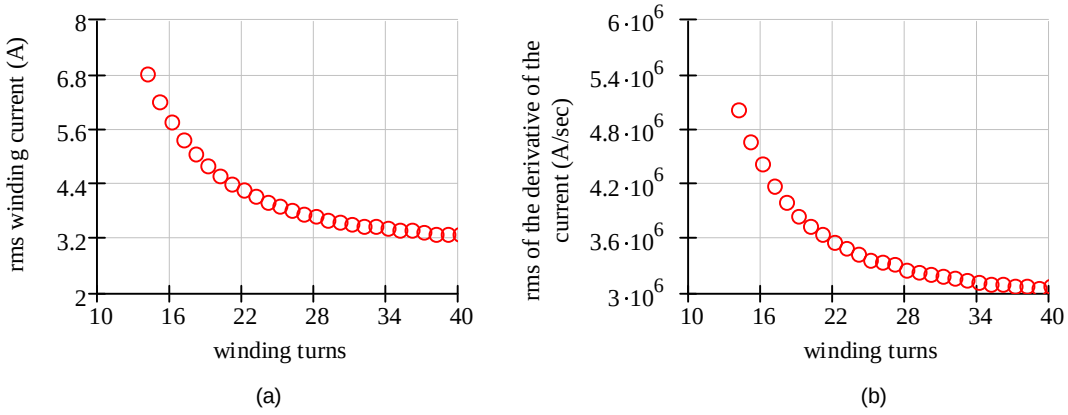

Figure 6.12: *The rms value of (a) the primary current and (b) the derivative of the primary current with respect to the number of the winding turns in a PSFB-CD.*

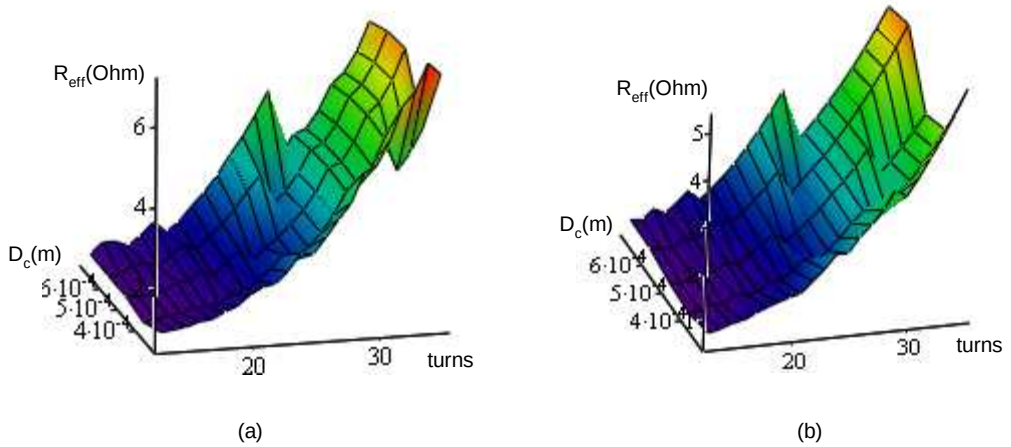

Figure 6.13: *The effective resistance of the primary winding of a (a) full wave rectifier and (b) current doubler.*

FWR in the secondary and 6.13(b) to a CD topology.

According to Hurley, the accuracy of the formula is very good for any current waveform for windings of two or more layers and its accuracy for smaller numbers of layers depends on the wave-shape. In this case the method predicts the effective resistance with high accuracy for the type of waveforms appearing in a phase-shifted full bridge power supply.

Hurley's equation for the effective resistance of a winding is expected to be even more accurate for the adjacent windings arrangement, as more winding layers would be needed (due to the smaller bobbin width).

The total conduction losses in the transformer windings and the MOSFETs are given by,

$$P_{loss} = I_{pri}(N)^2 \cdot R_{eff}(N, D_c) + 2 \cdot I_{sec}^2 \cdot R_{s_{eff}}(N, D_c) + 2 \cdot I_{pri}(N)^2 \cdot R_{ds_{on}} \qquad (6.31)$$

The optimum number of primary (and consequently secondary) turns as well as the wire thickness can be extracted from the 3D graph representing the above function. This graph appears in figure 6.14 for the PSFB with a current doubler and in figure 6.15 for the PSFB with a full wave rectifier.

In this design example the optimum wire thickness is 0.4mm (27SWG) gauge as was

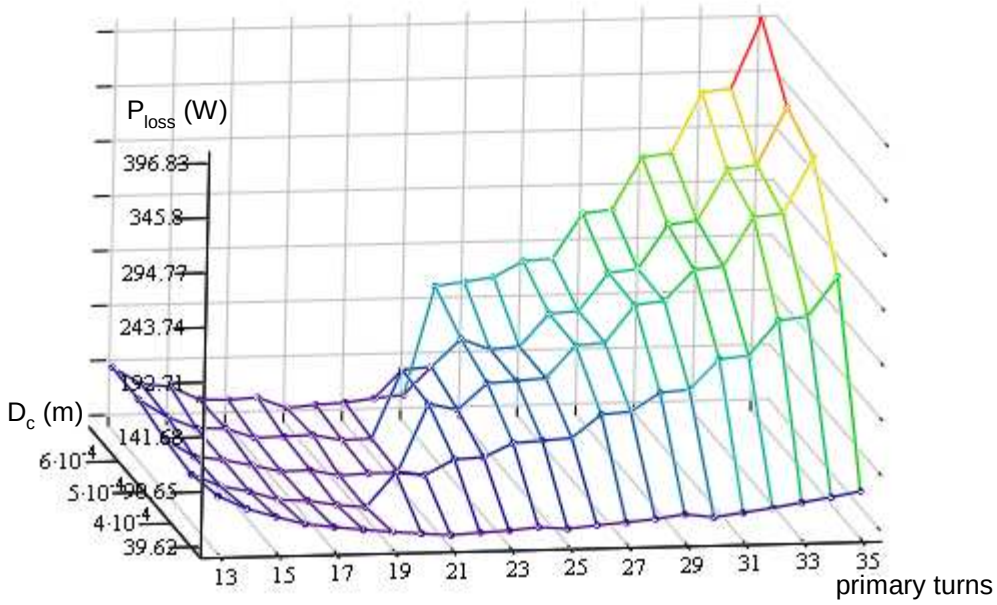

Figure 6.14: *Illustrates the conduction power loss P_{loss} of a PSFB with a full wave rectifier with respect to the primary number of turns and the wire thickness D_c.*

expected from the initial calculations of the penetration depth. The number of primary turns is slightly different, though in both cases it is around 19 turns as it can be seen from figures 6.14 and 6.15. A compromise had to be made at this point, as 19 turns in the primary would require 9 turns in the secondary, which do not fit in the limited volume between the two bobbins, if a 4+5 split winding arrangement is used to avoid the eddy current generation from the fringing field. Using 17 turns was considered a possible solution that would require around 8 turns (4+4) in the secondary with a penalty of 4W (at a 700W output) or 0.5% reduction of the efficiency). However, the efficiency reduction caused by the eddy currents induced in the secondary due to the fringing field proved to be greater. With this arrangement, the maximum power loss in both components (transformer and MOSFETs) is expected to be around 31W in the FWR topology and 47W in the CD. In terms of performance this indicates that the CD topology will dissipate around 6.7% of the total handled power on the MOSFETs and the transformer. The FWR will perform better with only 4.2% of power wasted in the MOSFETs and transformer wire. The breakdown of the losses as calculated by the algorithm for $N = 17$ and $D_c = 0.4mm$ appears in table 6.2.

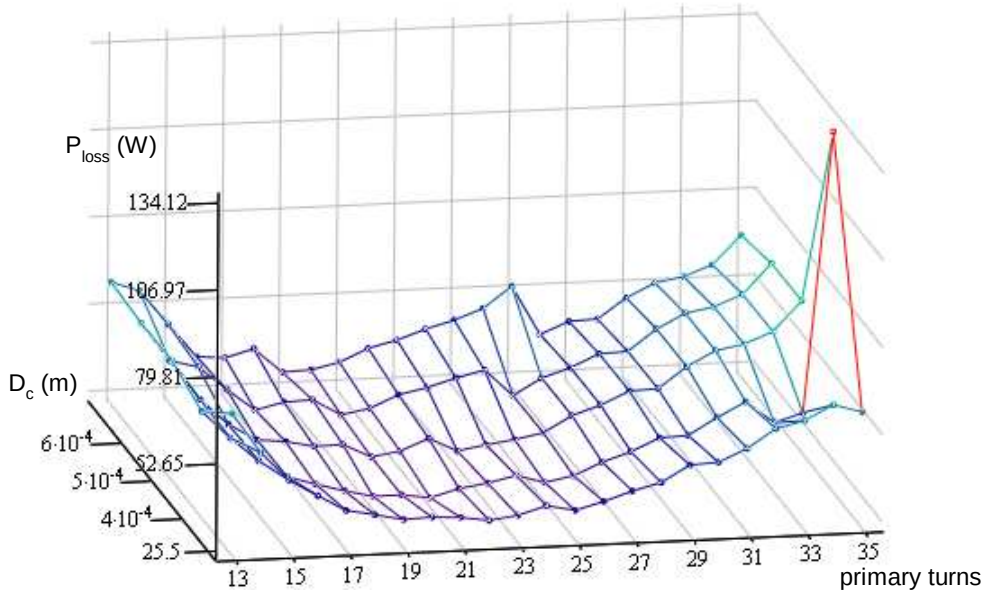

Figure 6.15: *Illustrates the conduction power loss P_{loss} of a PSFB with a full wave rectifier with respect to the primary number of turns and the wire thickness D_c.*

	FWR	CD
Primary winding loss (W)	16.1	22
Secondary winding loss (W)	0.5	1.9
MOSFET conduction loss (W)	14.7	23.1
TOTAL (W)	31	47

Table 6.2: *The power loss breakdown in a PSFB-CD*

6.2.6 Calculation of the voltage gain

The last step of the design and optimisation process is to check the voltage gain of the resulting transformer. This can be done using the transformer model that is presented in Chapter 4. The worst case scenario for the voltage gain appears at maximum loading of the transformer. The model parameters can be calculated using the transformer geometry or can be predicted using finite elements analysis for better accuracy. The calculated effective resistance of the windings can be incorporated into the model.

In an actual design the transformer is connected to a rectifier-filter-load configuration that has a non-linear behaviour due to the active components (e.g. diodes, synchronous rectifiers). According to [97] the assumption is fairly accurate for resonant converters when the voltage across the rectifier and the current through it are in phase and the load can be assumed to be ohmic,

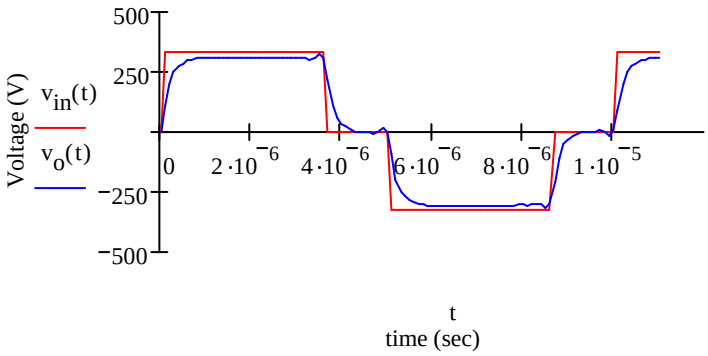

Figure 6.16: *The input and output waveforms of the rotating transformer of a PSFB-FWR topology (note that the secondary voltage is scaled by the turns ratio for comparison purposes).*

$$R_{o_{eff}} = R_o \cdot \frac{8}{\pi^2} \tag{6.32}$$

where $R_{o_{eff}}$ is the effective ohmic load that represents the rectifier and real load R_o.

In the proposed converter the waveforms are typical switching waveforms and therefore equation 6.32 is not totally accurate. The secondary current depends on the commutation of the diodes as well as the impedance of the filter. This is a complex problem that requires more investigation and it is proposed for future work. In these experiments equation 6.32 was used to emulate the non-linear load. The simulated and measured voltage gain values were found to be in relatively good agreement for the purposes of this work (assessment and comparison of different networks).

Full wave rectifier The voltage gain of the full wave rectifier is assessed using the transformer differential equations that are presented in Appendix B. The input and output voltage waveforms appear in figure 6.16

The input and output rms voltages are 240V and 219.5V respectively, which means that the average voltage is attenuated by 8.6%.

Current doubler The input and output voltage waveforms appear in figure 6.17. The rms input and output voltages are 240V and 217V. The voltage attenuation due to the leakage inductance is 9.3%.

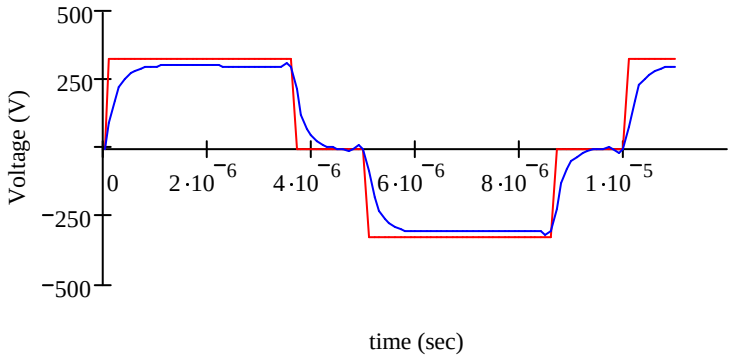

Figure 6.17: *The input and output waveforms of the rotating transformer of a PSFB-CD topology (note that the secondary voltage is scaled by the turns ratio for comparison purposes).*

It appears that both circuits satisfy the voltage gain requirement, as the available duty ratio can compensate for the voltage drop across the leakage inductance and winding resistances.

6.2.7 Design Summary

The resulting design details of the PSFB with a full wave rectifier appear in table 6.4.

6.3 Chapter Summary

In this Chapter, a novel methodology has been proposed for designing and optimising a power converter with a rotating transformer. The above methodology combines several design parameters in a set of equations. The number of the winding layers, the width of them, the number of turns and the wire thickness, the frequency of operation and the waveform shapes are some of the variables that the designer can adjust. By varying the frequency of operation another set of curves can be obtained and the optimum frequency of operation for a specific wire thickness and winding structure calculated. Similarly, as the harmonic content of the waveform directly affects the conduction losses the shape of the current waveform is important as well.

The power transfer capability of a rotating transformer is upper bounded by the con-

Component	Type	Characteristic	Value
Main switch	IRF450LC		
		Drain-to-source breakdown volt. V_{DSS}	500V
		Continuous drain current I_D	14A
		Drain-to-source on-resist. $R_{DS_{on}}$	0.4Ω
Rectifier	BYW99PI		
		rms forward current $I_{F_{rms}}$	35A
		Repetitive peak reverse voltage R_{RRM}	200V
		Junction capacitance	12pF
Transformer			
		Magnetic core	P66/56
		Core manufacturer	Ferroxcube
		Core material	3E1
		Core effective area	$717mm^2$
		Core effective length	$123mm^2$
		Primary winding turns N_1	17
		Primary winding wire	14x27SWG
		Secondary winding turns N_2	8
		Secondary winding wire	30x27SWG
		Windings arrangement	coaxial
		Air-gap length	1mm
		Expected magnetic flux density	111mT
Filter inductor			
		Core type	Toroid
		Inductance L_o	$2 \times 40\mu H$
Filter capacitor			
		Capacitance	$660\mu F$
		Equivalent series resistance ESR	0.3Ω

Table 6.3: *The optimised phase-shifted full bridge with a current doubler and a coaxial rotating transformer.*

Component	Type	Characteristic	Value
Main switch	IRF450LC		
		Drain-to-source breakdown volt. V_{DSS}	500V
		Continuous drain current I_D	14A
		Drain-to-source on-resist. $R_{DS_{on}}$	0.4Ω
Rectifier	BYW99PI		
		rms forward current $I_{F_{rms}}$	35A
		Repetitive peak reverse voltage R_{RRM}	200V
		Junction capacitance	12pF
Transformer			
		Magnetic core	P66/56
		Core manufacturer	Ferroxcube
		Core material	3E1
		Core effective area	$717mm^2$
		Core effective length	$123mm^2$
		Primary winding turns N_1	17
		Primary winding wire	14x27SWG
		Secondary winding turns N_2	2x4(coax)
		Secondary winding wire	25x27SWG
		Windings arrangement	coaxial
		Air-gap length	1mm
		Expected magnetic flux density	111mT
Filter inductor			
		Core type	Toroid
		Inductance L_o	$40\mu H$

Table 6.4: *The optimised coaxial transformer and output inductor characteristics for a PSFB with a full wave rectifier.*

duction losses. The trade-off is, as in most designs, between size, weight, cost and performance. The resulting transformer employs a bigger core (Ferroxcube P66/56) than would be used in a conventional 1kW converter. The reason is that a greater core window area is required to fit the extra copper that carries the magnetising current. The consequence is a not so good utilisation of the magnetic material (the maximum flux density is only 111mT). The low flux excursion in combination with the existence of the air-gap makes the magnetic core composition less critical for the converter operation and hence a reduction in cost may be achieved by selecting an economic material.

The rotating transformer behaves both as a transformer and as an inductor avoiding the use of an external inductor (in series with the transformer). With the extra magnetising current it secures the soft-switching of the MOSFETs for the whole range of loads and this partially compensates for the additional conduction losses that occur.

By applying the proposed optimisation algorithm the power losses are evenly distributed between the power switches and the rotating transformer. This reduces the hot spots of the converter and improves the reliability of the components themselves.

Chapter 7

Experimental Verification and Discussion

Chapter 6 introduced a design methodology that helps to incorporate a rotating transformer into a phase-shifted full bridge converter with minimum penalty on the conduction power losses. The methodology has been evaluated for different cases, such as the two topological variations (FWR and CD) as well as for two different transformer arrangements (adjacent and coaxial).

The experimental findings that are presented in this Chapter verify the design methodology predictions for some specific design examples. In these examples the independent variables are the number of the winding turns and the wire thickness. There are other variables, such as the frequency of operation, winding and core dimensions and the number of wire strands, that can be varied to obtain a global optimum. This requires the implementation of the optimisation algorithm in a software package with advanced optimisation solvers and is proposed for future work.

In this Chapter, the experimental set-up (equipment, operating conditions) is described. The evaluation starts with the experiments involving an optimised adjacent winding arrangement. The coaxial winding arrangement is also tested with a full wave rectifier and a current doubler secondary stage. The performance of these circuits is discussed focussing on the voltage gain and efficiency readings. Some pre-compliance EMI test are performed and the results are presented in section 7.5. Finally, the mechanical implementation of the rotary interface is discussed in section 7.6 along with the main difficulties and possible solutions.

7.1 Experimental Methodologies

The experimental work that is presented in this Chapter is based on standard measurements that are described in the following paragraphs.

7.1.1 Efficiency

Efficiency is the ratio of the output to input power of the converter,

$$Efficiency = \frac{P_o}{P_{in}} \tag{7.1}$$

Despite the clear definition of efficiency, the measurement can be inaccurate, if the form of the voltages and currents is not carefully considered. The output power P_o of a dc/dc converter in steady state is given by the product of the dc voltage across the dummy resistive load and the current through it.

The calculation of the input power is somewhat more complex as it involves a dc input voltage and a non-dc current. In practice, if a perfect voltage source is not used, both the current and voltage experience fluctuations. The average input power P_{in} can be calculated using an oscilloscope with mathematics function. The instantaneous values of the voltage and current are measured and the average of their product is calculated.

The efficiency has been measured across the entire load range of the converter and prior to each measurement 15 minutes were allowed for the circuit operation (temperatures, voltage drops etc) to stabilise. To be able to compare the efficiency readings of different circuits, efforts have been made to keep the room temperature at 22 degrees using air-conditioning and also to maintain a constant air flow around the circuit using a fan at a fixed distance of 8cm from the converter board.

7.1.2 Switching action

To study the switching action of the main MOSFET switches and calculate the switching power loss, the voltage and current through the semiconductor have to be recorded.

In practice it proved to be difficult to accurately measure the switch current due to the interference of the measuring equipment with the power converter operation. A current measuring loop introduces inductance, which slows down the voltage transition and also attracts electromagnetic radiation from the neighbouring components. Another solution was the use of a resistor in series with the MOSFET, to measure the voltage across it and convert to current. An ultra-small inductance and capacitance 0.01Ω 2W SMD resistor

was soldered in series with the source lead and the voltage that was expected across it was in the range of mV. The noise injected from the surrounding switches dominated over the wanted signal. Therefore this method was also abandoned.

A qualitative observation of the switching action was finally attempted by recording the V_{GS} and V_{DS} voltages of the MOSFETs. In the case of a successful resonant transition the voltage across the drain-source junction of the MOSFET becomes zero before the driving pulse rises to the positive rail. In reality, V_{DS} will slightly dip into the negative voltage scale due to the reverse recovery of the inherent diode when the switch turns on. This is an indication that the soft-switching has been successfully completed[1].

7.1.3 Conduction losses

The conduction losses are hard to measure accurately. The main sources of conduction power loss are the transformer windings (due to the dc resistance in combination with the high frequency phenomena), the MOSFETs $R_{DS_{on}}$, the rectifiers $V \cdot I$ and various smaller sources such as tracks, wires, capacitor ESR, inductors etc.

The transformer winding losses are not easy to assess due to the AC resistance that depends on the winding structure and the current waveform.

On the other hand, the MOSFET conduction losses are easier to estimate if the drain-source current is known. The $R_{DS_{on}}$ of the MOSFET is fixed[2]. This assumes a small temperature rise, so the product $I^2 \cdot R$ can be calculated. This is based on the assumption that the resonant time is much shorter than the on-time and the losses during resonance can be ignored.

The rectifier losses can be calculated once the primary current waveform has been recorded and the forward voltage drop is a known property of the diodes.

The aim of this particular project is to minimise the overall converter power losses, hence

[1] The ideal moment to turn the MOSFET on is when the voltage across it becomes 0. If more dead time is available the current will be redirected to the inherent body diode thus increasing the conduction losses in the semiconductor and also resulting in a reverse recovery current when the switch is turned on.

[2] For best accuracy the $R_{DS_{on}}$ variations due to the temperature should be taken into account, however assuming a fixed $R_{DS_{on}}$ (at the operating temperature of 45 degrees Celsius) is accurate enough for the purpose of this work.

knowledge of the absolute value of power losses is not essential. A comparative study (by looking at component temperatures) is enough to identify potential improvements. The different component temperatures are therefore recorded using appropriate equipment.

7.1.4 Temperature

A wireless temperature "gun" was used to monitor temperatures during the prototype operation. This infrared sensing device is ideal for measuring temperature from a distance and detecting overheating and possible damage of equipment. The conventional thermometer with thermocouples was found to be inaccurate during the operation of the circuit due to electromagnetic interference.

The circuit was allowed to operate for 15 minutes until it stabilised and then cooling and power were turned off to take accurate readings of the transformer (core, primary, secondary), MOSFET and rectifier temperatures, using thermocouples.

7.1.5 Electromagnetic field

To detect sources of electromagnetic radiation, a hand-held near-field probe has been used. The HP11941 is used for the identification and measurement of sources of Electromagnetic Interference (EMI) in electronic circuits [98]. Its operating range is between 9kHz and 30MHz. The probe can be used to measure magnetic field as well as electric field and power density provided the field impedance is known. To measure the magnetic field strength the following equation should be used,

$$\overrightarrow{H} - FieldStrength\left(dB\frac{\mu A}{m}\right) = V_{SA} + AF + K \tag{7.2}$$

where V_{SA} is the voltage (in $dB\mu V$) measured on the spectrum analyser, AF is the Antenna factor in dB($\frac{\mu A/m}{\mu V}$) at the specific frequency (see characteristic antenna factors in figure 7.1) and K is the loss or gain in dB between the close-field probe and the oscilloscope.

The measurement of the magnetic field is straight-forward, although the calculation of the electric field and power density assumes the knowledge of the field impedance [99]. An example for the calculation of the electric field is given below assuming a field

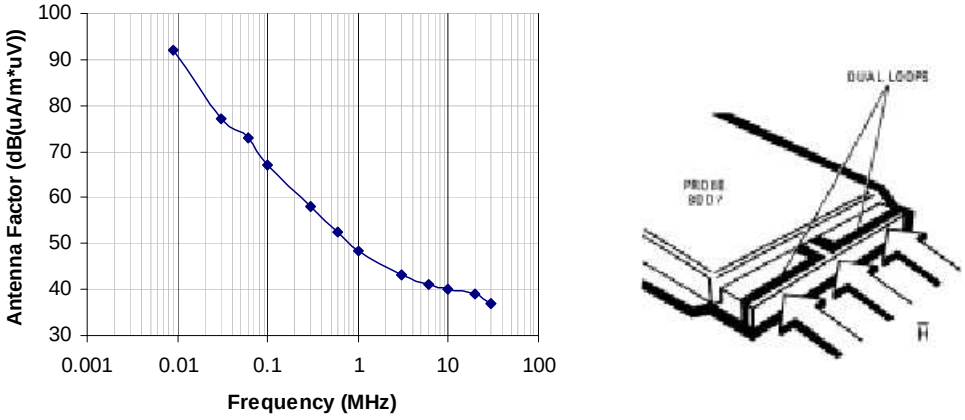

Figure 7.1: *The near field (a) characteristic antenna factors and (b) magnetic field orientation for maximum coupling.*

impedance of 377Ω[3]. The power density is also calculated assuming the fields are in phase.

$$E - FieldStrength\left(dB\frac{\mu V}{m}\right) = V_{SA} + AF + K + 20log(377) \tag{7.3}$$

$$PowerDensity\left(dB\frac{mW}{cm^2}\right) = V_{SA} + AF + K - 104.3 \tag{7.4}$$

Under special circumstances when the measured field induces less that $1mV$ on the scope amplifier input, additional amplification may be needed with an external broadband amplifier. In the specific application the power of the emitted waves was enough to produce an adequate signal across the oscilloscope input.

[3]Magnetic loop antennas respond primarily to the magnetic field component of an electromagnetic wave which is properly expressed in dB˚A/m. Loop antenna manufacturers commonly provide conversion factors for electric field strength, expressed in dB˚V/m, by adding a far field impedance correction of 51.5 dB (20 log 377Ω). In this case the measurement distance is clearly within the near field at all frequencies so the far field impedance conversion is technically incorrect but used here by convention to refer to an equivalent electric field strength [100].

7.2 Experimental Setup

The experimental setup that has been used to take the following measurements consists of the converter prototype along with the instruments listed in table 7.1. The main converter prototype is the phase-shifted full bridge with a current doubler (figure 7.2) that was offered by BAE systems as the basis for developing the new contact-less solution. The main modifications to this prototype were,

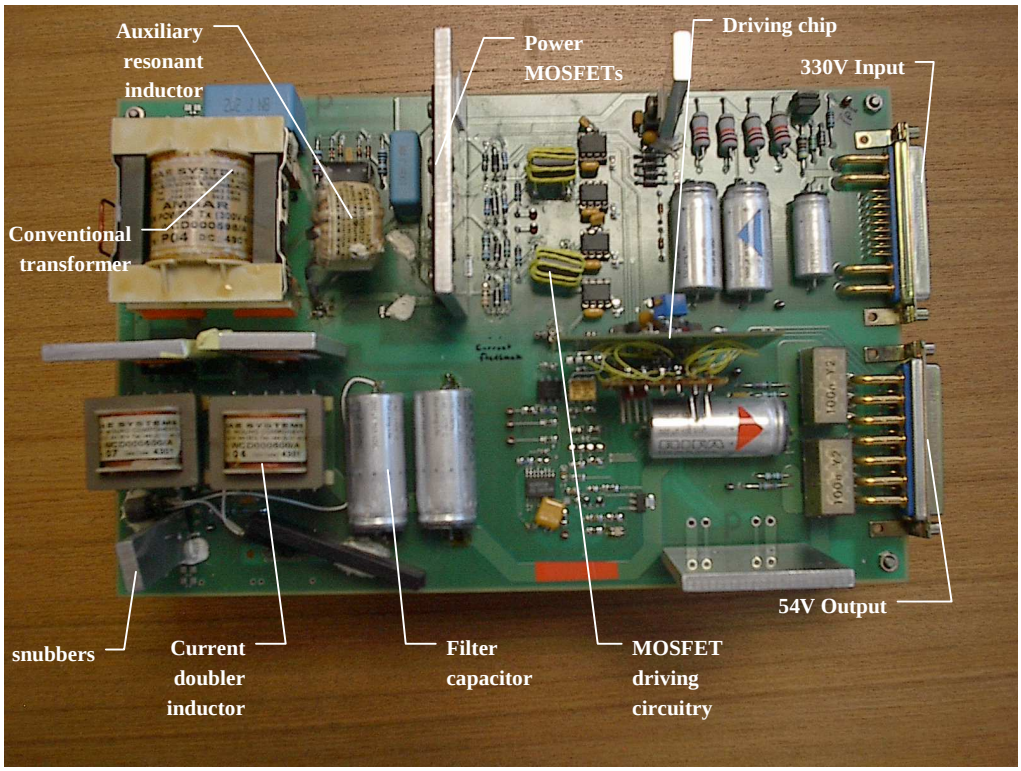

Figure 7.2: *The conventional BAE Systems prototype.*

- connecting the driving circuit to an external power supply so that the driving chip operates regardless of the input voltage level,
- deactivating the pulse synchronising circuit (which is normally used to synchronise the cascaded power converters with the radar scanning frequency),
- replacing the original transformer and removing the external series inductance.
- redesigning the MOSFET driving circuitry to obtain clear gate pulses.

Instrument	Type
Oscilloscope	Agilent 54624A, 200Msa/s - deep memory
Magnetics analyser	Wayne Kerr precision magnetics analyser, model-3260A
Thermometer	Digitron 12-Way type-K, 12 thermo-couples
Thermometer	Infrared thermometer Standard ST-8810, -20^{o}C-270^{o}C
Multimeter 2x	Philips PM-2525
Multimeter	Beckman Industrial 3020B
Power supply 2x	Farnell L30-2, 30V, 2A
Variac	Claude Lyons ltd, 270V-15A
Current probe	LEM LS50 dc/ac probe
Near-field probe	HP 11941A

Table 7.1: *The instruments used during the experiments*

Converter type	Topology	Windings	Magn.Core	Air-gap
Conventional	PSFB-CD	Coaxial, Pri: 26 turns, 2 x SWG21 Sec: 26 turns, 2 x SWG21	ETD49	0mm
Rotating secondary	PSFB-CD	Coaxial, Pri: 26 turns, 4 x SWG21 Sec: 26 turns, 4 x SWG21	P66/56	1mm
Rotating secondary	PSFB-FWR	Adjacent, Pri: 17 turns, 13 x SWG27 Sec: 4+4 turns, 26 x SWG27	P66/56	1mm
Rotating secondary	PSFB-CD	Coaxial, Pri: 17 turns, 13 x SWG27 Sec: 8 turns, 30 x SWG27	P66/56	1mm
Rotating secondary	PSFB-FWR	Coaxial, Pri: 17 turns, 13 x SWG27 Sec: 4+4 turns, 26 x SWG27	P66/56	1mm

Table 7.2: *The various topological variations and transformer prototypes that were tested.*

The circuit was modified so that a full wave rectifier board could be plugged on the existing board (figure C.3) to convert the circuit to a PSFB-FWR at any time without any hardware alterations. The various transformer prototypes could also be connected and disconnected using appropriate housings and connectors. Building a modular prototype with all the parts and even sub-circuits of interest being removable and replaceable allowed the use of the same main converter unit for all the experiments. Keeping all the other components unchanged is important for assessing the effect that any of the removable parts has on the converter operation.

The optimised adjacent windings transformer, the optimised coaxial windings transformer for a current doubler and the optimised coaxial windings transformer for a full-wave rectifier were tested and compared against the conventional BAE Systems prototype and a prototype with a non-optimised rotating transformer. The various configurations appear in table 7.2.

The test bench was supplied through an isolating transformer, a variac and a rectifier/filter to produce a smooth dc voltage. To load the converter, a combination of

variable resistive dummy loads with forced cooling was used.

7.3 Results

The following paragraphs present the experimental findings for the two different winding arrangements and the two rectifier topologies.

7.3.1 Adjacent windings

As seen in Chapter 4 the adjacent windings transformer (26:12 turns) has a high leakage inductance ($L_{lk1} = 58.17\mu H$ and $L_{lk2} = 11.86\mu H$ at 1mm of air gap) as a result of the physical separation of the windings. The AC analysis showed that a significant voltage drop is developed across the leakage inductance causing the collapse of the output voltage (figure 4.16).

On the other hand, the soft-switching operation benefits from the energy storage in the leakage inductance because this secures the zero voltage switching of the semiconductor switches. The parameters that were supplied to the algorithm and the resulting values for the number of turns and wire thickness are presented in table 7.3.

Input parameter	Symbol	Value
Switching frequency	f_{sw}	100kHz
Rectifier topology		Full-wave
Magnetic core		P66/56
Primary bobbin width	B_w1	$20mm$
Primary bobbin diameter	D_{bob1}	$31.1mm$
Secondary winding width	B_w2	$20mm$
Secondary bobbin diameter	D_{bob2}	$31.1mm$
Output parameters	Symbol	Value
Primary turns	N_{pri}	17
Wire type		SWG27
Number of strands		13
Number primary layers		1.9
Prim. eff. resistance	R_{eff_1}	1.89Ω
Secondary turns N_{sec}	N_{sec}	4+4
Wire type		SWG27
Number of strands		26
Number secondary layers		0.6
Sec. eff. resistance	R_{eff_2}	0.038Ω

Table 7.3: *The input and output parameters of the design algorithm for the adjacent winding arrangement in a full-wave rectifier.*

To test the adjacent winding arrangement the coil formers of figure A.8 were custom

P_o(W)	Efficiency	Duty ratio	T_{MOS}	T_{core}	T_{rect}	T_{pri}	T_{sec}
10	55.2	38%	23.4	20.9	21.8	43.0	26.1
100	81.5	81.4%	29.8	20.8	24.7	80.0	35.0
200	88.2	87.6%	29.8	20.9	25.6	84.8	40.0
300	88.9	92.2%	29.3	21.2	26.6	91.0	40.3

Table 7.4: *The optimised adjacent winding transformer efficiency, duty ratio and operating temperatures of the main components (MOSFETs, rectifier diodes and transformer core/windings) at different power levels.*

made in the school workshop. For the specific dimensions the algorithm predicted 40.5W (that is 34.8W on the primary and 5.7W on the secondary) of power dissipation on the windings at 75% of loading. These losses are developed on the primary and secondary windings resistance that were predicted to be around 1.89Ω and $38m\Omega$ respectively. The adjacent windings arrangement is expected to suffer higher proximity losses due to more winding layers being used.

In practice the losses were even higher than predicted, due to the significant increase of the magnetising current[4]. The reason for the increased magnetising current is the prolongation of the ON-time to compensate for the voltage drops across the parasitic inductances. The increased volt-seconds that are applied across the primary winding lead to a proportional increase of the magnetising current according to equation 5.30. The poor voltage gain of the transformer in these experiments is evident from the results of table 7.4. The switch duty ratio has almost reached its maximum value with only 300W of output load. Figure 7.3 illustrates the primary and secondary winding voltages at 200W of output power. The ratio between the two waveforms should ideally equal the turns ratio $n = 17 : 4$, however the actual voltage gain of the transformer is reduced by 18% due to the increased leakage inductance. The converter DC gain is given by,

$$\frac{V_o}{V_i} = n \cdot D \cdot G_v \tag{7.5}$$

where n is the turns ratio and G_v is the transformer voltage gain (which equals to 1.0 in an ideal transformer and is approx 0.82 for the present adjacent windings transformer at 200W). To keep the converter gain fixed for fixed input and output voltages, D must compensate for any reduction of G_v. The duty cycle loss is illustrated in figure 7.3.

[4]In its present state the algorithm does not compensate for large voltage drops across the leakage inductance, hence it cannot predict the increase of the duty ratio.

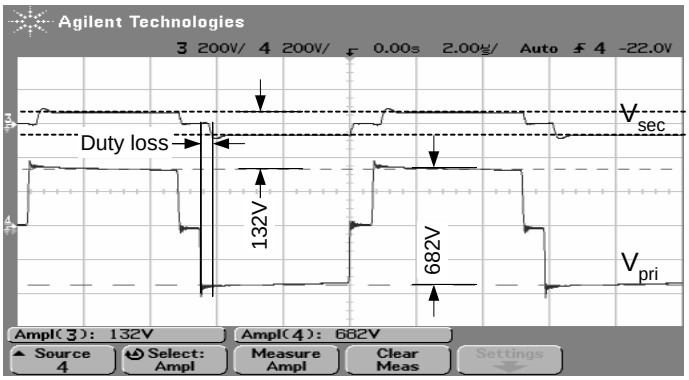

Figure 7.3: *The ratio of the primary (lower waveform) to secondary (upper waveform) voltages is approximately 17:3 (despite the turns ratio being 17:4).*

Apart from the duty cycle loss, an other problem was the heat dissipation on the primary winding. This is clearly shown in table 7.4 where the primary winding temperature reaches the 91^{o}C thermal limit for just 300W output load. Note that the secondary winding remains cooler at about 35^{o}C. The core temperature was kept low at 28^{o}C. The efficiency of the converter was kept relatively high as a result of the soft-switching that is evident from both the MOSFETs temperature (around 29^{o}C) and the $V_{DS} - V_{GS}$ graphs (figure 7.4). The overall efficiency was around 55% at 10W and about 89% at 300W.

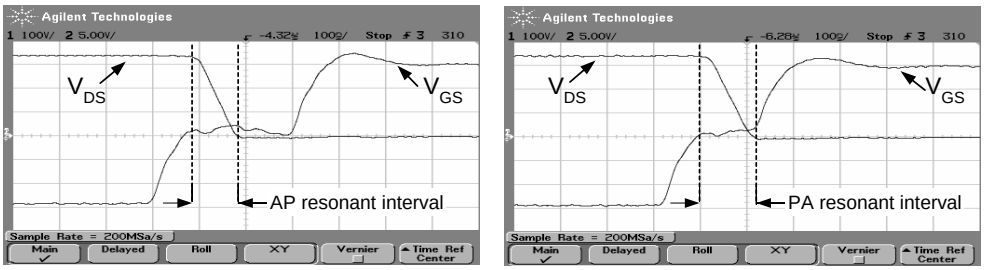

(a) (b)

Figure 7.4: *The soft switching ability of the PSFB-FWR converter with adjacent windings across (a) the AP leg and (b) the PA leg.*

Clearly, even when optimal number of turns and wire gauge are used, the adjacent winding transformer cannot deliver the required amount of energy (neither the specified output voltage) due to the excessive leakage inductance. Some researchers [45, 101] have concentrated their efforts on solving this problem and suggested the use of a resonant converter with capacitors connected in series or in parallel with the primary and secondary windings (to eliminate the series impedance). This is known as leakage in-

ductance compensation (see Chapter 2).

7.3.2 Fringing field

During the design process the effective resistance of the windings was calculated by taking into account the high frequency phenomena such as the skin and the proximity effects that redistribute the current flow within the conductor. In practice, apart from these high frequency effects the experiments involving a coaxial winding arrangement showed an additional phenomenon that took place in the vicinity of the air gap. The stray magnetic flux that is generated around the air-gap develops eddy currents in the conductive materials around the air gap. This was first noticed during the initial experiments when the metallic bolt that was holding the two core halves together exhibited high temperatures. In another experiment the temperature was measured at different points on the same winding using thermocouples. In a coaxial winding arrangement the turns that were placed directly over the air-gap exhibited a temperature around 100^{o}C, whereas the ones closer to the core cup exhibited 60^{o}C for a 500W of output loading. This proved the existence of the stray magnetic field around the air gap, that rearranges the current flow in the wire and as a result the local effective resistance increases. This effect is illustrated in figure 7.5.

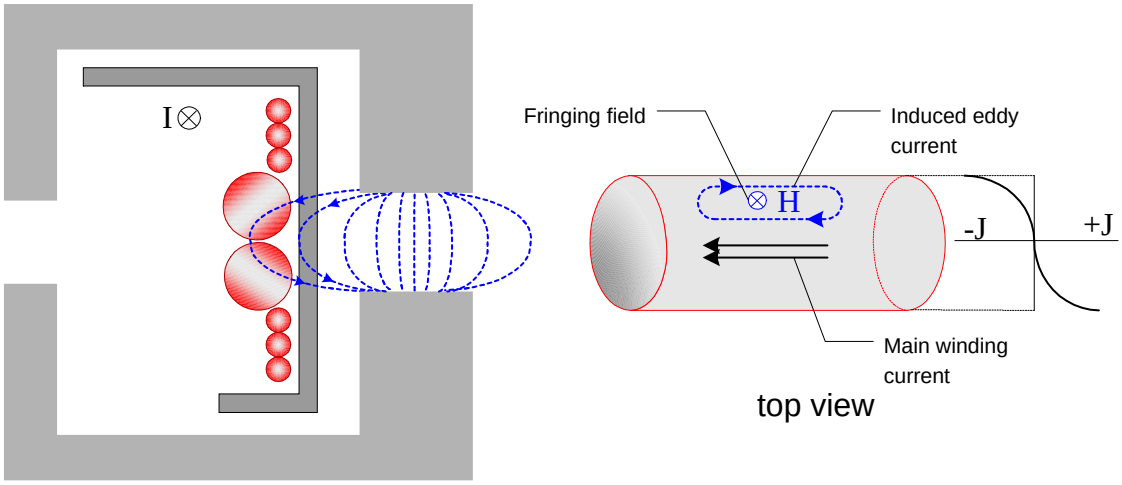

Figure 7.5: *The effect of the fringing field on the windings current density. The affected turns are magnified to illustrate the restriction of the current path.*

To visualise the fringing field effect, a finite element analysis has been employed on a simplified coaxial-windings transformer. The primary winding carries a 6A current

(including a magnetising current of 2A) and the secondary 8.5A with a 180 degrees phase-shift between the primary and secondary currents. The current waveforms are 100kHz sinusoidal. Figure 7.6(a) presents the current density in the transformer structure and around the air-gap, and figure 7.6(b) shows the increased current density (hence increased losses) of the gap-neighbouring turns. Figure 7.7 focuses on the current density vector of the turns directly in the high density area of the fringing field. Not only is the current density increased closer to the air gap (red arrows) but also the current direction is opposite to the useful load current on the right of the wire (which narrows down the effective conductor area). As expected, most of the current is flowing at the wire skin. The current direction in the secondary turns is the same all around the conductor skin except for a small opposite current induced by the neighbouring turns (proximity effect).

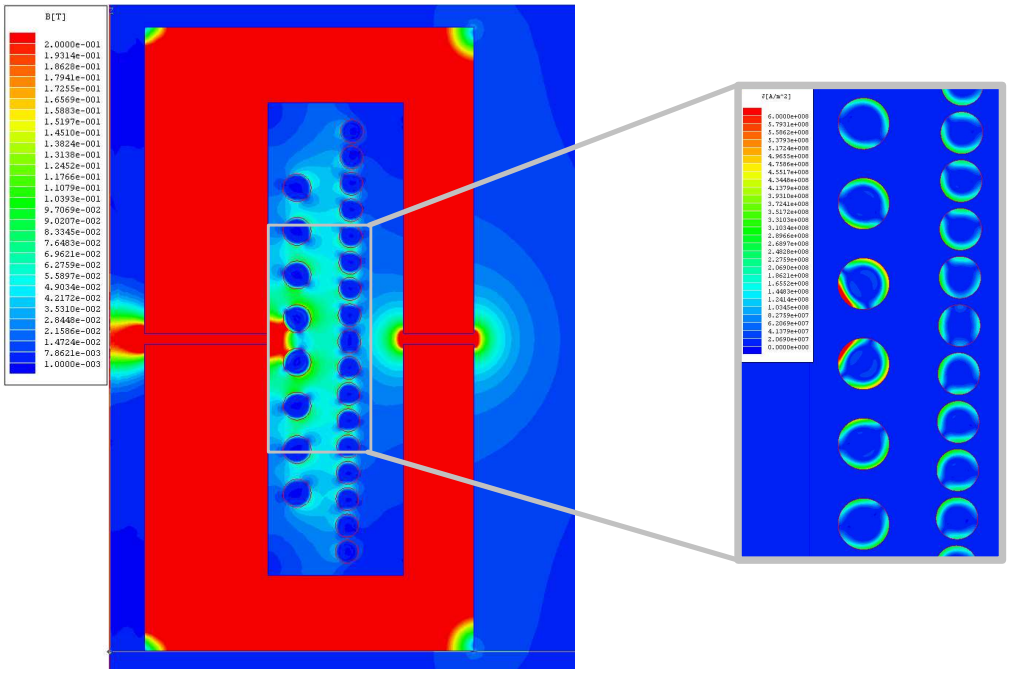

Figure 7.6: *Illustration of the effect of the fringing field around the air-gap: (a) the flux density (b) the current density in the windings.*

The fringing field affected mainly the coaxial winding arrangement dropping the overall circuit efficiency by 1-2% and making it impossible for the transformer to deliver the required output power because of the high temperature that was exhibited locally. This observation resulted in the split coaxial winding arrangement that appears in figure 7.8.

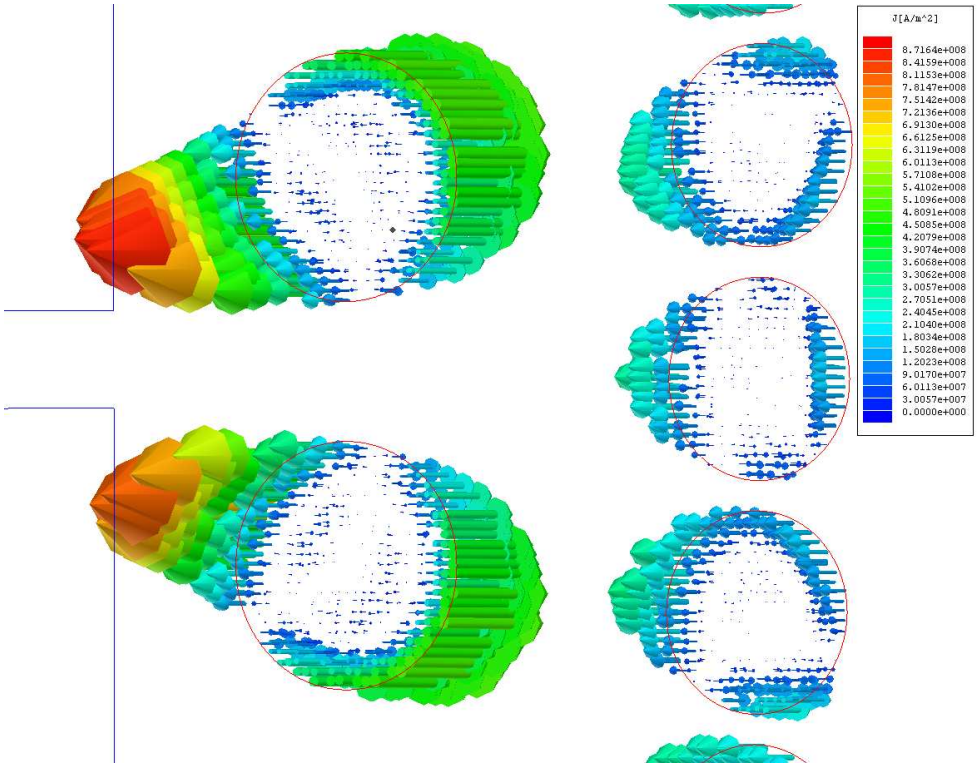

Figure 7.7: *The current density vector in the turns of interest. Red colour corresponds to a higher current density and the triangular shapes show the direction of the current.*

The inner winding is split in two sections that are placed away from the air-gap to avoid the interaction with the fringing magnetic field.

Note that an increased effective winding resistance not only increases the conduction power losses but also lowers the voltage gain due to the voltage drops across the winding.

7.3.3 PSFB with current doubler and coaxial windings

The adjacent windings arrangement failed to deliver the required amount of power across a 1mm air gap. The coaxial windings arrangement will be evaluated in the following pages. The preliminary study of the coaxial arrangement (Chapter 4) showed that it provides better coupling between the windings. This translates to a lower leakage inductance, hence the voltage gain is expected to be improved and consequently the losses to be reduced. The downside of a coaxial windings arrangement is that it has a narrower spectrum of applications because of the rotating part penetrating into the stationary part.

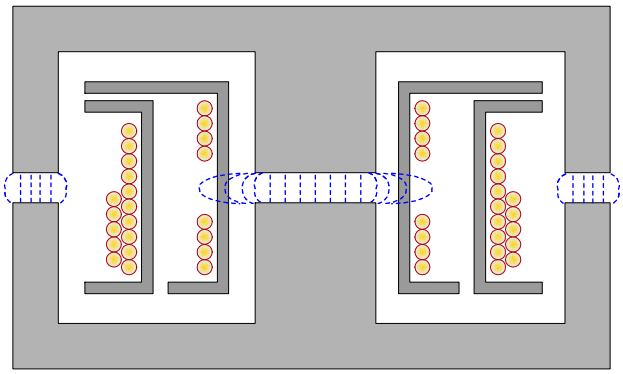

Figure 7.8: *Splitting the inner winding to two sections that are placed away from the fringing field.*

In Chapter 6 the characteristics of the optimum coaxial windings layout for a current doubler topology are derived and summarised in table 7.5.

Input parameter	Symbol	Value
Switching freq.	f_{sw}	100kHz
Rectifier topology		current doubler
Magnetic core		P66/56
Prim. bobbin width	B_w1	$32.7mm$
Prim. bobbin diameter	D_{bob}	$41.5mm$
Sec winding width	B_w2	$32.7mm$
Prim. bobbin diameter	D_{bob}	$31.1mm$
Output parameters	Symbol	Value
Primary turns	N_{pri}	17
Wire type		SWG27
Number of strands		13
Number primary layers		1.2
Prim. eff. resistance	R_{eff_1}	0.761Ω
Secondary turns	N_{sec}	8
Wire type		SWG27
Number of strands		30
Number secondary layers		0.9
Sec. eff. resistance	R_{eff_2}	0.38Ω

Table 7.5: *The optimised PSFB-CD with coaxial windings transformer.*

The predicted primary and secondary losses are 22W and 15.8W respectively and the MOSFET losses are 23W at 75% of loading. The prototype of this converter demonstrated a more balanced thermal behaviour than with the adjacent winding; the hot spots were nearly eliminated and the overall efficiency was increased. The temperatures of the MOSFETs, rectifiers, transformer core and windings appear in table 7.6

This design was the first that was able to operate up to full load (1kW) with a temperature rise that did not exceed 60^oC. The temperatures were measured after a period of 15 minutes allowing the operation to stabilise. The first impression taken from these

readings is a better heat distribution among the different components; particularly, the MOSFETs temperature is similar to that of the primary and secondary windings.

The soft-switching ability of the two legs is evident from the V_{DS} and V_{GS} waveforms that are presented in figure 7.9. The waveforms refer to a nearly no-load operation (1% of full load). Figure 7.9(a) illustrates a successful zero voltage transition of the AP leg and 7.9(b) shows in more detail the resonant operation. Similarly, the right hand side graphs (7.9(c) and (d)) refer to the critical PA leg switches, which also undergo zero voltage transitions. The duration of the resonance is around 75nsec for both legs. The equal transition time was expected as the converter operates under very light load so the carrier of the resonant operation is the magnetising current whose peak value is 2.4A. The fact that the MOSFETs undergo ZVT, even with no output current and with minimum duty ratio, means that the soft switching is guaranteed across the full load range.

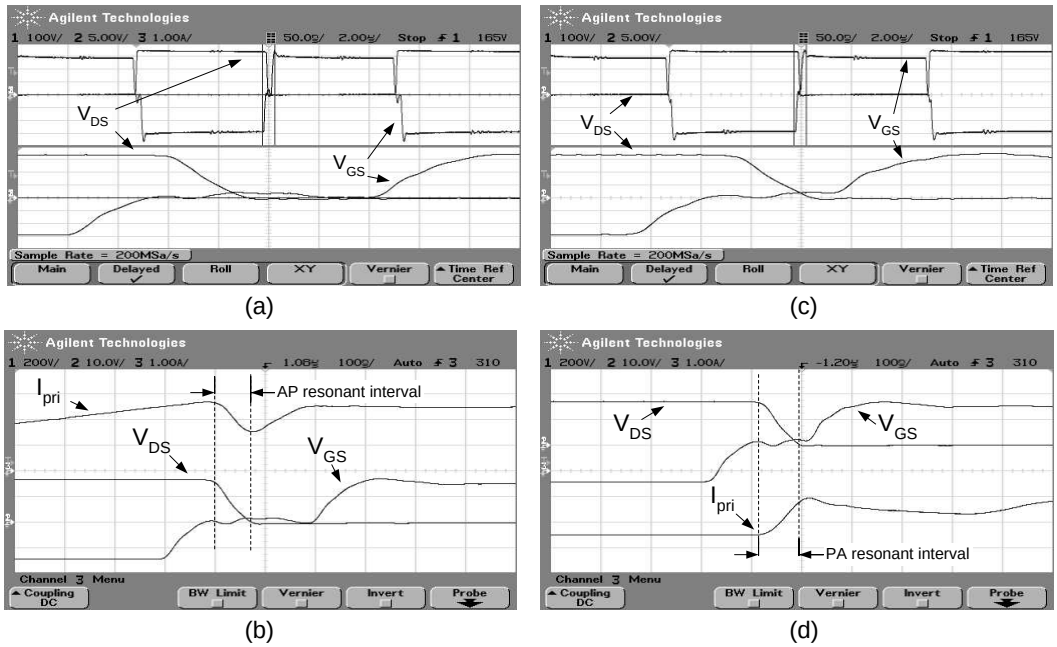

Figure 7.9: *Nearly no-load operation (1% of full load)of the PSFB-CD with a coaxial windings transformer. (a) The drain-source voltage V_{DS} and the gate-source voltage V_{GS} of an AP switch, (b) the successfully completed AP resonant transition interval in detail, (c) V_{DS} and V_{GS} of a PA switch and (d) the critical PA switches are successfully turned on under zero voltage.*

Regarding the voltage gain of the transformer, this is kept high throughout the entire load range as can be seen in table 7.6.

P_o(W)	Eff. %	Duty cycle %	T_{MOS}	T_{core}	T_{rect}	T_{pri}	T_{sec}
10	26.5	43,2%	24.2	21.5	21.0	25.7	25.5
100	74.2	69.9%	24.8	24.2	24.2	35.0	35.5
200	82.4	70,3%	26.0	25.0	26.8	36.7	36.5
300	86.2	71.0%	28.0	25.8	29.2	37.5	36.6
400	88.7	72.6%	29.3	26.1	32.5	41.5	40.0
500	89.8	72.6%	30.9	26.8	34.9	45.5	43.2
600	89.1	73.4%	33.8	26.8	37.1	46.5	42.9
700	90.2	74.9%	34.5	26.8	38.5	49.2	44.8
800	89.8	74.9%	37.5	26.8	42.0	57.5	52.1
900	89.5	75.7%	39.0	28.1	43.4	62.8	56.0
1000	88.9	76.6%	45.4	29.9	46.3	72	61.1

Table 7.6: *The efficiency, duty cycle, and component temperatures of the PSFB-CD with an 1mm gapped optimised transformer.*

Finally, the performance of the circuit is slightly lower than the target of 90% that has been set.

7.3.4 PSFB with full wave rectifier and coaxial windings

The PSFB with the current doubler rectifier and a coaxial windings transformer demonstrates the potential of using a rotating transformer provided the leakage inductance is kept relatively low. The duty ratio remained around 75% at the nominal input voltage and the efficiency of this circuit was also high (average 89%).

Input parameter	Symbol	Value
Switching frequency	f_{sw}	100kHz
Rectifier topology		Full-wave
Magnetic core		P66/56
Primary bobbin width	B_w1	$32.7mm$
Primary bobbin diameter	D_{bob1}	$41.5mm$
Secondary winding width	B_w2	$32.7mm$
Secondary bobbin diameter	D_{bob2}	$31.1mm$
Output parameters	Symbol	Value
Primary turns	N_{pri}	17
Wire type		SWG27
Number of strands		14
Number primary layers		1.2
Prim. eff. resistance	R_{eff_1}	0.874Ω
Secondary turns N_{sec}	N_{sec}	4+4
Wire type		SWG27
Number of strands		25
Number secondary layers		0.8
Sec. eff. resistance	R_{eff_2}	0.0023Ω

Table 7.7: *Input and output parameters of the design methodology for the PSFB-FWR rotating transformer.*

The second circuit under investigation is a PSFB with a coaxial windings transformer

and a full wave rectifier (table 7.7). The power losses representation of figure 6.15 gave an optimum of 19 turns of 0.4mm wire for the primary and consequently 5+5 turns for the secondary. However, to avoid the interference with the fringing magnetic field (see section 7.3.2), the primary turns were reduced to 17 and the secondary to 4+4. This was done in order to place the secondary winding on the left and right of the air gap in a split arrangement (see figure 7.8). The estimated (design algorithm) penalty in the conduction losses was around 6W at full load, whereas the demonstrated benefit from the split windings was a 30^{o}C lower operating temperature of the transformer windings.

The MOSFET and transformer estimated losses are 31W. The primary losses are expected to be around 16W, the secondary losses around 1W and the MOSFET losses 14.7W at 75% of the total load.

The primary leakage and magnetising inductances of the transformer are the same as the ones in the primary winding in a current doubler topology. Consequently, the magnetising current is also the same (same number of turns) and therefore the resonant transitions are expected to be successful down to no-output load. This is evident in figure 7.10 where the resonant operation under 1% of the full loading is shown.

Table 7.8 presents the temperatures that were measured on the MOSFETs, the rectifiers and the transformer core and windings. The temperature rise is less than 40^{o}C, which is in accordance with the specifications. It appears that the MOSFETs' temperature increased and the windings temperatures decreased in a way that the heat is balanced between the different components. This generally improves the operation of the converter as the hot-spots are eliminated and consequently the reliability and lifespan of the components is increased.

P_o	Eff. %	Duty cycle %	T_{MOS}	T_{core}	T_{rect}	T_{pri}	T_{sec}
10	59.4	31.0	25.5	23.6	25.5	28.9	27.6
100	80.5	69.8	27.7	24.4	25.6	27.1	30.2
300	91.9	71.3	29.5	24.4	25.9	28.4	32.4
500	92.7	72.1	33.3	26.3	30.1	32.8	36.2
600	93.3	72.1	37.0	27.0	31.5	34.5	37.7
700	93.6	73.6	40.2	27.2	33.3	36.6	40.7
800	92.4	74.4	42.5	28.2	34.5	39.6	41.0
900	92.1	74.4	46.0	28.5	34.7	40.5	46.0
1000	92.4	75.6	51.0	30.0	36.2	48.2	55.5

Table 7.8: *The efficiency, duty cycle, and component temperatures of the PSFB-FWR with a 1mm gapped optimised rotating transformer.*

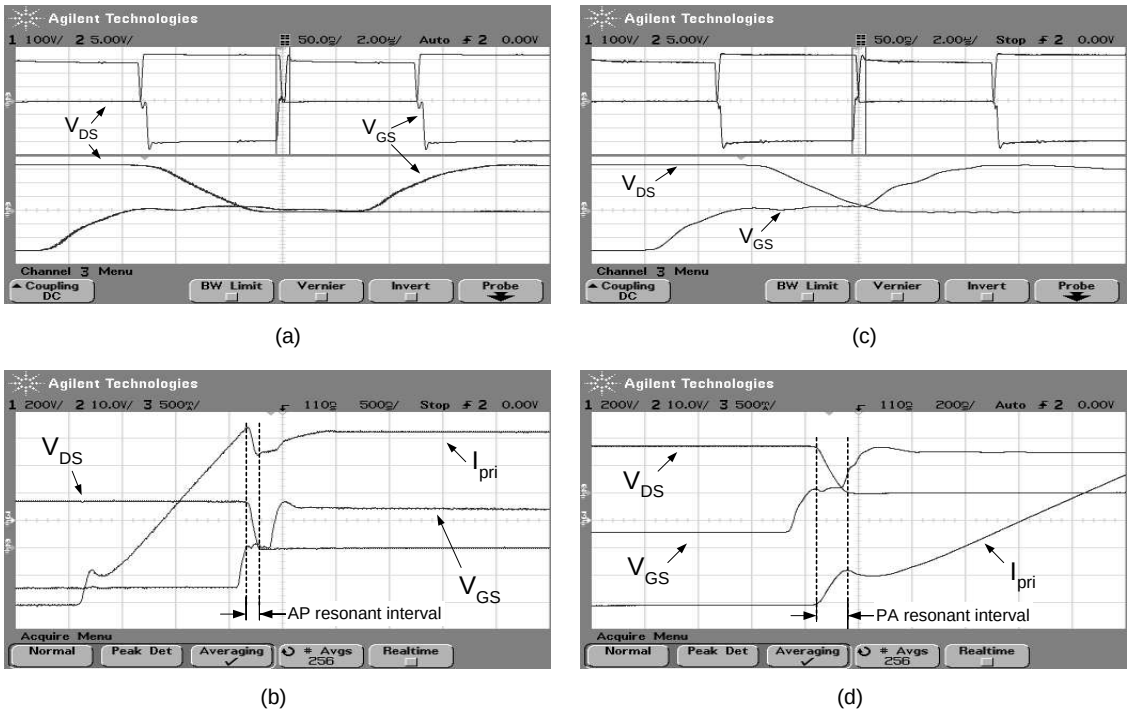

Figure 7.10: *Nearly no-load operation (1% of full load) of a PSFB-FWR with a coaxial windings transformer. (a) The drain-source voltage V_{DS} and the gate-source voltage V_{GS} of an AP switch, (b) the successfully completed AP resonant transition interval in detail, (c) V_{DS} and V_{GS} of a PA switch and (d) the critical PA switches are successfully turned on under zero voltage.*

The successful ZVT operation is reflected in the efficiency readings (table 7.8). The figures are considerably higher than those of the previously tested arrangements and the main reason is the minimised power dissipation on the transformer windings.

In this case the algorithm balanced out the losses between the MOSFETs and the transformer windings in order to increase the power capacity of the transformer.

7.4 Discussion

7.4.1 Switching losses

The calculation of the MOSFETs switching loss is difficult because it depends on many hard-to-quantify parameters. A rough approximation is given by equation 7.6, though measurements in the laboratory are essential to verify the results [102].

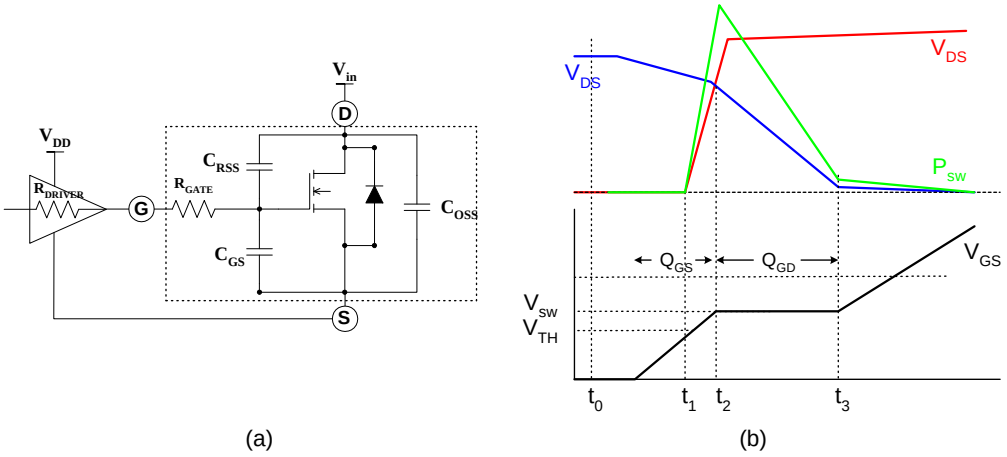

Figure 7.11: *The illustration of the switching action. (a) The MOSFET equivalent circuit with the parasitic capacitances and diode and (b) the voltage and current waveforms during a partial resonant transition ($t_0 \rightarrow t_1$) and the hard turn-on ($t_1 \rightarrow t_2$).*

$$P_{sw} = \frac{C_{RSS} \cdot V_{in}^2 \cdot f_{sw} \cdot I_{pri}}{I_{GATE}} \tag{7.6}$$

where C_{RSS} is the MOSFET's reverse transfer capacitance (figure 7.11(a)), f_{sw} is the switching frequency and I_{GATE} is the MOSFET gate-driver's sink/source current at the MOSFET's turn-on threshold. Assuming that all parameters are fixed for specific operating conditions, the switching losses are proportional to the switched current I_{pri}. In a conventional converter operating at low or no-load the switching losses are small as I_{pri} is also small. Therefore the low or no-load efficiency is not of primary importance. However, in a system with contact-less transfer of energy the magnetising current that circulates in the primary side is relatively high under any operating condition. The result of switching this circulating current ON and OFF is high switching losses. As a result, in a CTE application soft-switching is a desired feature for the entire load range.

In the laboratory the soft-switching ability of a converter can be assessed by looking at the switching voltage-current and the gate signal. Having obtained the voltage and current waveforms, the switching power loss of a transition can be calculated by averaging the V*I product over the switching period (averaging the green line over a period in figure 7.11(b)). As there is no direct access with a current probe to the MOSFET current, an indirect way is to look at the transformer current. However, this is not totally accurate as the transformer current may also contain the resonant current of the

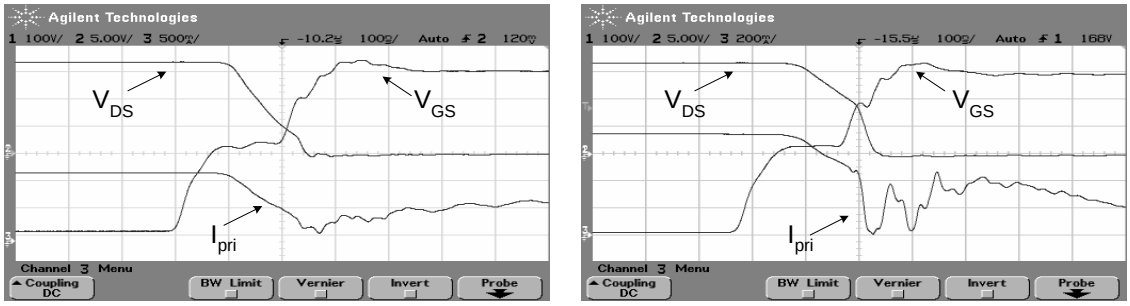

Figure 7.12: *Unsuccessful ZVT at no-load, when more than the calculated primary winding turns are used (a) in a PSFB with a current doubler and (b) in a PSFB with a full wave rectifier. The PSFB-CD provides more energy than the PSFB-FWR due to the reflected secondary current.*

other MOSFET of the same leg. The accurate calculation of the switching losses is a task to be included in future investigations. At this stage of the project it is considered sufficient to prove the existence or not of soft-switching.

According to the proposed design methodology, for a P66/56 magnetic core with 1mm of air gap the switching losses should be eliminated if less than 21 primary turns are used. This conclusion was based on the knowledge that when the converter operates with no output load the energy for zero voltage switching can be provided by the magnetising current.

Figures 7.12(a) and (b) illustrate the PA switching waveforms of the non-optimised CD and FWR converters respectively. The non-optimised transformers were used during the initial experiments and despite the relatively high leakage inductance (around 7μH) of the 26 primary turns they did not achieve soft-switching. The magnetising current was below the critical magnetising current of 2.1A that was calculated in Chapter 6. The resonance of PSFB-CD (figure 7.12(a)) was completed to a higher degree than that of the PSFB-FWR (figure 7.12(b)) proving once more that the PSFB-CD performs better at very low or no-load conditions. The reason for this is, as shown in Chapter 5, the reflected secondary current that flows in a current doubler through the two inductors even at no-load. On the other hand, the full wave rectifier topology runs in discontinuous mode at very light load not reflecting any current to the primary side.

The above observation brings to the surface another trade-off between increasing the

number of turns (to increase the leakage inductance) and decreasing them to increase the magnetising current. In both cases the stored energy is increased, however they both have consequences to the converter operation. Increasing the number of winding turns increases the leakage inductance but decreases the effective duty cycle/power transfer capability. On the other hand, decreasing the number of winding turns increases the magnetising current, but it also increases the conduction losses. To find the best compromise for this trade-off the optimisation algorithm calculates the maximum number of turns for which the magnetising current can successfully complete the soft-switching by itself (at no-load). Then the conduction losses evaluation takes place to select the optimum number of turns that should also satisfy the ZVT condition.

To quantify the benefit from soft-switching, a PSFB with a conventional transformer (with same specifications and a 26:12 2 strands of SWG21, ETD49 core) was tested at no-load conditions. Despite using an external series inductor to increase the leakage inductance the soft-switching performance was poor as can be seen in figures 7.13. At half-load operation the PA leg switches exhibit hard-switching reducing the efficiency by an estimated 1-2% (10-20W).

7.4.2 Conduction losses

The conduction losses are reflected in the temperature of the windings and the MOSFETs (assuming the switching losses are eliminated completely).

The initial tests that were performed using the BAE prototype converter and a rotating transformer with various air-gap lengths demonstrated increased winding losses. These losses were a direct result of the increased magnetising current. Figure 7.14 presents the temperature at different points of 4 different converter arrangements. The dark blue line corresponds to a conventional prototype designed by BAE systems. This prototype has a non-gapped transformer (26:12 turns with 2 strands of SWG21 wire in each winding) in series with an auxiliary inductor to assist soft-switching. The secondary stage features a current doubler rectifier with identical components to the ones used in the converters of Section 7.3. The magenta line corresponds to the same PSFB-CD design with a non-optimised rotating transformer. The non-optimised transformer has the same turns count as the conventional transformer, however the wire thickness/strands are adjusted to carry the additional magnetising current. The red line illustrates the temperature

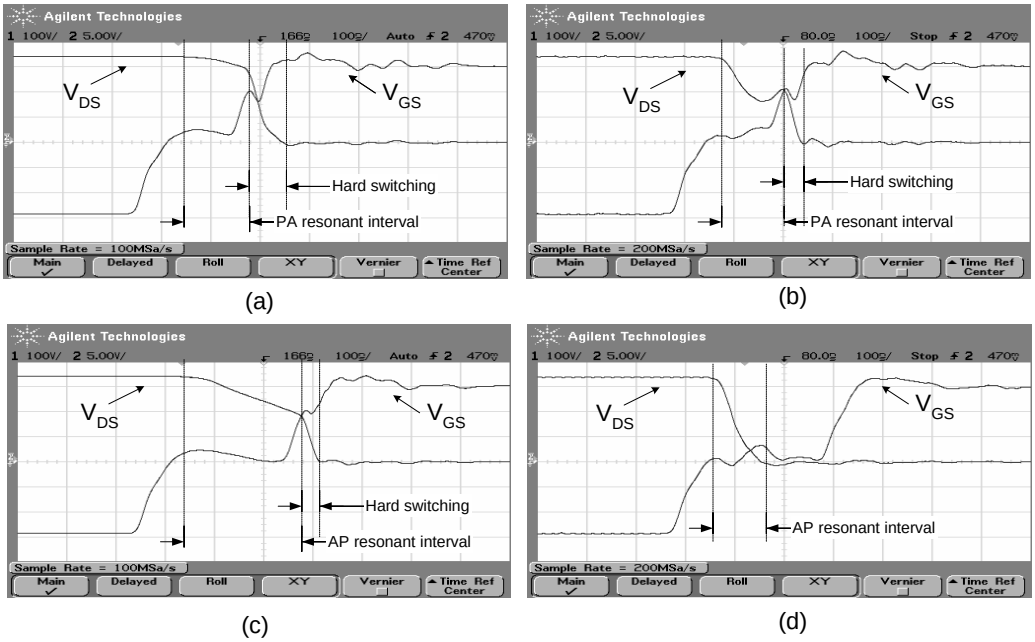

Figure 7.13: *Soft-switching waveforms of the BAE Prototype with a conventional transformer; (a) partial soft-switching of a PA leg switch with 10W output load, (b) partial soft-switching of a PA leg switch at half load (500W) (c) partial soft-switching of an AP leg switch with 10W output load (c) successful soft-switching of an AP leg switch at half load (500W).*

variation across the parts of a PSFB with a current doubler and the optimised coaxially wound rotating transformer (primary turns:17, 13 strands of SWG27 wire and secondary turns:8 30 strands of SWG27 wire). Finally, the green lines refer to various temperatures in a PSFB with a full wave rectifier when an optimised coaxial rotating transformer is used (primary turns:17, 14 strands of SWG27 gauge, secondary turns: 4+4 centre-tapped, 25 strands of SWG27 wire).

The PSFB-FWR with an optimised rotating transformer Among the 4 converters discussed here, the PSFB with a full-wave rectifier and an optimised rotating transformer demonstrated the highest efficiency (average of 92.6%). Having eliminated the switching losses of the main switches, the remaining MOSFET losses are clearly resistive. Consequently, the heat developed on the MOSFETs is primarily due to the conduction losses during the ON time and during the resonant interval and the conduction of the inherent diode.

On the other hand, the transformer winding losses are due to the effective resistance

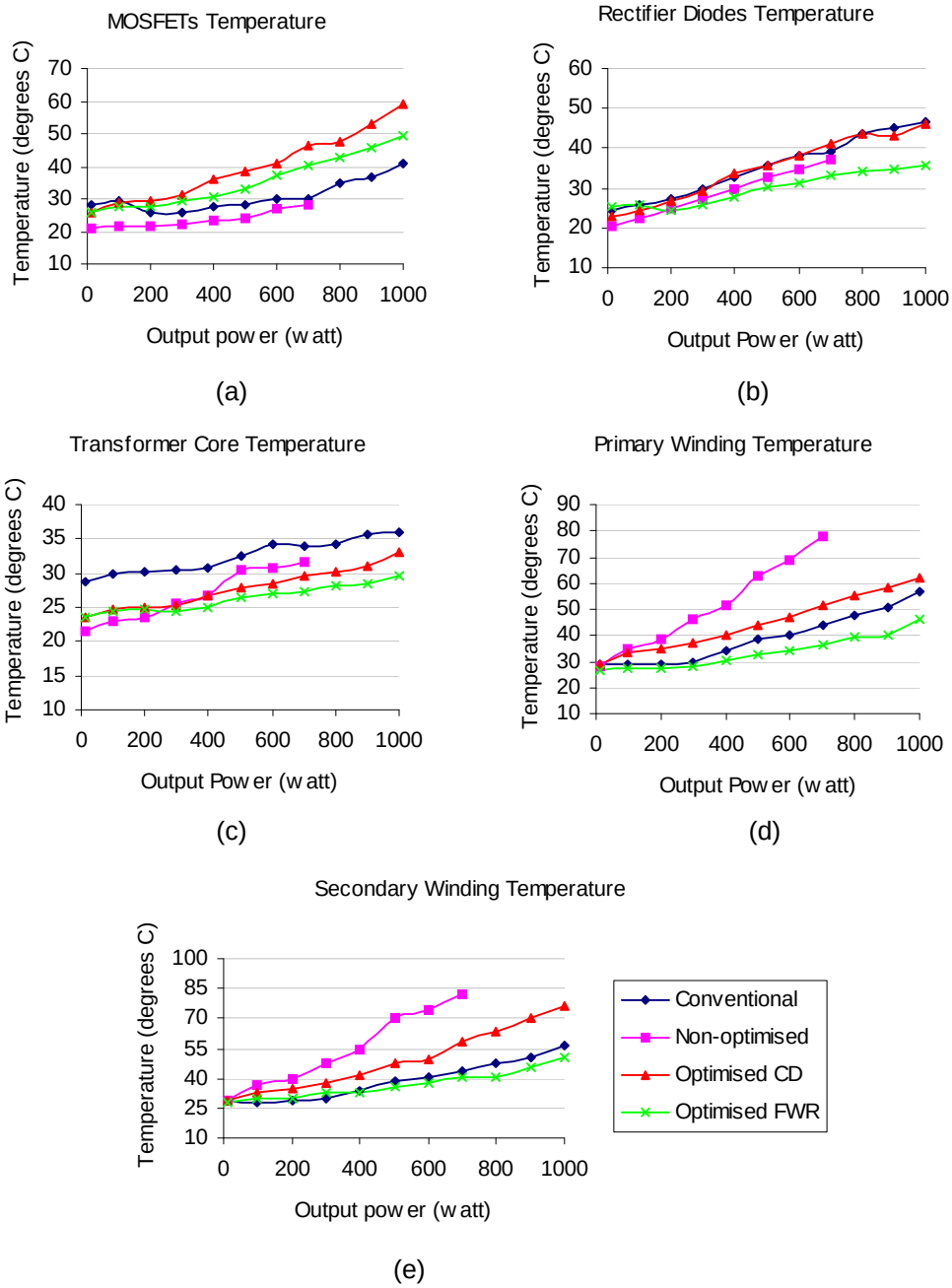

Figure 7.14: *The temperatures of the various bridge components (in a coaxial winding arrangement), (a) MOSFETs (b) rectifier diodes (c) transformer magnetic core (d) primary winding (e) secondary winding.*

which in turn depends on the length of the wires and the way they are wound on the bobbin. The PSFB-FWR converter demonstrated the lowest losses among all the topological alternatives.

Figure 7.14(d) and (e) show a lower operating temperature in the windings of the optimised FWR in comparison with the other circuits, whereas figure 7.14(a) shows an increased MOSFET temperature. This is the effect of the optimisation routine; the power dissipation on the windings has been reduced in order to allow the component to deliver more power. To do so the windings' resistance was reduced by reducing the number of winding turns. This boosted the magnetising current and consequently increased the MOSFETs on-time power loss. Optimising the objective function $I(N_{pri}, D_c)^2 \cdot R(N_{pri}, D_c, B_w, D_{bob})$ resulted in spreading the power losses between the power switches and the transformer.

The main reason for the lower secondary winding temperature is the use of a centre-tapped secondary. The two winding sections are wound away from the air-gap (see figure 7.8) and as a result the fringing field does not contribute to the conduction power losses.

The rectifier diodes also exhibit lower temperature but this is mainly due to the slightly different heat sinks that have been used in the full wave rectifier circuit. In practice, both diode sets conduct for equal time intervals ($(1-0.5D)T_{sw}$), however in a full-wave rectifier the diode current during the active interval is twice as much as in a current doubler (hence the name). Consequently, the power losses in a full wave rectifier are somewhat higher.

The transformer core ran steadily at around 28^oC as it did in most of the other arrangements except for the conventional converter that ran up to 37^oC. The conventional converter exhibited a higher core losses as the flux density in the smaller e-core was higher. Note that the pot core has the advantage of a wide surface that means lower thermal resistance and easy cooling. The disadvantage, in comparison with the e-core of the conventional converter, is that the air flow in a pot core is limited making the windings cooling problematic. The difficulty of removing the heat becomes even greater for the secondary winding nested into the primary.

The PSFB-CD with an optimised rotating transformer The original PSFB circuit with a current doubler and an optimised transformer gave the first signs of a feasible design. As shown in Section 7.3.3, the MOSFET switching losses were reduced, however the on-time resistive losses due to $R_{DS_{on}}$ were increased raising the temperature to around 50^oC (60^oC at full load).

The primary winding temperature, although reduced with respect to the non-optimised version, varies from 29^oC to 63^oC and the secondary from the ambient 29^oC to 76^oC. The primary temperature rise was within the specified maximum temperature rise ($\Delta\theta = 40^oC$) whereas the secondary temperature was 7^oC above the limit.

The main reason for the increased winding losses is the higher primary current of this topology due to the secondary current being reflected to the primary for a greater portion of the switching cycle than in a PSFB-FWR. Apart from this, in a current doubler a portion of the winding inevitably passes over the air-gap where the fringing field develops eddy currents.

The rectifier losses are similar to the ones in the PSFB-FWR converter and as a result the temperature rise is about 22^oC in both cases.

The PSFB-CD with a non-optimised rotating transformer The PSFB-CD with a non-optimised transformer was one of the first prototypes to be tested in order to examine the problems deriving from a large air-gap. The transformer had the same turns count as the original non-gapped BAE transformer and the wire thickness was adjusted to account for the expected magnetising current. The switching losses of this prototype were lower that those of the conventional circuit and this was reflected in the MOSFET temperature rise which was only 15^oC. The magnetising current was also kept low keeping the MOSFET on-time conduction losses low.

The rotating transformer with the 26 primary and 12 secondary turns, despite producing a lower magnetising current than its optimised counterparts, exhibited higher conduction losses raising its windings temperature by more than 50^oC. The converter was only tested up to 700W and the actual power handling capability of the transformer was only 400W (to keep the operating temperature within specification).

Regarding the core losses, these appeared to be relatively higher than in the PSFB-CD

and PSFB-FWR with optimised transformers. This is likely to be due to high winding losses of the non-optimised transformer.

As expected, the rectifier losses appeared to be lower than in the other PSFB-CD topologies. The reason is that the current doubler rectifier reflects a considerable current to the primary winding (e.g. to assist the resonant operation). This creates a secondary magnetising current that contributes to the winding losses. The non-optimised rotating transformer having more turns causes a lower magnetising current and thereby lower rectifier losses than the other CD topologies.

The conventional PSFB-CD Finally, the conventional PSFB-CD as it was designed by BAE Systems demonstrated an overall efficiency of around 90% (average). The reason for comparing this converter with the rotating transformer prototypes is to show that despite the radical increase of the magnetising current, the rotating transformer can be effectively utilised in a phase-shifted bridge to reduce the switching power losses and compensate for the increased transformer winding losses.

This prototype exhibited higher power losses in four out of five monitored components of the converter. The rectifier, magnetic core, primary and secondary winding losses were higher than in a PSFB-FWR topology. Only the MOSFETs' temperature was kept lower (despite the hard-switching up to 500W).

7.4.3 Voltage gain

The duty cycle of the phase-shifted full bridge with various transformer prototypes and different rectifier circuits was recorded. The duty cycle is a direct indicator of the converter's voltage gain and indirectly of the transformer's voltage gain. As the latter is only defined for sinusoidal waveforms, it is not valid to refer to the voltage gain of a switching power supply transformer. In an ideal transformer the input and output waveforms should have the same shape and their amplitude ratio should equal the turns ratio. If the output waveform is distorted this means that the magnitude and the angle of the gain function of the transformer is not constant for the entire frequency range of the input signal.

The duty cycle of the PSFB converter with various transformer arrangements and the

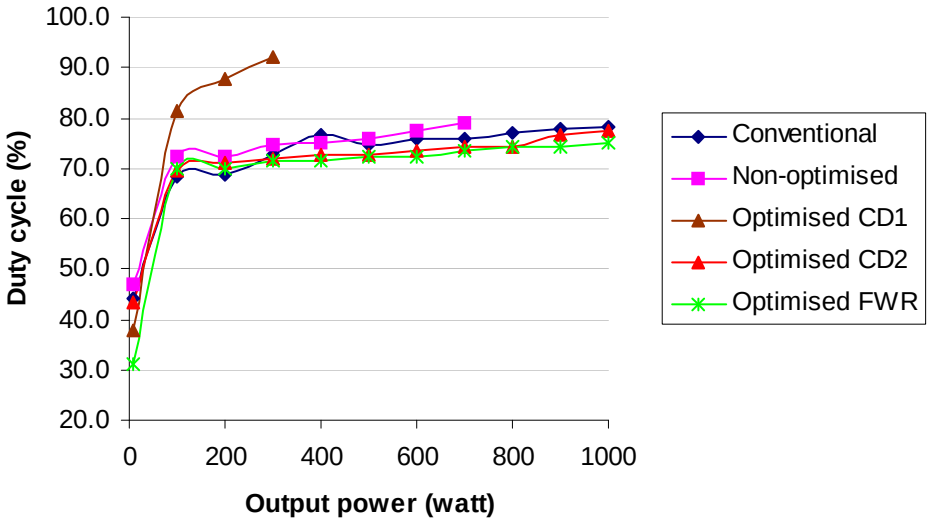

Figure 7.15: *The duty cycle of the phase shifted full bridge with different transformer arrangements and rectifier circuits. The optimised PSFB-FWR and PSFB-CD2 results in a similar duty ratio variation as the conventional BAE converter.*

two rectifier alternatives is shown in figure 7.15. The duty cycle was measured at the nominal input and output voltages, therefore any variation only reflects the voltage drops across the converter components. The dark blue line corresponds to the conventional BAE design that meets all the design specifications and it is used as a reference design. The magenta line corresponds to a problematic PSFB-CD with a non-optimised rotating transformer. The 26:12 rotating transformer exhibited high losses and the duty cycle of the converter was slightly increased (reached 79%). The brown line refers to the PSFB-CD with an optimised adjacent windings transformer. This converter was only tested up to 300W of output power because the transformer reached its thermal limits. The high leakage inductance resulted in poor voltage gain of the transformer and this is reflected in the rapid increase of the duty cycle. The red line corresponds to a PSFB-CD with an optimised coaxial winding rotating transformer with coaxial windings arrangement. The duty cycle of this arrangement was reduced mainly due to the decreased leakage inductance (as the primary and secondary turns are reduced by 35% from those of the non-optimised prototype and the primary leakage inductance is almost half). Finally, the optimised PSFB-FWR (green line) also operated with a normal duty cycle.

It is important to note at this point that conventional PSFBs require a series inductor

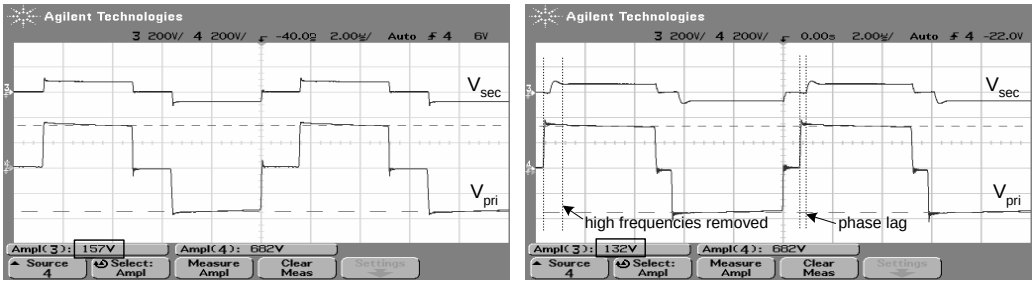

(a) (b)

Figure 7.16: *Primary and secondary voltages of the (a) optimised rotating coaxial transformer (b) optimised rotating adjacent transformer. The adjacent windings transformer acts as a low pass filter removing the high frequency ripple from the input waveform and introduces a phase-shift.*

to store energy for the resonant operation before turn-on. This inductor (external or transformer leakage) *slows down* the primary current change, and therefore it restricts the effective power transfer interval of the converter. On the other hand, a PSFB with a rotating transformer makes use of the magnetising energy so that the required leakage inductance is less. Having more duty cycle available in practice means that the power capability of the converter increases (i.e. the power density increases).

Figure 7.16(a) illustrates the primary and secondary voltages of the PSFB-FWR converter with an optimised (17:8) rotating transformer with coaxial windings arrangement. For comparison purposes the primary and secondary voltages of the PSFB-FWR with an optimised adjacent windings transformer are depicted in figure 7.16(b). The converters were tested at 200W of output power. The first observation is that the amplitude of the secondary voltage in (b) is less than the one in (a). This is compensated by the increased duty ratio of the waveforms in figure 7.16(b) where the on-time is 22% longer than in figure 7.16(a). Regarding the distortion of the waveforms, this does not appear to be a problem as only minor effects are observed. The effect of the leakage inductance (which makes the transformer behave like a low pass filter) is the removal of the high frequency ringing that is present in the primary waveforms. In addition to this, the off time of the secondary voltage in figure 7.16(b) lasts longer than that of the primary voltage. The reduced secondary duty cycle is a well-known result of the secondary leakage inductance. The coaxial windings transformer has a better response with an amplitude ratio equal to the turns ratio and no phase lags.

By operating the converter at the nominal voltage (and normal duty cycle) the optimum

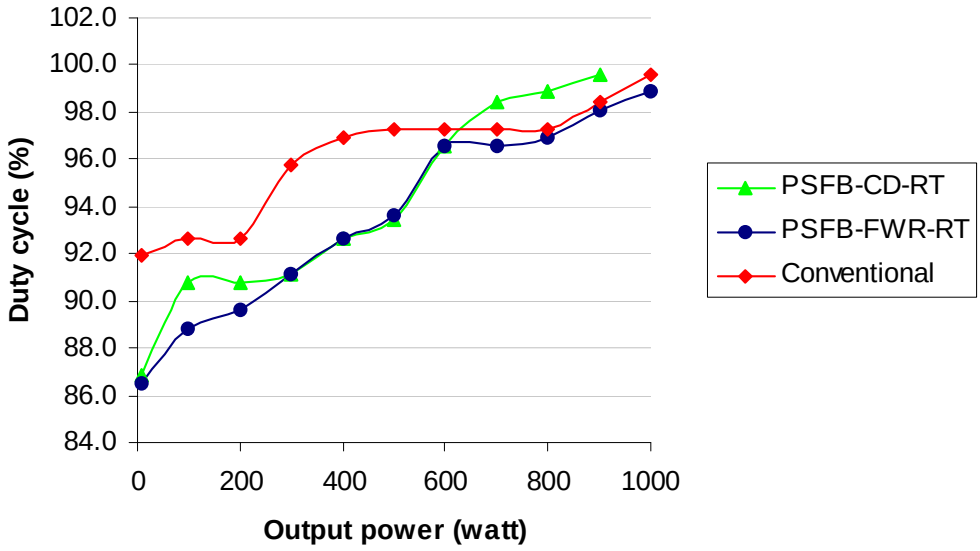

Figure 7.17: *Illustrates the duty cycle variation of a conventional PSFB (red line) and the optimised PSFB-CD (blue line) and PSFB-FWR (green line).*

arrangements proved to be the full-wave rectifiers and the current doubler with an optimised rotating transformer. The adjacent arrangement windings proved to be incapable of transferring the required amount of power in conjunction with a phase-shifted bridge. The extreme situation for testing the voltage gain is when the input voltage is at minimum. The available duty cycle should be enough to compensate for any voltage drops due to the leakage inductance. The duty cycle variation of a conventional PSFB and those of the PSFB-CD and PSFB-FWR for an input voltage 255V appear in figure 7.17.

Figure 7.17 shows that the PSFB-FWR converter was able to deliver the required output voltage even at the lowest rail of the DC input voltage (255V). The PSFB-CD was only tested up to 900W of output power where the maximum permissible duty cycle (96.6%) occurred. The PSFB-FWR generally operated with lower duty cycle than the conventional PSFB and the PSFB-CD which means that there is more headroom available for input voltage variations.

7.4.4 Efficiency

The results presented so far demonstrate an efficiency improvement of around 3% at full power (1kW) in comparison with the non-optimised prototype. The rotating transformer

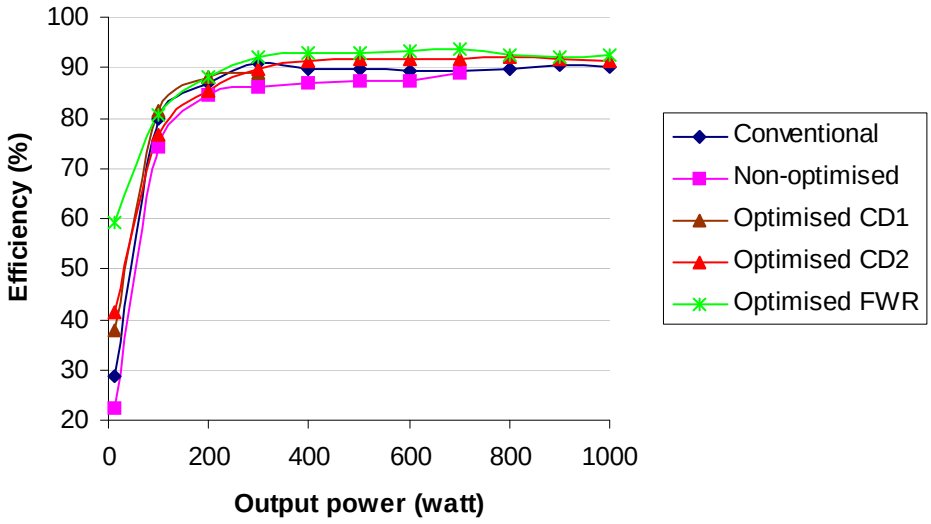

Figure 7.18: *Efficiency comparison of various PSFB arrangements. The green line refers to the PSFB-FWR prototype with an optimised rotating transformer with 1mm air-gap. The red and brown lines correspond to PSFB-CD converters with optimised split and non-split transformer windings respectively. The magenta and blue lines refer to PSFB-CD topologies with a non-optimised and a conventional transformer respectively.*

not only proves to be a viable option for a phase-shifted full bridge topology but it also seems to have improved performance. Figure 7.18 illustrates the efficiency readings taken on the PSFB with various rotating transformer modules and with two rectifier alternatives.

All converters performed well with the non-optimised and the conventional circuits delivering power with around 89% efficiency, whereas the optimised ones performed better (efficiency up to 94%). The optimised transformer with non-split windings was only tested up to 300W. Above this power the windings temperature exceeded the limits. The same happened with the non-optimised transformer, however this worked up to 700W of output power.

7.5 Electromagnetic Radiation

As seen in Section 7.3.2 the air-gap between the primary and secondary core halves results in a fringing magnetic field. The varying magnetic field creates a variable elec-

tric field and the result is an electromagnetic wave. The electromagnetic radiation can be accurately measured in certain specialised laboratories. The restriction of the electromagnetic emissions is required for both practical and regulation compliance reasons. Practically, the EM radiation should be reduced to avoid interference with other equipment or modules of the same system. For example, in the radar application the noise generated by the power supply is known to interfere with the radar receiver and thus reduce its accuracy. In addition to this there are national and international regulations that require the reduction of electromagnetic emissions to certain levels. Pre-compliance tests can be performed in the laboratory using a near field probe, an amplifier and a spectrum analyser/oscilloscope. The aim of the the pre-compliance tests performed here is the identification of the main noise sources and the comparison of the emitted radiation from a conventional converter and that with a rotating transformer.

Two tests were performed using the near field probe. Initially, the radiation around the transformer air-gap was investigated. It was suspected that the fringing field would cause emissions and this was quantified using the near field probe. The air-gap length was also considered. The acquired waveforms appear in figure 7.19 for different gap lengths (a) 1mm, (b) 0.5mm and (c) 0mm. For a 1mm air-gap the induced waveform has a peak value of 215mV and for an 0.5mm air-gap this is reduced to 106mV indicating a linear relationship between the air-gap length and the induced voltage.

As it can be seen in figures 7.19(a) and (b), the near-field probe waveform is practically the derivative of the magnetising current waveform. The reason is that the magnetic field energy stored in the air-gap represents the magnetising energy of the transformer[5]. As the magnetising inductance is high, it acts as a low pass filter rejecting the high frequency currents injected by the switching action. The linear relationship between the air-gap length and the induced voltage also shows that it is the result of the magnetising current. Dividing the air gap length by 2 results in (approximately) half the magnetising inductance and this in turn results in half the di/dt through it. Consequently, the voltage induced on the near-field probe is half of the one that would be induced around a 1mm air-gap. When there is no air-gap (note that the scale of channel 2 decreased from

[5]In an ideal transformer the primary ampere-turns equal the secondary ampere-turns and therefore the primary and secondary magnetomotive forces (MMF) cancel each other out. In a non-ideal transformer energy is being stored in the magnetic path (and mainly in the high-reluctance paths such as the air-gap).

200mV to 10mV in figure 7.19(c)) the induced voltage is almost zero. In practice when there is no air-gap the soft switching is partial as can be seen in figure 7.19(d) and as a result a small 15mV (peak) signal (with rich harmonic content) is induced on the probe.

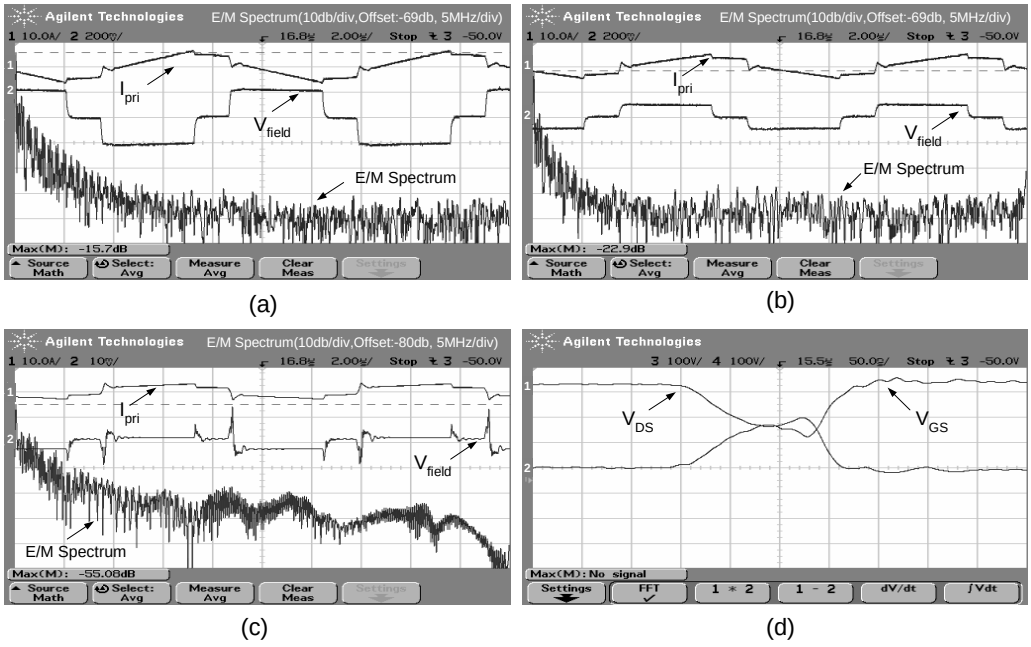

Figure 7.19: *The primary current I_{pri}, output of the near-field probe V_{field} and the respective frequency spectrum (Gain) of the electromagnetic radiation around a (a) 1mm, (b) 0.5mm, (c) 0mm air-gap, (d) shows the lack of soft-switching when the gap is 0mm hence the higher EMI. The converter operated at 500W of output power.*

The second test involves measurement of the switching-action related emissions. It is common knowledge that hard switching is a principal reason for high frequency electromagnetic radiation. The sharp edges of the currents and voltages turn printed circuit board tracks, components and every conductor of appropriate dimensions into antennas. So, the aim of this series of experiments is to demonstrate the improvement derived from quasi-resonant operation of the PSFB. The current slope (di/dt) and voltage slope (dv/dt) are decreased and the harmonic content of the current and voltage waveforms is reduced.

Considerable radiation of high frequency noise was detected close to the power switches. The noise originated from the PCB track connecting the middle point of the PA leg with the transformer. The probe tip was positioned along the track with an angle that resulted in maximum coupling of the noise. A way to locate the exact source of noise

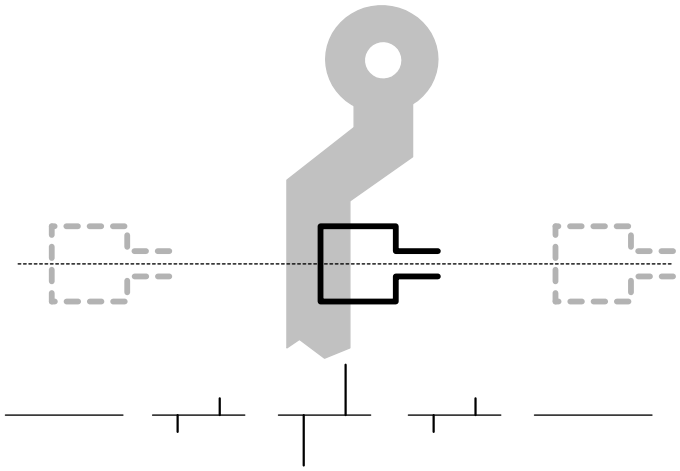

Figure 7.20: *Probe moving along an imaginary perpendicular to the track line.*

is by moving the near-field probe across an imaginary perpendicular to the track line (figure 7.20). The induced voltage will have a maximum amplitude when the probe is located directly above the emitting source.

The results of this test performed on the conventional BAE prototype (with a non-gapped coaxial windings and a pot core transformer) and the optimised PSFB-FWR with a rotating transformer appear in figure 7.21. The circuits were tested at different power levels to see what is the effect of no-soft switching (figure 7.21(b),(d)) and partial soft-switching (figure 7.21(f)). The indicator of the soft-switching ability of each circuit is the primary current waveform which appears at the top of each screen-shot. When the soft-switching is completed without the current reaching zero this means that there was more than enough energy to complete the resonant transition. As can be seen in figures 7.21(a), (c) and (e) that refer to the optimised converter the resonant operation was successfully carried by the primary current. However, in the figures on the right soft-switching was only partially completed. The resonant intervals of the switching cycle are indicated with the letter D.

The received signal from the near field probe is practically the derivative of the current waveform $L_{loop} \cdot \frac{di}{dt}$ (assuming perfect coupling between the track and the probe's loop). The voltage overshoots that are indicated with the letter B are the result of the current spikes due to switching. In the figures on the left (rotating transformer) the overshoot is lower than in the figures on the right (hard-switched conventional circuit). In particular the rotating transformer circuit induced 100mV on the probe versus a

250mV induced by the conventional circuit at 10W of output load. These figures are increased as the power output increases. However, as the power output increases the soft-switching ability of the conventional converter improves. At 500W of output power the conventional converter still produces higher voltage spikes than the circuit with the rotating transformer (approximately 600mV against 400mV for the resonant circuit).

Regarding the frequency spectrum of the induced voltage waveforms, the 100kHz component (point A) is higher in the converter with the rotating transformer. This is expected due to the higher current that circulates in the primary side. The main frequency of the additional magnetising current is 100kHz and the current waveform has a low harmonic content as its form is close to a sine-wave (no sharp edges). Therefore, the magnetising current is not a significant cause of electromagnetic noise.

Moving higher in the frequency spectrum, a peak can be observed in figures 7.21(a),(c) and (e) at 8.5MHz (indicated by point B). This is the resonant frequency between the MOSFET capacitance and the transformer's leakage inductance. At the resonant frequency the amplitude of the induced voltage on the probe is $54dB\mu V$ whereas the amplitude of the equivalent component of a conventional circuit is $67dB\mu V$. Note that the amplitude of the induced voltage around the area of 5-15MHz is higher in a conventional circuit. The area 5-30MHz marked as E in figures 7.21(b),(d) and (f) shows a higher radiated energy (with the exception of the 8.5MHz peak in the rotating transformer circuit). This is due to the high di/dt resulting from the hard switching of the MOSFETs. This proves that the harmonic content of the radiated waves is wider in the conventional circuit. The higher frequencies can turn components and heat sinks, even the power supply case into antennas that can cause the circuit to fail the regulation compliance tests.

The noise measurement results from the two circuits are summarised in tables 7.9 and 7.10 (at 100W of output power).

To summarise, more investigation is needed regarding the air-gap related emissions. Low frequency noise is apparently generated around the air-gap. However the high frequency radiation of the converter itself is reduced thanks to the soft-switching over the entire load range. The rotating transformer, although positioned next to the main switches and close to the driving circuit, did not cause any malfunction in the examined circuits.

Frequency (MHz)	H-field ($dB\frac{\mu A}{m}$)
0.1	150.0
5.0	110.0
7.5	96.8
10.0	105.0
15.0	80.5
20.0	75.0
25.0	75.0
30.0	67.8

Table 7.9: *The magnetic field around the pcb track of a PSFB with soft-switching operation (rotating transformer). The readings were taken at 100W of output load.*

Frequency (MHz)	H-field ($dB\frac{\mu A}{m}$)
0.1	138.0
5.0	115.0
7.5	107.8
10.0	103.0
15.0	84.5
20.0	94.0
25.0	90.0
30.0	73.8

Table 7.10: *The magnetic field around the pcb track of a PSFB with hard-switching operation (conventional converter). The readings were taken at 100W of output load.*

In practice, the rotating transformer will be enclosed in a case (see next section), so the possibility of interference with the circuit is reduced. Furthermore, EMI reduction measures can be taken into account when designing the rotating transformer housing in order to suppress the remaining radiation.

The magnetic field was also measured at 1m distance following the procedure described in the 'Radiation Limits and Measurement Standard' manual by the Radiocommunications Agency of UK [100]. The results appear in section C.3 of Appendix C.

7.6 Mechanical Implementation

The mechanical implementation of the rotating transformer is a challenging task. In the radar application the required clearance between the stationary and rotating part is 1mm or less. The power electronics design is tuned to accommodate the rotary interface.

A mechanical design of the rotating transformer is proposed in figure 7.22 (the prototype that was manufactured and used in the experiments, see figure C.3, is much simpler and

did not rotate). The rotating part has a diagonal line pattern and the stationary part is filled with a solid colour.

The housing shown in figure 7.22 is made of aluminum that is economic and lightweight. The mechanical design is expanded in figure 7.23.

When designing the transformer housing several requirements should be fulfilled:

- the accuracy of the relative positioning between the magnetic core halves,
- the magnetic core's expansion and contraction due to temperature variations,
- the high bandwidth feedback and data link between the stationary and rotating frames.
- any metallic parts (spacers, bushes, shafts) around the air-gap should be avoided or eddy currents will be developed.

Each of these aspects poses some additional constraints for the mechanical layout of the rotating transformer.

Relative positioning of the magnetic core halves This is an issue that becomes very important in applications such as the airborne radar where the system may operate under harsh conditions (extreme accelerations and decelerations as well as constant vibration during flights). The different forces should be taken into account when calculating the loading of the ball bearings.

In this work a modular solution is proposed according to which the rotating transformer is designed separately from the stationary and rotating frames of the radar. This approach has the advantage that the resulting rotating transformer can be reused in other designs. To dissociate the rotating transformer from the radar design the two modules are mechanically isolated (in that they do not have common parts).

The aim is an accurate relative positioning of the two core halves and consequently a possible reduction of the air-gap length. The vibration of the rotating frame and the centrifugal forces on the rotating load may cause instant displacement of the rotational axis. This could result in misalignment between the magnetic cores or even bring them

in contact and cause permanent damage. The solution to this problem is to make the stationary and rotating cores rotate around the same axis. This can be done using two deep groove ball bearings (Bore/Ext diameter: 2.953:3.74 inches of the SKF family) as shown in figure 7.22. The stationary part is then attached to the stationary frame of the radar using two sets of rod-end spherical bearings (maintenance-free plain spherical bearings SAKB 5 F family of SKF) (see figure 7.24). One of the rod-end spherical bearings is attached to the stationary frame and the other one to the housing of the primary core. The two bearings are connected to each other with a radius rod. The linked rod-end spherical bearings only remove one degree of freedom from the primary core; the rotational movement.

Figure 7.24: *The rod-end is used to allow movement in all dimensions but not rotation.*

Thermal issues The expansion and contraction of the ferrite pot core is an issue that requires special attention. Ferrite is very fragile and cannot tolerate external forces. The maximum operating temperature of the core is around 100^oC and, according to the manufacturers data, the tolerance in its dimensions (including the expansion and contration effects) is 0.25mm in the axial direction (air-gap) and 1.2mm in the radial direction for the selected material (3C90). The magnetic core should be allowed to expand in every direction. The temperature difference between different materials could also be an issue. Although the magnetic core itself exhibited very small temperature variations ($\Delta T_{max} = 10^oC$) measures were taken for the case of faulty operation resulting in high temperature rises. As seen in figure 7.23, several rubber o-rings may be used to allow space for the expansion of the magnetic core. The o-rings can also minimise the direct contact between the core and the housing which can be problematic at extreme temperatures.

To fix the axial position of the cores, a threaded bush should be glued in the centre hole

of the magnetic core (that also serves as housing for the LED).

Avoiding gluing any of the parts together is advantageous in that it allows quick replacement of the cores or any other parts in case of damage during prototyping.

Feedback loop Closing the feedback loop as well as transferring data is another issue when replacing the slip-rings with a rotating transformer. In this work an optical method is proposed for being immune to electromagnetic noise and the fringing magnetic field. A laser diode and receiver can be used to transfer analog or digital information. In case digital communication is preferred, the voltage sample of the power supply output has to be digitised using a converter. The information can be then transmitted with some type of modulation that will allow multiple channels of data. For transferring data through a rotary joint there are several commercial solutions such as the optical rotary joints (e.g. FO4698 by Moog components group[103]) that are based on optical fibres.

Many of the above difficulties during design could be avoided if a custom made magnetic core could be manufactured. As this design is only a proof of concept the use of existing materials and technologies for the construction was economically convenient. Further investigations and any possible commercial products should be custom made for optimum performance and reduced cost and processing time.

7.7 Chapter Summary

Initial experiments with non-optimised transformer structures showed that conventional design methodologies are not appropriate when a rotating transformer is used.

The potential of the phase-shifted full bridge converter was apparent from the initial experiments. Despite an abnormal transformer operation (high conduction losses), the converter efficiency reached 90%.

Both the adjacent and the coaxial winding arrangements were tested. As expected, the first performed poorly due to the high leakage inductance that caused voltage drops and hence deteriorated the voltage gain of the transformer. The duty cycle that was needed with an adjacent winding was 30% higher than that with a coaxial winding (to produce the same voltage and deliver 300W at the output).

Two topological alternatives were also tested. The current doubler has been traditionally used with a PSFB because of the assistance it provides to the soft-switching operation. This is done by providing more primary current during the PA interval. When a rotating transformer is used the primary current can be more than is needed for the resonant transitions. In this case the extra current provided by the current doubler causes extra conduction losses. This is the reason that the classic full-wave rectifier (with a tapped winding and two rectifier diodes) has performed better than the current doubler.

It is known that soft-switching in a converter reduces the power of the radiated electromagnetic field. Securing soft-switching down to no-load can help pass the, often troublesome, compliance tests. The rotating transformer itself is a source of noise due to the magnetic field escaping around the air-gap. Preliminary close-field measurements showed a low frequency content that did not affect the circuit operation. The radiation emitted by the PCB tracks adjacent to the power switches had a richer frequency content that was increased when the converter was hard-switching.

A possible mechanical implementation was discussed in section 7.6. Issues such as the expansion and contraction due to temperature, the accuracy in the relative positioning between the cores and the requirement for communications were discussed.

One of the main conclusions of this chapter is that the design of the rotating transformer is usually conduction loss limited. However, the magnetising current and winding resistance can be optimised so that minimum losses occur. The optimum transformer design in combination with a fully soft-switching converter gives a viable design.

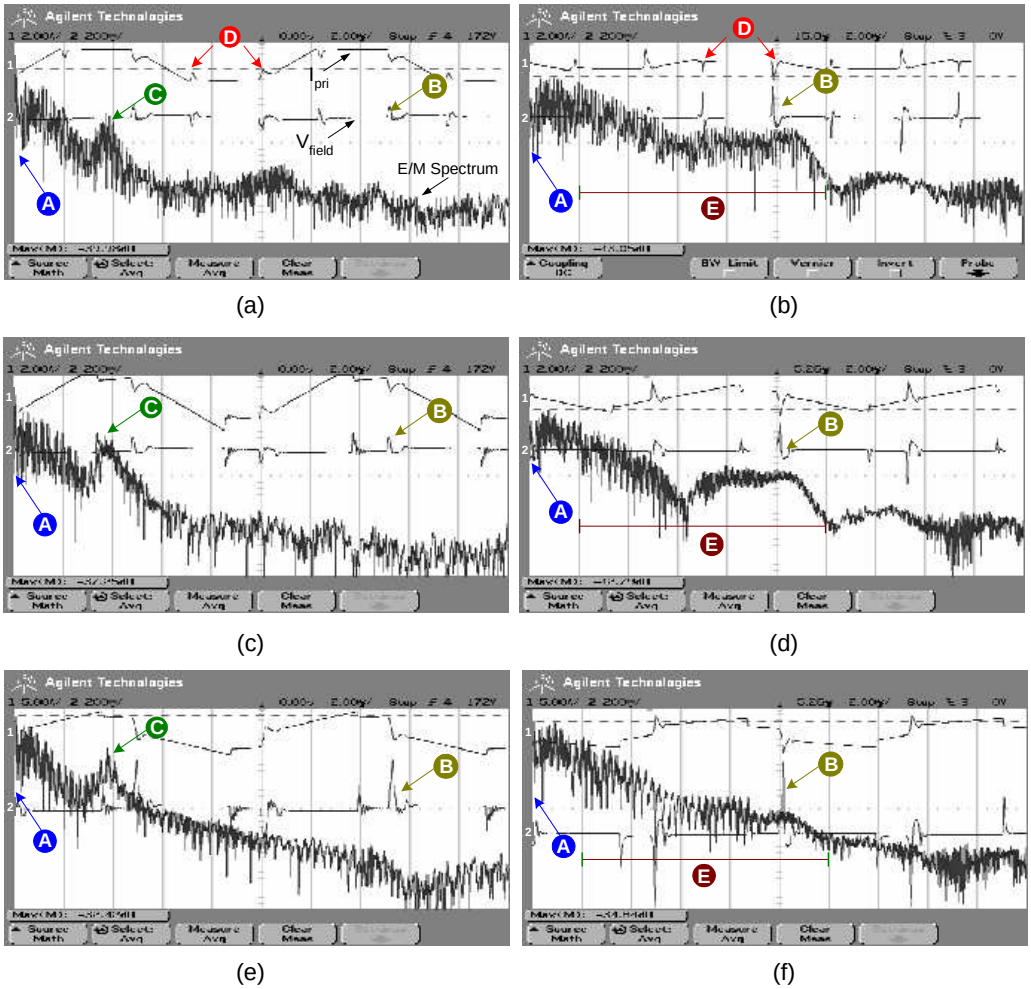

Figure 7.21: *Illustrates the primary current and near-field probe output waveforms along with the fft of the latter. The screenshots on the left ((a),(c),(e)) refer to a PSFB with a rotating transformer with an 1mm air-gap. The waveforms on the right ((b),(d),(f)) represent the conventional PSFB converter. (a) and (b) refer to 10W, (c) and (d) to 100W, (e) and (f) to 500W of output power.*

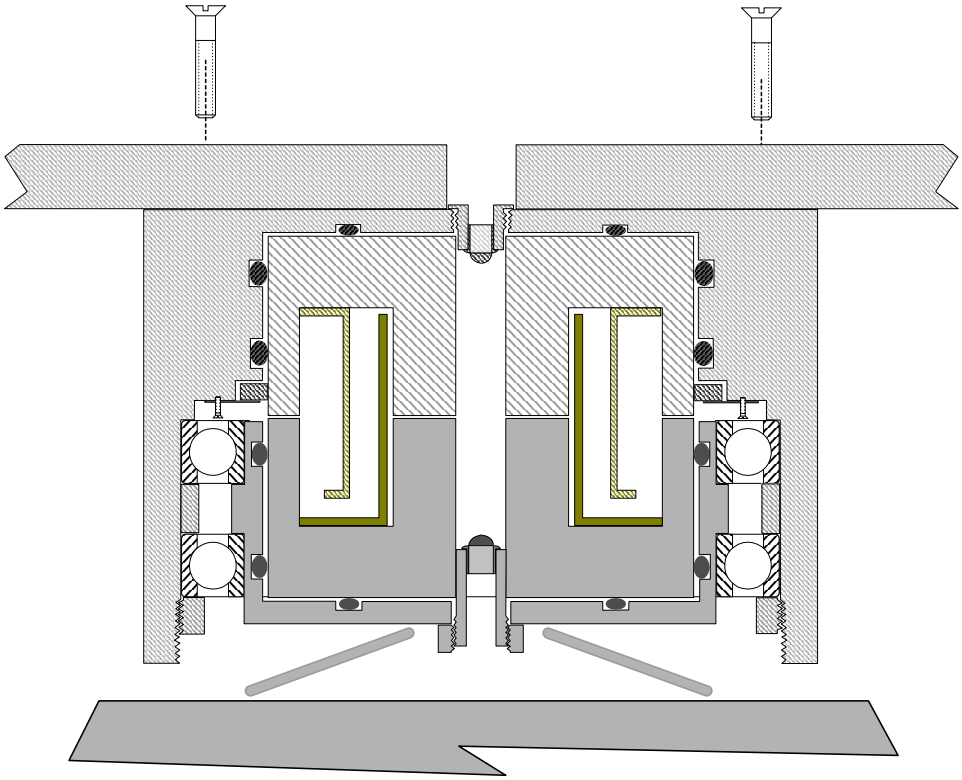

Figure 7.22: *The proposed assembly of the rotating transformer.*

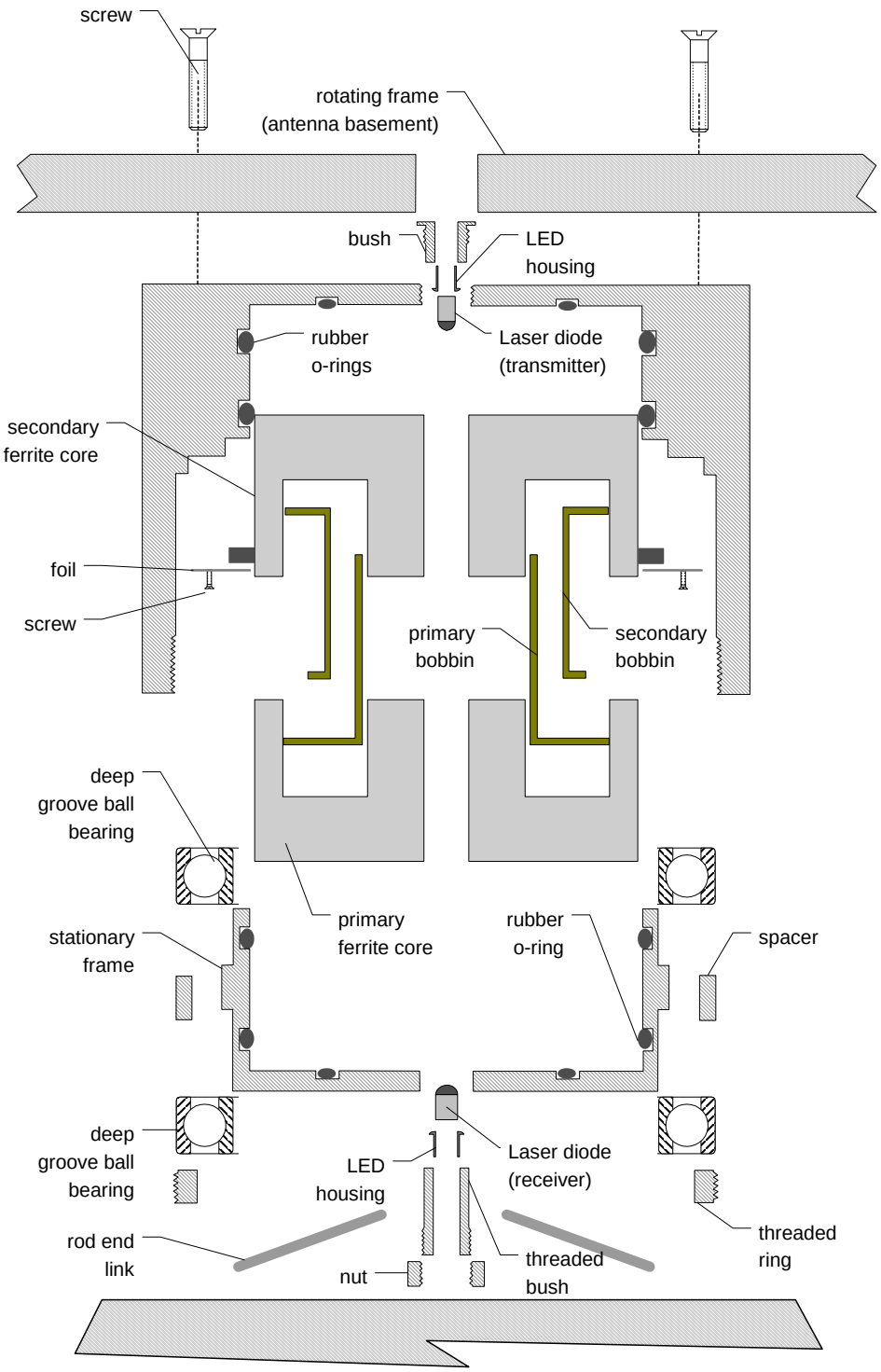

Figure 7.23: *The parts of the rotating transformer assembly.*

Chapter 8
Conclusion

Many applications require energy to be transferred from the stationary to the moving part of a device without the use of electrical contacts. This can be realised by using a magnetic link established by two coils, one on each side. The magnetic coupling between the stationary and moving equipment depends on the distance, alignment and the material between the coils. Designing a power supply that incorporates contactless transfer of energy requires combined optimisation of the magnetic component and the power electronics topology. The design process cannot be standardised, as the inductive couplers and their electrical behaviour differ considerably from application to application.

This project investigated a specific type of inductive coupler, the rotating transformer that is intended for use as an alternative to the traditional slip-rings. Regardless of the application the rotating transformers have some specific geometrical characteristics (pot core, fixed air-gap length, no windings misalignment) that result in a predictable electrical behaviour. This allows the derivation of a universal methodology for incorporating a rotating transformer into a phase-shifted full bridge converter.

To demonstrate the potential of the proposed methodology, a 1kW PSFB converter for an electronic scanning radar was designed and tested. BAE Systems, the sponsor of this project, typically use commercial slip-ring modules to supply the rotating frames of their radar systems. A more reliable and economic solution is in the company's interests. Replacing the rotary interface with minimum impact on the dc/dc converter design is an objective. Consequently, the use of the rotating transformer in conjunction with the PSFB was investigated.

Initial experiments demonstrated excessive winding losses and poor voltage gain of the rotating transformer. It was found that the inherent air-gap resulted in a very low magnetising inductance producing a very high magnetising current. This high magnetising current in turn produced high conduction losses. Additionally, the physical separation

of the transformer windings resulted in increased leakage inductance. The voltage drop across the leakage inductances was the reason for the poor voltage gain. The traditional transformer design methodology failed to produce a viable rotating transformer design. In the proposed design methodology, special consideration is given to the excessive magnetising current and its effect on the conduction and switching power losses.

During the course of this project the potential and the limitations of the PSFB with a rotating transformer were uncovered. The research was based upon the hypothesis that the phase-shifted full bridge can effectively utilise the parasitic components of the rotating transformer in order to achieve efficient (over 90%) power conversion at the kW range. This thesis has been verified by demonstrating a converter prototype with an average efficiency of 92.6% from 0.3 to 1kW of output power and a peak efficiency of 93.6% at 700W[1].

8.1 Conclusion

In the proposed phase-shifted bridge converter, the rotating transformer has a triple role: power transfer, isolation, and energy storage. The auxiliary inductance in a conventional PSFB is not required as the rotating transformer can secure the necessary energy storage to facilitate soft-switching. Provided that the transformer is designed according to the proposed methodology, zero voltage switching of the main switches takes place over the entire load range. Also, the soft-switching proves beneficial for the electromagnetic emissions of the converter due to the elimination of the steep slopes in the voltage and current waveforms[2]. When a rotating transformer is used, the magnetising current alone may cause considerable switching losses even at no-load operation. Therefore, soft-switching is valuable under any loading condition.

The rotating transformer power handling capability is usually limited by the winding power losses. As a result the magnetic core size usually depends on the required number of winding turns and their thickness rather than the flux density. To fit the required number of turns the rotating transformer requires a larger core than that of a conventional converter. In this project the cross sectional area of the rotating transformer is

[1] For comparison, the conventional converter by BAE Systems demonstrated a maximum efficiency of 91%.

[2] The reduction of the di/dt and dv/dt also reduces the possibility of a switch failure.

almost 3.5 times greater than it is actually required to handle the flux density. This is partly because of the need for multi-stranded windings and also to allow enough space between the stationary and rotating windings.

Among the two proposed winding arrangements, the adjacent and the coaxial, the latter performs better in terms of power losses and the voltage gain it delivers. The adjacent winding arrangement causes large voltage drops across the leakage inductances and as a result the duty ratio should increase to compensate. The increase of the duty ratio results in a higher magnetising current which in turn increases the conduction losses. As a conclusion, the adjacent winding arrangement limits the power capability of the converter. Leakage inductance compensation may be a solution, however this requires further investigation. On the other hand, the coaxial winding arrangement demonstrated a high efficiency and a voltage gain similar to that of a conventional transformer. To avoid eddy currents that limited the effective conductive area of the windings, the secondary winding turns were split in two groups placed away from the air gap area. This reduced the effective resistance of the windings considerable and boosted the overall efficiency of the converter. The disadvantage of the coaxial arrangement is the extra complexity in the mechanical design.

The current doubler and full-wave rectifiers were tested with the PSFB and the rotating transformer. The current doubler is often used with a PSFB topology because it extends the soft-switching capability of the bridge. In this application the magnetising current proved to be enough to handle the resonant transitions of the switches. Therefore the need for additional primary current provided by the current doubler is not justified. On the contrary, it was found to have a negative effect on the primary side conduction losses. On the other hand, the full wave rectifier performed equally well regarding the soft-switching and also slightly improved the converter efficiency. In terms of size and cost both rectifier circuits occupy the same space as they use the same number of diodes and the filter size is the same.

A comparison of the approximate weight, volume and cost of the key components of the slip-rings and rotating transformer solutions is presented in table 8.1[3].

[3]All values are per converter module for a total of 12 converters. All costs are estimated using the current supplier catalogues. Where customised constructions are needed, the labour cost is included.

	Slip-ring solution			Rot. transformer solution		
	weight (gr)	vol. (cm^3)	cost (sterling)	weight (gr)	vol. (cm^3)	cost (sterling)
Transformer	280	48.5	10.0	650	88.2*	60.0**
Aux. Inductor	120	13.4	4.0	-	-	-
MOSFETs	30	1.6	4.8	30	1.6	4.8
Slip-ring module	1400**	982.7	333.0	-		
Rotary Housing	-	-	-	2000**	880.2	80.0
Data link	-	-	-	200**	-	20.0**
TOTAL	1830	1046.2	351.8	2280	881.8	164.8

*This volume is included in the rotating transformer housing.
**This is an estimate.

Table 8.1: *Estimated weight, volume and cost of the slip-ring and rotating transformer solutions*

Figure 8.1: *The slip-ring module that is currently used for this applications by BAE Systems. Its diameter is approximately 200mm and its length is 369mm.*

The slip-ring module that is currently used by BAE Systems (AC6098-12 family by Litton-ps) provides 42 signal rings and 10 power rings (up to 30A at 600V). The component is a compact, well designed module that appears in figure 8.1 (the size depends on the total operating voltage and current). The size of the slip-ring module that is required in the radar application has a radius of 101mm and a length of 368mm. Ten to twelve rotating transformer modules (figure 8.2) are needed to transfer the same power as the slip ring module of figure 8.1. The total size of the rotating transformers stack would have a radius of 68mm and a length of around 1m (including the housing).

Figure 8.2: *The rotating transformer module. The rotating interface comprises of 10-12 such transformers and has a diameter of 136mm and a length of approximately 1000mm.*

The rotating transformer and associated components incur a 53% lower cost, occupy 15% less space and weigh approximately 25% more in comparison with the slip-ring solution.

The combination of the rotating transformer with a phase-shifted full bridge produces an efficient and reliable power supply. The rotating transformer with 1mm air gap between the core halves improved the overall efficiency of the power supply by approximately 2% surpassing the initial target of 90% that was set by the sponsoring company. This project concentrated on the electronic design of the contact-less power supply and proved its feasibility. During this study, some issues related to the mechanical implementation and the electromagnetic compatibility of the rotating interface were raised and proposed for future investigation.

8.2 Future Work

This 3-year project provided an opportunity for an in-depth study of the operation of a rotating transformer in combination with a phase-shifted bridge topology. Several aspects of this study generated additional questions and challenges for further investigation. Due to the limited time scales some of these research tasks are proposed for future work.

The fringing field effect proved to be important in this application. When a conventional winding technique was used, the winding losses were radically increased. The fringing field had an effect on the current distribution within the transformer windings. Quantifying the effect of the fringing field in the conduction losses could be carried out with a finite element package. As the fringing field results in considerable electromagnetic radiation, a more careful consideration of EMC should be part of any future work.

The optimisation algorithm could be used to predict the losses under variable frequency, air-gap, different waveforms, winding geometries etc. The effect of the frequency on the conduction losses is expected to be especially significant. Taking into account that the rotating transformer secures the soft-switching operation over the entire load-range, a higher frequency of operation should have minimum effect on the switching losses. The above assumption could be verified by optimising the objective function with respect to frequency, number of turns and wire thickness.

The total converter losses could be also optimised. The current optimisation algorithm starts by eliminating the switching losses and then minimises the winding and MOSFET conduction losses. This may not lead to minimum overall losses if the rotating transformer air-gap is very small so that the transformer resembles a conventional transformer. To extend the capabilities of the current optimisation algorithm the calculation of the switching losses with respect to the number of turns, air-gap length and frequency is needed.

The proposed design methodology assumes a relatively low voltage drop across the leakage inductances and does not adjust the duty ratio to compensate for the voltage drops. This is a limitation related with MathCad and its inability to perform iterative calculations with feedback. Despite the minor effect of this assumption (that only affected the adjacent windings results), implementing the optimisation algorithm in an advanced mathematical software should be one of the future steps.

Finally, the mechanical implementation of the rotating transformer is a challenging task for the mechanical engineers as several issues need to be resolved. In particular, stacking more than one transformer to increase the power capability is a requirement in the radar application. The ideal design would have a modular structure so that modules could be added and removed without the need to redesign the transformer housing. Special attention should be given to housing the stationary and rotating power and signal cables that exit the transformer cores. The magnetic core geometry is also something to reconsider if the product is to be commercialised. As mentioned above the core size is greater than it is magnetically needed (to accommodate the expected flux density). A way to keep the window area wide enough to accommodate the windings but also make better use of the magnetic material should be sought.

The design methodology presented in this thesis delivered a high-performance power converter with a rotating transformer. The efficiency of the circuit surpassed not only the initial target of 90% but also the efficiency of an equivalent PSFB converter with a conventional transformer. Among the most important findings of this work is that reducing the air gap does not necessarily result in an efficiency improvement despite the reduction in magnetising current and reactive power in the transformer. On the contrary the presence of leakage inductance in combination with an appropriate magnetising current may boost the overall efficiency and secure a wide range of soft-switching operation.

A universal approach for designing such systems does not exist due to the diversity in topologies and interfaces. The proposed design method offers a platform that can be easily adjusted to assist with the optimisation of any similar power supply architecture.

Appendix A
Transformer Modelling

A.1 Inductance Calculation

In the following analysis the magnetising and leakage inductances are associated with the physical characteristics of a gapped transformer. Assume the transformer of Figure A.1. The first step for calculating the wanted inductances is identifying the points where magnetic energy is stored (or in other words the magnetic flux paths).

Magnetising inductance In a gapped transformer the energy is mainly stored in the air gap. Nevertheless, for increased accuracy the energy in the magnetic core is also taken into account. In the following manipulation the magnetic core's cross sectional area A_c is assumed to be equal to that of the air gap A_g. It is useful to remember the equation giving the magnetic energy stored in a volume V.

$$E = \frac{1}{2}\int_V B \cdot H dV = \frac{1}{2}\int_V \mu_a \cdot H^2 dV \tag{A.1}$$

where B and H are the magnetic field density and magnetic field intensity integrated over the volume V of the medium were energy is stored. The total energy stored in the magnetic core and in the air gap is,

$$E = \frac{1}{2}\cdot\int_{V_g} \mu_0 \cdot H_g^2 dV_g + \frac{1}{2}\cdot\int_{V_c} \mu_{a_c} \cdot H_c^2 dV_c \tag{A.2}$$

where the subscript g denotes a quantity referring to the air gap and the subscript c denotes quantities related to the magnetic core. The volume occupied by the magnetic core and the air gap is given, respectively, by,

$$V_c = A_c \cdot l_c \qquad V_g = A_g \cdot l_g \tag{A.3}$$

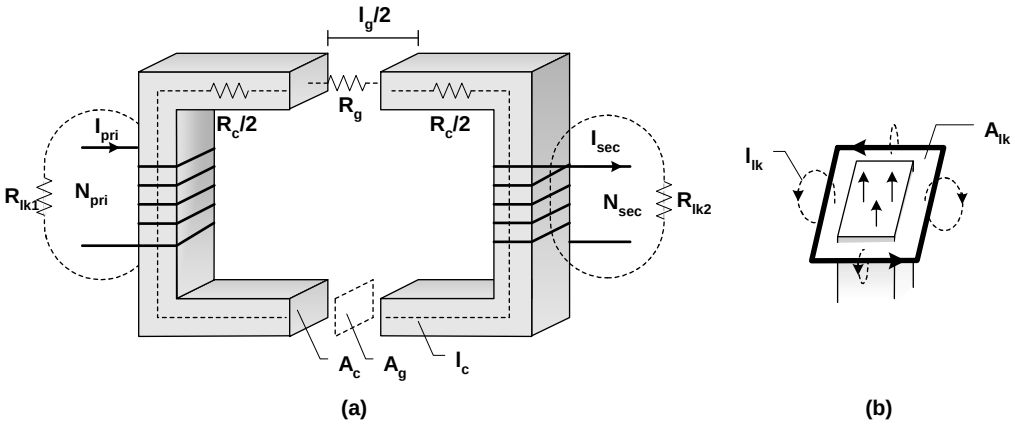

Figure A.1: *The magnetic flux paths in (a) a transformer with a gap between the core halves and (b) the top view of one of the limps*

The magnetic energy is also equal to,

$$E = \frac{1}{2} \cdot L_m \cdot I_{pri}^2 \tag{A.4}$$

where I_{pri} is the current in the primary winding. The field intensity H required in Equation A.1 is given by,

$$H = \frac{\Phi}{A\mu_a} \tag{A.5}$$

where Φ is the magnetic flux through the winding, A is its cross-sectional area and μ_a the absolute magnetic permeability of the material. The flux Φ is given by,

$$\Phi = \frac{N_{pri} \cdot I_{pri}}{R_c + R_g} \tag{A.6}$$

where R_c and R_g the reluctances of the core path and the air gap respectively,

$$R_c = \frac{l_c}{\mu_{a_c} \cdot A_c} \qquad R_g = \frac{l_g}{\mu_0 \cdot A_g} \tag{A.7}$$

where l_c,l_g the lengths of the core and air paths respectively and A_c,A_g their respective cross sectional areas. Note that Equation A.6 is the magnetic dual for Ohms law where

Φ is the dual quantity of the electric voltage, $N_{pri}I_{pri}$ is the magnetic current (equivalent of electric current) and the reluctances are equivalent to the electric resistances.

From Equations A.5 and A.6 we solve for the magnetic field intensity,

$$H_g = \frac{\Phi}{\mu_0 \cdot A_g} = \frac{N_{pri} \cdot I_{pri}}{\mu_0 \cdot A_g} \left(\frac{l_c}{\mu_{a_c} \cdot A_c} + \frac{l_g}{\mu_0 \cdot A_g} \right)^{-1} \tag{A.8}$$

$$H_c = \frac{\Phi}{\mu_{a_c} \cdot A_c} = \frac{N_{pri} \cdot I_{pri}}{\mu_{a_c} \cdot A_c} \left(\frac{l_c}{\mu_{a_c} \cdot A_c} + \frac{l_g}{\mu_0 \cdot A_g} \right)^{-1} \tag{A.9}$$

Combining Equations A.8 and A.9 with Equation A.2 and solving for L_m yields,

$$L_m = N_{pri}^2 \cdot (R_g + R_c)^{-1} \tag{A.10}$$

Equation A.10 gives the magnetising inductance measured from the primary side of the transformer. Note that the inductance is only depended on the number of turns and the physical structure of the transformer. This is a very important conclusion that can help in the optimisation of the design.

Leakage inductance A similar procedure can be followed to work out the leakage inductance of the primary and secondary windings. Equation A.10 was derived without taking into account any of the physical characteristics of the transformer. Therefore it must be valid for the leakage inductances as well,

$$L_{lk1} = N_{pri}^2 R_{sp1} \qquad L_{lk2} = N_{sec}^2 R_{sp2} \tag{A.11}$$

where R_{sp1} and R_{sp2} is the space where the primary and the secondary leakage flux stores energy, respectively. Generally, calculating the leakage inductance is more difficult as the exact path of the leakage flux is not known. In addition, the geometry of the path where leakage energy is stored is usually not symmetric resulting in difficult to solve elliptic and other integrals (can mention some papers on leakage calculation). Therefore, some assumptions are made in order to calculate the reluctance in cost of accuracy.

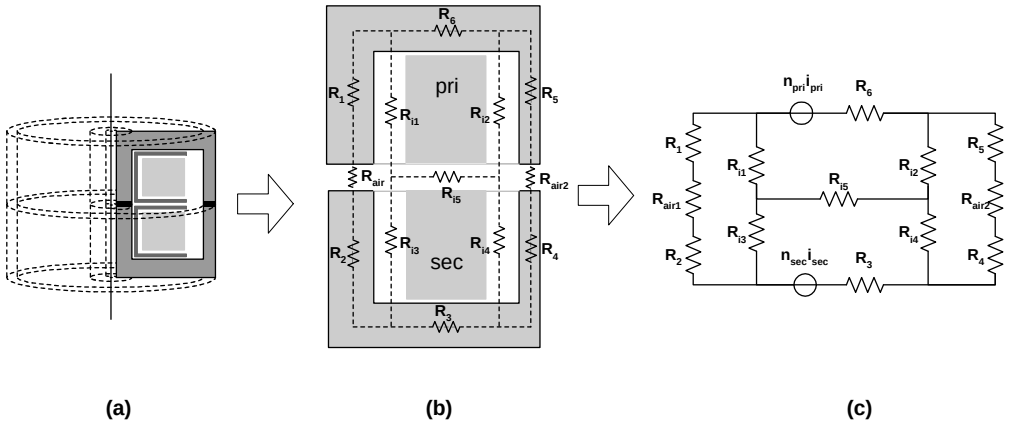

Figure A.2: *(a) Perpendicular cut of the adjacent windings transformer and (b) complete equivalent magnetic circuit*

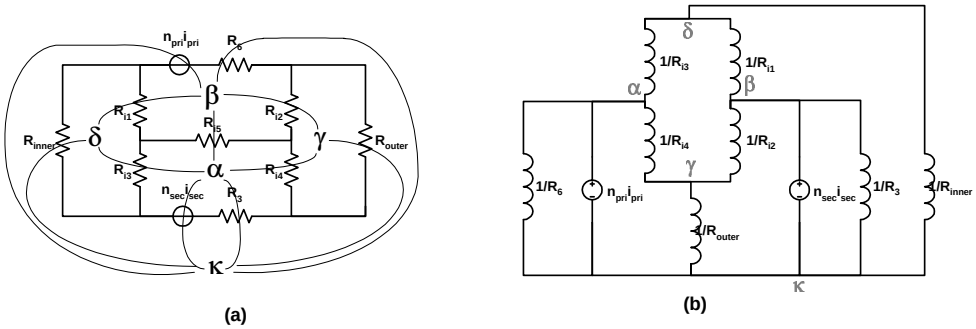

Figure A.3: *Duality transformation of the magnetic circuit of the adjacent windings transfomer.*

A.2 Complete Reluctance model for the adjacent arrangement

After the basic expressions have been derived for a simple transformer structure, a more detailed and accurate model for the same transformer can be discussed.

Figure A.2 illustrates a cut of the adjacent winding transformer and the equivalent magnetic circuit.

Figure A.3 demonstrates the duality transformation.

The resulting network is complicated and has no practical value as its relationship with the physical dimensions of the core and windings is vague. A simpler reluctance network is therefore used in chapter 4.

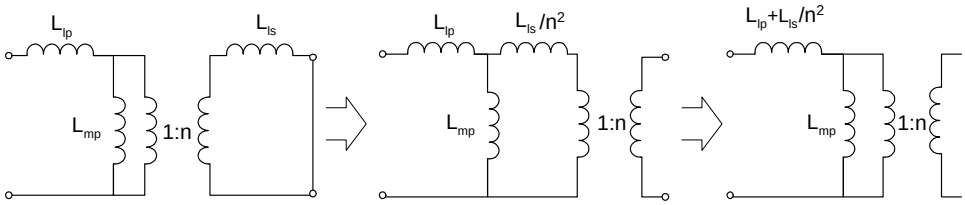

Figure A.4: *Transformation from a three element to two element T-model under the assumption that* $L_{mp} >> L_{lp}$.

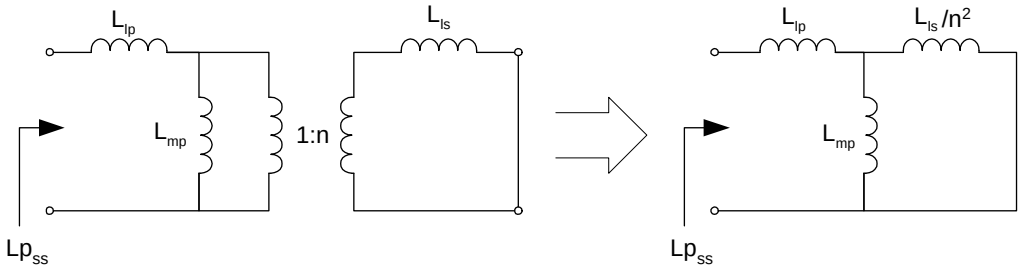

Figure A.5: *T-model and equivalent when measuring the* $L_{p_{ss}}$.

A.3 Transformer Characterization

To characterise a transformer electrically two major approaches are used. The two-test approach is quicker to perform and requires less calculations. It is however only accurate under conditions. The three test approach is only needed for transformers with high leakage inductance and requires some more calculations. They are both described below.

The two-test approach This is based on a simplification of the T-model of the transformer Figure A.4.

The assumptions allowing this simplification are that the magnetising inductance is very big compare to the primary and secondary leakage inductances and also that the primary and secondary leakage inductances are equal. Thus the current flowing through the magnetising inductance is very small and the secondary leakage can be moved to the primary side. Thereby, the leakage inductances add and are measured as one lumped element as shown in Figure A.4.

This test involves measuring the primary winding inductance $L_{p_{ss}}$ when the secondary is short-circuited and the second test requires measuring the primary winding inductance $L_{p_{oc}}$ when the secondary is open-circuited.

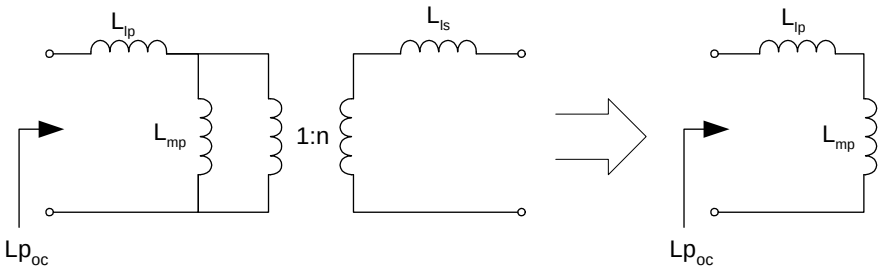

Figure A.6: *T-model and equivalent when measuring the $L_{p_{oc}}$*

As seen in Figure A.5 the equivalent input inductance $L_{p_{ss}}$ of a transformer with a short-circuited secondary winding is given as the sum of the primary leakage inductance L_{lp} and the parallel combination of the primary magnetising L_{mp} and secondary leakage inductance L_{ls} multiplied with the turns ratio (as it is moved to the primary):

$$L_{p_{ss}} = L_{lp} + \frac{1}{\frac{1}{n^2 L_{ls}} + \frac{1}{L_{mp}}} \tag{A.12}$$

Also, the equivalent input inductance $L_{p_{oc}}$ of a transformer with an open-circuited secondary winding is, as shown in Figure A.6, the primary leakage inductance L_{lp} plus the primary magnetising inductance L_{mp}.

$$L_{p_{oc}} = L_{lp} + L_{mp} \tag{A.13}$$

By combining Equations A.12 and A.13 remembering also that L_{mp} is assumed very large we get the following three equations:

$$L_{mp} = L_{p_{oc}} - L_{lp} \tag{A.14}$$

$$L_{lp} = \frac{L_{p_{ss}}}{2} \tag{A.15}$$

$$L_{ls} = \frac{n^2 L_{p_{ss}}}{2} \tag{A.16}$$

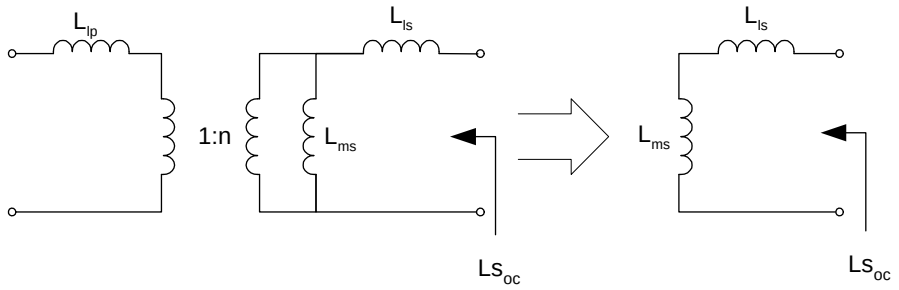

Figure A.7: *T-model and equivalent when measuring the $L_{s_{oc}}$.*

The three-test approach This approach involves one additional test, the output inductance $L_{p_{oc}}$ measurement under an open-circuited primary winding. This test is illustrated in figure A.7.

The impedance seen from the output is,

$$L_{s_{oc}} = L_{ls} + L_{ms} \tag{A.17}$$

The relationships between the primary and secondary magnetising inductances and the mutual inductance are,

$$L_{mp} = \frac{1}{n}M \tag{A.18}$$

and

$$L_{ms} = nM \tag{A.19}$$

By combining Equations A.12, A.13, A.17,A.18 and A.19 we get an expression for the mutual inductance:

$$M = \sqrt{(L_{p_{oc}} - L_{p_{ss}})L_{s_{oc}}} \tag{A.20}$$

Thus, using Equations A.18 and A.19 one can work out the magnetising inductances as seen from either side. Also by solving Equations A.17 and A.13 for L_{ls} and L_{lp} we get the the secondary and primary leakage inductances.

A.4 Custom made coil formers (bobbins)

The impact of the windings layout in the transformer electrical behaviour has been pointed out in 4. Customising the coil formers gives the engineer a relatively easy and cheap way of adjusting the leakage inductance and winding resistance of the windings. In this rotating transformer design priority was given to the reduction of both the windings resistance and the leakage inductance. Consequently, the aim was to reduce the distance between the two windings. This involves an increase of the manufacturing cost (that is proportional with the construction accuracy).

Three types of bobbins were constructed in the school workshops according to the mechanical designs appearing in figures A.8,A.9 and A.10. The first was used for the coaxial winding arrangement and the second and third for the coaxial windings (secondary and primary respectively).

A.5 Transformer model verification

The following graphs verify the accuracy of the transformer model that was derived for the transformer. Note that the model is valid around the 100kHz area where the transformer characteristics where measured. Also note that the model has a frequency dependence mainly regarding the windings AC resistance. The following graphs have been produced using an adaptive model that takes into account the frequency and adjusts the windings resistance.

The main discrepancy that can be observed is at frequencies below 1000Hz where the transformer starts being lossy and the quality factor of the winding drops. The very low quality factor essentially challenges the accuracy of the readings. As a result the phase graphs are different at low frequency. This however is well-below the operating frequency of the transformer therefore the discrepancy can be ignored.

The graphs illustrate the impedance magnitude vs frequency as measured with a bridge (left graph) and as calculated using the adaptive model (right graph). The adjacent winding arrangement with 0,1,2mm air gaps is first tested and the coaxial winding arrangement with the same air gap lengths follows.

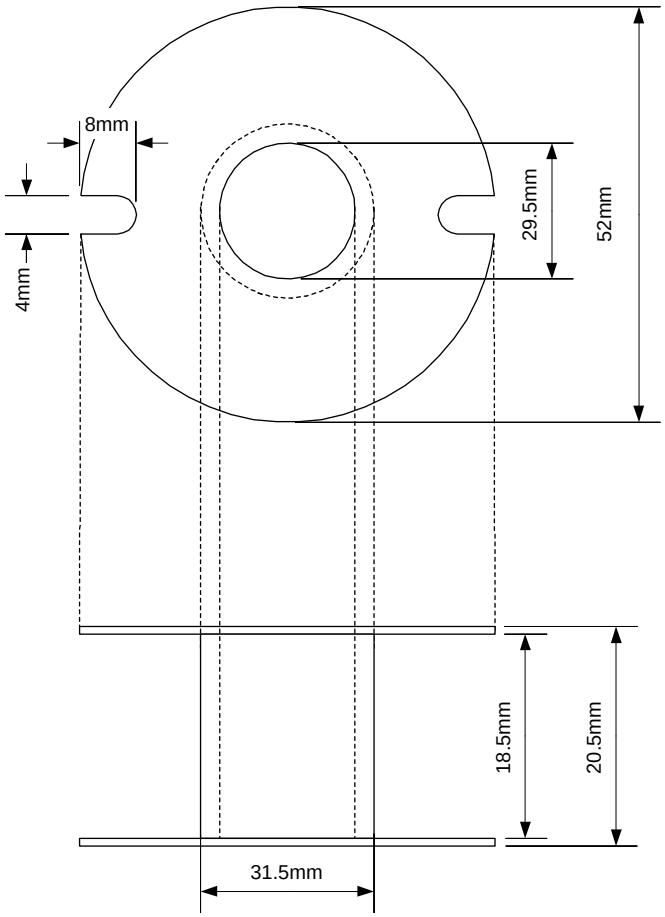

Figure A.8: *The mechanical layout of the custom made coil former used for the primary and secondary windings of the adjacent windings arrangement.*

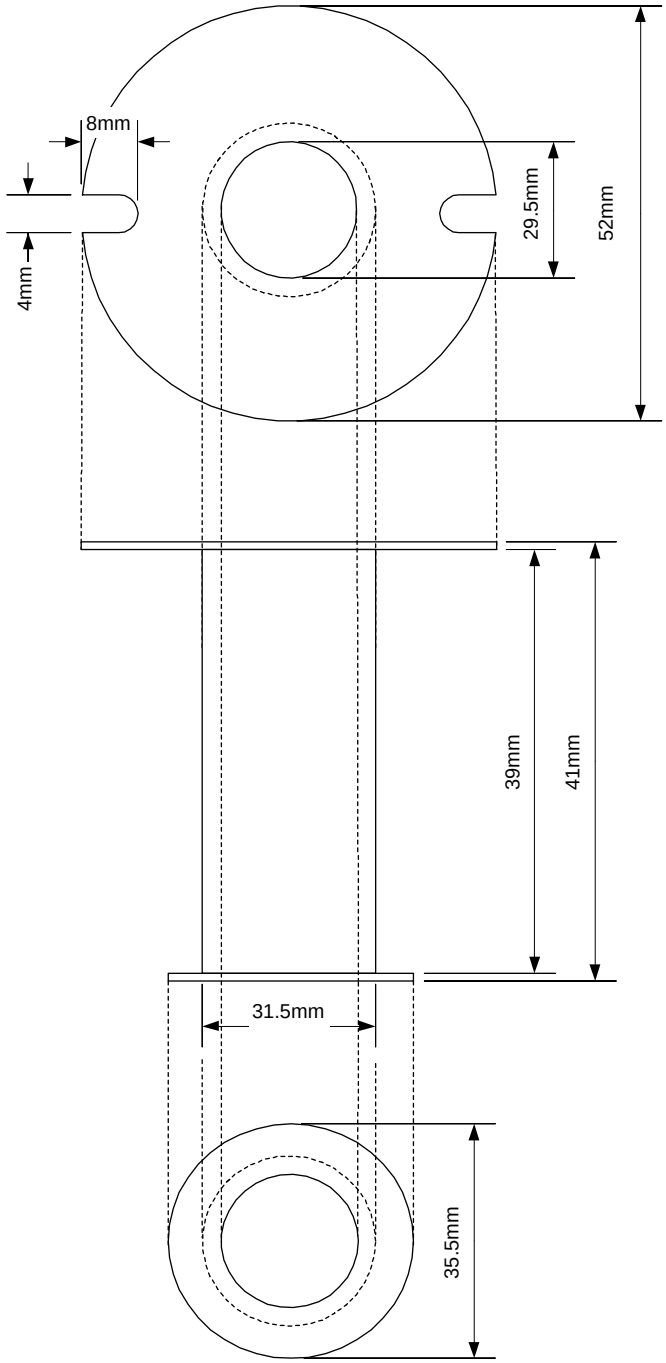

Figure A.9: *The mechanical layout of the custom made inner coil former used for the secondary winding of the coaxial windings arrangement.*

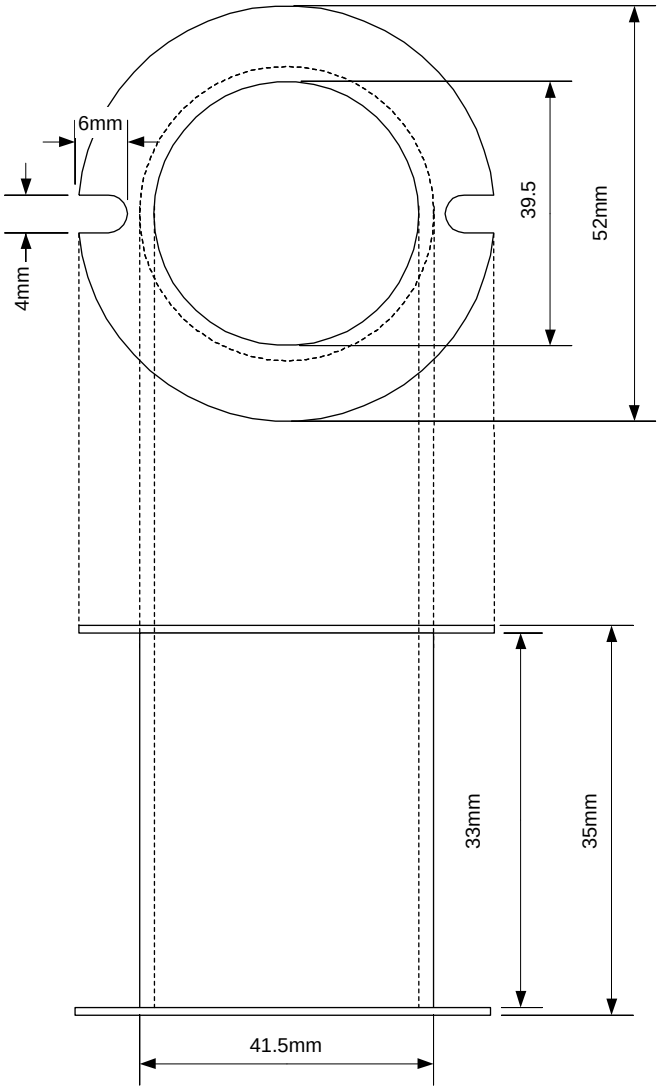

Figure A.10: *The mechanical layout of the custom made outer coil former used for the primary winding of the coaxial windings arrangement.*

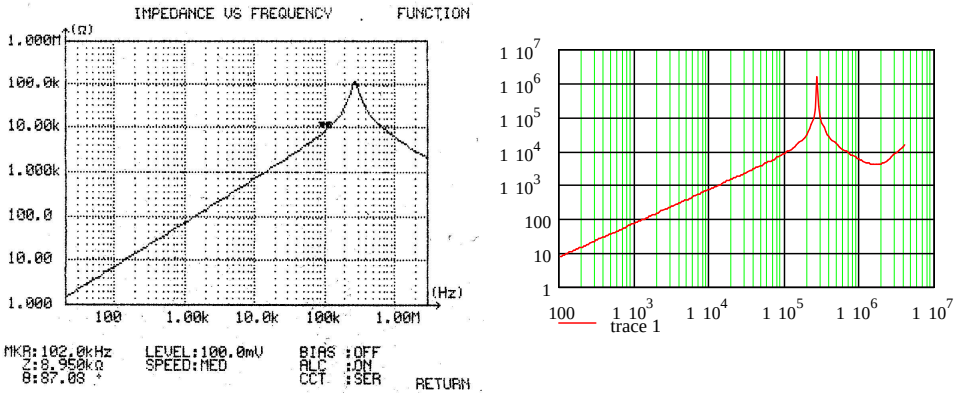

Figure A.11: *The graphs illustrate the magnitude of the input impedance $Z_{p_{oc}}$ (with the secondary winding open) versus frequency. The transformer has an adjacent winding arrangement and the distance between the magnetic core parts is 0mm. The measured results appear in (a) and the theoretical prediction in (b).*

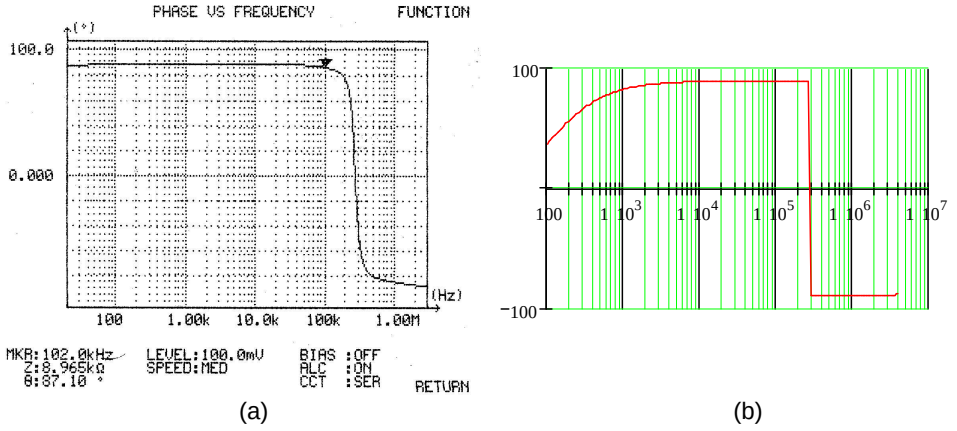

Figure A.12: *The graphs illustrate the magnitude of the input impedance $Z_{p_{oc}}$ (with the secondary winding open) versus frequency. The transformer has an adjacent winding arrangement and the distance between the magnetic core parts is 0mm. The measured results appear in (a) and the theoretical prediction in (b).*

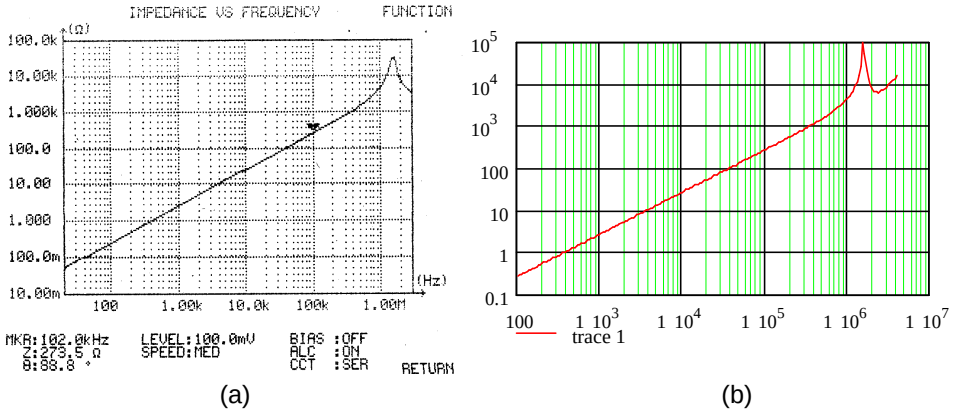

Figure A.13: *The graphs illustrate the magnitude of the input impedance Z_{poc} (with the secondary winding open) versus frequency. The transformer has an adjacent winding arrangement and the distance between the magnetic core parts is 1mm. The measured results appear in (a) and the theoretical prediction in (b).*

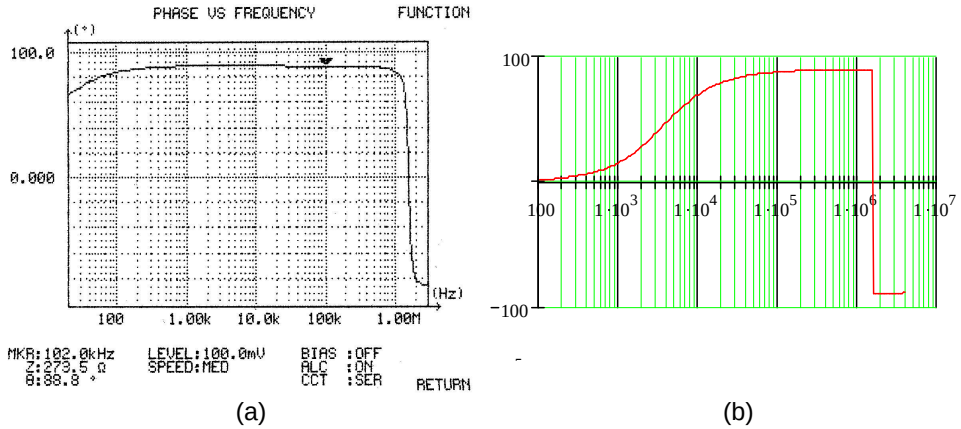

Figure A.14: *The graphs illustrate the magnitude of the input impedance Z_{poc} (with the secondary winding open) versus frequency. The transformer has an adjacent winding arrangement and the distance between the magnetic core parts is 1mm. The measured results appear in (a) and the theoretical prediction in (b).*

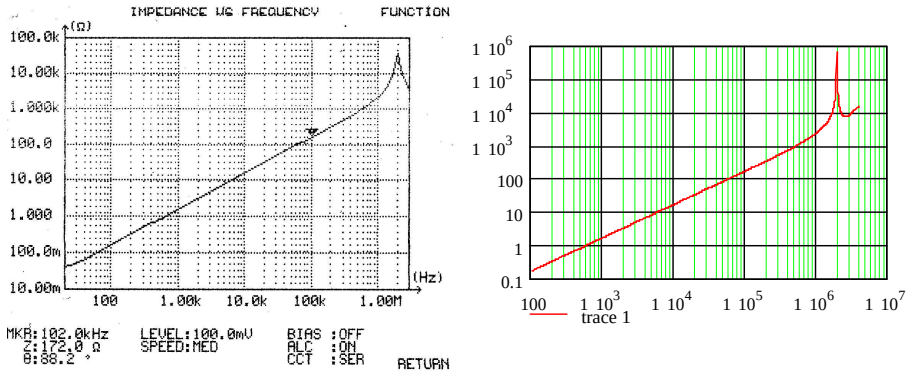

(a) (b)

Figure A.15: *The graphs illustrate the magnitude of the input impedance Z_{poc} (with the secondary winding open) versus frequency. The transformer has an adjacent winding arrangement and the distance between the magnetic core parts is 2mm. The measured results appear in (a) and the theoretical prediction in (b).*

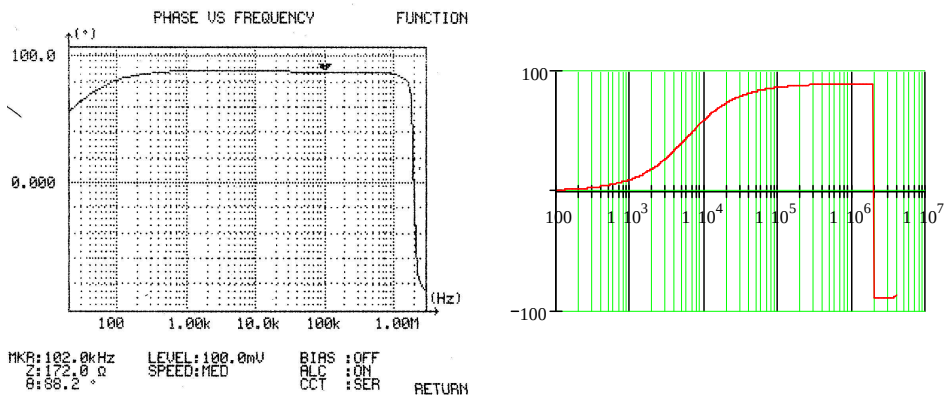

(a) (b)

Figure A.16: *The graphs illustrate the magnitude of the input impedance Z_{poc} (with the secondary winding open) versus frequency. The transformer has an adjacent winding arrangement and the distance between the magnetic core parts is 2mm. The measured results appear in (a) and the theoretical prediction in (b).*

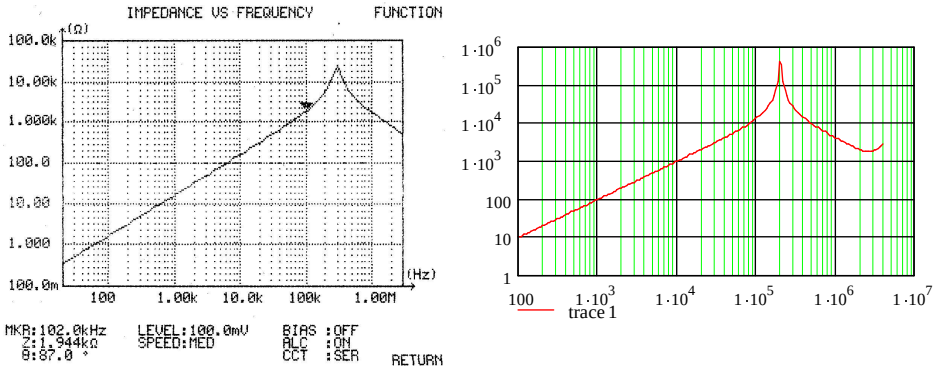

Figure A.17: *The graphs illustrate the magnitude of the input impedance Z_{poc} (with the secondary winding open) versus frequency. The transformer has an coaxial winding arrangement and the distance between the magnetic core parts is 0mm. The measured results appear in (a) and the theoretical prediction in (b).*

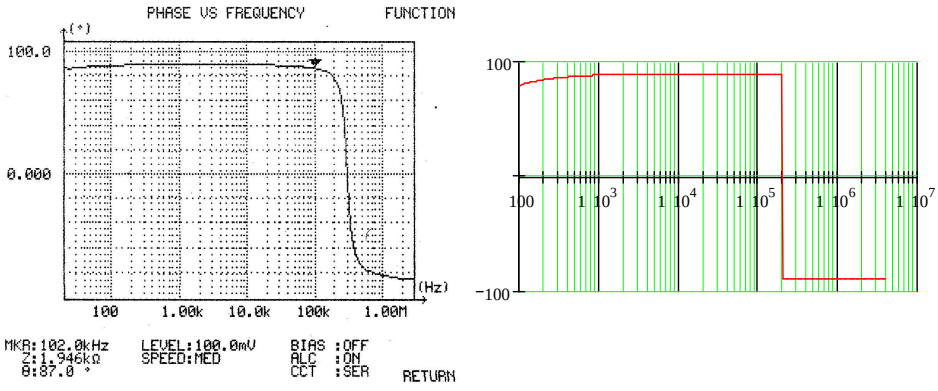

Figure A.18: *The graphs illustrate the magnitude of the input impedance Z_{poc} (with the secondary winding open) versus frequency. The transformer has an coaxial winding arrangement and the distance between the magnetic core parts is 0mm. The measured results appear in (a) and the theoretical prediction in (b).*

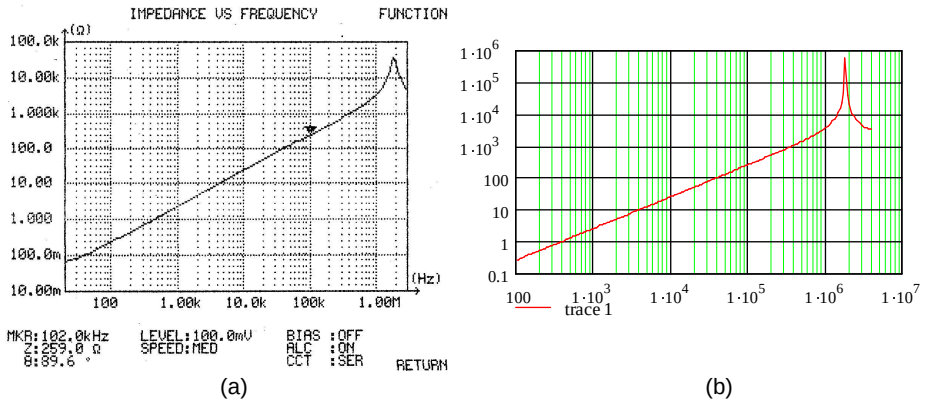

Figure A.19: *The graphs illustrate the magnitude of the input impedance $Z_{p_{oc}}$ (with the secondary winding open) versus frequency. The transformer has an coaxial winding arrangement and the distance between the magnetic core parts is 1mm. The measured results appear in (a) and the theoretical prediction in (b).*

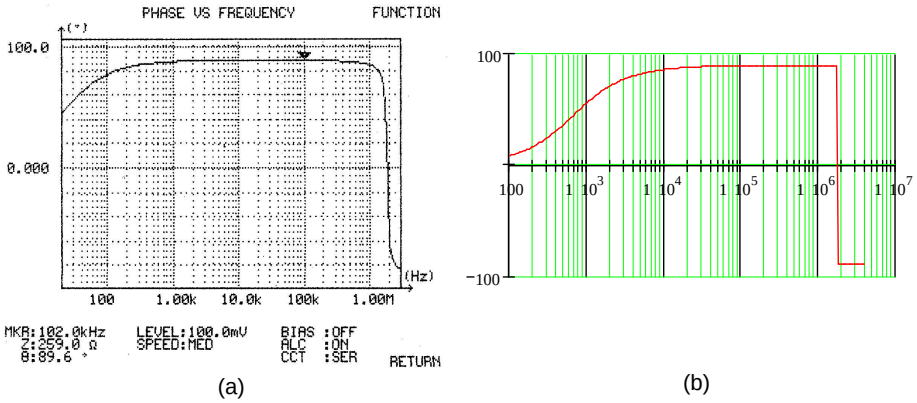

Figure A.20: *The graphs illustrate the magnitude of the input impedance $Z_{p_{oc}}$ (with the secondary winding open) versus frequency. The transformer has an coaxial winding arrangement and the distance between the magnetic core parts is 1mm. The measured results appear in (a) and the theoretical prediction in (b).*

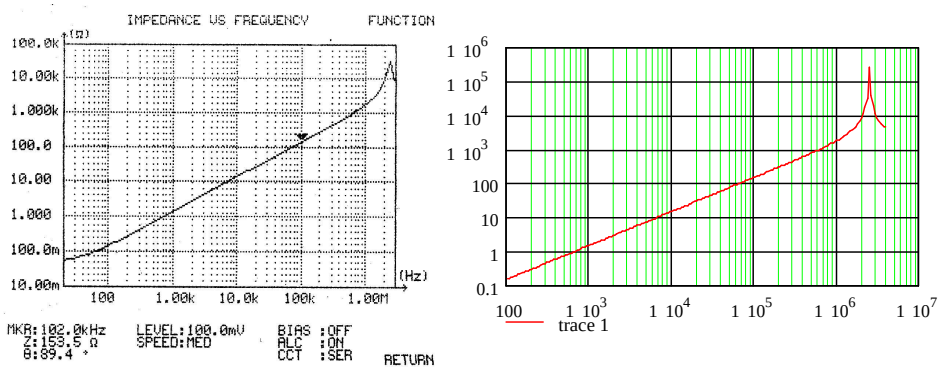

(a) (b)

Figure A.21: *The graphs illustrate the magnitude of the input impedance $Z_{p_{oc}}$ (with the secondary winding open) versus frequency. The transformer has an coaxial winding arrangement and the distance between the magnetic core parts is 2mm. The measured results appear in (a) and the theoretical prediction in (b).*

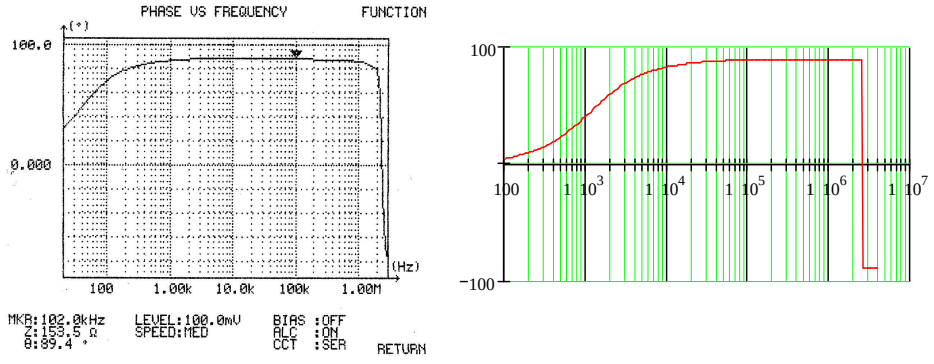

(a) (b)

Figure A.22: *The graphs illustrate the magnitude of the input impedance $Z_{p_{oc}}$ (with the secondary winding open) versus frequency. The transformer has an coaxial winding arrangement and the distance between the magnetic core parts is 2mm. The measured results appear in (a) and the theoretical prediction in (b).*

Appendix B
Phase-shifted bridge analysis

Figures B.1,B.2,B.3,B.4,B.5 illustrate the 5th to 10th state of operation of the phase-shifted full bridge with a full-wave rectifier.

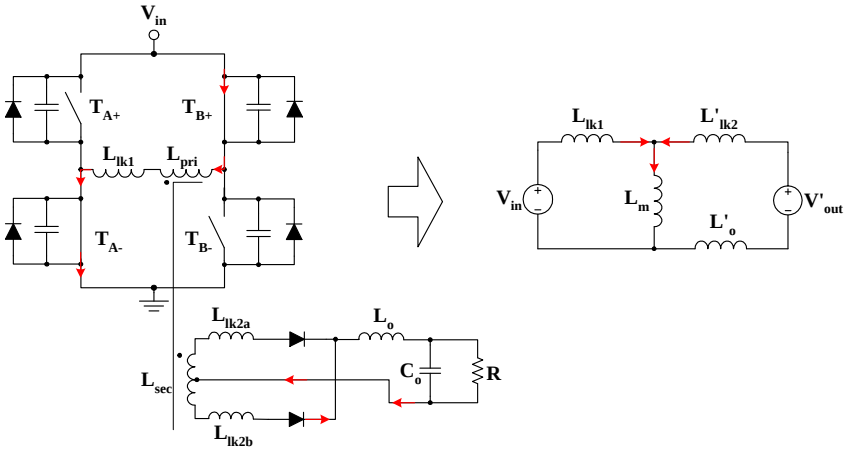

Figure B.1: *PSB modelling; Interval 6 ($t_5 \rightarrow t_6$).*

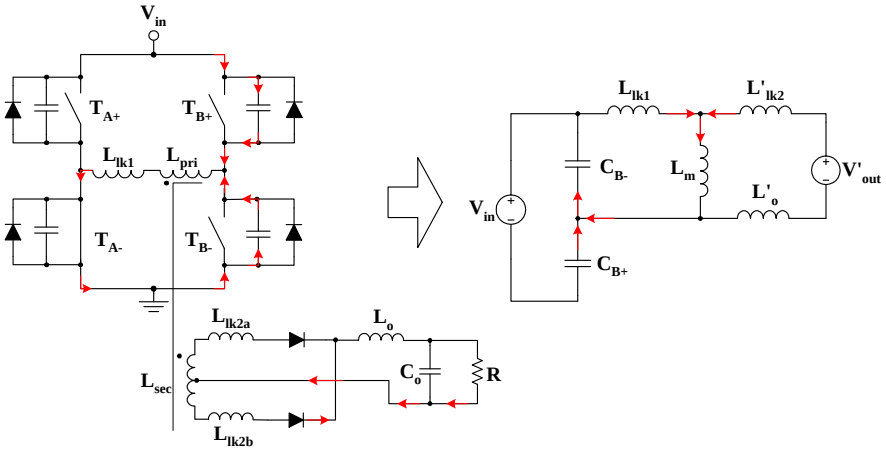

Figure B.2: *PSB modelling; Interval 7 ($t_6 \rightarrow t_7$).*

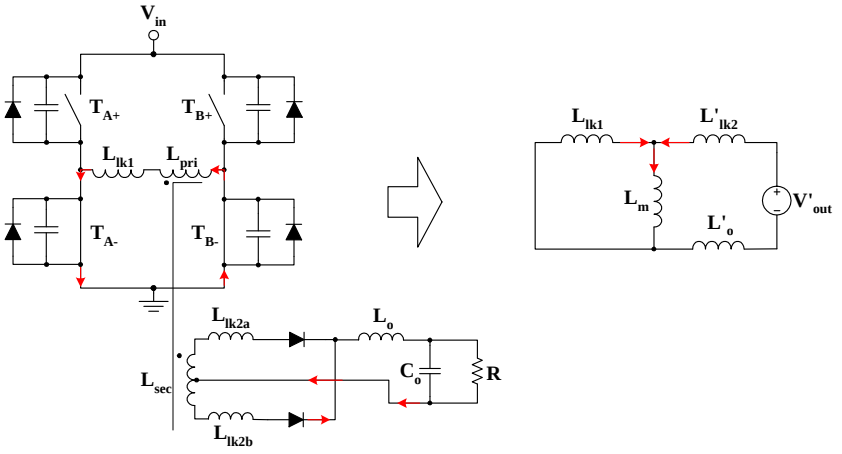

Figure B.3: *PSB modelling; Interval 8 ($t_7 \rightarrow t_8$)*

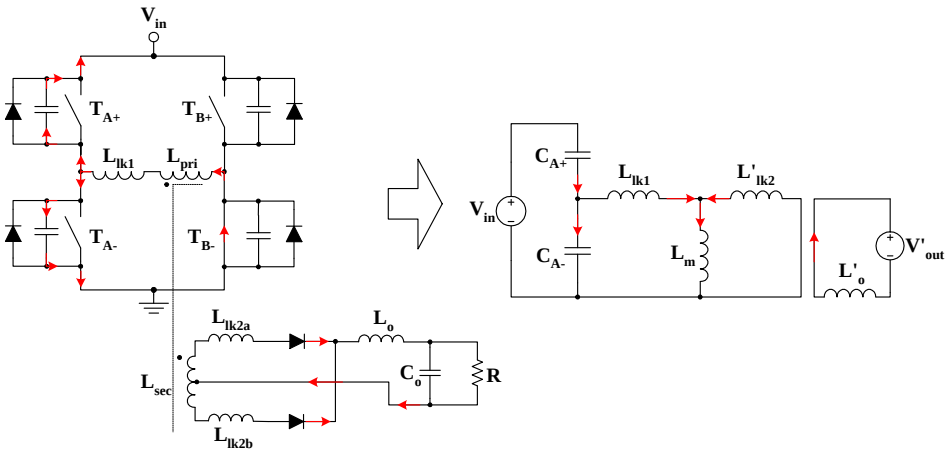

Figure B.4: *PSB modelling; Interval 9 ($t_8 \rightarrow t_9$)*

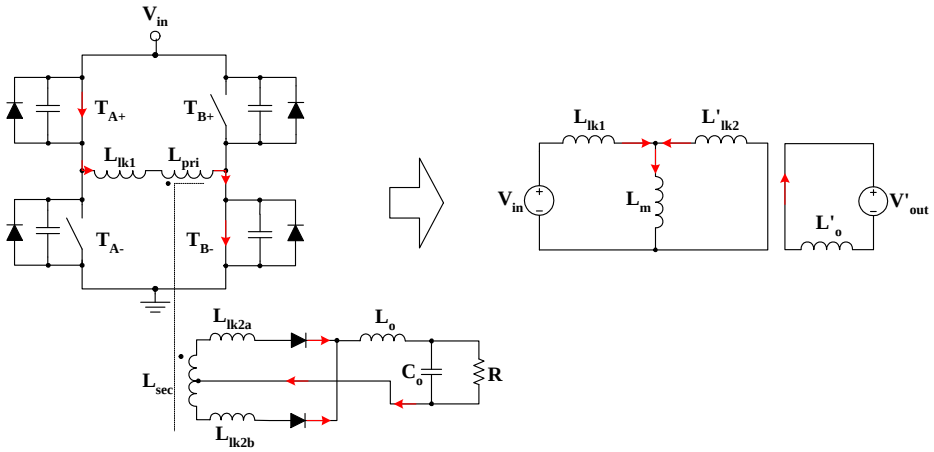

Figure B.5: *PSB modelling; Interval 10 ($t_9 \rightarrow t_10$)*

Appendix C
Experimental results

C.1 The Schematic diagrams

The schematic diagram of the prototype converter provided by BAE Systems appears in figures C.1 and C.2. The following modifications were made in order to integrate the rotating transformer:

C.2 Experimental set-up

Figure C.3 illustrates the modified PSFB circuit with the full-wave rectifier module plugged in. The modular approach allows quick prototyping using minimal construction work. The purpose is to use the same power circuit for every experiment and only change a module at a time, so that any electrical and thermal changes could be attributed to the changed component only.

Picture C.4 shows the bench were the experiments were conducted. The room temperature was kept between 21-22^{o}C.

C.3 Electromagnetic radiation

Figure C.5 illustrates the results from the measurement of the magnetic field at 1 metre distance from the circuit. The upper graphs refer to the circuit with a 1mm gapped rotating transformer. The lower ones correspond to a conventional converter that is hard-switching. All readings were taken a 500W of output power.

The amplitude of the electromagnetic radiation is greater in the hard-switched circuit (figure C.5(b)) than in the one with a rotating transformer (figure C.5(d)). This is also reflected in the spectrum of figures C.5(a) and (c) where the noise is much higher in the hard-switching circuit. The rotating transformer produces higher radiation only in the

low frequency area up to 5MHz which is easier to suppress. The scale of the frequency spectrum is 10dbV/div and the offset is -106dbV (middle axis).

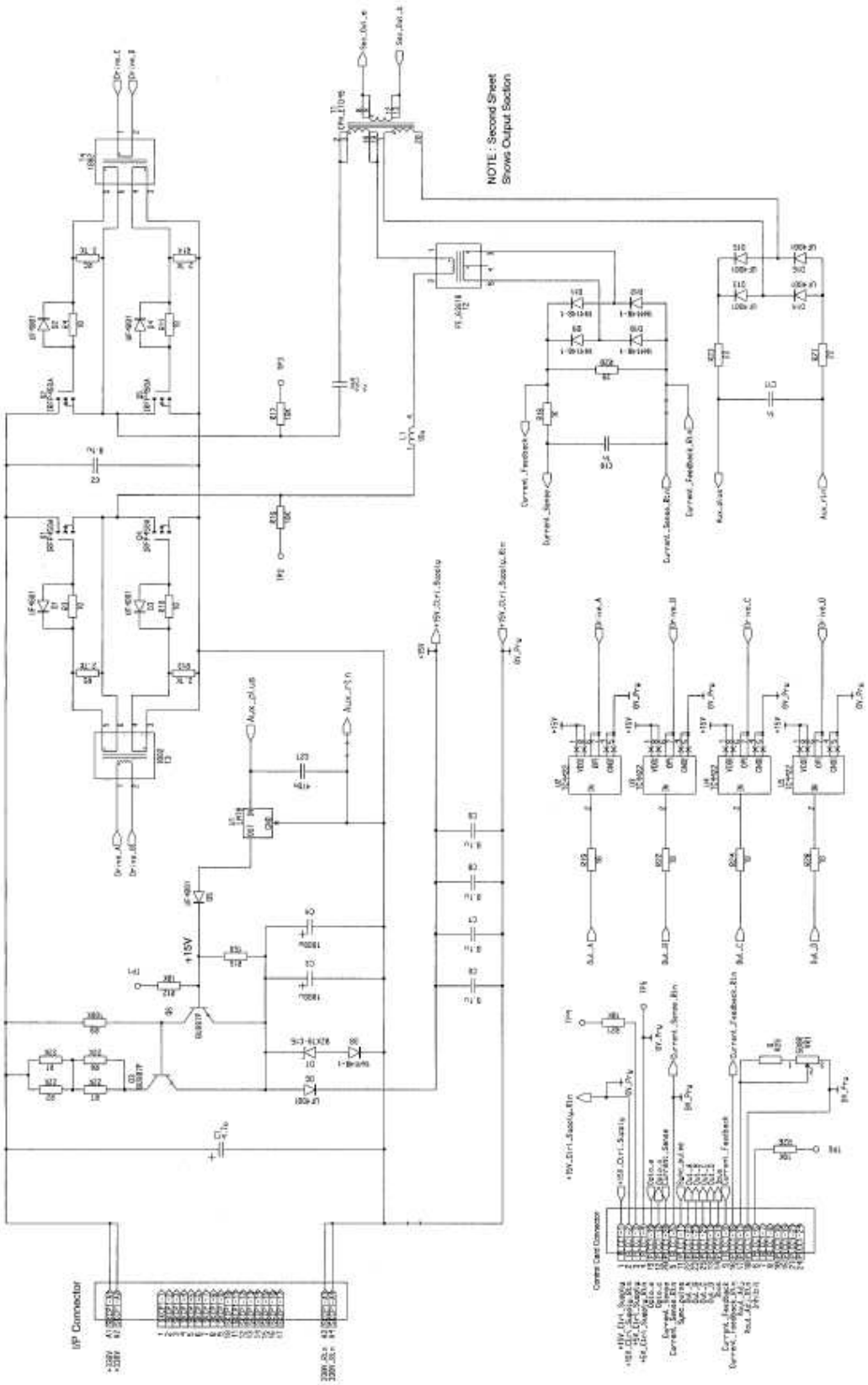

Figure C.1: *The secondary stage of the PSFB with a full-wave rectifier.*

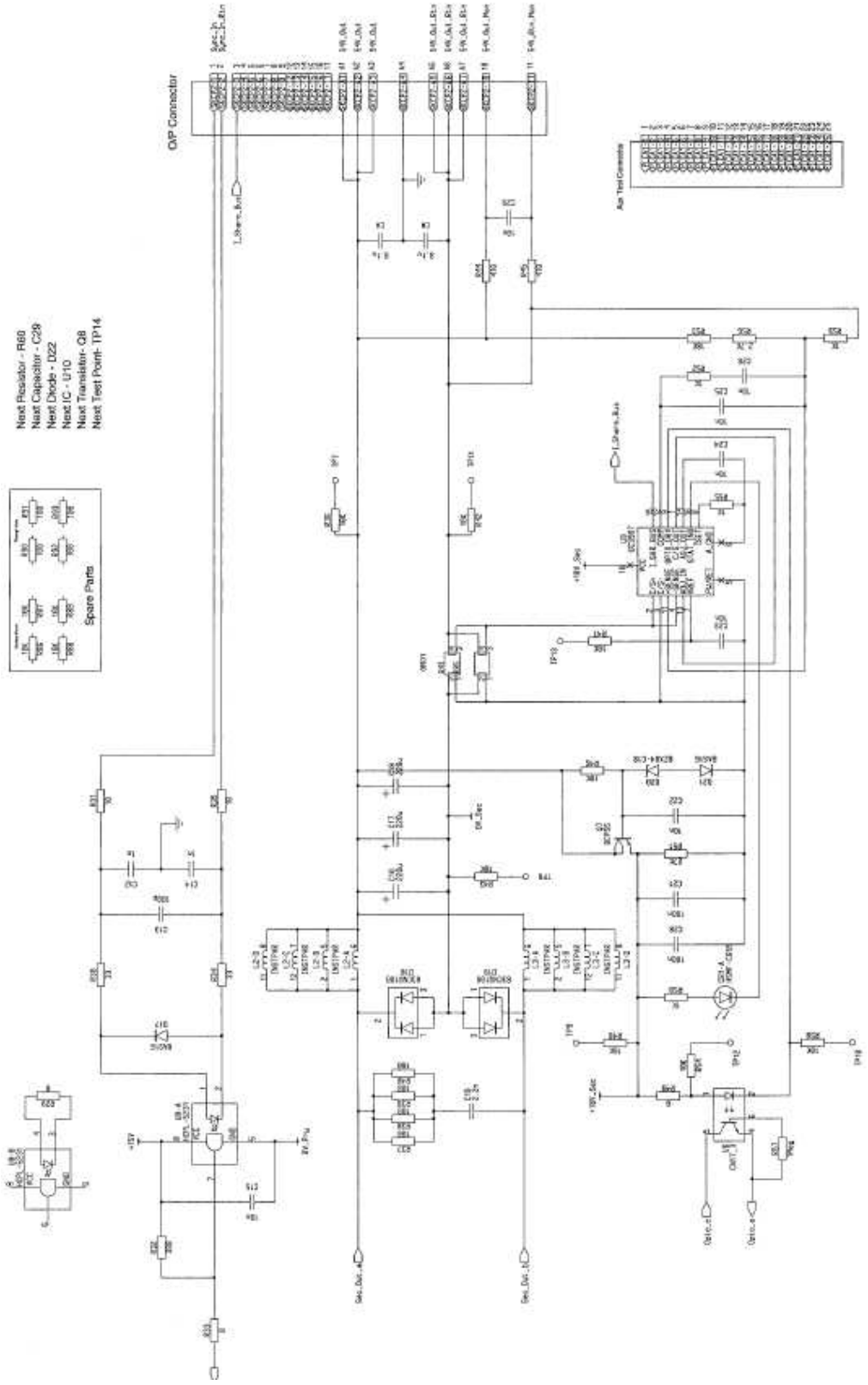

Figure C.2: *The secondary stage of the PSFB with a full-wave rectifier.*

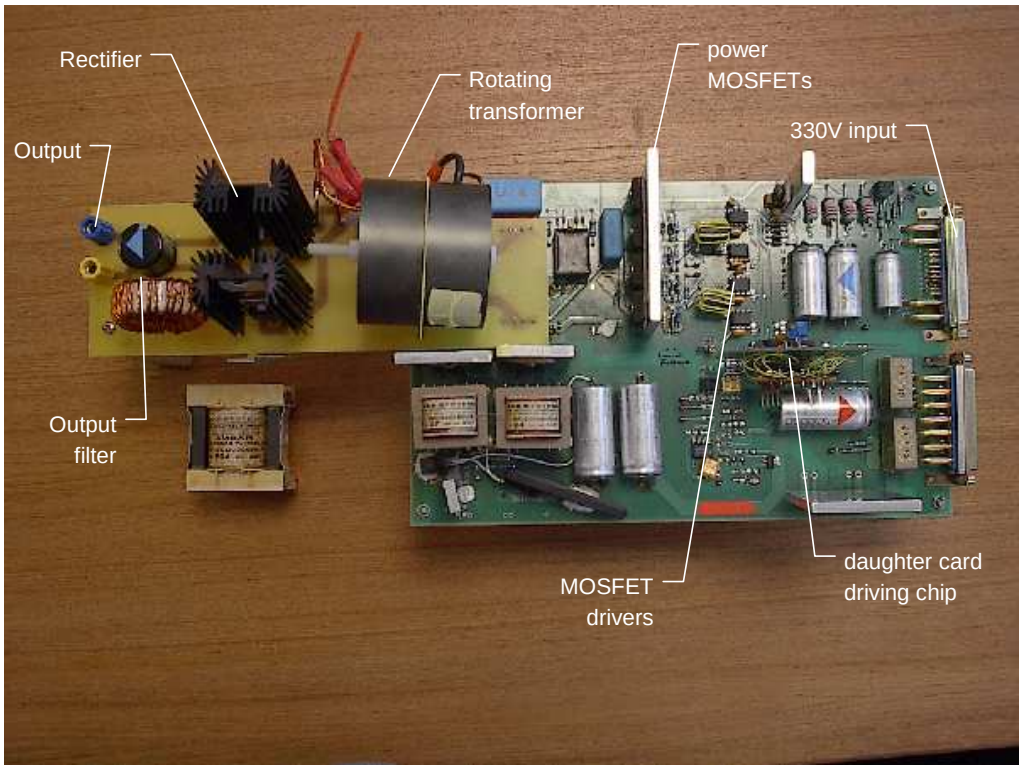

Figure C.3: *The modified PSFB with afull-wave rectifier.*

Figure C.4: *View of the bench and the experimental set-up.*

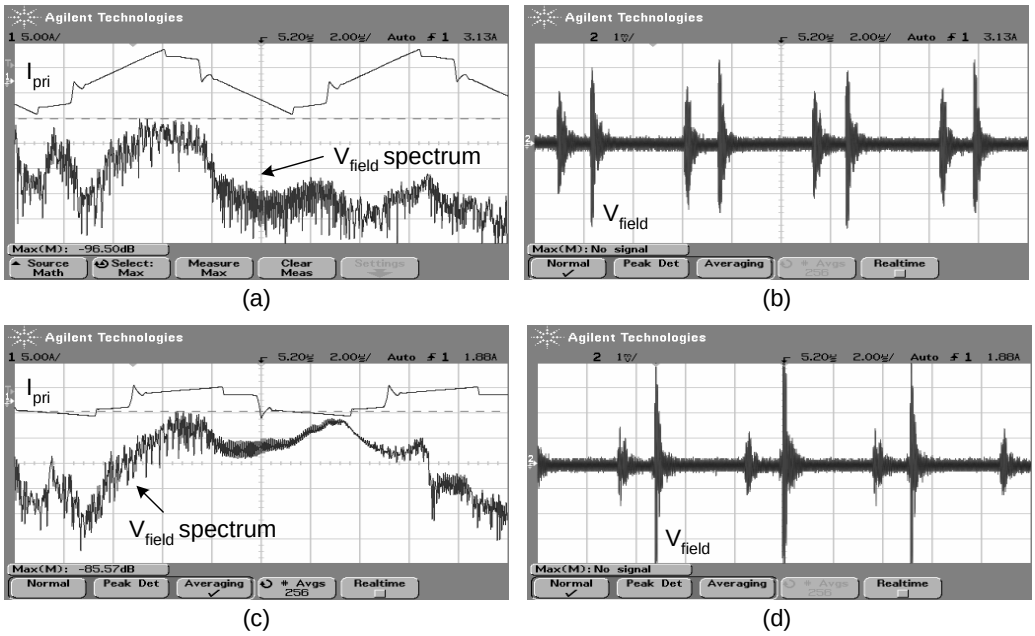

Figure C.5: *The electromagnetic field 1 metre away from the circuit. The upper waveforms refer to a circuit with an 1mm gapped rotating transformer: (a)the primary current I_{pri} and the spectrum of the induced voltage (b) the induced voltage waveform V_{field}. The lower graphs correspond to a non-gapped rotating transformer: (c) the primary current I_{pri} and the spectrum of the induced voltage and (b) the induced voltage waveform V_{field}.*

Appendix D
Publications

The following papers document the results of this research.

- *Contact-less Transfer of Energy by means of a Rotating Transformer*, Papastergiou K.D., Macpherson D.E., Fisher F., IEEE International Symposium on Industrial Electronics, ISIE 2005, Dubrovnic, Croatia.
- *A 1kW Phase-Shifted Full Bridge Converter incorporating Contact-less Transfer of Energy*, Papastergiou K.D., Macpherson D.E., Fisher F., IEEE Power Electronics Specialist Conference, PESC 2005, Recife, Brazil.

Contact-less Transfer of Energy by means of a Rotating Transformer

Konstantinos D. Papastergiou, and D. Ewen Macpherson
School of Engineering & Electronics, The University of Edinburgh, United Kingdom

***Abstract*— This paper examines the electrical properties of a rotating transformer used for contact-less transfer of energy to rotating equipment. Two winding layouts are analysed theoretically and experimentally. The reluctance modelling provides a deep understanding of how the geometry of the core and windings affect the electrical behaviour of the component. Theoretical calculations, measured results and finite element analysis are used to compare the proposed layouts. Basic design guidelines are given to adjust the leakage and magnetising inductances. The selection of a phase-shifted full bridge converter is suggested for applications at the power level of 1kW.**

I. Introduction

This paper examines a transformer with a rotating secondary winding for contact-less transfer of energy in devices that contain rotating parts. Traditionally, wires or slip rings have been used for transferring power to the rotating part of a device. Significant amount of research and development towards reliable and durable slip ring assemblies has established this technology as the standard solution for applications that involve rotating parts (electrical machines, industrial equipment, aerospace). Despite the standardisation of the design and the expertise gained, a customised slip ring design involves a high manufacturing cost especially when strict specifications apply. Furthermore, slip ring manufacturers guarantee good operation of the device for a certain number of revolutions and, only, under certain operating conditions. The contact wear as well as the vibration of the assembly can cause arcing and therefore can disrupt the operation of the equipment.

Depending on the specifications, the slip rings cost and maintenance requirements may be prohibitive for a design. The rotating transformer as a magnetic interface overcomes the problem of the contact wear and guarantees continuous operation. The cost level can be lower (depending on the assembly requirements) and its design can be completed in-house as an integral part of the power converter design. One of the first references to such a technology came from Landsman [1] who suggested this interface for a satellite application. The author calculated the main electrical properties of the transformer by using its geometry and then conducted an optimisation of the size and weight for a 1 kW application. Similar research for military applications was presented in [2] and [3]. The authors of these papers investigated modifications for the transformer layout and proposed different axial and radial alternatives. The use of the rotating transformer to transfer both energy and data across the joints of a robot was considered in [4]. This design is able to handle 20 kVA of power at a relatively low switching frequency of 25 kHz with a claimed efficiency of up to 96%. Finally, the authors of [5] looked at a linear interface for mining applications.

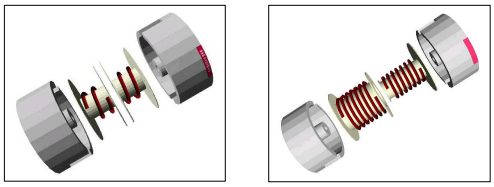

(a) (b)

Fig. 1. Rendered images of the investigated winding arrangements (a) the adjacent windings (b) the coaxial windings.

A rotating transformer essentially consists of a set of pot cores with a winding fitted into each of them as in Fig. 1. The core half that belongs to the rotating frame of the device rotates in respect to its counterpart. Due to the physical separation between the windings the rotating transformer exhibits a low coupling coefficient, hence storing a portion of the total supplied energy into the transformer structure itself (mainly within the air-gap). The magnetising inductance of such a transformer is much lower than that of a conventional transformer and can be comparable with the leakage inductance of the windings. As a result, in addition to the reflected load current, the primary winding carries a high magnetising current. This aggravates the primary-side conduction losses. The author of [6] tried to quantify the coupling problems for pot core transformers.

Apart from the low magnetising inductance the rotating transformer also exhibits increased leakage inductances in both windings. The reason is again the physical separation between the windings and the availability of alternative flux paths (air-space) rather than the ideal core path. The increased leakage inductance that appears in series with the windings causes a voltage drop across it, hence resulting in the second important weakness of a rotating transformer, the impaired voltage gain.

This paper presents a methodology based on [7], [8] for quantifying the electrical properties of a rotating transformer. Two winding layouts are considered and the electrical properties of each transformer are associated with the dimensions of the core and windings. The possibility of constructively utilising the parasitic elements of the rotating transformer is discussed.

II. The Rotating Transformer

A. Winding Layout

Two different transformer layouts are considered in this paper; these are the adjacent windings transformer (Fig. 1(a)) and the coaxial windings transformer (Fig. 1(b)). They are both built using a pot core because its rotation does not affect the magnetic cross-sectional area and the length of the magnetic path. As a result, the transformer would have the same electrical characteristics regardless of the relative positioning between the core halves. Secondly, a large range of pot cores is readily available in the market for prototyping.

The adjacent winding layout has also been mentioned in other applications such as satellite power supplies [1], transcutaneous energy transmission for pace-makers [9] or artificial organs [10] and inductive battery chargers [11]. The coaxial winding layout is proposed in this paper as an alternative. In this arrangement the secondary winding is wound on a separate bobbin that is inserted into the primary bobbin. Due to the smaller air space between the two windings this arrangement demonstrates lower leakage inductance. The magnetising inductance, on the other hand, is mainly determined by the air-gap so it remains relatively unchanged.

B. Mechanical layout

Two mechanical layouts are proposed for the rotating transformer (Fig. 2). A metallic body holds one of the core halves and the other one is mounted on the rotation shaft. Between the stationary and rotating frame there are standard deep groove and or thrust ball bearings. With the current technology of bearings the tolerances in both axial and radial movements are of the order of magnitude of tens of micro metres. Thereby, a minimum clearance between the primary and secondary cores can be achieved and the only restrictions are set by the tolerance in the dimensions of the ferrite core.

III. Analysis

The modelling of the magnetic component has been carried out using three different methods.

1) *Theoretical approach* (approximate, but gives a deep understanding as to how the physical layout of the transformer affects the electrical characteristics)

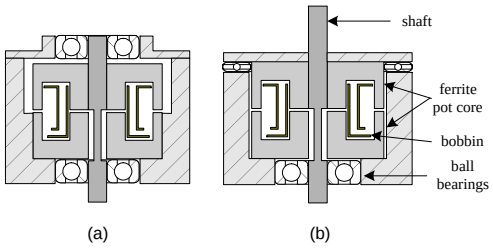

Fig. 2. The mechanical layout of a rotating transformer (a) for radial loading of the shaft and (b) for axial loading.

2) *Practical measurements* (performed after a prototype has been built to derive an accurate electrical model for the transformer)
3) *Finite element analysis* (can predict the electrical characteristics of the transformer before the actual prototype is built and initial optimisation can be done prior to manufacturing)

All the three characterising methods used in this paper have been applied in an attempt to assess their accuracy and study their advantages and disadvantages when used for designing a loosely coupled power transformer. The evaluated prototypes are part of a real design and have a 26:12 primary to secondary turns ratio. A P56/66 core was chosen from the Ferroxcube family to provide the required magnetic cross sectional area. The thickness of the wire as well as the number of layers and of the frequency of operation have a direct effect on the DC and AC resistance of the windings. However, the AC phenomena cannot be analysed with a static magnetic field simulation such as the one used in this work.

A. Reluctance modelling

The theoretical analysis is rather a qualitative analysis that gives a good insight to the connection between the dimensions of the core and windings and the resulting electrical characteristics. It is based on finding the reluctance model directly from the physical layout and then applying a duality transformation to convert the magnetic circuit to an electric circuit [8].

Associating the geometry of the transformer with its electrical properties is essential for the designing and optimisation of the magnetic component. Reluctance modelling is a tool used from the early stages of magnetism to analyse complex structures that are under the influence of a magnetic field. The magnetic flux paths are identified and their magnetic permeance is calculated based on the material properties. A schematic diagram similar to that of an electric circuit is constructed and the basic electric network laws can be applied to solve it. The analogy between the basic magnetic and electric quantities (such as reluctance and resistance, magnetic flux and electric current) is known as the duality property. Converting the magnetic circuit to the equivalent electrical one allows the accurate simulation of the converter.

Fig. 3(a) shows the physical structure of the coaxial transformer and Fig. 3(b) represents the magnetic paths in the transformer symbolised as resistors. The resulting reluctance network is depicted in Fig. 3(c) and following in Fig. 3(d,e) the reluctances are transformed to permeances. This is done by converting the series branches to parallel and the parallel branches to series in the same way as an electrical network comprising of resistances would be converted to an equivalent network comprising of conductances. The reason for converting the reluctance R to a permeance P component is because the permeance (magnetic quantity) of a magnetic path is analogous to the inductance (electrical quantity) of the same path according to the following equation,

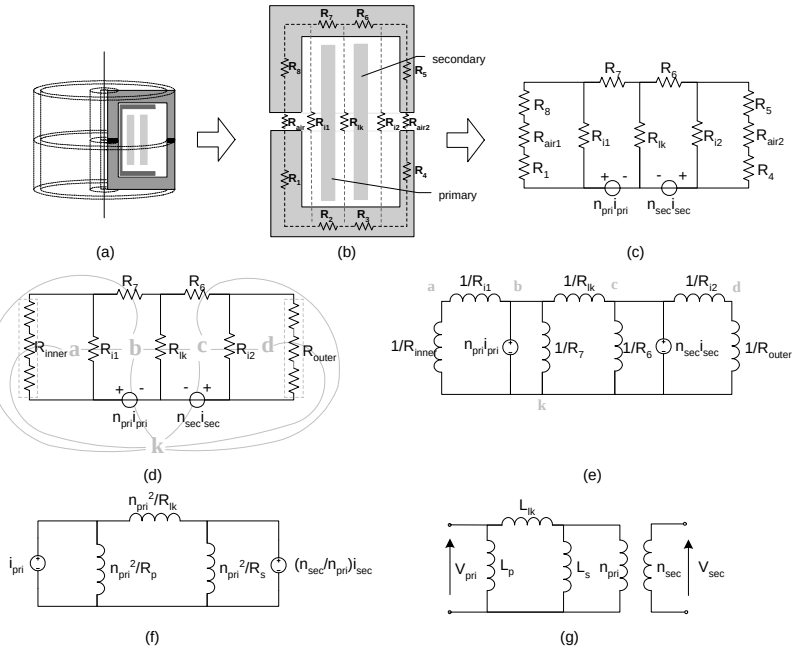

Fig. 3. Reluctance modelling for the coaxial winding arrangement (a) physical layout, (b) identifying the magnetic flux paths, (c) the reluctance model, (d) reluctance to permeance transformation (e) permeance model, (f)duality transformation and (g) the equivalent electrical network.

$$L = N^2 P = N^2 \frac{1}{R} \tag{1}$$

where N is the number of turns wound around the analysed magnetic path. Therefore, the permeance components $1/R$ in Fig. 3(e) are multiplied with the primary number of turns N_{pri}^2 whereas the flux sources are divided by the same quantity. This essentially means that the magnetic component $N_{pri}^2 P$ can be replaced by an electrical quantity, the inductance L. This procedure is called the duality transformation and is depicted in Fig. 3(f,g).

The reluctance modelling for the adjacent winding arrangement is summarised in Fig. 4.

The resulting electrical equivalent networks of the two winding arrangements (Fig. 4(c) and Fig. 3(g)) are equivalent as the τ-model can be transformed to a π-model and vice versa. However, by carefully looking at the reluctance modelling, it can be seen that a model such as that of Fig. 4(c) does not have any physical meaning (the inductances can not be related to any of the geometrical properties of the transformer) for the coaxial arrangement. On the contrary, the inductances in the model of Fig. 3(g) are connected with the initial geometry.

After the reluctance modelling and duality transformation have been performed the designer can see what the leakage inductance depends on. In the adjacent arrangement the leakage inductance is very high due to the separation between the windings. Moving one of the windings hardly affects the leakage inductance of the other (as long as the adjacent layout is preserved).

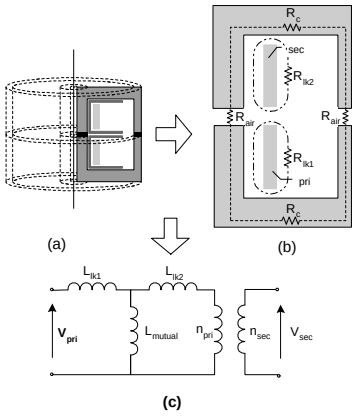

Fig. 4. Summarised reluctance modelling of the adjacent winding arrangement.

However, in the coaxial arrangements the leakage is a common component (as seen in Fig. 3(g)) defined by the relative positioning between the windings. Any change in the position or size of one of the windings would affect the common leakage element.

B. Measured results

The measurement method is generally very accurate and involves the usual open-circuit and short-circuit tests

and the calculation of magnetising and leakage inductances as well as the winding capacitances. The following quantities need to be measured; the inductance seen at the primary winding with the secondary open ($L_{p_{oc}}$), the inductance seen at the secondary with the primary winding open ($L_{s_{oc}}$) and the inductance seen at the primary with the secondary shorted ($L_{p_{sc}}$). The mutual inductance can then be calculated as,

$$M = \sqrt{(L_{p_{oc}} - L_{p_{sc}})L_{s_{oc}}} \tag{2}$$

The magnetising inductance as seen from the primary side is given by,

$$L_{mp} = \frac{1}{n}M \tag{3}$$

where n the transformer turns ratio. The magnetising inductance seen from the secondary side is,

$$L_{ms} = nM \tag{4}$$

Finally, the primary and secondary leakage inductances are respectively given by,

$$L_{lp} = L_{p_{oc}} - L_{mp} \tag{5}$$

$$L_{ls} = L_{s_{oc}} - L_{ms} \tag{6}$$

When measuring the inductance values, the choice of frequency and test voltage for obtaining accurate readings is an issue. In this work an inductance graph over the 10kHz to 3MHz range was obtained and a relatively low test voltage was used. The magnetic flux in the core was kept low in order to remain in the linear area of the B-H curve and keep the permeability ($\mu_r = B/H$) fixed. From the inductance-frequency graph it is possible to ensure that there is no resonant effects at the desired frequency and therefore the inductance curve is flat at the operating frequency, hence the reading obtained is realistic. It is also important to observe the quality factor while measuring the inductance. A very poor quality factor signifies an inaccurate inductance reading.

C. Finite elements analysis

The last test that has been performed to quantify the electrical characteristics of the rotating transformer was a finite element analysis. Due to the axial symmetry of the investigated layouts of Fig. 1 a 2-Dimensional analysis gives accurate results. The static magnetic field in the transformer structure can be studied and the different inductances of the windings can be calculated by manipulating the magnetic field quantities.

The procedure is comprised of three basic stages; drawing the 2-D model, defining material properties and boundary conditions and solving/post-processing the results. The software used is the Maxwell 2D by Ansoft.

At the post-processing stage different field quantities can be analysed and some interesting conclusions about the magnetic flux distribution and the energy storage can be drawn. This procedure can also help with the reluctance modelling of the transformer as it visualises the magnetic field and the magnetic paths can be easily identified. By performing the energy integration over a specific area of the 2-D model the respective inductance can be calculated. For example the energy stored in the magnetic core and air gap is associated with the magnetising inductance of the respective winding. By integrating the energy over the area where the leakage energy appears the leakage inductance of the respective winding can be obtained. In a static magnetic field the energy E stored in the inductance L as a result of the current I is,

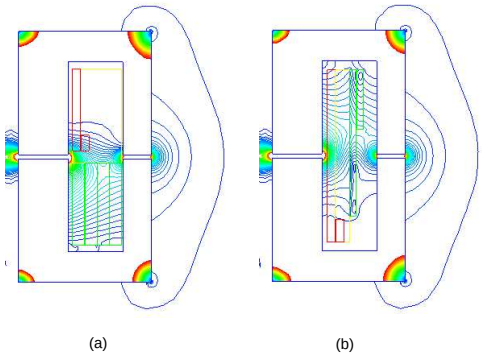

Fig. 5. The field density representation of the (a) adjacent winding arrangement and (b) the coaxial winding arrangement of a rotating transformer with a 1mm air-gap.

$$E = \frac{1}{2}LI^2 \tag{7}$$

This energy can be calculated by integrating the $\overrightarrow{A} \cdot \overrightarrow{J}$ ($\overrightarrow{A}$ the field vector and $\overrightarrow{J}$ current density vector) over the volume of the coil wire, hence,

$$E = \frac{1}{2}\int_r\int_z\int_\phi \overrightarrow{A}\,\overrightarrow{J}\,drdzd\phi \tag{8}$$

From 7 and 8 the inductance is derived:

$$L = \frac{\pi \int_r\int_z \overrightarrow{A}\,\overrightarrow{J}\,drdz}{I^2} \tag{9}$$

where the integration is only performed over the 2-D conductors surface due to the axial symmetry. With regard to the leakage inductance, the calculation is slightly more complex due to the difficulty in defining the magnetic leakage path. Fig 5 depicts the results of a the FE analysis for a transformer with an 1mm air-gap. In the adjacent winding layout (Fig 5(a)) (with the secondary open-circuited) the flux lines that escape from the core path are mainly linking the primary winding. This appears as leakage energy (stored in the primary leakage inductance) as it is not coupled to the secondary. The leakage flux in Fig. 5(b) is less as the windings are physically closer to each other. Having performed the reluctance analysis, the flux paths can be identified more easily and the energy stored in them can be calculated as:

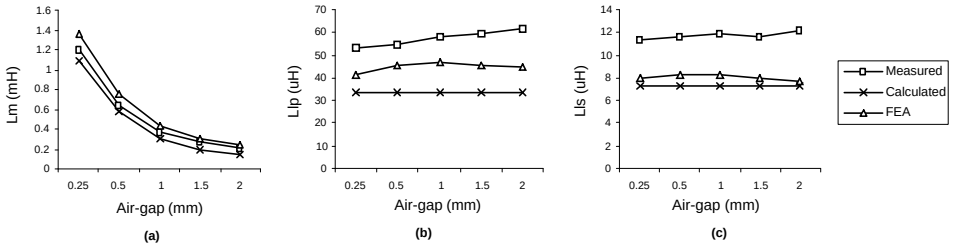

Fig. 6. The (a) primary magnetising inductance L_m, (b) primary leakage inductance L_{lk_p} (c) secondary leakage inductance L_{lk_s} of the adjacent windings transformer as found by three different characterising methods.

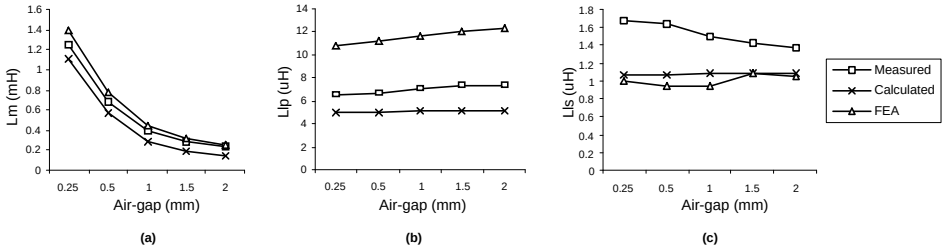

Fig. 7. The (a) primary magnetising inductance L_m, (b) primary leakage inductance L_{lk_p} (c) secondary leakage inductance L_{lk_s} of the coaxial windings transformer as found by three different characterising methods.

$$E = \frac{1}{2}\pi \int_r \int_z \overrightarrow{H}\overrightarrow{B} dr dz \tag{10}$$

Combining with (7) again yields:

$$L = \frac{\pi \int_r \int_z \overrightarrow{H}\overrightarrow{B} dr dz}{I^2} \tag{11}$$

D. Results

Associating the physical structure of the rotating transformer with its electrical characteristics is a tedious task. It usually involves many assumptions to overcome the modelling difficulties arising mainly from the asymmetries of the core and windings and the non-uniform magnetic materials. As a result, both calculations and the finite elements analysis give results whose accuracy is inversely proportional with the number of assumptions made during the modelling procedure.

Fig. 6 and 7 present the results of the three characterising methods (measurements, calculation and FEA). As expected, the graphs show a significant decrease of the magnetising inductance as the air-gap increases. The leakage inductance on the other hand remains unchanged regardless of the air-gap length. Note that although of the same order of magnitude, the calculated and FEA results of leakage inductance differ from the measured ones. This is mainly because of the difficulty in defining the area where the leakage flux resides. In the case of the magnetising flux, most of the flux is known to be in the magnetic core hence the integration in (11) is performed over the volume of the core. The leakage flux on the other hand is spread in the air space and the boundaries between useful (magnetising) flux and leakage (useless) flux are vague. Additionally, the leakage energy is a small fraction of the total transformer energy, hence any ”noise” (other magnetic flux) accounted as leakage flux can easily falsify the results.

The key conclusions of this work are discussed here:

- In a rotating transformer (with a relatively small air-gap) the value of the magnetising inductance mainly depends on the length and the cross-sectional area of the air-gap and not on the position of the windings
- The leakage inductance is independent of the air-gap length and only depends on the relative position of the windings.
- The leakage inductance can be eliminated by placing the windings; (a) physically together or (b) firmly on the magnetic core windings as close to the core as possible
- The leakage and magnetising inductances are proportional to the square of the number of turns of the respective winding.

Comparing the adjacent and coaxial winding arrangements, it can be seen that the coaxial has a much lower leakage inductance. The leakage inductance of a rotating transformer is important because together with the AC and DC winding resistance it determines the voltage gain of the transformer. The leakage inductance appears in series with the transformer, thereby causing

a voltage drop across it (which is proportional with the di/dt applied). This voltage drop causes the transformer secondary voltage to be less than expected. As a result, an excessive leakage inductance such as the one imposed by the adjacent winding could make the use of a rotating transformer impossible.

IV. Topology Selection

As the high magnetising current is unavoidable in a gapped transformer the power electronics topology has to either cope with it or, ideally, utilise it. One converter topology that inherently utilises the parasitic components of a transformer to achieve Zero Voltage Switching (ZVS) is the Phase Shifted Full Bridge [12] (PSFB) (Fig. 8). The PSFB topology is able to handle the amount of power that is required in industrial applications of 1-1.5kW of power. A conventional PSFB achieves a very efficient power conversion (over 90%) thanks to the ZVS of the MOSFET switches. To accomplish the soft switching, the PSFB relies on the energy that is stored during the power transfer interval in the leakage inductance of the transformer or some external series inductance. Just before a MOSFET turns on there is a transition interval when the leakage inductance resonates with the MOSFET channel capacitance. When the voltage across the MOSFET is zero the driver turns the switch on.

When the converter is operating at low load, the energy stored in the series inductor is not enough to completely discharge the MOSFET capacitance. As a result, soft switching is lost and the low load efficiency of the PSFB is poor. A rotating transformer can contribute some energy to the resonant operation due to the energy stored in the magnetising inductance. The magnetising current of a rotating transformer is, in most cases, enough to perform the discharging of the MOSFET's channel capacitance on its own. Hence, the need for additional series inductors (which are known to cause side effects such as duty cycle loss) is eliminated. An important property of the magnetising current is that it remains unchanged regardless of the loading conditions thus maintaining the ZVS operation down to no load.

A comparison between a conventional PSFB and a PSFB with a rotating transformer has shown a superiority of the latter in terms of zero voltage switching range.

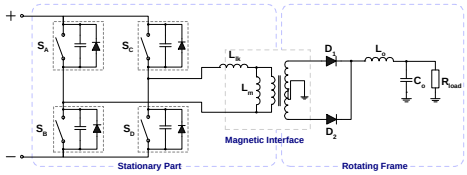

Fig. 8. The Phase Shifted Full Bridge topology.

V. Conclusion

Three different methods have been employed to characterise the rotating transformer. The electrical equivalent networks of the two proposed layouts have been derived. The theoretical analysis gives a good insight to the electromagnetics of the transformer but not very accurate results. The finite elements analysis can be used as a tool at the first stages of design and optimisation of the rotating transformer. The coaxial winding layout proves to be superior in terms of leakage inductance and is expected to improve the voltage gain of the transformer considerably. Finally, a phase shifted full bridge converter is proposed for applications of around 1kW of power. This topology can benefit from the low coupling coefficient of the rotating transformer.

Acknowledgment

The authors would like to thank BAE Systems for sponsoring this project and, personally Mr Frank Fisher for his valuable contribution to this work.

References

[1] E. E. Landsman. Rotary transformer design. In *Power conditioning specialists conference record*, pages 139–52, 1970.

[2] W. T. McLyman and A. O. Bridgeforth. Development of a rotary power transformer and inverter drive for spacecraft. In *Proceedings of the 18th Intersociety Energy Conversion Engineering Conference. AIChE. 1983*, pages 1102–5.

[3] T. A. Stuart, R. J. King, and H. A. Shamseddin. Rotary transformer design with fi xed magnetizing and/or leakage inductances. *IEEE Transactions on Aerospace and Electronic Systems*, AES-22(5):565–72, 1986.

[4] A. Esser and H.-C. Skudelny. A new approach to power supplies for robots. *IEEE Transactions on Industry Applications*, 27(5):872–875, 1991.

[5] K.W. Klontz, D.M. Divan, D.W. Novotny, and R.D. Lorenz. Contactless power delivery system for mining applications. *IEEE Transactions on Industry Applications*, 31(1):27–35, 1995.

[6] T O Howard and K H Carpenter. A numerical study of the coupling coeffi cients for pot core transformers. *IEEE Transactions on Magnetics*, 31(0018-9464):2249–2253, 1994.

[7] J.G. Hayes, N. O'Donovan, M.G. Egan, and T. O'Donnell. Inductance characterization of high-leakage transformers vo - 2. In *Applied Power Electronics Conference and Exposition, 2003. APEC '03. Eighteenth Annual IEEE*, volume 2, pages 1150–1156, 2003.

[8] Jian Wang, A.F. Witulski, J.L. Vollin, T.K. Phelps, and G.I. Cardwell. Derivation, calculation and measurement of parameters for a multi-winding transformer electrical model. In *Applied Power Electronics Conference and Exposition, 1999. APEC '99*, volume 1, pages 220–226 vol.1, 1999.

[9] A. Ghahary and B.H. Cho. Design of transcutaneous energy transmission system using a series resonant converter. *IEEE Transactions on Power Electronics*, 7(2):261–269, 1992.

[10] G.B Joung and B.H. Cho. An energy transmission system for an artifi cial heart using leakage inductance compensation of transcutaneous transformer. *IEEE Transactions on Power Electronics*, 13(6):1013–1022, 1998.

[11] H. Abe, H. Sakamoto, and K. Harada. A noncontact charger using a resonant converter with parallel capacitor of the secondary coil. *IEEE Transactions on Industry Applications*, 36(2):444–451, 2000.

[12] R A Fisher, K D T Ngo, and M H Kuo. A 500khz, 250w dc-dc converter with multiple outputs controlled by phase-shifted pwm and magnetic amplifi ers. In *High Frequency Power COnversion Conference*, pages p.100–110, 1988.

A 1kW Phase-shifted Full Bridge Converter incorporating Contact-less Transfer of Energy

K.D. Papastergiou and D.E. Macpherson
The University of Edinburgh
School of Engineering and Electronics
Mayfield Road, Edinburgh, UK
Email: D.E.Macpherson@ed.ac.uk

F.Fisher
BAE Systems Inc.
Crewe Toll, Ferry Road, Edinburgh, UK
Email: Frank.Fisher@baesystems.com

***Abstract*— This paper addresses the problem of reliable power transfer from the stationary to the rotating part of an airborne radar without any electrical contact. An inductive interface (rotating transformer) is proposed as a replacement for the well-established slip-ring technology. The aim is to design a reliable and efficient converter free of moving parts and mechanical faults. The resulting design has a long life expectancy and is ideal for equipment in aerospace, military and underwater applications, where minimal or no maintenance is a key objective. The paper initially examines the electrical properties of the rotating transformer and derives electrical equivalent models for the adjacent and coaxial winding arrangements. The phase-shifted full bridge converter is proposed as a topology that can effectively utilise the rotating transformer leakage inductance and poor coupling coefficient. A step-by-step design algorithm is described in the third section and the experimental results are finally presented and discussed.**

I. Introduction

The aim of this work is to investigate the possibility of using a transformer with a rotating secondary winding for contact-less transfer of energy across to the revolving part of an airborne electronic-scanning radar. This application requires the transmission of 1kW of power (per module) by converting the 330V DC bus voltage to a 54V DC output. The clearance between the fixed and rotating parts of the transformer is 1mm. The efficiency and reliability of the power supply are of special interest. The current practice for transferring power to the revolving antenna of the radar is through the use of slip-rings. This well-established technology suffers wear and is prone to arcing, hence, decreasing the reliability of the radar's power supply. Maintenance is not always available and the reliable operation of such equipment is critical.

A rotating transformer (Fig.1) essentially consists of a set of pot cores with a winding fitted into each of them. The core and winding that belong to the rotating frame of the radar rotate with respect to their counterparts. Due to the physical separation between the windings, the rotating transformer exhibits a low coupling coefficient. This is because it stores a portion of the total supplied energy into the transformer structure itself (mainly within the air-gap) rather that transferring it to the secondary. The magnetising inductance of such a transformer is lower than the one of a conventional transformer. As a result, in addition to the reflected load current, the primary winding carries an increased magnetising current aggravating the primary side conduction losses.

Apart from the low magnetising inductance, the rotating transformer also exhibits increased leakage inductance in both windings. The reason is, again, the physical separation between the windings and the availability of alternative flux paths (air-space) rather than the ideal core path. The increased leakage inductance, which appears in series with the windings causes a voltage drop across them, resulting in the second weakness of a rotating transformer, the impaired voltage gain. The contact-less transfer of energy has been under investigation from the early days of the switching power converters. Back in the seventies the rotating transformer appeared for the first time as a proposed technology for transferring power from the solar panels to the body of a satellite [1]. S H Marx also proposed a kilowatt rotary power transformer and concentrated his efforts in optimising the structure of the magnetic component [2]. Other applications include the transcutaneous energy transmission for pacemakers [3] and artificial organs [4]. Finally, a major application of this technology is the inductive charging for electric vehicles [5], [6]. Different approaches, such as leakage inductance compensation and resonant techniques, were employed to overcome the problem of the low voltage gain.

In all the above cases the researchers had to tackle the same problem; a poor coupling coefficient between the primary and secondary windings of the transformer (rotating or stationary). Therefore, the converter topology used in such an application must be able to tolerate or ideally constructively utilise the parasitic components of the rotating transformer. One such topology is the Phase-Shifted Full Bridge (PSFB) of Fig.2(a) [7], [8], [9]. The PSFB uses the parasitic leakage inductance of the primary winding to achieve zero voltage switching of the primary side MOSFETs (Fig.2(b)). A common problem of this topology is the loss of soft switching under light or no load conditions. The use of the magnetising current to assist the soft switching has been suggested in several papers [10], [11]. In this work the electrical properties of the rotating transformer are studied. Once the geometry of the magnetic

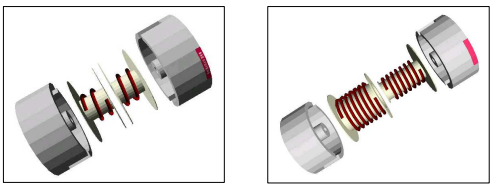

(a) (b)

Fig. 1. Rendered images of the investigated winding arrangements (a) the adjacent windings (b) the coaxial windings.

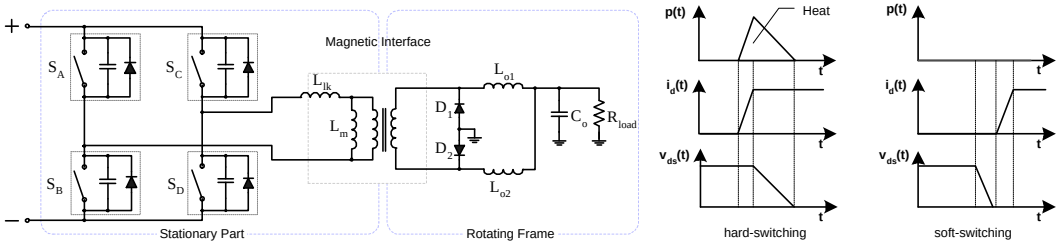

Fig. 2. The phase-shifted full bridge topology (a) schematic diagram (b) hard and soft-switching of the power semiconductors.

component has been associated with its electrical properties, the magnetising/leakage inductances and winding resistances can be tuned to fit the requirements of the PSFB converter. In the third section a design methodology is deployed and in the fourth section a 1kW example converter is built. Finally, the experimental results are presented and some conclusions are drawn.

II. The Rotating Transformer

Understanding what affects the electrical behaviour of the transformer is the basis of optimising its design. Some basic observations are made below and some design guidelines are produced by inference;

- The physical separation (air-space) between the windings results in increased leakage inductance.
- The leakage inductance does not depend on the air-gap length.
- The longer the air-gap, the lower the magnetising inductance of the windings is.
- The fringing field around the air-gap alters the current distribution in the windings and increases the effective winding resistance.

By keeping these observations in mind, two different winding arrangements are proposed and evaluated in this paper. The adjacent winding arrangement (Fig.1(a)) is commonly used in most of the designs proposed so far. The coaxial arrangement (Fig.1(b)) is proposed as the low leakage inductance and AC resistance alternative.

In the coaxial winding arrangement the secondary winding is wound on a bobbin that penetrates into the primary bobbin. Due to the smaller air space between them, the windings demonstrate lower leakage inductance. The magnetising inductance, on the other hand, is determined by the air-gap and therefore remains relatively unchanged. The manufacturing of the coaxial windings requires more effort and involves a higher cost than the usual adjacent arrangement. The resulting interface is however more economic and easier to design than the conventional slip-rings solution. It can be manufactured in-house together with the rest of the power supply.

As an initial approach, a deep understanding of the magnetic structure is essential. Associating the physical structure of the rotating transformer with its electrical characteristics is important; it helps the engineer to realise how a geometrical property (core size and shape, windings position, width etc) affects each of the parasitic elements (leakage inductances, capacitances etc.) of the component. Connecting the geometry with the electrical behaviour of the component is a tedious process. Some fundamental assumptions are made to overcome the modelling difficulties, arising mainly from the asymmetries of the core and windings and the non-uniform magnetic materials. The geometry of the transformer is converted to an equivalent magnetic circuit (using the reluctance modelling technique). A duality transformation is then applied to convert the magnetic circuit to its electrical equivalent. The procedure is fully described in [12] and is briefly depicted in Fig.3 and 4.

The resulting equivalent networks have a physical meaning; each inductance represents some space (volume) in the original transformer structure. These inductances can be adjusted to fit the power converter needs. The following equations show how the magnetising L_m and leakage L_{lk} inductances depend on the winding and core dimensions:

$$L_m = N_p^2 \left(\frac{l_c}{\mu_0 \mu_c A_c} + \frac{l_g}{\mu_0 \mu_{air} A_g} \right)^{-1} \quad (1)$$

$$L_{lk} = N_p^2 \left(\frac{l_{sp}}{\mu_0 \mu_{sp} A_{sp}} \right)^{-1} \quad (2)$$

where N_p is the number of primary turns, l_c and l_g are the lengths of the core and of the air-gap magnetic path, A_c and A_g are the cross-sectional areas of the core and of the air-gap respectively. Similarly, in (2), l_{sp} the equivalent length of the magnetic path and A_{sp} the equivalent cross-sectional area of the path. Note that leakage inductance is generally more difficult to approach as it is difficult to integrate the leakage energy over the air space volume.

The graphs in Fig.5 are the results of the measurements that were performed on two transformer prototypes. Both the adjacent and coaxial winding prototypes have 26 turns of 3 strands of SWG25 wire in the primary and 12 turns of 5 strands of SWG25 wire in the secondary.

As seen in Fig.5 the rotating transformer with an adjacent winding arrangement exhibits very high leakage inductances (primary and secondary). The reason for this is the fact that the windings are physically separated. According to the electrical equivalent models shown in Fig.3 the leakage inductance components are independent from each other as the leakage

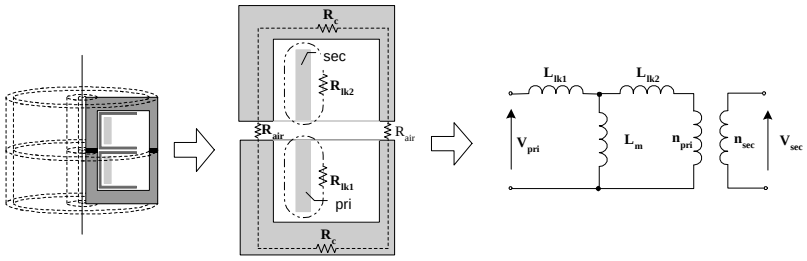

Fig. 3. Reluctance modelling for the adjacent windings arrangement.

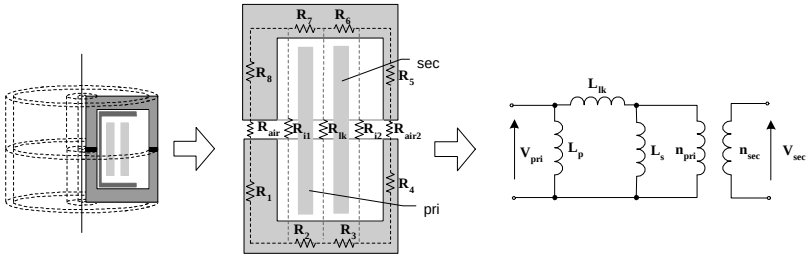

Fig. 4. Reluctance modelling for the coaxial windings arrangement.

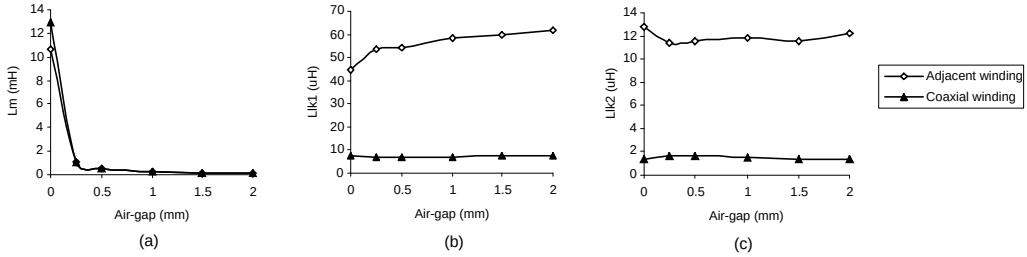

Fig. 5. Comparison of (a) the magnetising inductance (b) the primary leakage inductance and (c) the secondary leakage inductance between the adjacent (line with rhombic points) and coaxial (line with triangle points) winding arrangements.

flux of each winding occupies different space. In the coaxial arrangement there is only one leakage component Fig.4 whose value depends on the relative position between the two windings. As a result, the closer the windings are the better the coupling is. Since, there is less space for the leakage flux, the resulting inductance is smaller than that of the adjacent windings. The magnetising inductance is similar in both cases when a gap is present. This is expected as (1) instructs.

An important quantity for the rotating transformer is the effective winding resistance. This is made of two components; the AC and the DC resistance. The latter is the result of the material's electrical resistivity whereas the first one is the result of the high frequency effects taking place in the winding conductor when a high frequency current flows in it. Hurley et al. [13] derived an equation for calculating the resistance of a winding based on its structure and the current waveform. The following analysis for the optimisation of the rotating transformer windings is based on this method.

III. Design and optimisation

There are certain characteristics of an inductive interface that make its use difficult in energy transfer applications. The previous research has concentrated on the inductive interface itself and limited work has been done on the surrounding electronic parts. In this work the hypothesis is that the phase-shifted full bridge topology can effectively utilise the parasitic components of the transformer. According to the hypothesis the increased magnetising current assists the resonant transition and this compensates for the increased conduction losses that a rotating transformer yields.

The key target of the following design algorithm is the minimisation of the conduction losses while securing the soft-switching of the semiconductors. The conduction losses P_c of the MOSFETs and the transformer are given by (3).

$$P_c = I_{p_{rms}}^2 (R_{p_{eff}} + R_{DS_{on}}) + I_{s_{rms}}^2 R_{s_{eff}} \quad (3)$$

where $I_{p_{rms}}$ is the primary rms current, which is made of two components; the reflected load current and the magnetising current. The reflected load current is simply equal to the secondary current multiplied by the turns ratio of the transformer. Also, $R_{p_{eff}}$ is the primary winding effective resistance and $R_{s_{eff}}$ is the respective secondary resistance.

Due to the magnetising component the primary current is depended on the number of primary turns (or the size of the magnetising inductance),

$$I_m = \frac{V_{in} D T_{sw}}{2 L_m} \quad (4)$$

where V_{in} is the converter input voltage, D the duty ratio of the switches and T_{sw} the switching period. L_m is given by (1).

By combining (1) and (4) it becomes clear that for a specific input voltage and duty ratio the magnetising current is inversely proportional to the square of the number of turns,

$$I_m = \frac{\alpha}{N_p^2} \quad (5)$$

where

$$\alpha = V_{in} D T_{sw} \left(\frac{l_c}{\mu_0 \mu_c A_c} + \frac{l_g}{\mu_0 \mu_{air} A_g} \right) \quad (6)$$

There is a critical value of the current I_m, below which the resonant transition of the switches would not be successful (under light or no load). The critical energy E_{cr} needed to charge/discharge the capacitance of the MOSFETs is given by,

$$E_{cr} = \frac{1}{2} C_r V_{in}^2 \quad (7)$$

where the combined series capacitance is:

$$C_r = \frac{8}{3} C_{oss} + C_{xfmr} \quad (8)$$

C_{oss} being the MOSFET inherent capacitance at V_{in} and C_{xfmr} being the seen transformer capacitance. The critical current $I_{m_{cr}}$ can be calculated using the following equation,

$$I_{m_{cr}} = \sqrt{\frac{2 E_{cr}}{L_{lk_1}}} \quad (9)$$

where L_{lk_1} is the primary winding leakage inductance (or a series-connected external inductor). Regarding the winding resistance R_{eff}, this is given by,

$$R_{eff} = R_{DC} + \frac{\Psi}{3} \Delta^4 R_{DC} \left[\frac{I'_{rms}}{\omega I_{rms}} \right]^2 \quad (10)$$

where each component is expanded in the Appendix.

R_{eff} increases as the number of turns (hence, R_{DC} and the number of winding layers) increase. Fig.6 illustrates the effect of the number of winding turns in the conduction and the switching losses. These qualitative graphs visualise the main design trade off; the number of turns is a critical parameter that defines the magnetising current and thereby the soft-switching capability and the conduction losses of the converter.

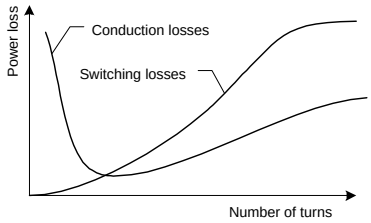

Fig. 6. The trade off between switching and conduction losses

By adjusting the number of primary turns N_p the designer could essentially eliminate the hot spots in the converter. The losses can be distributed between the power MOSFETS and the rotating transformer according to their thermal resistance and cooling capability.

The proposed algorithm (Fig.7) starts with the assumption that the primary side semiconductors perform resonant transitions for the entire range of output load. The major stages of the algorithm are:

1) *Set design specifications.* The input and output voltages (V_{in} and V_o), the frequency of operation, and the power level of the converter should be specified. The type of cooling that will be used as well as other details may help the decision making during the execution of the algorithm.
2) *Select converter topology and components.* During this stage the designer selects the rectifier type (full wave, current doubler). The calculation of the current and voltage levels is essential to select the components, transformer turns ratio etc
3) *Decide on the soft-switching range.* The resonant tank components are calculated at this stage. The target is a soft-switching operation under the entire range of loads. The energy that is needed to charge/discharge the MOSFET inherent capacitances must be calculated (7). The magnetising inductance will provide the required current to power the resonant transition. Hence, the magnitude of the critical magnetising current $I_{m_{cr}}$ is calculated using (9).
4) *Select core shape and size.* The appropriate shape for a rotating transformer application is the pot core. Regarding the size of the core, the starting point would be the calculation of the flux density using Amperes law. To improve the coupling a big cross-sectional area is needed. In a rotating transformer application the limitation is rarely the high flux density (and hysteresis losses). It is rather limited by the coupling requirements (the length of the air-gap and the number of winding turns). Once the core has been specified the required number of turns can be calculated by solving (5) for N_p for a known critical current.
5) *Winding optimisation.* The winding optimisation algorithm takes as input the winding geometry, the number

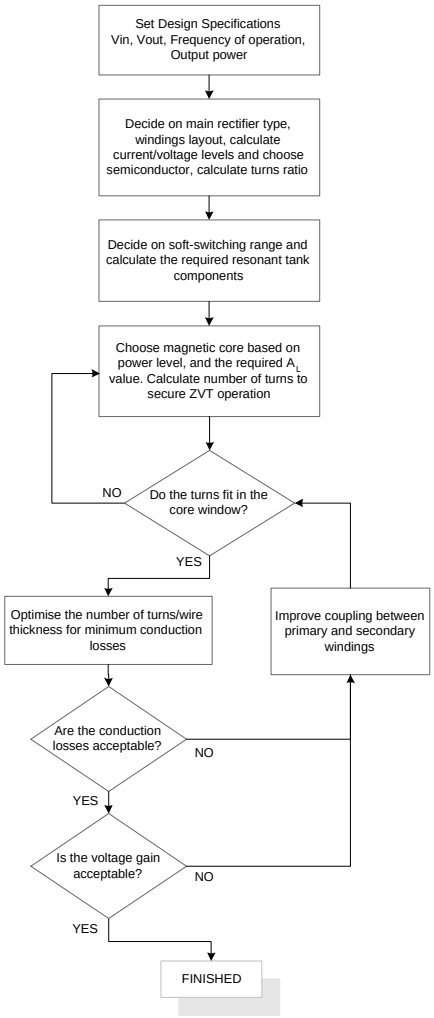

Fig. 7. Flow chart of the design and optimisation algorithm

of layers and the rms values of the current waveforms. It calculates the optimum values for the number of turns and wire thickness in order to minimise the goal function which is the overall conduction losses in the MOSFETs and the transformer windings.

6) *Check the voltage gain.* After the transformer design procedure has been completed an AC analysis is performed to test the resulting voltage gain. If the duty cycle cannot compensate for a possible impairment of the voltage gain, the leakage inductance of the transformer or the windings effective resistance (or both) need to be minimised. This will most likely require the use of fewer winding turns and possibly the increase of the magnetic core cross-sectional area.

IV. Experimental verification

To test the proposed algorithm a converter has been designed following the 6-stage process described in the previous section. The specifications for this converter appear in Table I.

TABLE I
Converter Specifications

	Min.	Nom.	Max.
Input voltage (V_{in})	250V	330V	380V
Output Power (P_{out})	0W		1000W
Output voltage (V_o)		54V$\pm$ 2%	
Switching frequency (F_{sw})		100kHz	

The converter topology is the current doubler. This type of rectifier/filter is preferred at high power levels ($> 500W$) due to the good utilisation of the magnetic core. It has also the ability to virtually double the secondary current using two inductors whose currents add at the load. To step down the voltage (worst case is for minimum input voltage) a transformer turns ratio of approximately 2.125 is needed with this type of rectifier. The maximum primary current is approximately 5.8A. At the specified voltage and current ratings IRFP450LC was the selected MOSFET. Two fast recovery diode sets (BYP99P-200) were used as the secondary side rectifier (although silicon carbide diodes or synchronous rectification could be used to further improve the efficiency).

In the third stage of the algorithm the soft-switching range of the converter must be specified. This is a proof of concept design and therefore, we set the soft switching range from 0-1000W (the full load range). Thus we will be able to weigh the benefits from fully resonant transitions at low load against the high conduction power losses at maximum loading. To allow the converter to soft-switch at minimum load, the critical magnetising current is 1.75A according to (9).

The next step is to choose the magnetic core type and size. For a rotating transformer the most appropriate core shape is the pot core due to its rotational symmetry. The distance between the two core halves is very important as it affects the electrical characteristics of the transformer and also defines the cost of manufacturing. Precise ball bearings can be used to achieve a air-gap clearance. The minimum distance between the core halves that can be realised with low cost ball bearings is in the range of a few tens of micrometres. This would be very close to a conventional transformer in terms of electrical behaviour. However, in this work we will assume the need for a clearance distance of a millimetre. The magnetising inductance needed is known from the previous step, so the magnetic core should have adequate size to produce the required inductance. After calculating the required cross-sectional area A_c of the core (to achieve the maximum possible magnetising inductance), P66/56 of the Ferroxcube family is selected.

In the next stage, (3) is evaluated iteratively to produce the 3D graph appearing in Fig.8 and the optimum number of turns and wire thickness are extracted from it.

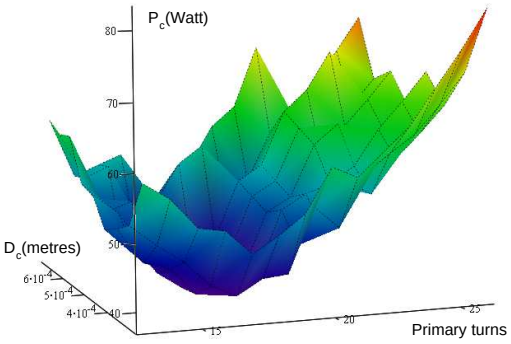

Fig. 8. Conduction power losses P_c with respect to the number of primary turns N_p and the wire thickness D_c

The resulting transformer has 17 turns of 14 strands of SWG27 (0.4mm) wire in the primary and 8 turns of 28 strands of SWG27 wire in the secondary. The windings are arranged in a coaxial form (the adjacent arrangement resulted in excessive winding resistances and leakage inductances). The electrical characteristics of the transformer appear in Table II.

TABLE II
TRANSFORMER ELECTRICAL PROPERTIES

Property	Value
Primary magnetising inductance	$177.45\mu H$
Primary leakage inductance	$3.03\mu H$
Secondary leakage inductance	$2.55\mu H$
Primary capacitance	$5pF$
Primary effective resistance	0.78Ω
Secondary effective resistance	0.042Ω

Finally, the voltage gain of the transformer is tested over the load range (Fig. 9) using the transfer function presented in the Appendix. The voltage gain should be adequate to produce the desired output voltage under the worst case operation (minimum input voltage and maximum loading).

The resulting converter efficiency readings appear in Fig.10(a) and are compared with the readings of a conventional PSFB. The duty cycles of the two circuits are also compared in Fig.10(b) to demonstrate the voltage gain effect.

The passive to active transition waveforms appear in Fig.11. The upper graphs refer to a PSFB with a conventional transformer and an external inductor to assist the resonant transitions. The lower graphs are for a PSFB with the rotating transformer. The proposed converter demonstrates a resonant operation for the entire load range whereas as seen in Fig.11(c) the conventional topology partially resonates even at 1kW of output power. The availability of more power in the resonant tank of the proposed converter is also proven by the slope of the V_{ds} during the capacitance discharge.

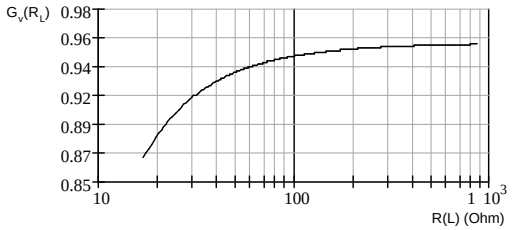

Fig. 9. The transformer voltage gain G_v as a function of the converter load R_L

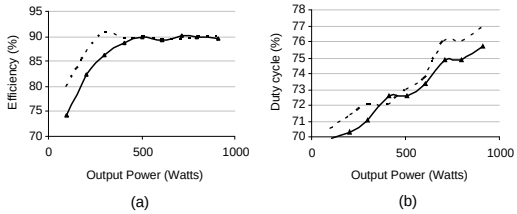

Fig. 10. The PSFB (a) efficiency and (b) duty cycle with respect to the load for the rotating transformer (solid line with triangular points) and the conventional transformer (dashed line)

During the converter operation a shift of a portion of the dissipated power from the rotating transformer to the power semiconductors is observed. This is important for two reasons; firstly, the transformer cooling is hard due to its core shape and the lack of air circulation in the structure (unless the rotational movement facilitates cooling). Secondly, it is advantageous to have a uniform distribution of the dissipated power rather than having hot spots in the power converter.

Finally, unlike the conventional converter, improving the soft-switching capability of a converter with a rotating transformer is important even at minimum loads. This is because the magnetising current could significantly contribute to the switching losses.

V. CONCLUSION

The aim of this work is to eliminate the use of slip rings for transferring power to the rotating parts of a device. This is done by using a magnetic interface (rotating transformer). The resulting converter is more economic, easy to manufacture and reliable. The optimisation of the magnetic interface can be achieved by using the derived equivalent electrical model. Its electrical parameters can be tuned by adjusting the geometry and layout of the windings. A design methodology is proposed that optimises the integration of a rotating transformer into a phase-shifted full bridge converter. It extends the soft switching range of it, hence compensating for the increase of the conduction losses due to the poor coupling coefficient. A 1kW prototype is evaluated and the results demonstrate an efficiency similar to that of the conventional topology (around 90%).

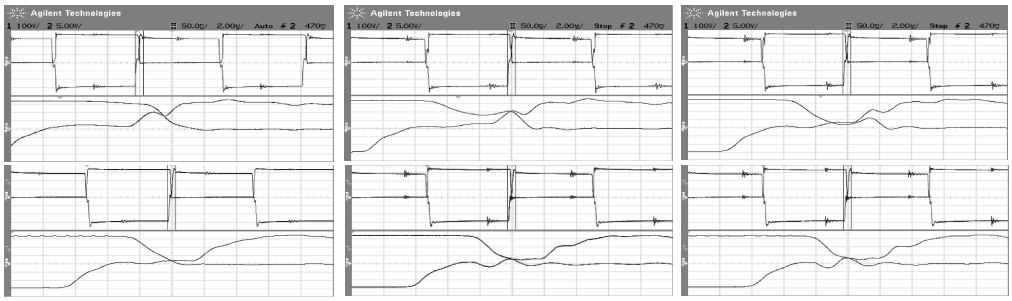

(a) (b) (c)

Fig. 11. Gate-source V_{gs} and drain-source V_{ds} voltages of the passive to active leg MOSFETs for different output power levels (a) 10W (b) 500W (c) 1000W. The upper graphs are of a conventional PSFB and the lower ones for a PSFB with a rotating transformer

APPENDIX

$$R_{eff} = R_{DC} + \frac{\Psi}{3}\Delta^4 R_{DC}\left[\frac{I'_{rms}}{\omega I_{rms}}\right]^2 \quad (11)$$

$$\Psi = \frac{5p^2 - 1}{15} \quad (12)$$

$$\Delta = \frac{d}{\delta_0} \quad (13)$$

where $R_{DC}(N)$ is the DC resistance which is a function of the number of turns N, d_c is the wire thickness, p is the number of winding layers, I_{rms} is the rms value of the current and I'_{rms} is the rms value of the derivative of the current flowing in the winding. The penetration depth δ_0 at the cyclic frequency ω, in a conductor of material with magnetic permeability μ_0 electrical conductivity σ is given by,

$$\delta_0 = \sqrt{\frac{2}{\omega\mu_0\sigma}} \quad (14)$$

Regarding the voltage gain, we assume a sinusoidal waveform at the fundamental frequency of the transformer current waveform and use the transfer function to work out the gain.

$$G_V(s) = \frac{s\gamma}{s^2\delta + s\epsilon + \zeta} \quad (15)$$

$$\gamma = L_m R_o \quad (16)$$

$$\delta = L_1 L_m + L_1 L_2 + L_m L_2 \quad (17)$$

$$\epsilon = L_m R_2 + L_m R_o + L_1 R_2 + L_1 R_o + R_1 L_m + R_1 L_2 \quad (18)$$

$$\zeta = R_1 R_2 + R_1 R_o \quad (19)$$

The rectifier/load circuit is approximated by a single resistor element R_o of value $(\pi^2/8) \cdot R_{load}$ where R_{load} is the real load resistance. This is done to avoid the complications caused by the non-linear behaviour of the rectifier circuit. Although this assumption [4] has been made for a resonant converter (with sinusoidal waveforms) it has been found to give accurate enough results for the purpose of engineering design.

REFERENCES

[1] E. E. Landsman, "Rotary transformer design," in *Power conditioning specialists conference record*, 1970, pp. 139–52.

[2] S. H. Marx and R. W. Bounds, "A kilowatt rotary power transformer," *IEEE Transactions on Aerospace and Electronic Systems*, vol. AES-7, no. 6, pp. 1157–63, 1971.

[3] A. Ghahary and B. Cho, "Design of transcutaneous energy transmission system using a series resonant converter," *IEEE Transactions on Power Electronics*, vol. 7, no. 2, pp. 261–269, 1992.

[4] G. Joung and B. Cho, "An energy transmission system for an artifi cial heart using leakage inductance compensation of transcutaneous transformer," *IEEE Transactions on Power Electronics*, vol. 13, no. 6, pp. 1013–1022, 1998.

[5] R. Mecke, C. Rathge, W. Fischer, and B. Andonovski, "Analysis of inductive energy transmission systems with large air gap at high frequencies," in *European Power Electronics and Applications 2003*, EPE, Ed. Toulouse, France: EPE Association, 2003.

[6] H. Abe, H. Sakamoto, and K. Harada, "A noncontact charger using a resonant converter with parallel capacitor of the secondary coil," *IEEE Transactions on Industry Applications*, vol. 36, no. 2, pp. 444–451, 2000.

[7] J. N. Park and R. L. Steigerwald, "Resonant inverter with improved control," 9 June 1987 1987.

[8] O. Patterson and D. Divan, "Pseudo-resonant full bridge dc/dc converter," *IEEE Transactions on Power Electronics*, vol. 6, no. 4, pp. 671–678, 1991.

[9] R. A. Fisher, K. D. T. Ngo, and M. H. Kuo, "A 500khz, 250w dc-dc converter with multiple outputs controlled by phase-shifted pwm and magnetic amplifi ers," in *High Frequency Power Conversion Conference*, 1988, pp. p.100–110.

[10] Y. Jang, M. Jovanovic, and Y.-M. Chang, "A new zvs-pwm full-bridge converter," *IEEE Transactions on Power Electronics*, vol. 18, no. 5, pp. 1122–1129, 2003.

[11] G. B. Koo, T. S. Kim, G. W. Moon, and M. J. Youn, "Analysis and design of a new phase shift full bridge converter with series-connected two transformers," in *European Power Electronics and Applications 2003*, E. Association, Ed. Toulouse, France: EPE, 2003.

[12] K. D. Papastergiou and D. E. Macpherson, "Contact-less transfer of energy by means of a rotating transformer," in *International Symposium on Industrial Electronics, ISIE*, Dubrovnic, Croatia, To appear.

[13] W. G. Hurley, E. Gath, and J. G. Breslin, "Optimizing the ac resistance of multilayer transformer windings with arbitrary current waveforms," *IEEE Transactions on Power Electronics*, vol. 15, no. 2, pp. 369–376, 2000.

References

[1] B. Carsten, *Modern Power Conversion Design Techniques. Segment three: Magnetics Design for High-Frequency Applications.* San Rafael: Bloom Associates Inc., 1st ed., 2001.

[2] F. Fisher, "The application of power electronics to airborne radar systems," tech. rep., The Institute of Electrical Engineers (IEE), 1999.

[3] F. Fisher, "Transfer of power across a moving interface," tech. rep., BAE Systems Inc, August 2002 2002.

[4] K. Milne, "Phased arrays in radar," tech. rep., The Institution of Electrical Engineers (IEE).

[5] C. Fernandez, O. Garcia, R. Prieto, J. Cobos, and J. Uceda, "Overview of different alternatives for the contact-less transmission of energy," in *IECON 02*, vol. 2, pp. 1318–1323 vol.2, 2002.

[6] H. Matsuki, Y. Yamakata, N. Chubachi, S.-I. Nitta, and H. Hashimoto, "Transcutaneous dc-dc converter for totally implantable artificial heart using synchronous rectifier," *Magnetics, IEEE Transactions on*, vol. 32, no. 5, pp. 5118–5120, 1996.

[7] H. Matsuki, M. Shiiki, K. Murakami, and T. Yamamoto, "Investigation of coil geometry for transcutaneous energy transmission for artificial heart," *Magnetics, IEEE Transactions on*, vol. 28, no. 5, pp. 2406–2408, 1992.

[8] C.-C. Tsai, B.-S. Chen, and C.-M. Tsai, "Design of wireless transcutaneous energy transmission system for totally artificial hearts," in *Circuits and Systems, 2000. IEEE APCCAS 2000. The 2000 IEEE Asia-Pacific Conference on*, pp. 646–649, 2000.

[9] R. Mecke, C. Rathge, W. Fischer, and B. Andonovski, "Analysis of inductive energy transmission systems with large air gap at high frequencies," in *European Power Electronics and Applications 2003* (EPE, ed.), (Toulouse, France), EPE Association, 2003.

[10] C. Zierhofer and E. Hochmair, "Geometric approach for coupling enhancement of magnetically coupled coils," *Biomedical Engineering, IEEE Transactions on*, vol. 43, no. 7, pp. 708–714, 1996.

[11] D. Pedder, A. Brown, and J. Skinner, "A contactless electrical energy transmission system," *IEEE Transactions on Industrial Electronics*, vol. 46, no. 1, pp. 23–30, 1999.

[12] K. Klontz, D. Divan, D. Novotny, and R. Lorenz, "Contactless power delivery system for mining applications," *IEEE Transactions on Industry Applications*, vol. 31, no. 1, pp. 27–35, 1995.

[13] J. Hirai, T.-W. Kim, and A. Kawamura, "Wireless transmission of power and information and information for cableless linear motor drive," *IEEE Transactions on Power Electronics*, vol. 15, no. 1, pp. 21–27, 2000.

[14] A. Kawamura, J. Hirai, and Y. Aoyama, "Autonomous decentralized manufacturing system using high-speed network with inductive transmission of data and power," in *Proceedings of the 1996 IEEE IECON 22nd International Conference on Industrial Electronics, Control, and Instrumentation, 1996*, vol. 2, pp. 940–945 vol.2, 1996.

[15] C.-G. Kim, D.-H. Seo, J.-S. You, J.-H. Park, and B. Cho, "Design of a contactless battery charger for cellular phone," *IEEE Transactions on Industrial Electronics*, vol. 48, no. 6, pp. 1238–1247, 2001.

[16] K. D. Papastergiou and D. E. Macpherson, "A 1kw phase-shifted full bridge converter incorporating contact-less transfer of energy," in *Power Electronics Specialists Conference, PESC 2005*, (Recife, Brazil), IEEE, 2005.

[17] W. T. McLyman and A. O. Bridgeforth, "Development of a rotary power transformer and inverter drive for spacecraft," in *Proceedings of the 18th Intersociety Energy Conversion Engineering Conference. AIChE. 1983*, pp. 1102–5.

[18] A. Esser and H.-C. Skudelny, "A new approach to power supplies for robots," *IEEE Transactions on Industry Applications*, vol. 27, no. 5, pp. 872–875, 1991.

[19] E. E. Landsman, "Rotary transformer design," in *Power conditioning specialists conference record*, pp. 139–52, 1970.

[20] S. H. Marx and R. W. Bounds, "A kilowatt rotary power transformer," *IEEE Transactions on Aerospace and Electronic Systems*, vol. AES-7, no. 6, pp. 1157–63, 1971.

[21] J. Hirai, T.-W. Kim, and A. Kawamura, "Study on intelligent battery charging using inductive transmission of power and information," *IEEE Transactions on Power Electronics*, vol. 15, no. 2, pp. 335–345, 2000.

[22] J. Hirai, T.-W. Kim, and A. Kawamura, "Practical study on wireless transmission of power and information for autonomous decentralized manufacturing system," *IEEE Transactions on Industrial Electronics*, vol. 46, no. 2, pp. 349–359, 1999.

[23] V. Niemela, G. Skutt, A. Urling, Y.-N. Chang, T. Wilson, J. Owen, H.A., and R. Wong, "Calculating the short-circuit impedances of a multiwinding transformer from its geometry," in *Power Electronics Specialists Conference, 1989. PESC '89 Record., 20th Annual IEEE*, pp. 607–617 vol.2, 1989.

[24] A. Urling, V. Niemela, G. Skutt, and T. Wilson, "Characterizing high-frequency effects in transformer windings-a guide to several significant articles," in *Applied Power Electronics Conference and Exposition, 1989. APEC' 89. Conference Proceedings 1989., Fourth Annual IEEE*, pp. 373–385, 1989.

[25] E. C. Cherry, "The duality between interlinked electric and magnetic circuits and the formation of transformer equivalent circuits," tech. rep., Imperial College, London, 29th January 1948 1948.

[26] R. Severns, E. Yeow, G. Woody, J. Hall, and J. Hayes, "An ultra-compact transformer for a 100 w to 120 kw inductive coupler for electric vehicle battery charging," in *Applied Power Electronics Conference and Exposition, 1996. APEC '96. Conference Proceedings 1996., Eleventh Annual*, vol. 1, pp. 32–38 vol.1, 1996.

[27] C. Fernandez, O. Garcia, R. Prieto, J. Cobos, S. Gabriels, and G. Van Der Borght, "Design issues of a core-less transformer for a contact-less application," in *Applied Power Electronics Conference and Exposition, APEC 2002*, vol. 1, pp. 339–345 vol.1, 2002.

[28] J. van Vlerken and P. Blanken, "Lumped modeling of rotary transformers, heads and electronics for helical-scan recording," *Magnetics, IEEE Transactions on*, vol. 31, no. 2, pp. 1050–1055, 1995.

[29] M. Jufer, N. Macabrey, and M. Perrottet, "Modeling and test of contact-less inductive energy transmission," *Mathematics and computers in simulation*, vol. 46, pp. 197–211, 1998.

[30] Y.-T. Huang, C.-J. Chen, and W.-B. Shu, "Finite element analysis on characteristics of rotary transformers," *Magnetics, IEEE Transactions on*, vol. 30, no. 6, pp. 4866–4868, 1994.

[31] J. Hayes, M. Egan, J. Murphy, S. Schulz, and J. Hall, "Wide-load-range resonant converter supplying the sae j-1773 electric vehicle inductive charging interface," *Industry Applications, IEEE Transactions on*, vol. 35, no. 0093-9994, pp. 884–895, 1999.

[32] S. Valtchev, B. Borges, and J. Klaassens, "Contactless energy transmission with optimal efficiency," in *IECON 02 [Industrial Electronics Society, IEEE 2002 28th Annual Conference of the]*, vol. 2, pp. 1330–1335 vol.2, 2002.

[33] Y. Kanai, M. Mino, T. Sakai, and T. Yachi, "A non-contact power-supply card powered by solar cells for mobile communications," in *Applied Power Electronics Conference and Exposition, 2000. APEC 2000. Fifteenth Annual IEEE*, vol. 2, pp. 1157–1162 vol.2, 2000.

[34] E. Rikos and E. Tatakis, "A high efficient 2kw on-board charging unit for electric vehicles, based on the flyback topology," in *European Power Electronics Conference* (E. Association, ed.), (Toulouse, France), 2003.

[35] C. Zierhofer and E. Hochmair, "High-efficiency coupling-insensitive transcutaneous power and data transmission via an inductive link," *Biomedical Engineering, IEEE Transactions on*, vol. 37, no. 7, pp. 716–722, 1990.

[36] H. Sakamoto and K. Harada, "A novel converter for non-contact charging with electromagnetic coupling," *IEEE Transactions on Magnetics*, vol. 29, no. 6, pp. 3228–3230, 1993.

[37] H. Sakamoto and K. Harada, "A novel circuit for non-contact charging through electro-magnetic coupling," in *Power Electronics Specialists Conference, 1992. PESC '92 Record., 23rd Annual IEEE*, pp. 168–174 vol.1, 1992.

[38] H. Sakamoto and K. Harada, "A novel converter for noncontact charging with electromagnetic coupling," in *Telecommunications Energy Conference, 1993. INTELEC '93. 15th International*, vol. 1, pp. 87–93 vol.1, 1993.

[39] R. D. Dowling, L. A. Gray, Jr, S. W. Etoch, H. Laks, D. Marelli, L. Samuels, J. Entwistle, G. Couper, G. J. Vlahakes, and O. H. Frazier, "Initial experience with the abiocor implantable replacement heart system," *Journal of Thoracic and Cardiovascular Surgery*, vol. 127, no. 1, pp. 131–141, 2004.

[40] S.-H. Lim, S.-R. Lee, and B.-S. Han, "A novel noncontact electric energy transfer system with regulating ac voltage/frequency," in *Power Electronics Specialists Conference, 2001. PESC. 2001 IEEE 32nd Annual*, vol. 2, pp. 713–717 vol.2, 2001.

[41] W. Becker, A. Engelhardt, F. Sorel, P. Schlittenhardt, and E. Wehner, "Technical aspects of the magnetic transcutaneous coupling of emg signals," *Magnetics, IEEE Transactions on*, vol. 6, no. 2, pp. 334–337, 1970.

[42] W. Weiss, G. Rosenberg, A. Snyder, T. Cleary, R. Gaumond, D. Geselowitz, and W. Pierce, "Permanent circulatory support systems at the pennsylvania state university," *Biomedical Engineering, IEEE Transactions on*, vol. 37, no. 2, pp. 138–145, 1990.

[43] T. Nishimura, T. Eguchi, K. Hirachi, Y. Maejima, K. Kuwana, and M. Saito, "A large air gap flat transformer for a transcutaneous energy transmission system," in *Power Electronics Specialists Conference, PESC '94 Record., 25th Annual IEEE*, pp. 1323–1329 vol.2, 1994.

[44] A. Ghahary and B. Cho, "Design of transcutaneous energy transmission system using a series resonant converter," *IEEE Transactions on Power Electronics*, vol. 7, no. 2, pp. 261–269, 1992.

[45] G. Joung and B. Cho, "An energy transmission system for an artificial heart using leakage inductance compensation of transcutaneous transformer," *IEEE Transactions on Power Electronics*, vol. 13, no. 6, pp. 1013–1022, 1998.

[46] G. Joung and B. Cho, "An energy transmission system for an artificial heart using leakage inductance compensation of transcutaneous transformer," in *Power Electronics Specialists Conference, PESC '96.*, vol. 1, pp. 898–904 vol.1, 1996.

[47] C. Zierhofer and E. Hochmair, "The class-e concept for efficient wide-band coupling-insensitive transdermal power and data transfer," in *Engineering in Medicine and Biology Society, 1992. Vol.14. Proceedings of the Annual International Conference of the IEEE*, vol. 2, pp. 382–383, 1992.

[48] R. Ridley, "The electric car; what does the future hold?," *Switching Power Magazine*, vol. 6, pp. 8–25, 2005 2005.

[49] N. Kutkut, D. Divan, D. Novotny, and R. Marion, "Design considerations and topology selection for a 120-kw igbt converter for ev fast charging," *Power Electronics, IEEE Transactions on*, vol. 13, no. 1, pp. 169–178, 1998.

[50] K. Klontz, D. Divan, and D. Novotny, "An actively cooled 120 kw coaxial winding transformer for fast charging electric vehicles," *IEEE Transactions on Industry Applications*, vol. 31, no. 6, pp. 1257–1263, 1995.

[51] H. Sakamoto and K. Harada, "A novel high power converter for non-contact charging with magnetic coupling," *IEEE Transactions on Magnetics*, vol. 30, no. 6, pp. 4755–4757, 1994.

[52] H. Sakamoto, K. Harada, and K. Yamasaki, "A novel high power converter for non-contact charging with magnetic coupling," in *Proceedings of 1995 International Conference on Power Electronics and Drive Systems, 1995*, pp. 461–464 vol.1, 1995.

[53] H. Sakamoto, K. Harada, S. Washimiya, K. Takehara, Y. Matsuo, and F. Nakao, "Large air-gap coupler for inductive charger [for electric vehicles]," *IEEE Transactions on Magnetics*, vol. 35, no. 5, pp. 3526–3528, 1999.

[54] J. Hirai, T.-W. Kim, and A. Kawamura, "Study on crosstalk in inductive transmission of power and information," *IEEE Transactions on Industrial Electronics*, vol. 46, no. 6, pp. 1174–1182, 1999.

[55] A. Green and J. Boys, "10 khz inductively coupled power transfer-concept and control," in *Power Electronics and Variable-Speed Drives, 1994. Fifth International Conference on*, pp. 694–699, 1994.

[56] J. Boys, G. Covic, and A. Green, "Stability and control of inductively coupled power transfer systems," *Electric Power Applications, IEE Proceedings-*, vol. 147, no. 1, pp. 37–43, 2000.

[57] Y. X. Xu, J. Boys, and G. Covic, "Modeling and controller design of icpt pick-ups," in *Power System Technology, 2002. Proceedings. PowerCon 2002. International Conference on*, vol. 3, pp. 1602–1606 vol.3, 2002.

[58] A. Esser and A. Nagel, "Contactless high speed signal transmission integrated in a compact rotatable power transformer," in *Fifth European Conference on Power Electronics and Applications (Conf. Publ. No.377). IEE. 1993*, pp. 409–14 vol, 1993.

[59] Y. Jang and M. Jovanovic, "A contactless electrical energy transmission system for portable-telephone battery chargers," *Industrial Electronics, IEEE Transactions on*, vol. 50, no. 3, pp. 520–527, 2003.

[60] H. Sakamoto and K. Harada, "A novel convertor for non-contact charging with electro-magnetic coupling," in *Magnetics Conference, 1993. INTERMAG '93., Digest of International*, pp. DQ–13, 1993.

[61] H. Abe, H. Sakamoto, and K. Harada, "A noncontact charger using a resonant converter with parallel capacitor of the secondary coil," *IEEE Transactions on Industry Applications*, vol. 36, no. 2, pp. 444–451, 2000.

[62] H. Abe, H. Sakamoto, and K. Harada, "Load voltage stabilization of noncontact energy transfer using three resonant circuit," in *Power Conversion Conference, 2002. PCC Osaka 2002. Proceedings of the*, vol. 2, pp. 466–471 vol.2, 2002.

[63] H. Abe, H. Sakamoto, and K. Harada, "A noncontact charger using a resonant converter with parallel capacitor of the secondary coil," in *Applied Power Electronics Conference and Exposition, 1998. APEC '98. Conference Proceedings 1998., Thirteenth Annual*, vol. 1, pp. 136–141 vol.1, 1998.

[64] W. H. Hayt, *Engineering Electromagnetics.* McGraw-Hill International Editions, 4th ed., 1981.

[65] A. F. Kip, *Fundamentals of Electricity and Magnetism.* Fundamental of Physics, Tokyo: McGraw-Hill International Editions, 2nd ed., 1969.

[66] N. Mohan, T. Underland, and W. Robbins, *Power Electronics, Converters Applications and Design*, vol. New York. J.Wiley and Sons Inc., 2nd ed., 1995.

[67] Unitrode-Corporation, *Unitrode Magnetics Design Handbook.* Merrimack: Unitrode Corporation, 1st ed., 2001.

[68] R. Williams, *High Frequency Multi-Element Transformers for Switched-Mode Power Supplies.* PhD thesis, University of Bristol, 1992.

[69] P. E. Wellstead, *Introduction to Physical System Modelling.* London: Academic Press INC, 1st ed., 1979.

[70] J. Wang, A. Witulski, J. Vollin, T. Phelps, and G. Cardwell, "Derivation, calculation and measurement of parameters for a multi-winding transformer electrical model," in *Applied Power Electronics Conference and Exposition, 1999. APEC '99*, vol. 1, pp. 220–226 vol.1, 1999.

[71] J. Hayes, N. O'Donovan, M. Egan, and T. O'Donnell, "Inductance characterization of high-leakage transformers vo - 2," in *Applied Power Electronics Conference and Exposition, 2003. APEC '03. Eighteenth Annual IEEE*, vol. 2, pp. 1150–1156, 2003.

[72] Ansoft-Corporation, *Magnetostatic problem solver handbook.* Ansoft.

[73] P. L. Dowell, "Effects of eddy currents in transformer windings," in *Proc. Inst. Elec. Eng.*, vol. 113, 1966.

[74] R. Ridley, "Proximity loss in magnetics windings," *Switching Power Magazine*, vol. 4, 2003 2003. MAGN.

[75] W. G. Hurley, "Optimizing core and winding design in high frequency transformers," in *IEEE International Power Electronics Congress*, pp. 2–13, 1996.

[76] W. G. Hurley, E. Gath, and J. G. Breslin, "Optimizing the ac resistance of multilayer transformer windings with arbitrary current waveforms," *IEEE Transactions on Power Electronics*, vol. 15, no. 2, pp. 369–376, 2000.

[77] W. G. Hurley, E. Gath, and J. G. Breslin, "Optimizing the ac resistance of multilayer transformer windings with arbitrary current waveforms," in *Power Electronics Specialists Conference*, vol. 1, pp. 580 –585, 1999.

[78] W. G. Hurley, W. H. Wolfle, and J. G. Breslin, "Optimized transformer design: inclusive of high-frequency effects," *IEEE Transactions on Power Electronics*, vol. 13, no. 4, pp. 651–659, 1998.

[79] J. G. Breslin and W. G. Hurley, "Derivation of optimum winding thickness for duty cycle modulated current waveshapes," in *Power Electronics Specialists Conference*, vol. 1, pp. 655 –661, 1997.

[80] J. N. Park and R. L. Steigerwald, "Resonant inverter with improved control," 9 June 1987 1987.

[81] R. L. Steigerwald, K. D. T. Ngo, and K. D. T, "Full-bridge lossless switching converter," April 28, 1988 1988.

[82] R. A. Fisher, K. D. T. Ngo, and M. H. Kuo, "A 500khz, 250w dc-dc converter with multiple outputs controlled by phase-shifted pwm and magnetic amplifiers," in *High Frequency Power Conversion Conference*, pp. p.100–110, 1988.

[83] L. Mweene, C. Wright, and M. Schlecht, "A 1 kw, 500 khz front-end converter for a distributed power supply system," in *Applied Power Electronics Conference and Exposition, 1989. APEC' 89.*, pp. 423–432, 1989.

[84] L. Mweene, C. Wright, and M. Schlecht, "A 1 kw 500 khz front-end converter for a distributed power supply system," *IEEE Transactions on Power Electronics*, vol. 6, no. 3, pp. 398–407, 1991.

[85] O. Patterson and D. Divan, "Pseudo-resonant full bridge dc/dc converter," *IEEE Transactions on Power Electronics*, vol. 6, no. 4, pp. 671–678, 1991.

[86] G. Ludwig and G. Franz, "Control study of a 500 khz, 250 w dc-dc converter," in *Applied Power Electronics Conference and Exposition, 1989. APEC' 89.*, pp. 433–438, 1989.

[87] Unitrode-Corporation, ed., *Unitrode Switching Regulated Power Supply Design Seminar Manual SEM-1100*. Merrimack: Unitrode Corporation, 1st ed.

[88] R. L. Steigerwald, "A review of soft-switching techniques in high performance dc power supplies," in *International Conference on Industrial Electronics, Control, and Instrumentation*, vol. 1, pp. 1–7, 1995.

[89] C. K. R. L. Loh, *Phase Shifted Bridge Converter for a High Voltage Application*. PhD thesis, University of Edinburgh, 2004.

[90] J. Sabate, V. Vlatkovic, R. Ridley, F. Lee, and B. Cho, "Design considerations for high-voltage high-power full-bridge zero-voltage-switched pwm converter," in *Applied Power Electronics Conference and Exposition, 1990. APEC '90, Conference Proceedings 1990., Fifth Annual*, pp. 275–284, 1990.

[91] V. Vlatkovic, J. Sabate, R. Ridley, F. Lee, and B. Cho, "Small-signal analysis of the phase-shifted pwm converter," *IEEE Transactions on Power Electronics*, vol. 7, no. 1, pp. 128–135, 1992.

[92] R. Ayyanar and N. Mohan, "Novel soft-switching dc-dc converter with full zvs-range and reduced filter requirement. i. regulated-output applications," *IEEE Transactions on Power Electronics*, vol. 16, no. 2, pp. 184–192, 2001.

[93] G. B. Koo, T. S. Kim, G. W. Moon, and M. J. Youn, "Analysis and design of a new phase shift full bridge converter with series-connected two transformers," in *European Power Electronics and Applications 2003* (E. Association, ed.), (Toulouse, France), EPE, 2003.

[94] R. Redl, L. Balogh, and D. Edwards, "Optimum zvs full-bridge dc/dc converter with pwm phase-shift control: analysis, design considerations, and experimental results," in *Applied Power Electronics Conference and Exposition, 1994. APEC '94. Conference Proceedings 1994., Ninth Annual*, pp. 159–165 vol.1, Theoretical or Mathematical Experimental, 1994.

[95] R. Redl, N. Sokal, and L. Balogh, "A novel soft-switching full-bridge dc/dc converter: analysis, design considerations, and experimental results at 1.5 kw, 100 khz," *Power Electronics, IEEE Transactions on*, vol. 6, no. 3, pp. 408–418, 1991.

[96] Unitrode-Corporation, ed., *Unitrode Switching Regulated Power Supply Design Seminar Manual SEM-600*. Merrimack: Unitrode Corporation, 1st ed.

[97] R. W. Erickson, *Fundamentals of Power Electronics*, vol. 1. Boston: Kluwer Academic Publishers, 1st ed., 1997.

[98] Agilent, "Operation note: 11941a close-field probe," 1987.

[99] D. S. Smith, "Signal and noise measurement techniques using magnetic field probes," in *IEEE 1999 EMC Symposium*, IEEE, 1999.

[100] "Radiation limits and measurement standard (mpt-1570)," Technical paper MPT1570, Radiocommunications Agency, December 1999 1999. Useful to base my EMI measurements.

[101] S. Pirog and R. Stala, "Ac to dc converter for contactless electrical energy transmission. practical results," in *European Power Electronics and Applications 2003* (EPE, ed.), (Toulouse, France), EPE Association, 2003.

[102] "Power supply engineer's guide to calculate dissipation for mosfets in high-power supplies," white paper AN1832, Dallas Semiconductor - Maxim, December 2002 2002.

[103] MoogComponents, "Fiber optic rotary joint (forj) datasheet."